STRONTIUM AND SAMARIUM DIFFUSION IN DIOPSIDE

by

MARK ALBERT SNEERINGER

S. B., Massachusetts Institute of Technology

SUBMITTED IN PARTIAL FULFILLMENT
OF THE REQUIREMENTS FOR THE
DEGREE OF

DOCTOR OF PHILOSOPHY

at the

MASSACHUSETTS INSTITUTE OF TECHNOLOGY

December, 1981

Signature of Author _____
Center for Geoalchemy, Department of Earth and Planetary Sciences
December 18, 1981

Certified by _____
Stanley R. Hart
Thesis Supervisor

Accepted by _____
Chairman, Departmental Committee on Graduate Students

STRONTIUM AND SAMARIUM DIFFUSION IN DIOPSIDE

by

MARK ALBERT SNEERINGER

Submitted to the

Department of Earth and Planetary Sciences, M.I.T.

December, 1981

in partial fulfillment of the requirements

for the degree of

Doctor of Philosophy

ABSTRACT

The volume diffusion of strontium has been measured as a function of temperature, pressure, and crystallographic direction in a synthetic diopside ($CaMgSi_2O_6$), using a Cameca IMS 3f ion microprobe. Temperatures ranged from 1100 to 1300°C for pressures to 20 Kbar. Sr diffusivities were also determined for the c direction of the synthetic crystals by a radiotracer (^{85}Sr) and sectioning technique and Rutherford backscattering spectroscopy; and for natural samples by the radiotracer method. The natural sample diffusion coefficients were approximately two orders of magnitude higher than those for the synthetic samples, although the activation energies were similar. The diffusion of samarium in the synthetic crystals was also studied with respect to temperature, pressure, and crystallographic direction using the ion probe. Results for the two cations were comparable (within a factor of 2 at most T's).

Arrhenius relations for diffusion ($D = D_o \exp[-\Delta H_a/RT]$) were calculated for different pressures and analytical systems, and activation volumes (ΔV_a) were derived from the equation $D = D' \exp[-P\Delta V_a/RT]$. Values of ΔV_a were negative for strontium diffusion. An empirical relation which adequately described the temperature and pressure dependence of D was calculated for Sr in the c direction of the synthetic samples. The result is:

$$D(P,T) = 1200(cm^2/sec)\ \exp[-122(Kcal/mol)/RT(°K)]\ \exp[-P(bar)/(2.94T - 4640)R]$$

The expression for D_{Sr} in the natural samples at one atmosphere is:

$$D(0,T) = 54(cm^2/sec)\ \exp[-97(Kcal/mol)/RT(°K)]$$

A single compensation trend for all the data was evident for all values of D_0 and ΔH_a in the synthetic crystals. In the study temperature range at one

atmosphere, transport rates for the three crystallographic directions were nearly identical due to compensation with a crossover point at 1111°C and $6 \times 10^{-17} cm^2/sec$. Directional compensation was also observed in two other studies (Misener, 1974; Clark and Long, 1971).

Comparison of the three analytical techniques yielded excellent agreement in the study range at one atmosphere (D's within a factor of two). The comparison illustrated the fact that technique-generated effects can cause the observed concentration curves to differ from the true diffusion profiles. Treatment for removal of these modifiers was effected through variations in analytical parameters and through empirical data reduction methods. Ion probe depth profiling was proven to be a useful tool for the study of diffusion in crystalline silicates, where extremely slow transport rates limit the applicability of more established techniques such as radiotracer and sectioning.

The data were examined in the context of other studies which used similar methods and/or investigated the same variables. Pressure dependence of D in most experiments resulted in positive values of ΔV_a, as opposed to the activation volumes calculated here. The comparisons showed that there are three basic sources of differences between diffusivities for a given phase and element. Sample defect composition, experimental techniques, and analytical methods are all capable of causing variations in the measured D's.

A number of models of geologic processes were investigated in light of the present data. Closure temperatures (T_c) were calculated for examples of mineral-mineral age-dating, and major and trace element geothermometry. High values of T_c indicate that pyroxenes record emplacement events and are generally not disturbed unless a fluid enters the system. Isotopic equilibration times were examined for lower crustal xenoliths and the mantle source region for MORB using the formula of Hofmann and Hart (1978). Equilibration was shown to be too fast for production of isotopic anomalies in MORB via dis-equilibrium melting. Also, reasonable residence times at lower crustal temperatures were shown to produce the mineralogical-scale isotopic homogeneity observed in a nodule from Kilbourne Hole, New Mexico. Models which use diffusion control of exsolution textures of pyroxenes to infer cooling rate information were evaluated with data from this study. Depending on the originally assumed diffusivities, cooling times were either shortened considerably or remained unchanged. Finally, values of electrical conductivity (σ) derived from the data and the Nernst-Einstein equation were compared with measured values of σ for pyroxenes, with no agreement being shown.

Thesis supervisor: Stanley R. Hart, Professor of Geology and Geochemistry.

TABLE OF CONTENTS

I. INTRODUCTION

> Persons attempting to find a motive in this narrative will be prosecuted; persons attempting to find a moral in it will be banished; persons attempting to find a plot in it will be shot.
> BY ORDER OF THE AUTHOR
>
> --Twain

Interest in the kinetic processes of geologic systems has increased rapidly in the recent past (e.g., Lasaga and Kirkpatrick, 1981). This is due mainly to the evolving petrogenetic models which require non-equilibrium behavior to account for chemical variations in rocks produced by processes which cannot be directly observed. Diffusion in both solids and liquids is an important component in many of these models, and significant advances have been made in the characterization of diffusive parameters in melts (for summary, see Hofmann, 1980). However, data for important elements in rock-forming minerals are considerably less abundant, primarily because of the scarcity of usable material and the slow transport rates in crystalline solids. The existing numbers do point to one important conclusion; namely that diffusion in liquids is orders of magnitude faster than in coexisting minerals at the same temperature. Thus, for problems like non-equilibrium phenocryst growth, knowledge of the diffusion coefficient (D) in the solid does not significantly change the resulting elemental distributions. Solid state transport does play a major role in processes such as geothermometry/geobarometry, the survival of phenocryst zonation, and isotopic heterogeneities in crystalline systems.

The mineral class pyroxene occurs in many igneous rocks and the kinetic behavior of pyroxenes in general is being investigated for a number of

reasons. The chemical composition of coexisting pairs of clino- and orthopyroxenes (CPX and OPX, respectively) are used to determine the pressure and temperature conditions of rock formation or metamorphism. Certain necessary assumptions regarding the attainment of chemical equilibrium can be examined if kinetic factors are known. Pyroxene fractionation is frequently involved in the production of the melts which cool to form the oceanic crust. Chemical variations in these mid-ocean ridge basalts are not yet completely understood and the diffusive behavior of certain elements in pyroxenes may hold part of the answer. Diopside (Di) is a representative clinopyroxene with the chemical formula $CaMgSi_2O_6$.

Strontium is a significant trace element for two basic reasons. (1) Because of size and charge similarities to the major element calcium, it may be possible to model the behavior of Ca with that of Sr. (2) Strontium is also involved in a geologically important radioactive decay scheme, ^{87}Rb to ^{87}Sr, which is used to date rock-forming events and as an isotopic tracer to gain information on a given sample's source and history. Considerable and systematic variations have been found in the initial ratio of $^{87}Sr/^{86}Sr$ within a given rock type. Kinetic factors are called upon to explain the observed fluctuations by a number of authors.

This study presents data on volume diffusion of Sr in diopside measured as a function of temperature, pressure, and crystallographic direction. Diffusion coefficients have also been derived for samarium, a representative rare earth element and the parent in the Sm/Nd radioactive decay system.

While attempting to derive the diffusion parameters for Sr and Sm in diopside, this study has also become a comparison of materials, experimental methods, and analytical techniques. Early experiments utilized natural samples and a radioactive tracer and sectioning technique. Later, large,

iron-free single crystals of diopside were synthesized (both with and without Sr and Sm) and a Cameca IMS 3f ion microprobe became available for analyzing the samples. Emphasis of this study then shifted to diffusion couples with concentration gradients analyzed via the depth profiling mode of the ion probe. Another series of one atmosphere experiments using a surface-deposited stable tracer was also examined with the ion probe and by a third technique, Rutherford Backscattering Spectroscopy. Radiotracer and sectioning runs with the synthetic crystals have made possible a comparison with the natural samples. High pressure data were derived from synthetic crystal diffusion couples and ion probe analysis.

Data from each method and sample type are internally consistent, giving good Arrhenius relations and logical time studies. Comparison among analytical techniques at one atmosphere shows agreement for a given sample type. Activation energies are comparable as are the D values in the measured temperature range (1100 to 1300°C). Large differences in the transport rate were measured between the natural and synthetic diopsides, which may be due to different defect levels in the two materials. The effect of crystallographic direction does not appear to be significant, with observed variations falling within the range of experimental uncertainty. Increasing pressure appears to cause an increase in D at constant temperature, but structural factors may be able to explain this unexpected result.

The data will be discussed with respect to diffusion theory, the experimental and analytical variables, and other pertinent measurements in solids and liquids. Applications of the data to geochemical problems will also be considered.

II. DIFFUSION THEORY

"The study of diffusion is the perfect crime." - Shimizu

There are essentially two ways to describe diffusion. It can be approached as a macroscopic process which generally obeys a set of empirical rules or it can be dealt with on an atomistic level, involving structural and thermodynamic properties of the material and the diffusant. Although the latter provides a more rigorous treatment based on fundamental physical principles, exact calculations are impossible for most materials (including silicates) because of nonavailability of thermodynamic data and poor understanding of the transport process. Nevertheless, the approach is important because its derivations give significance to the values generated from the observed phenomena and provide a framework for the discussion of diffusion mechanisms.

Empirical Calculations of D

A pair of equations first developed for diffusion by Adolph Fick in 1855 are the basis for any description of the transport process. Fick's First Law states that the flux of a diffusant through a plane is proportional to its concentration gradient perpendicular to that plane. The equation in one dimension has the form:

$$J = -D\ (dc/cx) \qquad (2\text{-}1)$$

where J is the flux and D is a proportionality constant known as the diffusion coefficent. The negative sign is a convenience arising from the flux direction, which is toward lower concentration. Experiments show that D is independent of the magnitude of dc/dx for a given concentration. Thus its form is similar to Fourier's equation for heat conduction:

$$F = -K\ (\partial\Theta/\partial x)$$

where Θ is the temperature and K the thermal conductivity. The independence

of the proportionality constant from the other terms of the flux equation is also observed in Ohm's Law:

$$I = K(E/R)$$

I is the current, E the potential, and R the resistance. K is a constant which, by use of standard units, is equal to one.

In three dimensions the diffusion equation can be written

$$J = -D\nabla c$$

The simple flux equation is not very useful in experimental systems which have not reached steady state, which leads to the development of the time dependent Second Law. Equation (2-1) is combined with a mass balance expression for flux into and out of the opposite ends of a volume element Δx thick. (Figure 1).

$$J_1 = J_2 - \Delta x(\partial J/\partial x) \qquad (2\text{-}2)$$

The net increase of diffusant in the volume element is given by

$$-\Delta x(\partial J/\partial x) = \Delta x(\partial c/\partial t) \qquad (2\text{-}3)$$

Substitution of equations (2-1) and (2-3) into equation (2-2) gives Fick's Second Law (in one dimension):

$$\frac{\partial c}{\partial t} = \frac{\partial}{\partial x}\left(\frac{D\partial c}{\partial x}\right)$$

The dependence of D on concentration is often negligible or assumed to be so, leading to:

$$\frac{\partial c}{\partial t} = \frac{D\partial^2 c}{\partial x^2} \qquad (2\text{-}4)$$

Solutions of equation (2-4) have been developed for a variety of initial and boundary conditions and a fairly complete list of pertinent solutions can be found in Crank (1975) or other diffusion texts. Two solutions which are of interest to this study are the so-called "thin film" and "constant surface concentration" solutions. D is assumed to be independent of diffusant

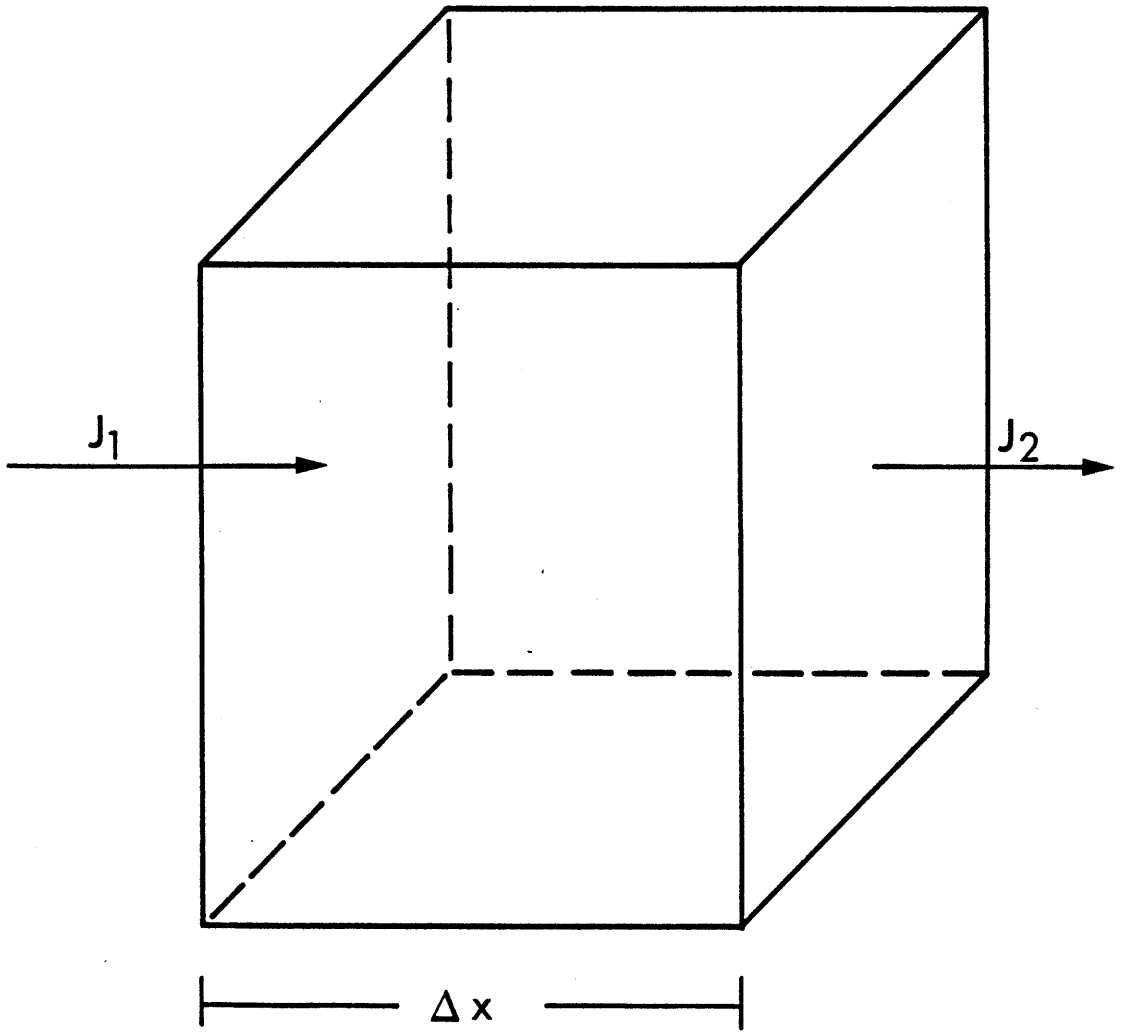

Figure 2-1. Element of volume with length Δx along the flux direction. Faces perpendicular to flux are defined to have unit area. J_1 and J_2 are fluxes.

concentration in both cases discussed here. The treatment of D varying with concentration will be examined later.

If an infinitely thin film of solute is coated on the end of a rod in which the x axis coincides with the long direction, the following initial and boundary conditions are true.

$$\begin{aligned} C(x) &= 0, \quad t = 0 \\ C(\infty) &= 0, \quad t \geq 0 \\ C(0) &\to \infty, \quad t \to 0 \end{aligned}$$

The solution to equation (2-4) which satisfies these conditions is:

$$C(x,t) = \frac{M}{\sqrt{\pi Dt}} \; e^{-x^2/4Dt} \qquad (2\text{-}5)$$

where M is the total amount of diffusant. If the film were at the center of the rod, equation (2-5) would have a two in the denominator of the pre-exponential term but would otherwise be unchanged. This is due to the additive nature of the diffusion equation such that any material which would have diffused beyond a boundary is simply reflected at that plane. In the above case, the boundary is at x = 0.

The solution of constant surface concentration is an outgrowth of the problem of a diffusion couple. In this situation the conditions are:

$$\begin{aligned} C(x) &= 0, \; x \geq 0, \; t = 0 \\ C(x) &= C_o, \; x < 0, \; t = 0 \\ C(-\infty) &= C_o, \; t \geq 0 \\ C(\infty) &= 0, \; t \geq 0 \end{aligned}$$

The equation that satisfies the above is

$$C(x,t) = \frac{C_0}{2} \; \mathrm{erfc}(x/2\sqrt{Dt}) \qquad (2\text{-}6)$$

where erfcα is called the error function complement and has the form

$$\mathrm{erfc}\alpha = 1 - \frac{2}{\sqrt{\pi}} \int_o^{\alpha} e^{\eta^2} \, d\eta$$

Useful qualities of erfcα are erfc(0) = 1, erfc (∞) = 0, and erfc(-α) = 1 + erfcα. It is seen that $C(0,t) = C_o/2$ for all values of t > 0. Therefore,

the solution for constant surface concentration is

$$C(x,t) = C(0,t)\text{erfc}(x/2\sqrt{Dt}) \qquad (2\text{-}7)$$

for positive values of x. These two solutions (equations (2-5) and (2-7)) are used extensively in the data treatment of this study.

In the strict sense, the D defined by Fick's First Law is actually the self-diffusion coefficient (D). Experiments which measure this quantity use a minor or radioactive isotope of the solvent element as a tracer, enabling the observation of movement among otherwise identical atoms.

Tracer diffusion (D*) is the transport of a low concentration diffusant in a solvent which has different chemical characteristics. The equation that relates D* to D is:

$$D = D^* \left(1 + \frac{d\ln\gamma'}{d\ln N}\right) \qquad (2\text{-}8)$$

where γ' is the activity coefficient of the solvent species and N is its mole fraction (Shewmon, 1963, p. 126). In a dilute solution where Henry's and Raoult's laws apply, γ' is a constant and equation (2-8) reduces to $D = D^*$. Also, if the labelled and unlabelled atoms are chemically equivalent, γ' does not depend on the ratio N/N^* so that for $N + N^* =$ constant, $(d\ln\gamma'/d\ln N) = 0$ and (2-8) again reduces to $D = D^*$ (self diffusion).

The chemical diffusion coefficient ($\tilde{D}$) is the quantity measured in an interdiffusion experiment, in which D generally varies with concentration. From the analysis first applied by Darken (1948) and reproduced in various texts (e.g., Shewmon, 1963; Crank, 1975; Anderson, 1981) the relationship of $\tilde{D}$ to D is:

$$\tilde{D} = D_1 N_2 + D_2 N_1 \qquad (2\text{-}9)$$

where the subscripts refer to the components of a binary system. In the case of a trace element (species 1), $N_1 \ll N_2 \simeq 1$ and equation (2-9) becomes $\tilde{D} = D_1$. $\tilde{D}$ is also related to D_1^* and D_2^* by substituting equation (2-8)

into (2-9).

$$D = D_1^* N_2 \left(1+\frac{d\ln\gamma'_1}{d\ln N_1}\right) + D_2^* N_1 \left(1+\frac{d\ln\gamma'_2}{d\ln N_2}\right) \qquad (2\text{-}10)$$

This is simplified by a consequence of the Gibbs-Duhem equation

$$N_1 d\gamma'_1 + N_2 d\gamma'_2 = 0$$

such that

$$\frac{d\ln\gamma'_1}{d\ln N_1} = \frac{d\ln\gamma'_2}{d\ln N_2} \quad .$$

This leads to a final form of equation (2-10):

$$\tilde{D} = (D_1^* N_2 + D_2^* N_1) \left(1 + \frac{d\ln\gamma'_1}{d\ln N_1}\right) \qquad (2\text{-}11)$$

Although $\tilde{D}$ and D^* may often be the same as D, it must be remembered that these apparent equalities arise from particular experimental conditions. Under other, non-ideal conditions the above relations are necessary to extract the self diffusion coefficient.

The initial formulation of the diffusion equations does not take into account multicomponent systems where the transport of all species is coupled. Fick's first law states that the flux of a component occurs in the direction opposite to its concentration gradient. However, examples are plentiful where an element appears to diffuse up it's concentration gradient, at least for finite times. Onsager (1945) developed an extension of the first law which deals with this flux (J_i) of component i:

$$J_i = -\sum_{k=1}^{n} D'_{ik} \left(\partial c_k/\partial x\right) \qquad (2\text{-}12)$$

where D'_{ik} is the coefficient for diffusion of i due to the concentration gradient $(\partial c_k/\partial x)$ of component k, and n is the number of components. Since the concentration gradients and the fluxes (J_{ik}) are not linearly independent, one of each can be eliminated from the above. This leads to:

$$J_i = -\sum_{k=1}^{n-1} D_{ik} \left(\partial c_k/\partial x\right) \qquad (2\text{-}13)$$

where D_{ik} does not necessarily equal D'_{ik}. Equation (2-13) is often written in matrix notation.

$$(J) = -[D]\ (dc/cx) \tag{2-14}$$

For n = 3, the expanded version of the above is:

$$\begin{pmatrix} J_1 \\ J_2 \end{pmatrix} = -\begin{bmatrix} D_{11} & D_{12} \\ D_{21} & D_{22} \end{bmatrix} \begin{pmatrix} \partial c_1/\partial x \\ \partial c_2/\partial x \end{pmatrix} \tag{2-15}$$

The negative sign in the matrix formulation of Fick's Law (equation 2-14) requires that D be positive, but does not put such a limit on the individual D_{ik}'s. D_{ii} will be positive because it is derived from the effects of the species' own concentration gradient. The off-diagonal terms can be negative and, if sufficiently large, will dominate the flux of component i, thus giving "uphill" diffusion. Using component 2 in equation (2-15) as an example:

$$J_2 = -D_{21}\partial c_1/\partial x - D_{22}\partial c_2/\partial x,$$

If $-D_{21} >> D_{22}$ and the gradients are of the same direction and magnitude, J_2 will have a negative sign, meaning atoms are moving toward higher concentration of component 2.

Since the effect produced by the concentration gradient of one element on another is not readily apparent, the concept of irreversible thermodynamics has been applied to the problem. In this approach, the fluxes are expressed in terms of chemical potentials (μ_k) instead of concentrations (Onsager, 1945). An equation analogous to (2-13) which incorporates μ_k's is:

$$J_i = \sum_{k=1}^{n-1} L_{ik}(\partial\mu_k/\partial x) \tag{2-16}$$

where L_{ik} is known as the thermodynamic or phenomenological diffusion coefficient. One term has been eliminated as before because of the conservation of the flux and the Gibbs-Duhem equation which states:

$$\sum_{i=1}^{n} c_i d\mu_i = 0$$

Once again, a matrix notation is useful in describing the overall interdiffusion.

$$(J) = [L]\ (\partial\mu/\partial x) \tag{2-17}$$

The chemical potential of component i (μ_i) is a function of the concentrations of all species in the system. If μ_{ik} is defined as $(\partial\mu_i/\partial c_k)_{T,P,c_n}$, the concentration gradients and chemical potential gradients are related by:

$$\partial\mu_i/\partial x = \sum_{k=1}^{n-1} \mu_{ik}(\partial c_k/\partial x), \tag{2-18}$$

It is seen that the effect of the concentration gradients on the flux is not a simple relationship. For complex natural systems it may be easier to deal with μ_i's, which cannot be directly measured but whose behavior follows the laws of thermodynamics, than to predict the effect of variations in concentration gradients through time.

Equation (2-14) can be simplified by diagonalizing the matrix [D] to give a series of equations which are equivalent to Fick's law and can be solved in a similar fashion. In order to do this, another matix [S] must exist which, when related to the generally non-symmetric [D], gives the following:

$$[S]^{-1}[D]\ [S] = [\Lambda] \tag{2-19}$$

where $[S]^{-1}[S]$ = the identity matrix and $[\Lambda]$ is a diagonal matrix. Substituting equation (2-19) into (2-14) gives:

$$[S]^{-1}(J) = [\Lambda]\ [S]^{-1}(\partial c/\partial x) \tag{2-20}$$

or for each component i:

$$\overline{J}_i = {}_i\overline{\partial c/\partial x} \tag{2-21}$$

where $\bar{J}_i$ and $\overline{\partial c/\partial x}$ are elements of the vectors $[S]^{-1}(J)$ and $[S]^{-1}(\partial c/\partial x)$, respectively. This is equivalent to Fick's First Law (equation (2-1)). In matrix terminology, the Λ_i's are eigenvalues of [D] and the columns of [S] are the eigenvectors. Kirkaldy (1970, p. 74) shows that by knowing a series of boundary conditions the Λ's can be calculated. Once these are established the columns of [S] can be derived.

An easier and therefore less general approach to multi-component diffusion involves treating the system as a pseudobinary problem between the flux of one component and that of all others combined. This gives rise to what is known as an "effective binary diffusion coefficient" (EBDC) (Cooper, 1968) which obeys Fick's laws under certain conditions. These are: (1) that all concentration gradients are along the same direction although sign may vary, and (2) the system is semi-infinite in the diffusion direction or at steady state. An EBDC measured for a particular system would not be applicable to a system containing different components or having a different pattern of concentration gradients. Within geologic systems it may be safe to apply an EBDC for Ca in one basalt melt to another basalt, but not to a granitic liquid. Also, description of diffusion by EBDC's has no meaning in the case of "uphill" diffusion. Various points on the concentration curve will give values of $\partial c/\partial x$ which will be negative or infinite.

The situation for measurement of multicomponent diffusion is complicated. On one hand is a general theory requiring the difficult determination of a set of parameters and which has only been applied to fairly simple systems. On the other is a simplification which allows measurement of an effective diffusion coefficient but which lacks the generality needed to predict behavior in different systems. Fortunately, trace elements can be assumed

to diffuse independently within a system, allowing direct measurement of values pertinent to processes such as isotopic re-equilibration.

All diffusion coefficients are measured with respect to some frame of reference. In an experimental study this is usually a fixed point or set of points to which the movement of the diffusing species is related. The container is often chosen as this point and that leads to the name "cell-fixed or laboratory" reference frame. Brady (1975) discussed the pitfalls of this sort of frame in that there are many choices that can lead to different results for the same experiment. Therefore, frames of reference that are independent of external controls are necessary for easy comparison of data.

A number of choices exist that use as their reference points some weighted average of the velocities of the chemical components of the system. This can be the velocity of the center of volume, for instance. Calculations in these "mean velocity" reference frames are presented here. The velocity of component i is measured with respect to a laboratory frame L, yielding a value v_i^L. A set of dimensionless weighting factors w_i^a, such as the mole percent, mass fraction, or partial volume, are chosen such that:

$$\sum_{i=1}^{n} w_i^a = 1 \qquad (2\text{-}22)$$

The mean velocity $\bar{v}^{aL}$ is defined for n components by:

$$\bar{v}^{aL} = \sum_{i=1}^{n} w_i^a v_i^L \qquad (2\text{-}23)$$

and the velocity of the ith component with respect to this mean velocity is:

$$v_i^a = v_i^L - \bar{v}^{aL} \qquad (2\text{-}24)$$

The flux of this species can be written:

$$J_i^a = c_i v_i^a \tag{2-25}$$

where c_i is the concentration of i. If equation (2-24) is substituted into this expression which is then multiplied by w_i^a/c_i and summed for all i, an equation which defines mean velocity reference frames appears (Anderson, 1981).

$$\sum_{i=1}^{n} (w_i^a/c_i)J_i^a = \sum_{i=1}^{n} w_i^a v_i^L - \bar{v}^{aL} \sum_{i=1}^{n} w_i^a = 0 \tag{2-26}$$

The four common frames can be related through this expression. For the molecular frame, referred to by the use of the superscript n:

$$w_i^n = x_i = c_i \bar{V} \tag{2-27}$$

where x_i is the mole fraction and $\bar{V}$ the molar volume of the phase. Substituting equation (2-27) into (2-26) yields:

$$\bar{V} \sum_{i=1}^{n} J_i^n = 0 = \sum_{i=1}^{n} J_i^n \tag{2-28}$$

In the mass-fixed or mean mass frame:

$$w_i^m = \omega_i = c_i M_i \tag{2-29}$$

where ω_i is the mass fraction and M_i the gram formula weight of component i. Therefore:

$$\sum_{i=1}^{n} M_i J_i^m = 0 \tag{2-30}$$

For the volume-fixed or mean volume reference frame:

$$w_i^v = c_i V_i \quad \text{and} \quad \sum_{i=1}^{n} V_i J_i^v = 0 \tag{2-31,2-32}$$

where V_i is the partial molar volume. The fourth is the lattice-fixed or kth component frame where the velocities are referred to the velocity of a single component k. In this case:

$$w_i^o = \delta_{ik} \tag{2-33}$$

with $\delta_{ik} = 0$ except for i = k for which $\delta_{ik} = 1$. This gives:

$$J_k^o = 0 \tag{2-34}$$

Anderson (1981) relates a measured value of D^v to the other frames of reference (D^a) for a simple binary interdiffusion problem. Using $(J^a) = -[D^a]\ (\partial c_i/\partial x)$ with component 2 as the dependent species, he reaches the equation:

$$D^a = (w_2^a/w_2^v)D^v \tag{2-35}$$

or specifically:

$$D^o = (1000/c_2V_2)D^v \tag{2-36a}$$

$$D^m = (M_2/V_2)D^v \tag{2-36b}$$

$$D^n = (x_2/c_2V_2)D^v \tag{2-36c}$$

In a very dilute solution, as in tracer diffusion, it can be assumed that there is no volume change or shift in the center of mass. Thus $\bar{v}^{aL} = 0$ and all reference frames are coincident with the laboratory frame and all choices of fixed points give the same D. However, in experiments where volume or mass changes occur such that, for instance, the boundary between two interdiffusing phases shifts, the different reference frames will affect the calculated diffusion coefficient.

Atomistic Approach to D

Now that the basic equations have been presented, the atomistic properties of the diffusion coefficient will be discussed. In the absence of applied fields, such as strain or electrical fields, the movement of a diffusing atom is random. The presence of a concentration gradient does not imply that an atom moves preferentially in the direction of decreasing concentration. Flow occurs because there are more ions to jump from a

higher concentration plane to an adjacent lower one than vice versa.

If two adjacent planes are separated by distance α, the number of atoms leaving one plane for the other is given by:

$$N = (1/2)n_i \Gamma \delta t$$

where n_i is the number of atoms on the plane i and Γ is the jump frequency. Calculating a net flux for this system gives:

$$J = (1/2)\ (n_1 - n_2)\Gamma \qquad (2\text{-}37)$$

Substituting $n_i/\alpha = c_i$ and $c_1 - c_2 = -\alpha \partial c/\partial x$ into equation (2-37) gives a form of Fick's First Law:

$$J = -(1/2)\alpha^2 \Gamma (\partial c/\partial x) \qquad (2\text{-}38)$$

Therefore, in one dimension:

$$D = (1/2)\alpha^2 \Gamma \qquad (2\text{-}39)$$

The factor 1/2 comes from the fact that there are two sites into which an atom on a given plane can jump (+x or -x), one of which is down the concentration gradient. This number changes as the number of possible jumps changes. In a simple three dimensional case, the factor is 1/6. The jump frequency (Γ) is proportional to the number of nearest neighbors (γ), the probability that any given neighbor site is vacant (p_v), and the frequency with which the atom will jump into that vacancy (ω). Thus:

$$\Gamma = \gamma p_v \omega \qquad (2\text{-}40)$$

A number of schemes for the movement of an atom in a lattice have been suggested and examples of most have been documented. The vacancy mechanism requires that the diffusant move by jumping to an adjacent lattice position which is vacant. Thus the jump frequency is strongly dependent on p_v. In the interstitial mechanism, the diffusing atom moves on a sub-lattice composed of the interstices of the structure. p_v is derived for this sub-lattice, as opposed to the main structure, and for the case of very little

diffusant, can be assumed to be unity. A variation of this process is interstitialcy. The atom moves from an interstice to a lattice site, "bumping" the solvent ion on that site into another interstice. When this mechanism is delocalized along a line in the structure (n+1 ions for n sites) it is called crowdion. The involvement of both lattice and interstitial sites and the possibility for delocalization severaly hamper the derivation of a meaningful jump frequency. When diffusion occurs without the benefit of vacancies or interstitialcy, the simple trading of position of two ions requires a relatively large amount of energy to deform the lattice as they pass. On the other hand, the correlated movement of three or more ions requires considerably less distortion of the lattice. This ring mechanism is thought to dominate because of the lower energy involved, even though the probability of all the atoms moving at once is considerably less than for two ions.

For the case of the vacancy mechanism, p_v can be assumed to be the fraction of vacant sites (N_v) in the lattice if the diffusant is similar in charge and size to the atom it replaces. This is true in self diffusion and nearly so in strontium substitution for calcium. Therefore, combining equations (2-39) and (2-40) gives:

$$D = \gamma a_o^2 N_v \omega \qquad (2\text{-}41)$$

where $a_o = \sqrt{2}\alpha$ and γ incorporates the factor 1/2 from equation (2-39). The diffusion coefficient is thus a function of atomistic properties which can be calculated or estimated for certain materials and diffusion mechanisms.

The number of nearest neighbors (γ) and the distance to them (a_o) can be derived for crystalline solvents using structural data and assumed diffusion mechanisms. Estimation of vacancy density is not so straight-

forward. A value for the equilibrium number of vacancies (N_v^e) is given by the ideal mixing of two components (in this case, solvent and vacancies). The equation which results is:

$$N_v^e = \exp(-\Delta G_v/RT) \tag{2-42}$$

where

$$\Delta G_v \equiv \Delta H_v - T\Delta S_v \tag{2-43}$$

is the change in free energy per mole of added vacancies, over and above the energy of mixing (Shewmon, 1963). ΔH_v dominates the right hand side of equation (2-43) and it is reasonable to ignore the entropy term. This change in enthalpy has been measured for a number of metals, simple oxides, and halides. The range is typically 20 to 60 Kcal/mole. The relationship of this enthalpy to measured activation energies will be discussed later. Examination of equation (2-42) shows that as temperature increases, N_v^e does likewise.

The concept of the "activated complex" must be introduced at this point in order to evaluate the jump frequency ω. An activated complex is defined as a region containing an atom midway between two stable sites. Within this formalism it is assumed that local equilibrium is obtained. Thus the average jump frequency can be written:

$$\omega = N_n \nu = \nu \exp(-\Delta G_n/RT) \tag{2-44}$$

where N_n is the mole fraction of activated complexes, ν is the frequency with which the complexes result in a new position for the diffusing atom, and ΔG_n is the difference in free energy between a region without and one with an activated complex. Once again the entropy term is much smaller than the enthalpy component and ΔG_n can be replaced by ΔH_n. The values of the frequency factor (ν) are at best estimates and therefore only a rough idea of the size of ω and D can be obtained.

Substituting equation (2-42) and (2-44) into (2-41) gives the following:

$$D = \gamma a_o^2 \nu \exp\ (-(\Delta H_v + \Delta H_n)/RT) \qquad (2\text{-}45)$$

This is equivalent to the empirical Arrhenius relationship derived from experimentation:

$$D = D_o \exp(-\Delta H_a/RT) \qquad (2\text{-}46)$$

where D_o is the value of D at $1/T = 0$ and is known as the frequency factor and ΔH_a is the activation energy. The two components of ΔH_a (ΔH_v and ΔH_n) can be described as the enthalpy of vacancy formation and the enthalpy of vacancy movement, respectively. (Although only vacancies have been discussed so far, the arguments are applicable to any point defects such as impurity ions.) At relatively low temperatures the number of equilibrium defects (N_v^e) is so small compared to the impurity level of the material that the defect fraction is independent of T and the ΔH_v term can be ignored. Therefore, in this temperature span $\Delta H_a = \Delta H_n$. This natural impurity level control of diffusion gives rise to the term extrinsic region. At high temperatures N_v^e becomes important and ΔH_a incorporates both ΔH_v and ΔH_n. This is called the intrinsic region because of the control that the equilibrium formation of defects has on the diffusion process. The temperature (T_x) where the natural impurity concentration equals the equilibrium defect concentration (N_v^e) calculated by equation (2-42) is the point at which the switch from extrinsic to intrinsic control ideally occurs. It can be calculated by rearranging equation (2-42) to give:

$$T_x = -\Delta H_v/R\ln C \qquad (2\text{-}47)$$

with C the natural defect concentration. The transition from intrinsic to extrinsic control manifested as a change in slope of a line plotted on an Arrhenius plot of lnD vs 1/T. The break occurs at $1/T_x$.

Although these intrinsic and extrinsic domains are well documented in metals where activation energies are low and high purity materials can

be obtained, it is debatable whether this phenomenon have ever been observed in silicates. Using ΔH_a's obtained for diffusion of major elements in olivine by Buening and Buseck (1973) and Morioka (1980) where a break in slope was observed, a natural defect level which is improbably low is required to generate the apparent T_x. The experimental results may be attributable to other factors such as a thermally activated change in diffusion mechanism (and/or creative curve fitting).

A number of authors have noted a positive linear correlation between $\ln D_o$ and ΔH_a within a given solvent structure type (most recently: Winchell, 1969; Winchell and Norman, 1969; Hofmann, 1980; Hart, 1981; and Lasaga, 1981). Equation (2-46) shows that when increases in both D_o and ΔH_a tend to balance each other, the diffusion coefficient does not change drastically. This empirical relation is thus known as the <u>compensation effect</u>. Ruetschi (1958) used potential energy surfaces and statistics to explain this coupling for a variety of kinetic processes. The end result for diffusion is given by modification of his equation (20):

$$D = [\nu r_o^2 \exp(\frac{\alpha r_o}{k} \gamma^* U_o)] \exp(-U_o/kT) \qquad (2\text{-}48)$$

where ν is a thermal vibration frequency, r_o is the interatomic distance, α is the coefficient of thermal expansion, γ^* is a proportionally constant, U_o is the potential energy barrier, and k is Boltzman's constant. The term in brackets is equivalent to D_o and so the potential energy (U_o) is a common factor of both ΔH_a and D_o. Earlier, local thermodynamic equilibrium was assumed for the activated complex. Examining the more general form of equation (2-45):

$$D = \gamma a_o^2 \nu \exp(-(\Delta G_v + \Delta G_n)/RT) \qquad (2\text{-}49)$$

and making use of the relationship $\Delta G = \Delta H - T\Delta S$, the exponential term can be split to give:

$$D = [\gamma a_o^2 \nu \exp(\frac{\Delta S_v + \Delta S_n}{R})] \exp(\frac{-\Delta H_v + \Delta H_n}{RT}) \qquad (2\text{-}50)$$

Once again the bracketed term equals D_o (no T dependence). A relationship between ΔS and ΔH is predicted by Ruetschi's analysis and its application to an equilibrium system, and this relation has been observed for both kinetic and equilibrium processes.

Thus there is a theoretical basis for the empirically derived compensation effect. An application for this is to use it as a rough test of the reliability of data. If on a plot of lnD vs ΔH_a a point falls significantly off the compensation line for the material studied, chances are that the data are derived from some other process than diffusion. Hart (1981) discusses the usefulness of compensation in the study of closure temperature (T_c) for cooling minerals. Closure temperature, the apparent T at which diffusion becomes insignificant, is related to D_o and ΔH_a by the following equation (Dodson, 1973):

$$T_c = (\Delta H_a/R)/\ln\left(\frac{-ART_c^2 D_o/a^2}{\Delta H_a dT/dt}\right) \qquad (2\text{-}51)$$

where A is a geometric factor for grain shape, a is the radius of the grains, and dT/dt the average cooling rate over the closure temperature range. The area of a $\ln D_o$ vs ΔH_a compensation plot can be contoured for T_c with a given dT/dt. Thus the different but systematic closure temperatures for various elements in a single structure type can be examined easily.

It has been implicitly assumed up until this point that all possible jumps that a diffusing atom can make are equally probable and independent of each other. This requires that all the neighbors of the ion are identical, which is not true in the case of vacancy controlled diffusion. One of the neighbors is a vacancy from which the atom has just moved. There is a higher probability that the atom will next move to that site than to another site. The movement is said to be correlated and equation (2-41) is no longer accurate. Instead:

$$D = \gamma f a_o^2 N_v \omega \tag{2-52}$$

where f is the correlation coefficient. For tracer diffusion a fairly good estimate of the quantity f can be obtained by applying the equation:

$$f = 1 - 2/z \tag{2-53}$$

with z equal to the number of nearest neighbors (Shewmon, 1963). This assumes that the movement of the vacancy itself is not correlated (all neighbors are equivalent). More complicated calculations of f can be undertaken but for most purposes the above equation suffices.

If vacancy movement is correlated the factor f will be much smaller than predicted by equation (2-53). This can occur in a dilute solution where the solute is "bound" to a vacancy by size or charge considerations. The probability of the solute exchanging with the vacancy (ω_2) is greater than that of the solvent (ω_1), but the speed at which the solute will move through the lattice is dependent on the rate of exchange between the solvent and the vacancies, so that:

$$D_2 \propto a_o^2 \omega_1 = f a_o^2 \omega_2 < a_o^2 \omega_2 \tag{2-54}$$

Calculation of f (Shewmon, 1963, p. 107) yields:

$$f = \frac{\omega_1}{\omega_1 + \omega_2} \quad \text{and} \quad D_2 \propto a_o^2 \frac{\omega_1 \omega_2}{\omega_1 + \omega_2}$$

It is seen that the slower of the two jump frequencies determines D_2. If $\omega_2 >> \omega_1$, $D_2 \propto a_o^2 \omega_1$ and if $\omega_1 >> \omega_2$, $D_2 \propto a_o^2 \omega_2$. In the case of $\omega_1 = \omega_2$, $D_2 \propto a_o^2 \omega_2/2$.

To complete the treatment, a term for the dissociation of vacancy-solute pairs must be incorporated in D_2. In this case f is calculated to be:

$$f = \frac{\omega_1 + nk_1/2}{\omega_1 + \omega_2 + nk_1/2} \tag{2-56}$$

where n is the number of neighbors of a vacancy which do not have an adjacent solute atom and k_1 is the frequency of the exchange between the vacancy and one of these neighbors. Substituting this f into equation (2-52) yields:

$$D_2 = \frac{\gamma N_v a_o^2 \omega_2 (\omega_1 + nk_1/2)}{\omega_1 + \omega_2 + nk_1/2} \qquad (2\text{-}57)$$

Correlation of solute atoms to vacancies can cause large differences between measured diffusion coefficients and those expected by simply assuming that the tracer will diffuse at the same rate as the solvent.

Pressure Effects and ΔV_a

The systems for which the preceding equations have been developed have all been isobaric. A pressure dependence of D can be obtained by differentiating the atomistic expression (equation 2-49) with respect to pressure:

$$\left[\frac{\partial \ln(D/\gamma a_o^2 \nu)}{\partial P}\right]_T = -\frac{1}{RT}\left[\left(\frac{\partial \Delta G_v}{\partial P}\right)_T + \left(\frac{\partial \Delta G_n}{\partial P}\right)_T\right] \qquad (2\text{-}58)$$

Thermodynamics provides the equality:

$$\left(\frac{\partial \Delta G}{\partial P}\right)_T = \Delta V$$

which can be substituted into equation (2-58) to give:

$$\left[\frac{\partial \ln(D/\gamma a_o^2 \nu)}{\partial P}\right]_T = -\frac{1}{RT}(\Delta V_v + \Delta V_n) = -\frac{\Delta V_a}{RT} \qquad (2\text{-}59)$$

where ΔV_v is the partial molar volume of vacancies, ΔV_n the partial molar volume of activated complexes, and ΔV_a is called the activation volume. As pressure is increased, a number of vacancies are destroyed in an attempt to relieve this pressure. The same is true of activated complexes. The decrease in these species will cause a corresponding drop in D. This physically reasonable scheme is the basis for equation (2-59). For a given ΔV_a (the coefficient of the rate at which vacancies and activated complexes

are eliminated) an increase in P will cause a decrease in D.

This behavior has been reported in numerous experiments and ΔV_a has been calculated empirically from a plot of lnD vs P (slope = $-\Delta V_a/RT$). The equation thus developed is similar to equation (2-46) and is:

$$D = D'\exp(-P\Delta V_a/RT) \qquad (2\text{-}60)$$

with D' being the value of D for a given temperature at "zero" pressure.

Various attempts to study the effect of temperature on ΔV_a, of pressure on ΔH_a, and the relationship between the two have been undertaken. Rice and Nachtrieb (1959) used a model whereby transport takes place by the proper combination of the normal vibrations which occur in the lattice. Their result for the effect of P is identical to equation (2-59). They further developed an equation which incorporates the melting temperature of the material at pressure (T_m) to give the overall expression:

$$\frac{d\ln D}{d(T_m/T)} = -RT_o\left[H_o - \frac{\Delta V_a}{(dT_m/dP)}\right] \qquad (2\text{-}61)$$

where T_o and ΔH_o are the melting point and activation energy, respectively, at zero pressure.

An outgrowth of equation (2-60) which is often used to approximate the observed behavior of D is:

$$D(P,T) = D_o\exp(-\Delta H_a/RT)\exp(-P\Delta V_a/RT) \qquad (2\text{-}62)$$

A question arises as to which values of D_o and ΔH_a are to be used in this equation; either the values at P = 0 as suggested by equation (2-60) or values derived from equations which include a pressure effect within each term. A similar problem can be seen for ΔV_a with respect to temperature. Experimental results show that the dependence of D_o and ΔH_a on pressure and of ΔV_a on temperature vary from positive to negative depending on the system. So, equation (2-62) is useful only if the relationships describing

D_o, H_a, and ΔV_a are known for the phase and diffusant in question.

Directional Effect

So far, the equations used have been for diffusion in an isotropic medium, where D is the same in all directions. This is not the case in non-cubic crystals. In order to take this anisotropy into account the equation $J = - D\nabla c$ is replaced by:

$$J_x = -D_{11}\partial c/\partial x - D_{12}\partial c/\partial y - D_{13}\partial c/\partial z \qquad (2\text{-}63a)$$

$$J_y = -D_{21}\partial c/\partial x - D_{22}\partial c/\partial y - D_{23}\partial c/\partial z \qquad (2\text{-}63b)$$

$$J_z = -D_{31}\partial c/\partial x - D_{32}\partial c/\partial y - D_{33}\partial c/\partial z \qquad (2\text{-}63c)$$

with x, y, and z being mutually perpendicular axes. These equations can be rewritten:

$$\begin{pmatrix} J_x \\ J_y \\ J_z \end{pmatrix} = -\begin{bmatrix} D_{11} & D_{12} & D_{13} \\ D_{21} & D_{22} & D_{23} \\ D_{31} & D_{32} & D_{33} \end{bmatrix} \begin{pmatrix} \partial c/\partial x \\ \partial c/\partial y \\ \partial c/\partial z \end{pmatrix} \qquad (2\text{-}64)$$

where $[D_{ij}]$ is a second-order tensor and the other terms are vectors (first-order tensors). Diffusion is centrosymmetric, meaning transport occurs at equal rates along a given direction and its opposite. This is a quality of a second-order tensor. Another quality is that if a concentration gradient is applied along a symmetry axis, the flux will also be along that axis. And if the gradient is applied along a direction contained in a symmetry plane, the direction of the flux will also be in that plane. Diopside is monoclinic, with b as the symmetry axis and a mirror plane contained in the ac plane. If the orthogonal axes are chosen such that y coincides with b and z coincides with c, four terms become zero in D_{ij}.

$$D_{ij} = \begin{bmatrix} D_{11} & 0 & D_{13} \\ 0 & D_{22} & 0 \\ D_{31} & 0 & D_{33} \end{bmatrix} \qquad (2\text{-}65)$$

Thus for a concentration gradient along the c axis, the flux is given by the vectoral sum $J_x + J_z = -D_{13}\partial c/\partial x - D_{33}\partial c/\partial z$. Calculation of the flux due to a gradient along the a axis is more complicated because it does not coincide with a principal axis. First, the gradient $\partial c/\partial a$ is expressed in terms of the perpendicular axes:

$$\frac{\partial c}{\partial a} = \frac{\partial c}{\partial x} + \frac{\partial c}{\partial z} \qquad (2\text{-}66)$$

The flux due to the terms on the right are calculated:

$$J_x = -D_{11}\partial c/\partial x - D_{13}\partial c/\partial z \qquad (2\text{-}67a)$$

$$J_z = -D_{31}\partial c/\partial x - D_{33}\partial c/\partial z \qquad (2\text{-}68b)$$

and the sum of these two gives the flux due to $\partial c/\partial z$:

$$J_a = -(D_{11} + D_{31})\partial c/\partial x - (D_{13} + D_{33})\partial c/\partial z \qquad (2\text{-}68)$$

A summary of D_{ij} for each crystal class is given in Table 1.

Examining equation (2-41), $D = \gamma a_o^2 N_v \omega$, it is seen that the directional variation of D can be attributed to changes in a_o and ω. Distances to the nearest neighbors and the energy to create an activated complex (ΔG_n) are dependent on the crystal structure. If it is assumed that Sr moves in diopside by a vacancy mechanism over the M_2 sites, an ordering of the expected diffusion coefficients for the different crystallographic directions can be derived from jump distances and estimates of the "ease of jump".

The diopside structure contains chains of corner sharing silica tetrahedra oriented along the c axis. The chains form layers in the bc plane and the M_2 sites lie between the layers at the bases of the tetrahedra. (Figure 2). Movement in the a direction means crossing these sheets, a dis-

Table 2-1. Matrices for the second order tensor, Dij.

cubic

$$\begin{bmatrix} D_{11} & 0 & 0 \\ 0 & D_{11} & 0 \\ 0 & 0 & D_{11} \end{bmatrix}$$

tetragonal

$$\begin{bmatrix} D_{11} & 0 & 0 \\ 0 & D_{11} & 0 \\ 0 & 0 & D_{33} \end{bmatrix}$$

orthorhombic

$$\begin{bmatrix} D_{11} & 0 & 0 \\ 0 & D_{22} & 0 \\ 0 & 0 & D_{33} \end{bmatrix}$$

monoclinic (b = symmetry axis)

$$\begin{bmatrix} D_{11} & 0 & D_{13} \\ 0 & D_{22} & 0 \\ D_{31} & 0 & D_{33} \end{bmatrix}$$

triclinic

$$\begin{bmatrix} D_{11} & D_{12} & D_{13} \\ D_{21} & D_{22} & D_{23} \\ D_{31} & D_{32} & D_{33} \end{bmatrix}$$

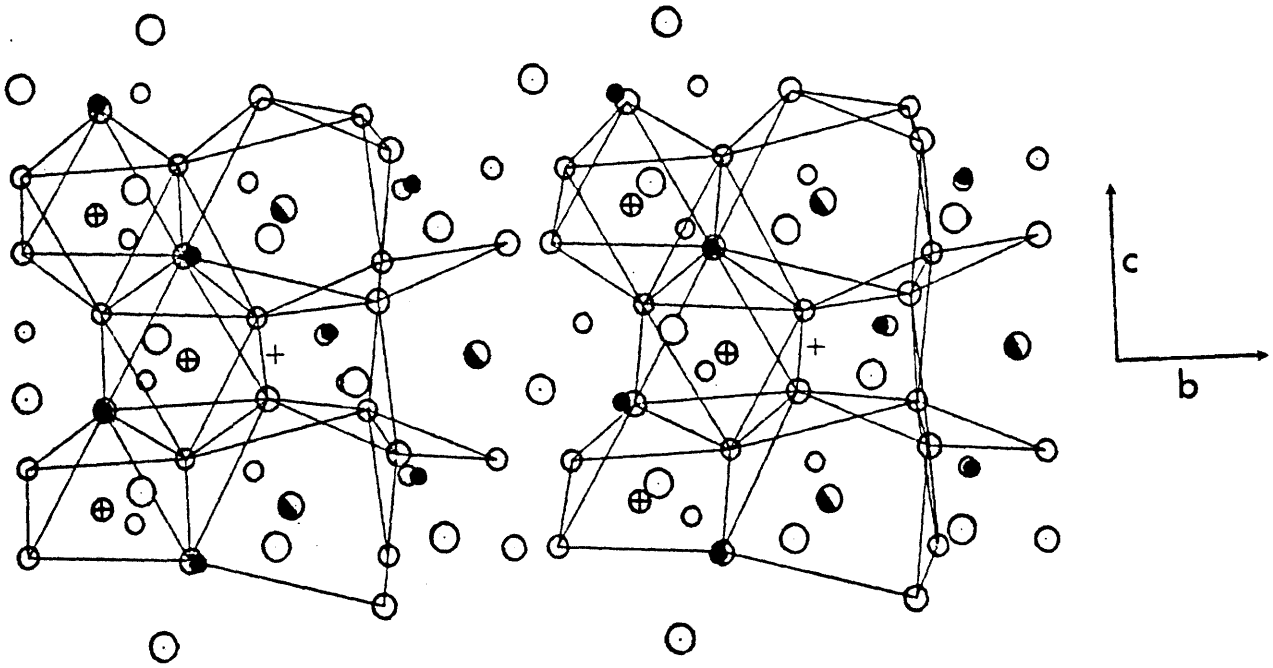

a. Cation polyhedra version

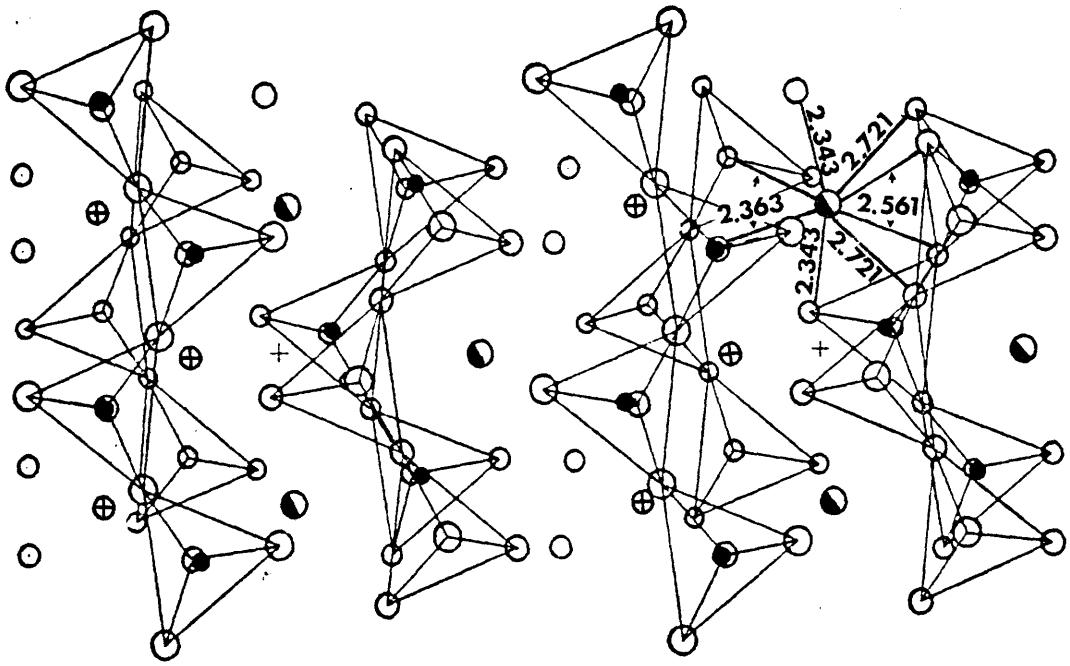

b. Silicate chain version

Figure 2-2. Diopside structure (Matsui, 1973). (a) outline of M(1) and M(2) polyhedra. (b) oultine of silica tetrahedra chains showing M(2)-O bond lengths; values (in Å) are from Levien and Prewitt (1981). Oxygen-open circles, silicon-filled circles, calcium-half filled circles, magnesium-crosses.

tance of about 6 Å while "pushing" through a highly distorted octahedral site between two chains. Diffusion in the b direction occurs within the plane of the M_1 and M_2 sites but must cross a row of the smaller M_1's to reach the next M_2 approximately 6 Å away. The c direction should be the fastest diffusion due to a zig-zag chain of adjacent M_2 sites along the c axis. The jump distance is about 3 Å. So, qualitatively, it would appear that the ordering of transport rates should be first c, followed by a, because although the distance is great the path is independent of the movement of the atoms on the M_1 site. The b direction has this problem and thus would rank last. However, counterbalancing effects of distance and intermediate positions, and experimental errors may well make the relative values indeterminant. Data will be brought to bear on this question in a later chapter.

D as a Function of Concentration

If the diffusion coefficient is a function of concentration, Fick's Second Law takes on the more general form:

$$\frac{\partial c}{\partial t} = \frac{\partial}{\partial x}\left(D\frac{\partial c}{\partial x}\right) \qquad (2\text{-}69)$$

Solutions to this are numerical in nature with the most widely used the Boltzmann-Matano analysis. The conditions of the experiments studied with this formalism are:

$$C = C_o,\ x < 0,\ t = 0$$

$$C = 0,\ \ x > 0,\ t = 0$$

$$C = C_o,\ x = -\infty,\ t > 0$$

$$C = 0,\ x = \infty,\ t > 0$$

This is a graphical solution in which experimental data are plotted on a graph of $C(x)/C_o$ vs distance. The slope of the curve through the data (dc/dx) must equal zero at both $x = \infty$ ($C = 0$) and $x = -\infty$ ($C = C_o$). From

the boundary conditions it follows that:

$$\int_0^{C_o} x\,dc = 0 \qquad (2\text{-}70)$$

There is a point of origin for the x axis (x = 0) which satisfies the boundary conditions and the equation above. Physically, this means x equals 0 at a point where the amount of solute which has diffused out of the $x < 0$ region is equal to the amount which has diffused into the $x > 0$ region. (Figure 2-3).

Boltzmann (1894) showed that within the conditions defined above, C may be expressed as a function of a variable $\eta = x/2\sqrt{t}$. Matano (1933) first used this fact to determine D(C). This single variable provides ordinary differential equations from the partial differentials $\partial c/\partial x$ and $\partial c/\partial t$.

$$\frac{\partial c}{\partial x} = \frac{1}{2\sqrt{t}} \frac{\partial c}{\partial \eta} \qquad (2\text{-}71)$$

$$\frac{\partial c}{\partial t} = \frac{x}{4\sqrt{t}} \frac{\partial c}{\partial \eta} \qquad (2\text{-}72)$$

and

$$\frac{\partial}{\partial x}\left(D\frac{\partial c}{\partial x}\right) = \frac{\partial}{\partial x}\left(\frac{D}{2\sqrt{t}} \frac{dc}{d\eta}\right) = \frac{1}{4t} \frac{d}{d\eta}\left(D\frac{dc}{d\eta}\right) \qquad (2\text{-}73)$$

Substituting equations (2-72) and (2-73) into equation (2-69) gives:

$$-2 \frac{dc}{d\eta} = \frac{d}{d\eta}\left(D\frac{dc}{d\eta}\right) \qquad (2\text{-}74)$$

Integration of η with respect to c from 0 to C_1 yields:

$$-2 \int_0^{C_1} \eta\,dc = \left[D\frac{dc}{d\eta}\right]_{c=0}^{c=C} = \left(D\frac{dc}{d\eta}\right)_c = C_1 \qquad (2\text{-}75)$$

since $dc/d\eta = 0$ at $\eta = \infty$ (no change in slope). If x and t are returned to equation (2-75) and the terms are rearranged:

$$D_c = C_1 = \frac{1}{2t} \frac{dx}{dc} \int_0^{C_1} x\,dc \qquad (2\text{-}76)$$

t has been moved outside the integral because measurements are made at a given time. Measureable quantities are taken from the plot of x vs $C(x)/C_o$ to determine $D_{c=C_1}$. For a given C_1, t is known, and the slope of the tangent dx/dc and the area $\int_0^{C_1} xdc$ can be determined. The various quantities are illustrated in figure (2-3).

Other schemes have been developed to use equation (2-76), usually focusing on areas where the Boltzmann-Matano treatment is subject to large uncertainties. Two such treatments are discussed by Crank (1975, p. 232). The first takes advantage of the fact that a plot of x vs $(\ln C)^{1/2}$ is nearly linear in some systems. The final product of integration by parts of (2-76) is:

$$D_{c=C_1} = \frac{1}{4t} \frac{x_1}{(\ln C_1)^{1/2}} \frac{dx}{d(\ln C_1)^{1/2}} \left(1+\frac{1}{x_1 C_1} \int_{x_1}^{\infty} c dx_1\right) \qquad (2\text{-}77)$$

where x_1 is the value of x at C_1. This equation can be used for a semi-infinite medium ($x > 0$) with a homogeneous source ($C = C(t)$ for $x < 0$) and $x = 0$ at the surface. An example of this would be a crystal in a well stirred melt with no boundary layer in the liquid.

The second gives more reliable calculations of D at low concentrations than Boltzmann-Matano by plotting the curve on a plot of u vs $\eta = x/\sqrt{t}$ where:

$$\frac{1}{2}(1 + \text{erf } u) = C_1/C_o \qquad (2\text{-}78)$$

This is a probability plot. At the two ends of the concentration range, straight lines can usually be drawn through the data. Thus for this point:

$$u = m\eta + b \qquad (2\text{-}79)$$

and

$$C_1/C_o = \frac{1}{2}(1 + \text{erf}(m\eta + b)) \qquad (2\text{-}80)$$

Differentiation of η with respect to C yields:

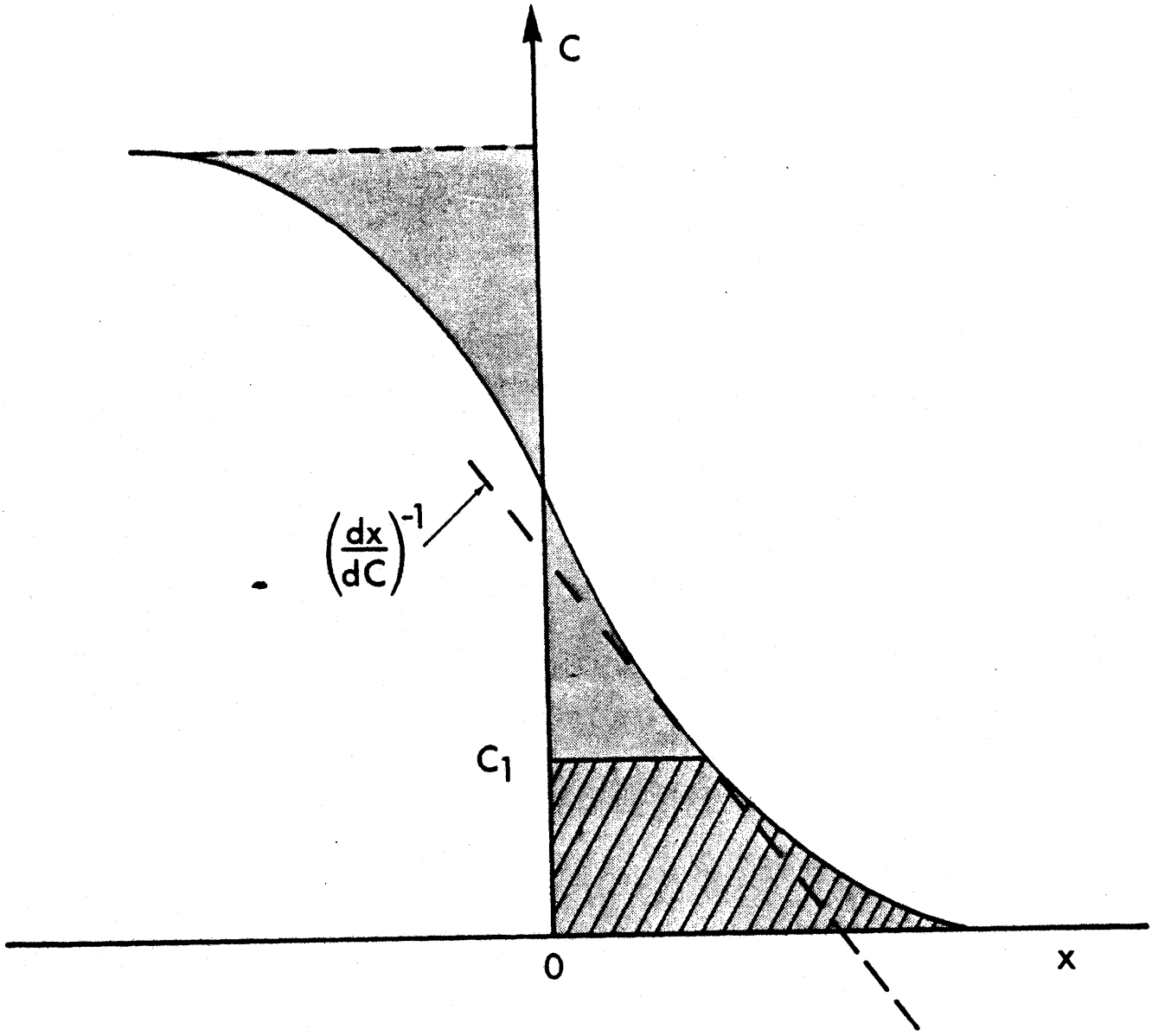

Figure 2-3. Concentration profile showing elements of Boltzmann-Matano analysis, concentration vs distance. x = 0 is located such that the shaded regions to the left and right of it have equal area. Tangent to the curve at C_1 gives dx/dC and hatched area gives $\int xdC$.

$$\frac{d\eta}{dc} = \frac{\pi^{1/2}}{mC_o} \exp(u^2) \qquad (2\text{-}81)$$

from the definition of the error function. Integration from 0 to C_1 gives:

$$\int_0^{C_1} \eta dc' = \frac{C_o}{2m\sqrt{\pi}} \exp(-u^2) - \frac{bC_1}{m} \qquad (2\text{-}82)$$

and the substitution of equations (2-81) and (2-82) into equation (2-75) ultimately reduces to:

$$D(c) = \frac{1}{m^2} + \frac{b\sqrt{\pi}}{m^2} (1 + \text{erf } u)\exp(u^2) \qquad (2\text{-}83)$$

This has proven in practice to be more accurate at the ends of the concentration range, but at the center the slope (m) and the intercept (b) must be that of a tangent to the curve. This is not a significant improvement over Boltzmann-Matano in that region.

An attempt has been made here to examine the theoretical aspects of diffusion which have bearing on the data discussed in the following chapters. This is by no means a complete treatment. A number of publications are available which give a much more rigorous discussion from which the above has been gleaned, and these should be consulted for further information (e.g., Crank, 1975; Shewmon, 1963; Lasaga and Kirkpartick, 1981; Kirkaldy, 1970).

III. EXPERIMENTAL METHODS

Boston baked beans start with beans.

--Child

A variety of experimental and analytical techniques have been employed in the course of this study. This chapter will outline the sample preparation, run parameters, and analysis variables for each method.

Radiotracer and Sectioning

The first experiments (run numbers 2a to 14) utilized ^{85}Sr as a radioactive tracer and natural diopside (Zillerthel, Austria) as the sample material. Single crystals were oriented, cut, and polished to 0.05μm alumina, and heated at run temperature overnight in a nitrogen atmosphere. This pre-anneal was done to remove damage to the lattice caused by the polishing. It also conditioned the samples to a specific oxygen fugacity which minimized any change in the valence state of the iron in the diopside. Samples contained approximately 1.5 wt.% FeO by electron microprobe (see Table 3-1 for analysis). Any adjustment in the Fe^{3+}/Fe^{2+} should occur during this pre-anneal treatment. Some samples became cloudy at this stage and were discarded.

The tracer was ^{85}Sr ($t_{1/2}$ = 62.5 days, 0.514 MeV gamma) in the form of a chloride in weak HCl. The ^{85}Sr accounted for only a few percent of the total strontium in the solution. The liquid was deposited by drops on the polished surface of a given sample and then dried. The crystal was heated for one to two hours in nitrogen at 800°C to induce the tracer

Table 3-1. Electron microprobe analyses of starting materials (wt.%).

	natural	synthetic		
	Zillerthal	GR 4	GR 5	GR 6†
SiO_2	53.99	56.83	56.82	56.39
Al_2O_3	0.30	-	-	-
FeO*	1.54	0.00	0.00	0.00
MgO	18.19	19.17	19.21	18.75
CaO	25.39	25.86	25.73	26.13
TOTAL	99.41	101.86	101.77	101.27

*Total iron reported as FeO; concentration was below the detection limit of normal analysis conditions for the synthetic samples.

†Growth run melt was doped with Sr and Sm, resulting in ∿450 ppm Sr and ∿250 ppm Sm in the crystal.

to bond to the surface. After cooling, the diopside was washed in 6N HCl to remove any unattached tracer. Count rates usually decreased by 30 to 60% following this cleaning. All faces except the doped one were lightly ground (600 grit SiC) to remove any attached tracer from the sides and back of the crystal. Most samples were then packaged face to face with a similar piece in a Pt envelope and placed in the furnace. Others were run as single specimens. Heat-up and cool-down were done gradually ($\sim$20°/min). Run temperatures ranged from 1200 to 1300°C and run times varied from 5 to 30 days, depending on the temperature.

Upon removal from the furnace, the sample was washed in distilled, deionized water and then acetone and dried for 20 minutes at 110°C. It was then weighed on a microbalance (Perkin-Elmer model AD-2) and its radioactivity measured with a well-type NaI scintillation detector and single channel analyser. The sides and back were removed by grinding to a depth approximately 10μ on each to eliminate any tracer which had migrated over the specimen surface before penetrating. The surface area of the doped face was then measured with a microscope and a calibrated grid. The crystal was once again cleaned and dried. After weighing and counting, the doped surface was polished with 0.3μ alumina. The sample was then cleaned, weighed and the activity measured. This cycle of polishing, washing, weighing and counting was repeated until less than 10% of the initial activity remained. The thickness of the removed layers was calculated from the weight change, surface area, and an assumed density of 3.25 gm/cm^3. Reproducibility of the weights was monitored occasionally and drift in the balance was checked with a calibrated standard weight. Drift in the detector was measured by counting a ^{85}Sr standard before and after each sample count. The largest variations within a day's counting were 2 to 3%. Normalization of sample

activity to this standard also removed the effect of decay time between countings.

Data was thus collected in the form of residual activity as a function of depth below the initial doped surface. Profiles ranged from 5 to 30 microns.

Runs 15, 18, and 36 utilized synthetic samples which were cut from large single crystals which contained only trace amounts of iron (<0.2 wt.%). (A description of the growth procedure is given in the appendices.) Their treatment was idenitcal to the natural samples except that the nitrogen atmosphere was not used. Concentration profiles of 2 to 10 microns were measured with run times similar to the earlier radiotracer and natural sample experiments. A comparison of the two sample types for this technique will be presented later.

Stable Isotopes and Ion Microprobe

With the introduction of the ion microprobe to this study stable isotopes could be used . Single crystal growth runs were undertaken with Sr and Sm added to the melt. These produced large specimens containing approximately 450 ppm Sr and 250 ppm Sm although there were large variations on a centimeter scale. Pieces of this material were cut and a face polished to 0.3 μm alumina. Oriented undoped samples were cut from other synthetic crystals and single faces were polished to 0.05 μm and the specimens heated overnight at 1100°C. Pairs of undoped and doped samples were then placed face to face and wrapped with a strip of Pt foil to secure their relative position. Three such pairs were placed in a Pt crucible with the doped specimens on top. Two zircon ($ZrSiO_4$) plugs of about 20 mg each were then placed on top of the samples to promote contact between the faces of the couples (Figure 3-1). The crucible was lowered into a platinum wound, large

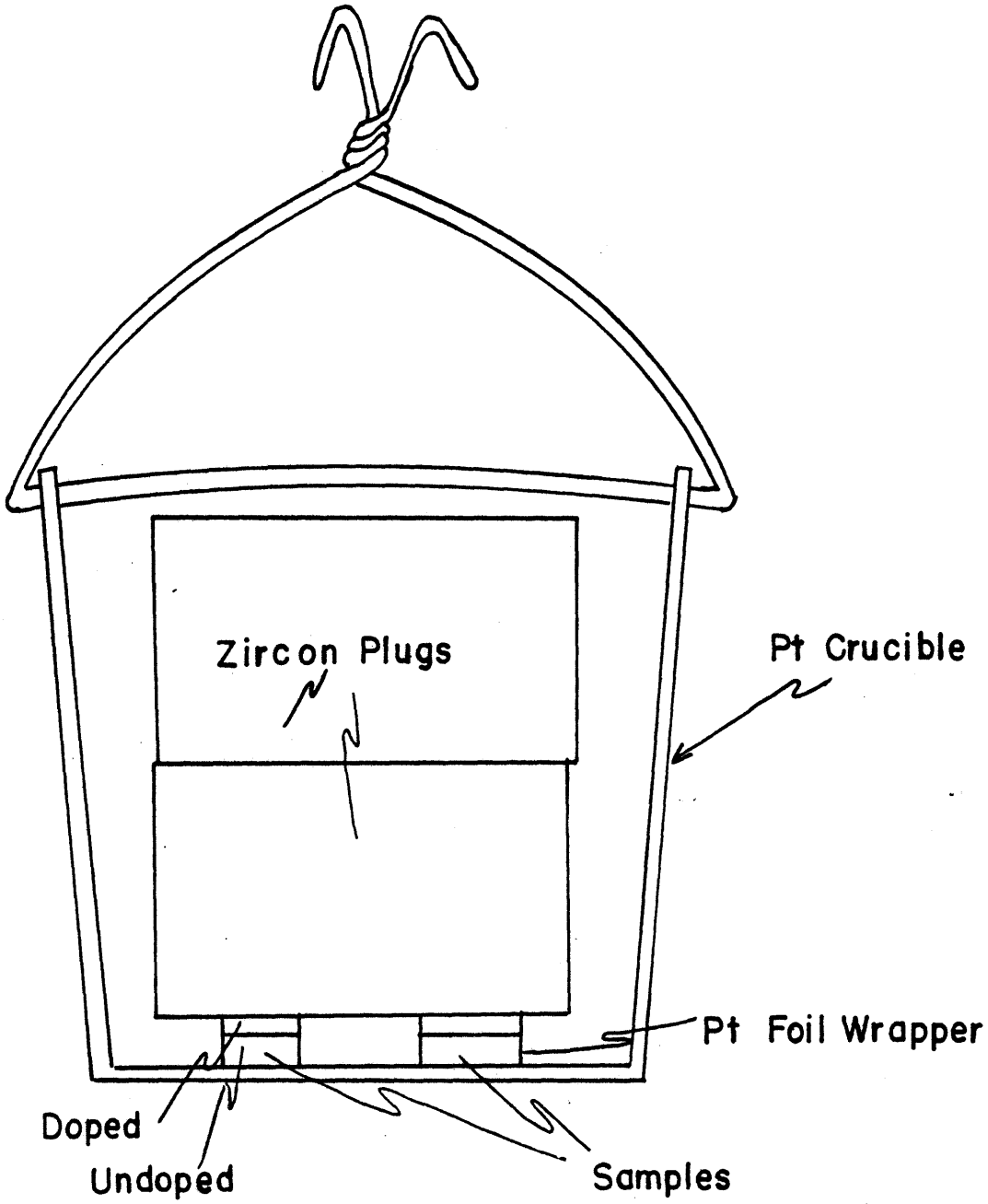

Figure 3-1. Schematic cross section of crucible for ion probe diffusion couple experiments (one atmosphere). Three sample pairs were placed in the bottom of the crucible with doped halves on top. Zircon ($ZrSiO_4$) weights were placed on top of the samples to promote surface contact between the crystals.

bore, quench furnace and brought to run temperature within a half hour. Temperature in all one atmosphere runs was monitored with Pt 10% Rh/Pt thermocouples calibrated to the melting points of gold and nickel or palladium. Control was within ±5°C. Annealing times ranged from 4 to 36 days for these experiments (run numbers 21 to 35) at temperatures from 1150 to 1325°C.

At the end of the anneal the crucible was removed from the furnace and the samples were unpacked. Occasionally specimens would crumble at this point, however sizeable sections of the originally unspiked halves with undisturbed surface areas could usually be recovered. Pairs which adhered to each other were generally separated without harm to the surface. The undoped samples were then mounted on an Al plug and coated with approximately 200 Å of gold for ion probe examination. Analysis of the doped halves proved inconclusive although some gradients were recognized. This failure indicated that the sample pairs were not true diffusion couples.

Various parameters within the ion probe had to be balanced to give optimum results. Whereas a small primary beam spot size and large rastered area minimize the contribution to the signal by material from the walls of the hole, they also yield a slow rate of penetration. A larger beam area to rastered area ratio increases both the edge effect and the sputtering rate. A more complete treatment of this problem is presented in the next chapter. Therefore, only the settings which proved best will be given here. The machine used in this study was a Cameca IMS 3f ion microprobe located at M.I.T. and administered by a consortium of M.I.T., Brown University and Harvard University. The primary beam of O^- ions accelerated to 10 KV was adjusted for a beam current of 45 nA and a spot size of 30 to 35μm. This was rastered over an area 100μm square. The secondary ion signal was

extracted at a voltage of 4425 V (-75 V offset) from an imaged area 25 μm in diameter at the center of the rastered region. This analysis area was further reduced by a mechanical aperture (#2) to the center 13μm region. The ions were mass analysed by a combined electrostatic and magnetic analyser and then counted with an electron multiplier in the pulse-counting mode. ^{28}Si and ^{40}Ca counts were accumulated for six seconds each while the trace elements, ^{88}Sr and ^{152}Sm, were counted for 60 seconds. Each cycle of four isotopes, including magnet switching and stabilization, took approximately 3 minutes. Penetration rates are constant for a given set of parameters and ranged from 45 to 140 Å per cycle, depending on primary beam focus and size. Machine backgrounds were established by occasionally monitoring count rates one half mass unit below each isotope. Background levels of the trace elements in the starting materials were also measured.

The data collected by the ion probe depth profiling were in the form of counts as a function of elapsed analysis time. To convert this time axis to a depth scale most of the pits were measured with a stylus-type profilometer (Sloan Dektak) accurate to 100 Å. Others were examined with an optical interferometer with corrections made for the difference in reflectivity between the gold coat and the diopside.

Experiments carried out at high pressure also used diffusion couples (run numbers P15 to P43). These were undertaken in a piston-cylinder apparatus (Boyd and England, 1960) in the R.P.I. Geology department. Undoped specimens used for diffusion in the c crystallographic direction were cored from polished sections and had a diameter of about 1.5 mm. Pieces for the a and b directions were cut from polished sections with a diamond saw and then rounded on the corners. This was done because attempts to core the diopside in these directions yielded samples which easily separated

along cleavage directions. Doped specimens were platelets which were cleaved from drill cores taken in the [110] direction. A pair of spiked and unspiked pieces were wrapped face to face in Pt foil and sealed in a Pt capsule using a "milk carton" weld.

The capsule was then surrounded by powdered Al_2O_3 inside an alumina sleeve in a high pressure assembly (Figure 3-2). The heating element was a graphite tube through which a current was passed. Temperature was monitored with a W3%Re/W25%Re thermocouple and controlled to ±5°C. Outside the graphite furnace was a pyrex tube surrounded by either talc or NaCl as the pressure medium. The pyrex shields the furnace from water generated from the talc or the corrosive action of the salt. The entire assembly measured 1.25 inches long by 0.5 inches in diameter. Pressure was applied by pushing a piston against the bottom of the confined assembly and its magnitude was calculated from the oil pressure forcing the ram. Start-up consisted of pressurization sufficient to insure electrical contact between the current-carrying components of the apparatus and the graphite tube, followed by heating above the pyrex softening point(∿800°C). Run pressure was then applied and temperature raised to the set point. The whole process took 5 to 10 minutes. During the run, pressure was known within a kilobar and the temperature set point was accurate to about 5°C with respect to the desired temperature. Experiment times were 5 to 50 hours and covered a range of 8 to 20 Kbar and 1100 to 1250°C. Pressure was decreased slowly at the end of a run (∿0.5 Kbar/min) while temperature remained elevated for salt cells. This slow release was effected after thermal quench for talc assemblies.

The platinum capsule was recovered from the set-up and embedded in epoxy attached to an ion probe sample holder. The capsule was oriented so that the

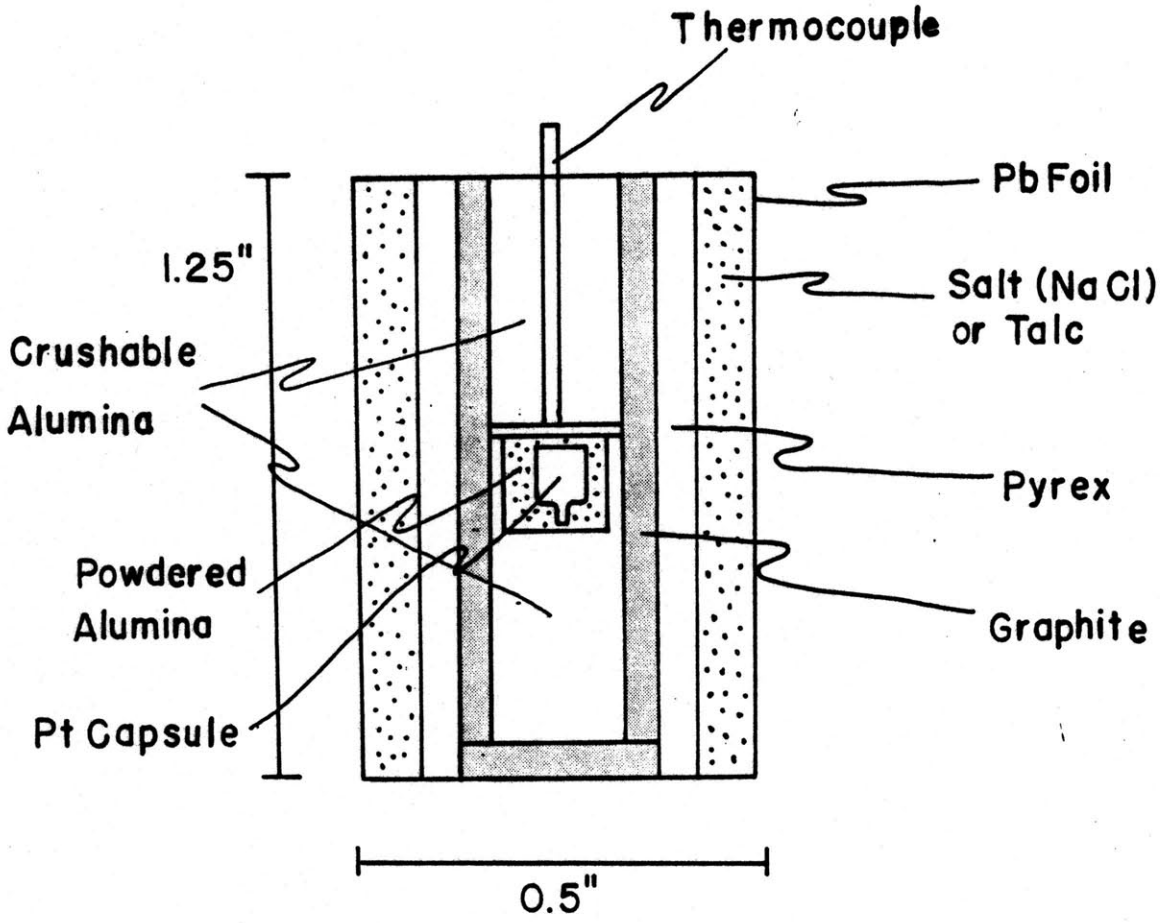

Figure 3-2. Piston-cylinder high-pressure assembly. Sample pair was sealed in a Pt capsule and placed in assembly. Each unit was used for one run.

doped piece was on top. The hardened epoxy and capsule were filed down until the diopside was exposed. The pieces of the spiked disc were then removed with dissection needles and an ultrasonic cleaner, revealing the surface of the initially undoped crystal. By orienting the two specimens in different crystallographic directions, the natural cleavage of the diopside assisted in locating this interface. The lower sample contained some cracks but undisturbed regions with surface dimensions larger than the rastered area and depths many times greater than the expected diffusion distance were available for analysis. The epoxy and Pt were filed to within a millimeter of the sample surface before gold coating. Ion probe procedures were identical to those described for the one atmosphere runs.

Rutherford Backscattering Spectroscopy

Another series of one atmosphere experiments (run numbers B6 to B23) were done using a surface-deposited stable tracer and the synthetic diopside. Sample preparation was the same as for the radiotracer runs except that furnace atmosphere control was unnecessary. The tracer solution of 0.20 mg SrO per ml of H_2O was delivered to the sample surface by microsyringe. After drying, the piece was heated to 200°C for 1.5 hrs. on a hot plate. Two crystals were then placed face to face in a platinum envelope and taken to run temperature over 1 to 2 hours. Temperatures and run times varied from 1000 to 1250°C and from 0 to 69 hours. Cooling covered a time span similar to the heating. The samples were unpacked when cool and washed in boiling water for five minutes to dissolve any remaining SrO.

One half of each c direction pair was examined with the ion probe under conditions described above. The other was analysed by Rutherford backscattering spectroscopy (RBS) at the linear accelerator facility of the State

University of New York at Albany. RBS data were not collected for the other crystal directions although they were analysed with the ion probe. The RBS samples were bombarded with a 2 MeV alpha particle beam which had a current of 15 to 20 nA over a 5 mm^2 spot. Minimum sample surface size for this technique was approximately 4 mm square. The α particles backscattered from the sample atomic nuclei were counted by a silicon surface barrier detector positioned at an angle of 175° from the incident beam (Figure 3-3). The detector output was processed with respect to particle energy by a multi-channel analyser. The energy of the rebounding α particles depends on the mass of the target nucleus and the depth of penetration before collision. In the case of a homogeneous mono-atomic material, this energy is limited by the value given by collision of α particles with the surface atoms. Energy levels lower than the surface value arise from backscattering of the α's from nuclei at various depths in the sample. For the mono-atomic example, the energy distribution of rebounding particles forms a smooth curve such as that shown in Figure (3-4).

For poly-atomic phases, the energy spectrum is complicated by the effect of the different target masses on the rebound energy. The characteristic curve for such a material (Figure 3-5) can be interpreted as the summation of the individual spectra of the component species. Backscattering from each element produces an energy distribution similar to the mono-atomic material with the relative count rates dependent on the concentrations of the different species. For instance, in the hypothetical compound A_2B, the count rate at the surface backscattering energy will be twice that at the B surface value assuming that their backscattering cross sections are equal.

In the present experiments, a third factor effecting the spectrum is the variable concentration of the diffusant, Sr. Each depth corresponds to an energy level for a given element, and teh count rate at that energy is de-

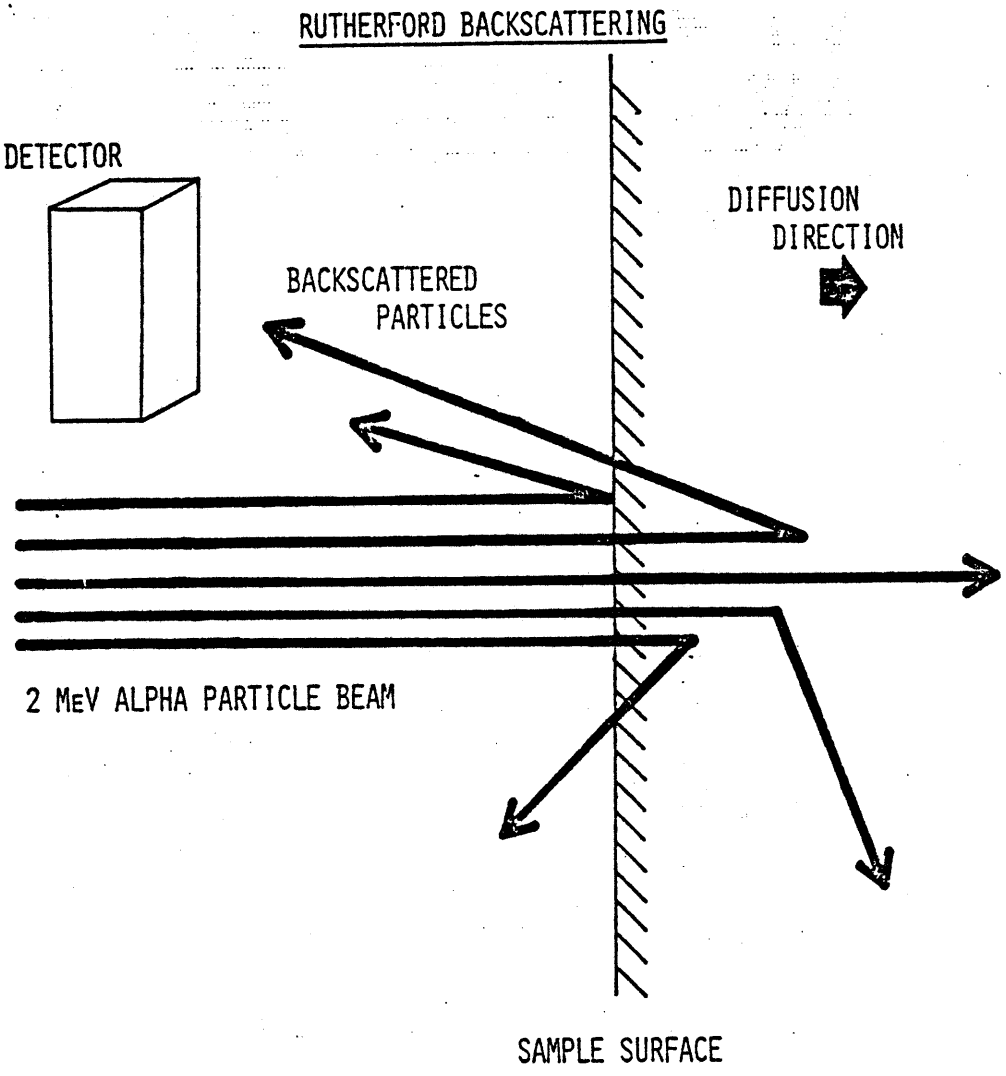

Figure 3-3. Rutherford backscattering spectroscopy schematic. High-energy alpha particles collide with atomic nuclei in the sample and backscattered particles are analysed by a silicon surface-barrier detector.

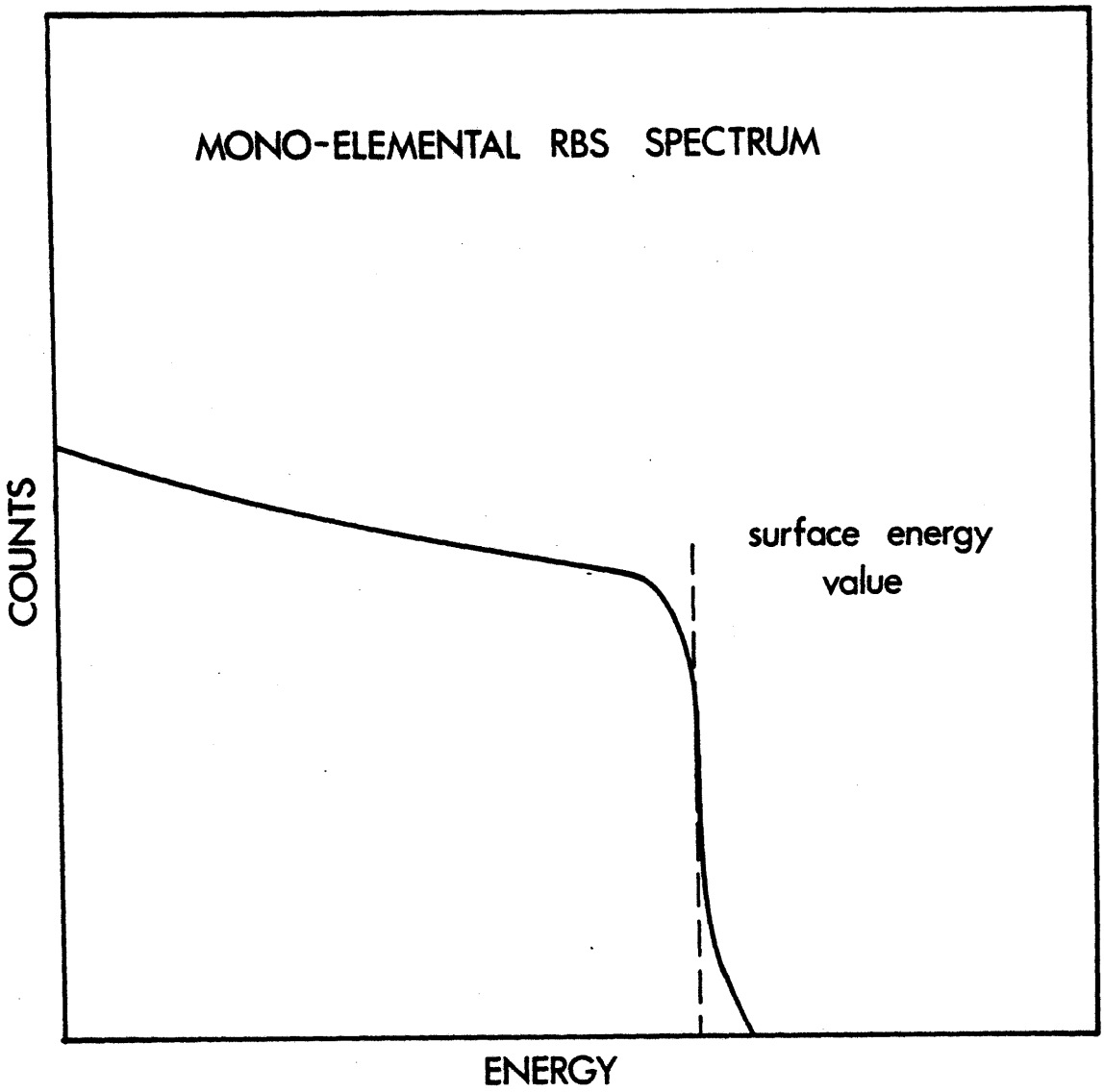

Figure 3-4. Mono-elemental RBS spectrum. Surface energy value depends on the mass of the target and the energy of the impinging particles. Increase in count rates at lower E is due to non-collisional interactions, and values greater than the surface value are due to peak broadening.

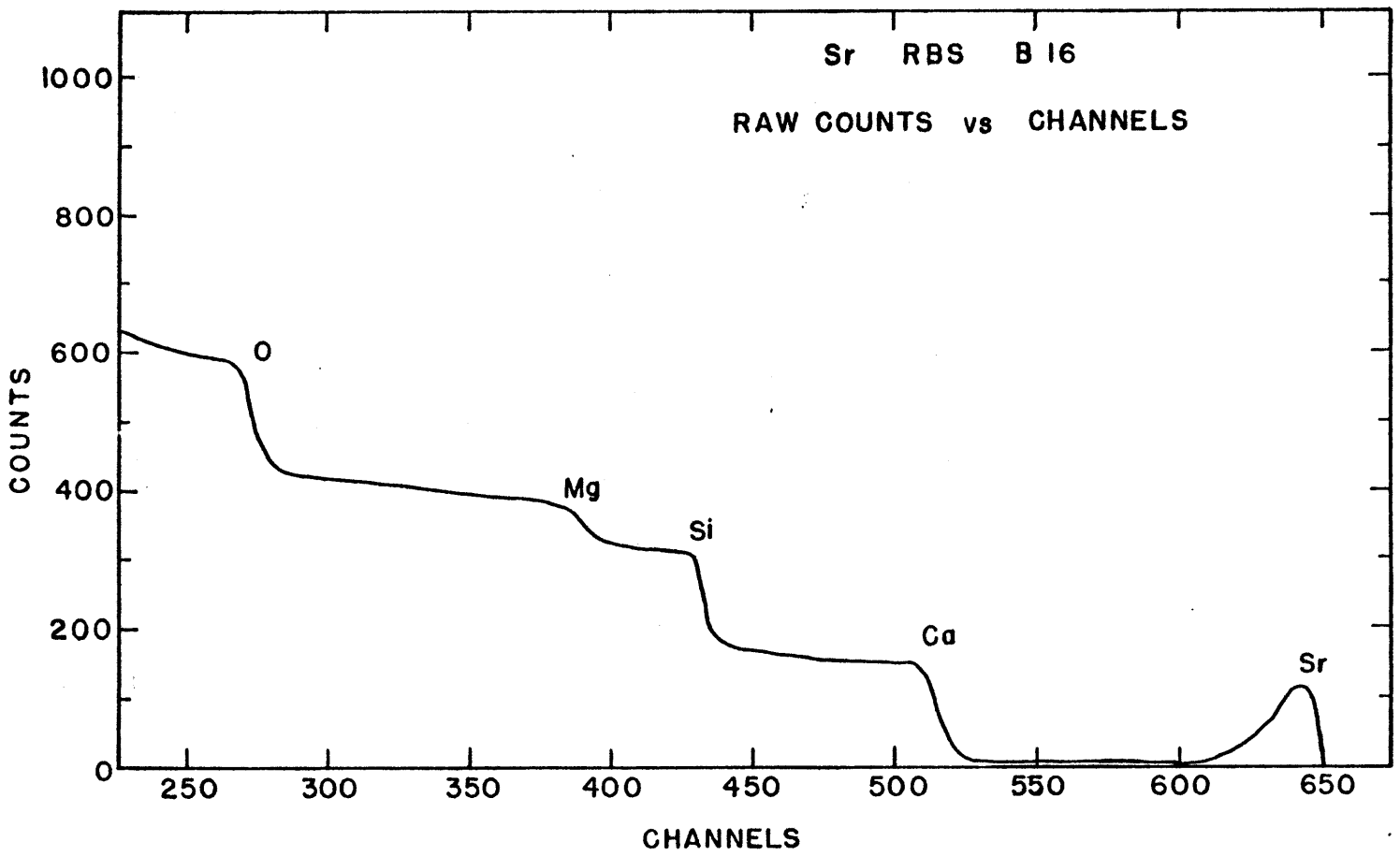

Figure 3-5. Poly-atomic material RBS spectrum. Diopside curve is made up of the elemental spectra for O, Mg, Si, Ca, and Sr. Steep slopes occur at the surface energy values for the components. The Sr peak is not continuous to low E because it is not homogeneously distributed in the sample.

pendent on the elemental concentration. Decreasing concentration with depth will cause lower count rates as energy decreases (Figure 3-5).

Due to the mass difference between Sr and Ca, the heaviest species in diopside, a portion of the energy spectrum between the surface backscattering values of the two cations contained counts derived solely from strontium. The energy scale was converted to a depth scale by applying the stopping power of diopside, which was calculated from the chemical formula and the density. It was seen that the rebound energy range over which Sr was the only contributor to the spectrum was equivalent to 0.5 μm depth. Further information on Rutherford backscattering can be found in Chu et al., (1978).

Data reduction schemes for the different analytical methods and estimations of uncertainties in the measured quantities will be described with the presentation of the numbers. More detailed descriptions of the apparatuses are given in the appendices.

IV. ION PROBE DEPTH PROFILING AS AN ANALYTICAL TOOL

"Depth profiling is boring." - Anonymous

In recent years, the ion microprobe or secondary ion mass spectrometer (SIMS) has become an important analytical tool in trace element and isotopic applications. The basic concept involves a primary ion beam, such as oxygen or argon, impinging upon the surface of a sample and blasting away part of the specimen as ions. These sample ions are then mass-analysed. The detection limit for most elements is very low and the technique is capable of detection of light elements, including hydrogen. This sort of in-situ isotope and trace element analysis technique is well suited to geochemical studies.

Most geochemical applications have used the probe for spot analyses on the surface of samples. Some recent examples are: trace element and isotopic zonation in single crystals (Shimizu, 1981; Hart et al., 1981), detection of evidence of extinct radioactive isotopes (Huneke et al., 1981), and grain boundary diffusion (Giletti and Nagy, 1981). Another available mode of operation is to take advantage of the destructive nature of the process and analyse sample composition as a function of depth in the pit caused by the beam. Depth profiling is particularly useful in diffusion studies where the concentration of the diffusant can be monitored as progressively deeper layers of the specimen are exposed. The raw data are in the form of elemental signal on the y axis and elapsed analysis time on the x axis. A number of factors affect the conversion of these quantities to diffusant concentration and depth penetration, respectively. These will be discussed shortly.

Advantages

The lower limit to the length of a measurable diffusion profile is much less for depth profiling techniques like the ion probe or Rutherford backscattering spectroscopy than for sectioning methods or surface analyses.

Depth resolution is ultimately controlled by the mean escape depth of the secondary ions in an ion probe study. Theoretical calculations of the sputtering process show that most sample ions originate from within the first three or four atomic layers (Ishitani and Shimizu, 1975). This is a lower limit which is only approached when all instrument-generated effects are minimized. These factors do not necessarily actually enlarge the sampled layer but increase the uncertainty in its location. One of the most important factors in determining the actual depth resolution is the implantation range of the primary beam ions. At depths greater than this range, the relative resolution is usually defined as $\Delta z/z$, where Δz is the broadening of a sharp step in concentration at depth z. Various sputtering models predict dependences of $\Delta z/z$ ranging from proportional to $1/\sqrt{z}$ to a constant (Zinner, 1980). In any case, diffusion profiles can be reliably measured for distances greater than a few hundred angstroms. This is considerably less than most of the commonly used diffusion measurement techniques. Step scanning with an electron or ion probe is limited by the diameter of the beam and the area it affects. Autoradiography resolution depends on the range of the particles, and radiotracer and sectioning is limited by the accuracy of the step measurement. Short profiles greatly reduce the experimental annealing time as diffusion distance is proportional to the square of the time. With depth resolution on such a fine scale, short time transients in the transport experiment become important. These can be transcended by increasing the run time, and this will be addressed more fully in the next chapter when data pertinent to the discussion will be examined. The depth resolution of the ion probe is good enough that it may not be the limiting factor which determines the necessary length of the diffusion profile.

The precision of the depth measurement of a shallow hole need not enter

into the above considerations. The penetration rate, the rate at which material is removed from the exposed surface of the sample, has been shown to be constant with time for a given material and primary beam parameters (Figure 4-1). Thus, the final hole depth can be increased to an easily measured distance by extending the analysis beyond the diffusion profile.

The surface area required for an analysis is also considerably less than that for a sectioning technique. The incident beam can be focused to sizes as small as a micron in diameter on the IMS 3f. The rastered area for this machine is continuously adjustable from zero to 500 microns square and the imaged area in steps from 1.3 to 400 microns in diameter. Practical limits for these parameters are set by the count rates of the isotopes being examined. Electronic noise levels are independent of the size of the imaged field. If the sample background is insignificant, larger analysed areas will increase the precision of measurements for trace isotopes. Another controlling factor is sample homogeneity. It may be desirable to increase the sputtered and imaged fields to average out local variations in concentration. However, these heterogeneities must be on a scale of tens of microns for this to be effective. Larger scale variations will fall outside the range of the IMS 3f. Even with a "large" analysed field, the surface area of a sample needed for ion probe depth profiling is much less than for sectioning techniques or for RBS profiling.

The ion probe is capable of monitoring a number of isotopes simultaneously during a run by switching the magnetic field to focus different isotopes on the collector at different times in a cycle which is repeated throughout the analysis. Major elements can be analysed for the purpose of normalization and multiple tracers can be examined in a single specimen. The normalization to a homogeneous isotope removes variations in the secondary signal

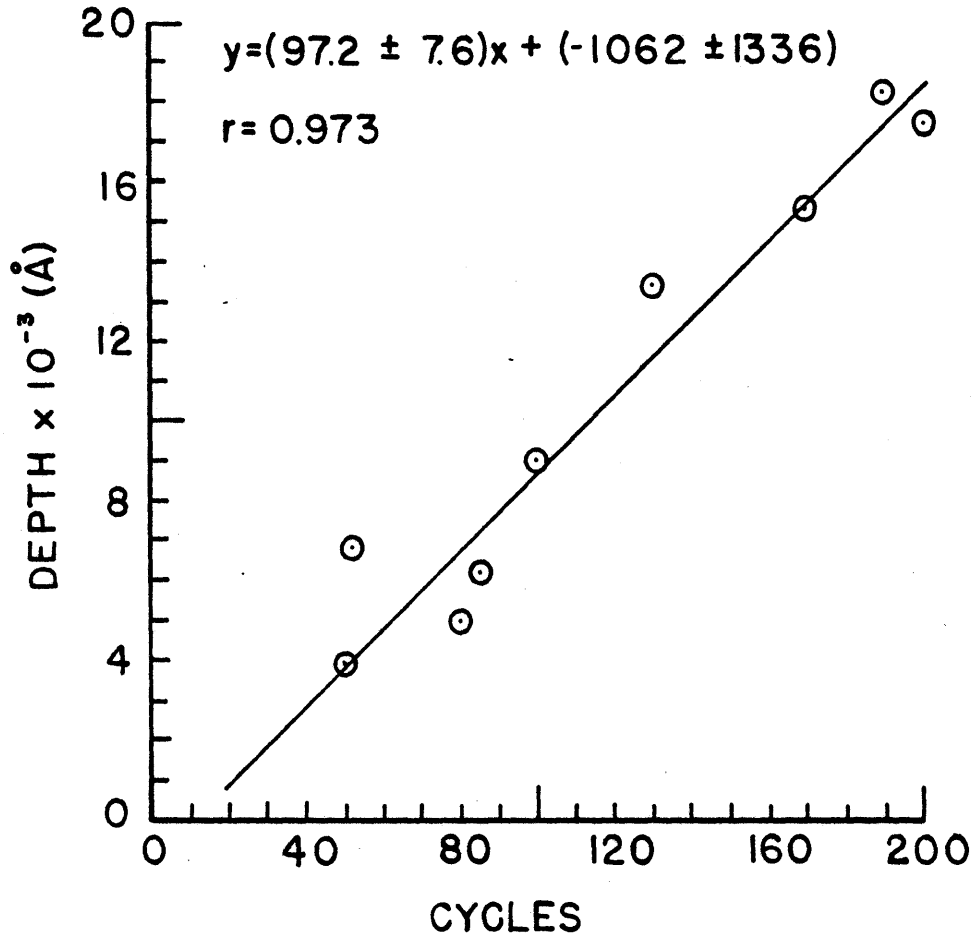

Figure 4-1. Final depth of analysis pit vs number of cycles. All points are from a single analytical session. Best fit straight line was calculated by the major axis formula (York, 1966).

caused by fluctuations in the primary beam intensity and also allows comparisons among analyses performed at different times. A single experimental charge can be used for diffusion of a number of trace elements or the inter-diffusion of major elements. The savings in sample material and run times are immense. It is necessary, however, to limit the individual tracer concentrations to levels at which independent behavior can be assumed. Otherwise, effective binary diffusion coefficients (EBDC) are derived and these have reduced applicability to compositions different than that of the specimen.

Background levels generated in the machine itself are very low. Values measured one-half mass unit below the peaks of the isotopes studied ranged from 0.05 to 0.2 counts per second. The background is attributed to random electronic noise, and its low value facilitates accurate measurement of count rates of less than one per second, and concentrations in some cases as low as parts per million. Diffusion profiles can therefore be observed using small amounts of dopant, insuring that D is effectively independent of concentration.

Disadvantages

Problems which arise while employing the ion probe in a diffusion study can be divided into two categories, on the basis of whether or not they are common to both surface analysis and depth profiling. Examples of difficulties which affect both methods are preferential sputtering, charging effects, and molecular interferences. Some of those unique to depth profiling are edge effects, knock-on, and slow penetration rates. Remedies for some of these are available and will be discussed with each problem. Others must be handled by an empirical treatment whose derivation is discussed separately.

Molecular interferences have been a major obstacle to the development of high precision ion probe analysis. The sputtering process not only

dislodges single-atom ions from the sample but also a large variety of molecular ions. These interfere with the detection of a given isotope if their masses are the same as the single-atom ion (e.g., ^{56}Fe and $^{40}Ca^{16}O$, ^{28}Si and $^{27}Si^{1}H$). This problem can be extreme in complex phases like natural silicates where the probable combinations of two and three elements number in the thousands. Added to this is a small but sometimes important presence of hydrocarbons in the sample chamber from such sources a vacuum pumps, cleaning reagents, and handling of samples. Design characteristics of recent ion probes, including the IMS 3f, have made it possible to select certain analytical conditions which have greatly alleviated the interference problem. Variation of the secondary accelerating voltage, employment of energy-selective slits, and high mass resolution facilitate the reduction of interferences to near background levels in many cases. Most molecular ions have a considerably lower high energy component than single-atom ions and energy filtering has been shown to be an effective means of eliminating them (Herzog et al., 1973; Shimizu et al., 1978). The filtering is accomplished by shifting the energy bandpass of the secondary ion optics, by means of a voltage offset, so that the lower energy ions are not accepted by the analyser. An energy slit placed after the electrostatic sector can be adjusted to further limit the range of secondary ion energies. Ray (1980) showed that secondary offset voltages of greater than 25 V (negative) yield intensities of Sr isotopes which give the correct ratio of $^{86}Sr/^{88}Sr$. This study used a -75 V offset and an energy slit width of ±25 V (i.e., analysed secondary ion energies ranged from -100 to -50 V) to effectively eliminate molecular interferences and to give the proper $^{86}Sr/^{88}Sr$ ratio.

The negatively charged primary ion beam utilized in this work builds up an electric charge on the surface of an insulating target such as a

silicate. The resultant electric field eventually reaches proportions that partially deflects the beam and effect secondary ion extraction. The most direct way to deal with this is to coat the sample with a conducting material or to place a conductive grid on the surface. This is sufficient except when large areas of the conductor are removed by the beam during the analysis. In the present study, an approximately 200 Å gold coat was vacuum deposited on the sample from a plasma and a rastered area of about 100 μm square was used. These conditions appeared to avoid charging problems, even in analyses lasting over five hours. However, occasional secondary ion yield variations not attributable to primary beam fluctuations may have been caused by sample charging. These variations were obvious and were removed from the final profiles (Figure 4-2).

The interaction of the primary beam with the sample gives rise to another situation which has importance to both spot analysis and depth profiling. All elements do not have the same sputtering yield. In oxygen rich materials such as silicates, where the effect of the chemical action of the primary O^- beam on the sputtering process may be considered insignificant, the observed differences are due solely to preferential ejection and ionization. Zinner (1978) examined a feldspar sample and showed that for each element there is a transient in the secondary ion signal which quickly approaches a steady state condition. The length of this transient appears to be proportional to the penetration range of the primary beam. The sputtering process can be represented by a surface layer which is the source of the analysed ions. This layer becomes enriched in the low sputtering species with respect to those with higher yields. The steady state occurs when the composition of the surface layer is such that depletion by sputtering is balanced by the "influx" of material from below. This is graphically illustrated by

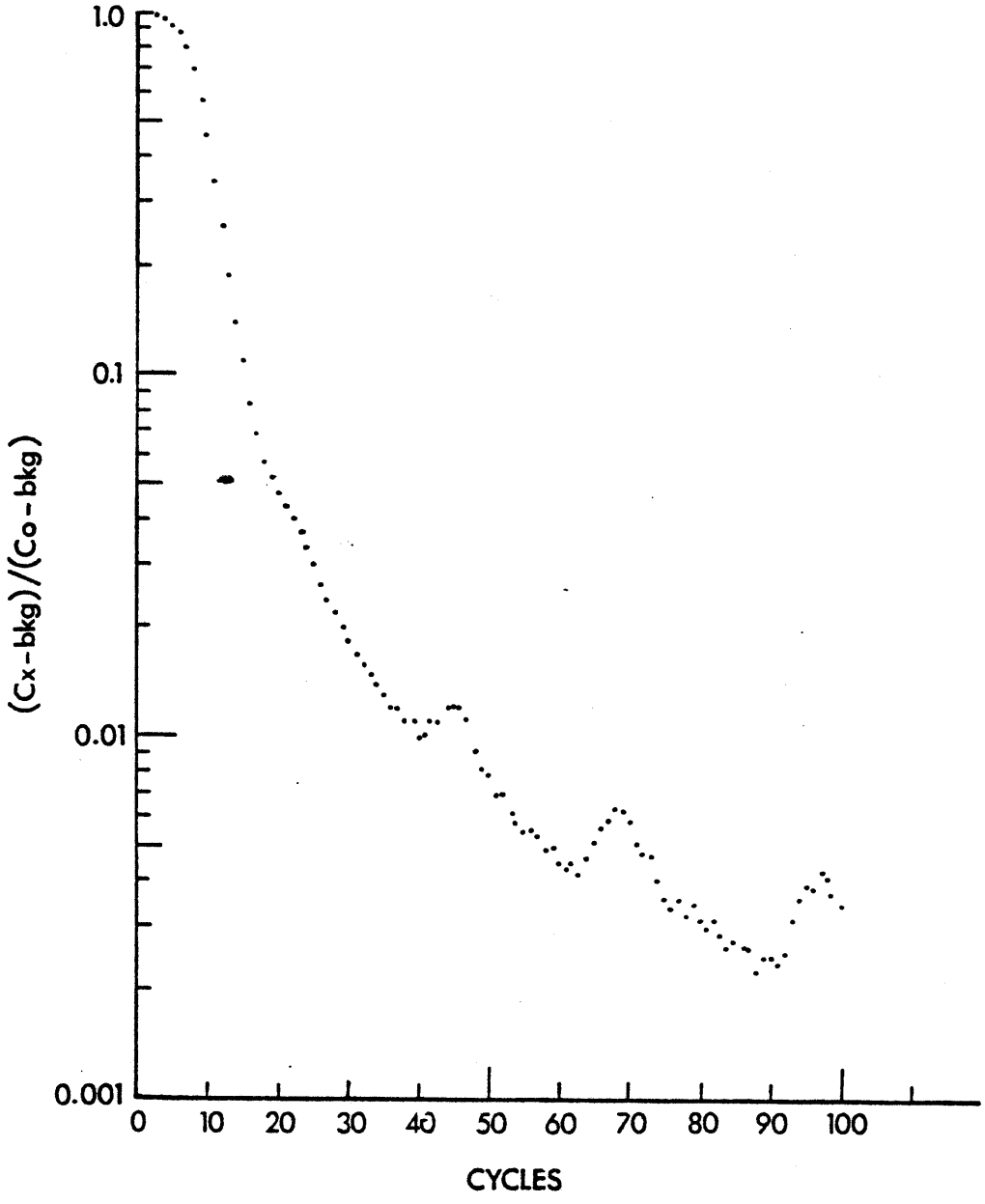

Figure 4-2. Normalized counts minus background divided by value at x = 0, vs cycles for ^{88}Sr in diopside. The three low peaks are machine generated and their cause may be sample-surface charging.

Shimizu and Hart (1981) in their figure 9 (reproduced here as Figure 4-3). The steady state secondary ion beam composition is related to the true sample composition through the ionization probabilities (R_i^+) of the various species, such that:

$$I_i = R_i^+ S_i \qquad (4\text{-}1)$$

where I_i is the number of detected ions and S_i is the number of sputtered atoms of a given species. Ionization probability is the measure of how efficiently the sputtered atoms of an element are ionized to the plus one state and the value of R_i^+ is dependent on a number of factors, including the primary ion beam energy. For labradorite, Zinner found the following sputtering yield ordering:

$$S_{Li} > S_{Na} > S_{Si} > S_{Mg} > S_{Al} > S_{Ca} \qquad (4\text{-}2)$$

which shows that S_i is not dependent solely on atomic mass as predicted by kinetic models. Data for Si and Ca in diopside from this study agree with the above ordering. Preferential sputtering presents a problem both within the diffusant profile and when normalizing to another element, but since absolute concentrations are not required, differences in ionization probabilities can be ignored. An allowance must be made for the first few cycles before the steady state region is reached.

Difficulties arise in depth profiling analysis from a variety of sources which are insignificant in surface analysis. One of these is the contribution to the secondary ion beam of material not derived from the exposed surface at the bottom of the hole, but from the edges of the pit. This causes higher apparent concentrations to be measured in the case of a decreasing gradient. The main source of this extraneous material is the walls of the pit, and a number of techniques have been employed to minimize their effect. The ideal case of a flat bottom hole with vertical, non-contributing sides

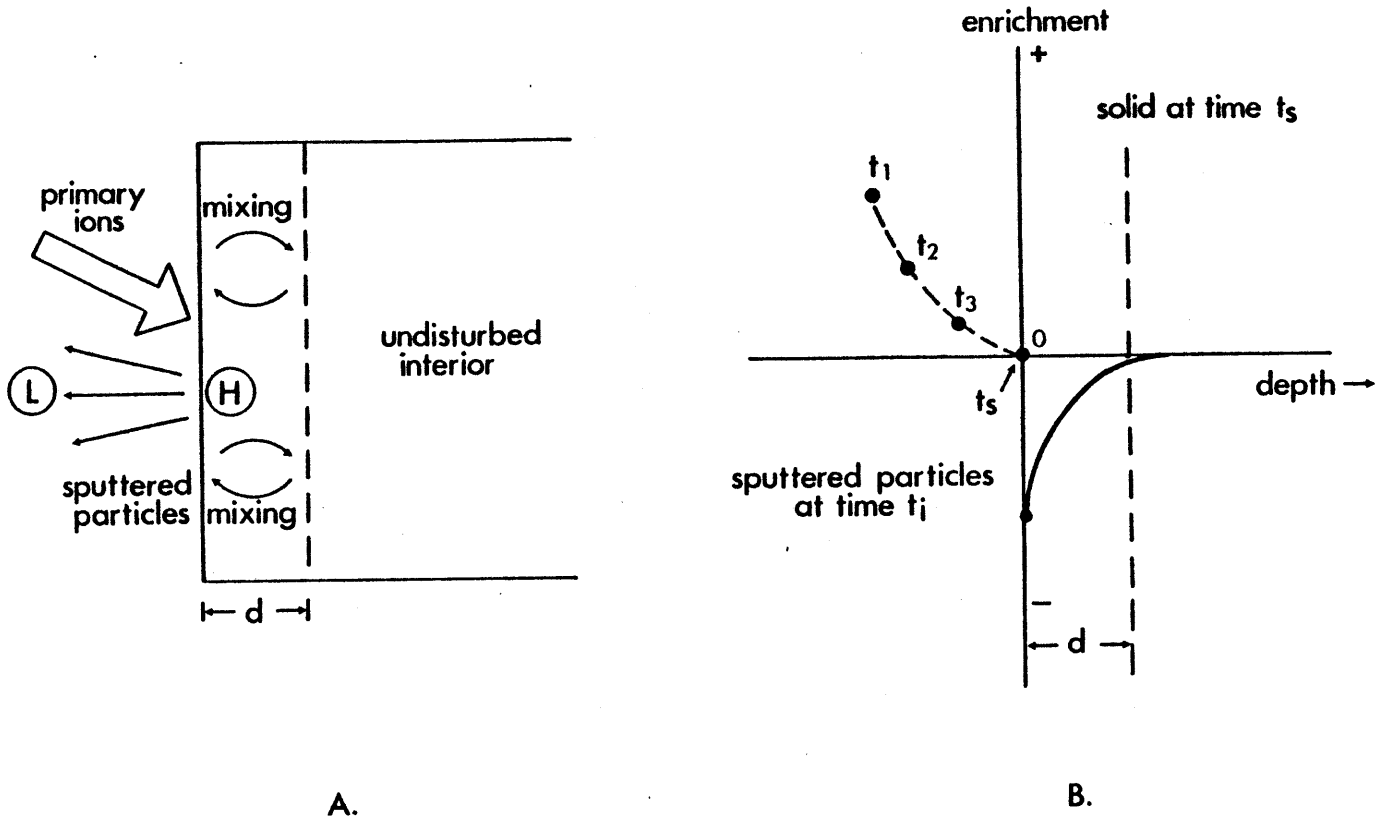

Figure 4-3. Schematic diagram showing the change in the surface chemical composition with time during initial transient. (a) Preferential sputtering results in enrichment of the L component in the sputtered particles and the residual solid is thus enriched in the H component. Mixing occurs over the penetration range of the primary ions. (b) As the sputtering continues, enrichment of the L component in the sputtered particles decreases from t_1 to t_s, due to the finite rate of mixing. At steady state, the sputtered particles have the same chemical composition as the undisturbed interior and the distribution of the L component in the solid at steady state is shown on the curve. (from Shimizu and Hart, 1981b)

can be approached by rastering a small beam over a comparatively large area. This averages any nonuniformity in the primary beam, delivering the same intensity to a larger percentage of the area than a stationary beam can. Rastering the beam over a region larger than the imaged field helps by removing the pit edges from the analysed area. The lower limit of the beam to rastered area ratio is controlled by the desired penetration rate. Whereas a small ratio gives sharp edges, the penetration rate and the secondary ion yield may be too low for reasonable analysis times and count rates. A compromise between hole shape and sputtering yield must be reached which allows accurate profiles to be derived in practical lengths of time.

Another means of treating the edge effect available with the IMS 3f is a mechanical aperture (field aperture) placed in the secondary beam path. The instrument is designed for direct imaging of the secondary ions. This means the behavior of the ion optics is similar to light optics and the 180° path reverses the image twice to give a direct image. Two other methods not employed in this study are an "electronic aperture", and a grid or mask placed directly on the sample. The first is achieved by gating the secondary beam detector to accept counts only when the rastered primary beam is in the central portion of the analysed area (Zinner, 1980). The second involves placing a grid of some material, usually a conductor, on the surface and analysing the area within one spacing (Poumellec et al., 1981).

The techniques used with the IMS 3f help greatly but do not appear to remove the edge effect completely. The exact nature of the particles which make up the edge contribution is unclear. Possibilities include neutral atoms which are plowed up by the primary beam but remain on the sample surface. Profilometer traces across analysed areas show a slight mound surrounding the hole. If the primary beam scatters some material out of the

pit, it is logical that some is also spread from the edges to the central analysed area. These atoms can then be ionized and extracted by a later collision with a primary ion. Another source may be a small amount of direct extraction of positive ions from outside the imaged area. A third possibility is ions which have been deposited on the extraction lens immediately above the sample surface and then sputtered from there at a later time. The incident particles for this process may be secondary electrons. A certain low percentage of the primary beam is not contained in the focused spot. These "halo" ions may sputter sample from outside the rastered area. This apparently occurs in this study since during long analyses the edge of the gold coating recedes with time. There is evidence that all the other contributors also operate to a certain extent. An empirical subtraction from the observed profile which deals with the edge effect not controlled by machine variables will be presented shortly.

A further problem caused by the action of the primary beam is known as knock-on. In this case ions from the surface are driven deeper into the lattice and sampled later. A theoretical approach using a Monte Carlo treatment of the multiple collisions in the sputtering process is given by Ishitani and Shimizu (1975). Their results agree with experimental studies which show that the size of the effect depends on the energy of the incident beam and the masses of the primary ions and sample atoms. The mixing can be minimized by decreasing the primary beam energy and the use of incident ions with large mass to charge ratios (Zinner, 1980). The accelerating voltage (10 KV) and the primary species (O^-) used in this work are not optimum for decreasing the knock-on effect but were chosen because of machine priorities and convenience. Like the edge effect, knock-on extends the apparent length of the diffusion profile. Within this study, the separation

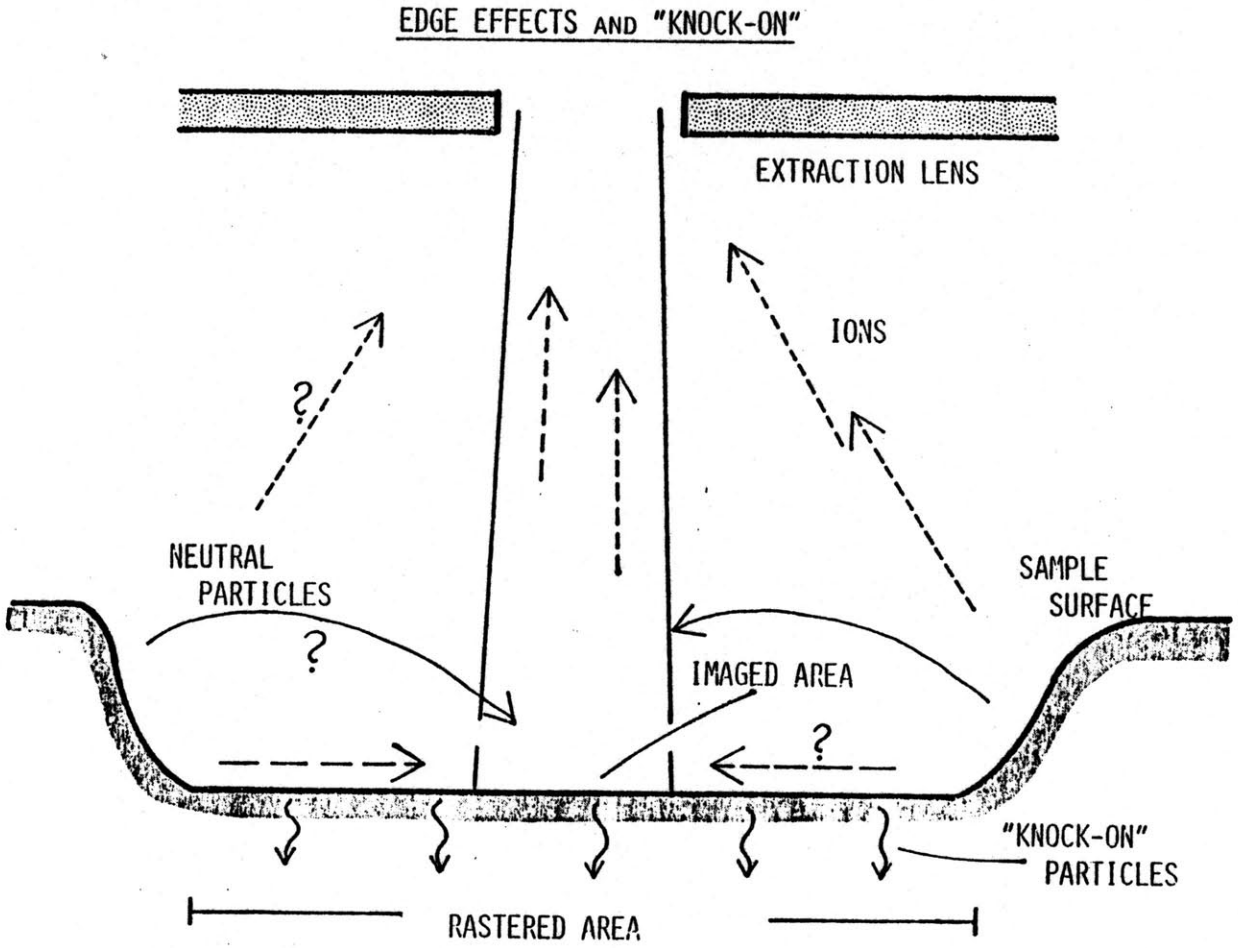

Figure 4-4. Schematic cross section of analysed pit and extraction lens (drawing not to scale) showing various sources of extraneous secondary ions.

of the two contributions is impossible. Therefore, compensation for knock-on is included in the treatment mentioned above.

Problems involving the penetration rate can also limit the applicability of ion probe depth profiling. One was mentioned earlier and is mostly a matter of convenient analysis time. Penetration rates in silicates such as diopside are very low unless some sacrifice is made in the shape of the pit. The measured rate for a beam size of 20 μm and 6nA current with a rastered area 120 μm square on diopside was approximately 3 Å/min. Increasing the beam size and intensity to ∿35 μm and 45nA raised the penetration rate to about 30 Å/min, decreasing analysis time by a factor of ten while not seriously changing the hole shape. Still, this requires over five hours to penetrate one micron.

A necessary assumption in using the final pit depth to assign a distance scale to the time axis is the constancy of the penetration rate. This constancy is not always observed near the surface of the material where composition varies during the initial transient stage. The variation can be an important factor in very short profiles. As the analysis depth increases, it becomes less significant. Compositional variations in the sample also cause changes in the penetration rate. However, these can be assumed to be very slight for the nearly identical compositions within the single phase used in this project. Drastic changes are seen in multi-phase layer structures with rates needing to be determined for each phase encountered. Various checks of the penetration rate during this study have shown it to be constant for a given set of primary beam conditions.

A number of factors can cause the bottom of the hole to be rough. Accentuation of original surface roughness is one of these. Different penetration rates of impurities can initiate points which are magnified as the

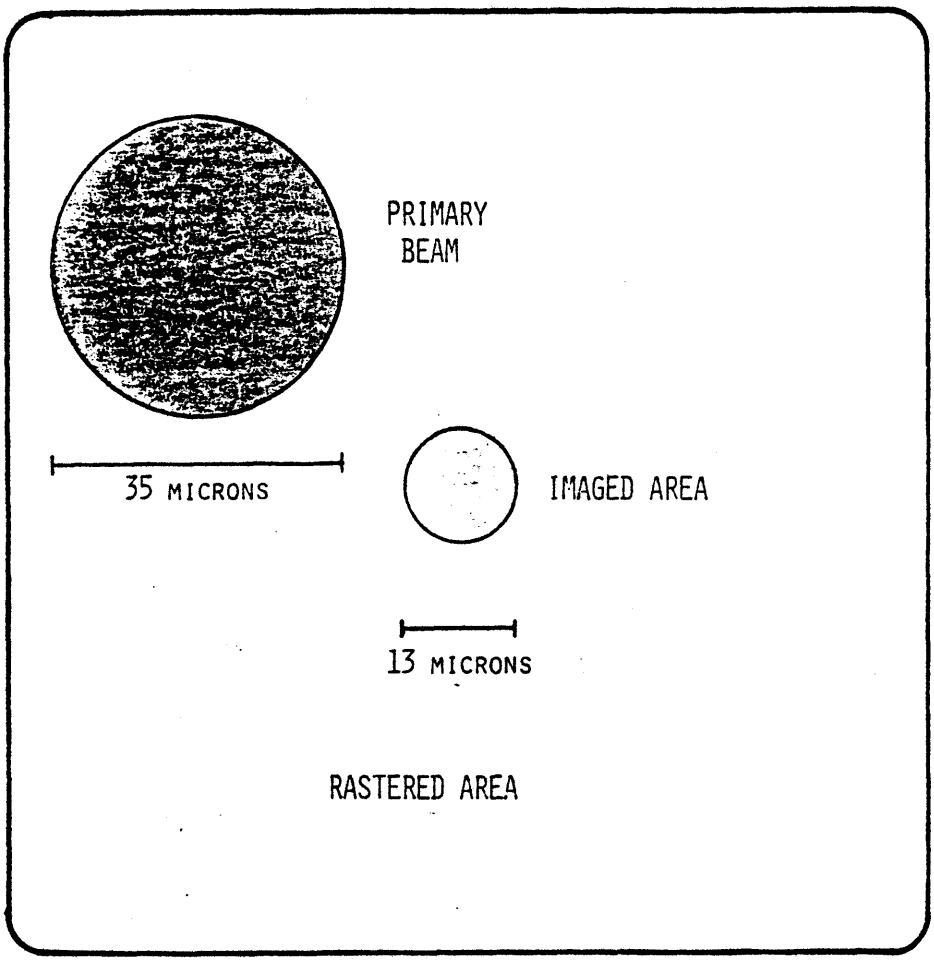

Figure 4-5. Comparison of sizes of primary beam spot, rastered area, and imaged area. Primary beam is rastered over large area while secondary ions are extracted from the central, imaged area.

analysis continues. Finally, certain crystallographic directions produce preferential rates which will cause roughness if the analysis direction is oblique to one of them. Roughness increases the uncertainty in the depth from which a concentration is derived. Experiments have shown that the amount of relief increases as the hole gets deeper (Zinner, 1980). Depths utilized in this work produce small variations (<100 Å) in the bottom topography for initially smooth surfaces.

Compositional changes not only cause variable penetration rates, but also affect the yield of secondary ions. This matrix effect has been studied empirically for a number of geologically interesting phases and elements (Steele et al., 1981; Ray, 1980; Shimizu and Hart, 1981b) and it must be taken into account when major element variations occur in the depth profile. Standard working curves are used to compensate for this effect and can be used to extract true compositions from the profile. The standards must be of similar composition and structure and be analysed under the same machine conditions. The contribution to tracer experiments can be assumed to be negligible if comparisons are made between the runs using the same starting material.

Empirical Edge and Knock-on Compensation

As explained earlier, analytical considerations and limitations resulted in measurable edge and knock-on contributions to the observed profiles. Experiments were designed to examine these additions with the aim of deriving a procedure capable of recognizing and removing them from the diffusion curves.

The first experiment used a sample with a thin film of strontium which was vacuum deposited on a polished surface. Areas of this specimen were analysed under a variety of machine conditions which were modified so as to shorten the observed profile. Variables were: the beam size and current;

the rastered area; the imaged field; and the field aperture. The ratio of the beam size to rastered area which gave acceptable penetration rates was approximately 0.08. The rastered area of 100 μm square was 20 times larger than the 25 μm diameter imaged field. The image was further reduced by using the #2 field aperture which gave an imaged diameter of 13 μm in conjunction with the 25 μm setting. After several alternatives had been tried, these conditions were chosen because they gave maximum shortening of the profiles while maintaining a reasonable sputtering yield.

The primary beam and rastered area positions were optimized for each analysis by first adjusting the beam placement for maximum secondary ion intensity with the #1 aperture (30 μm), no secondary voltage offset, and zero raster. The #2 aperture was then brought into place and the voltage offset applied. The offset changes the electrical field around the sample surface and bends the primary beam slightly. The beam position was therefore readjusted for maximum count rate under these conditions. Since rastering occurs around the stable beam position, the imaged field was thus centered in the rastered area. Peak positions were located with the depth profile program standardization routine and the sample was moved slightly to provide a fresh surface for analysis. This procedure was followed before each run in the study.

The results for the surface tracer test sample are represented by the plot in Figure (4-6a). The initial increase in the major isotopes ^{28}Si and ^{40}Ca is caused by sputtering through the gold coat. The coat had been breached by the time ^{88}Sr was counted on the first cycle. In Figure (4-6b), the ^{88}Sr counts have been normalized to the ^{40}Ca counts and machine and sample backgrounds have been subtracted. These data can be effectively modeled by the sum of two exponential curves. First, the least squares

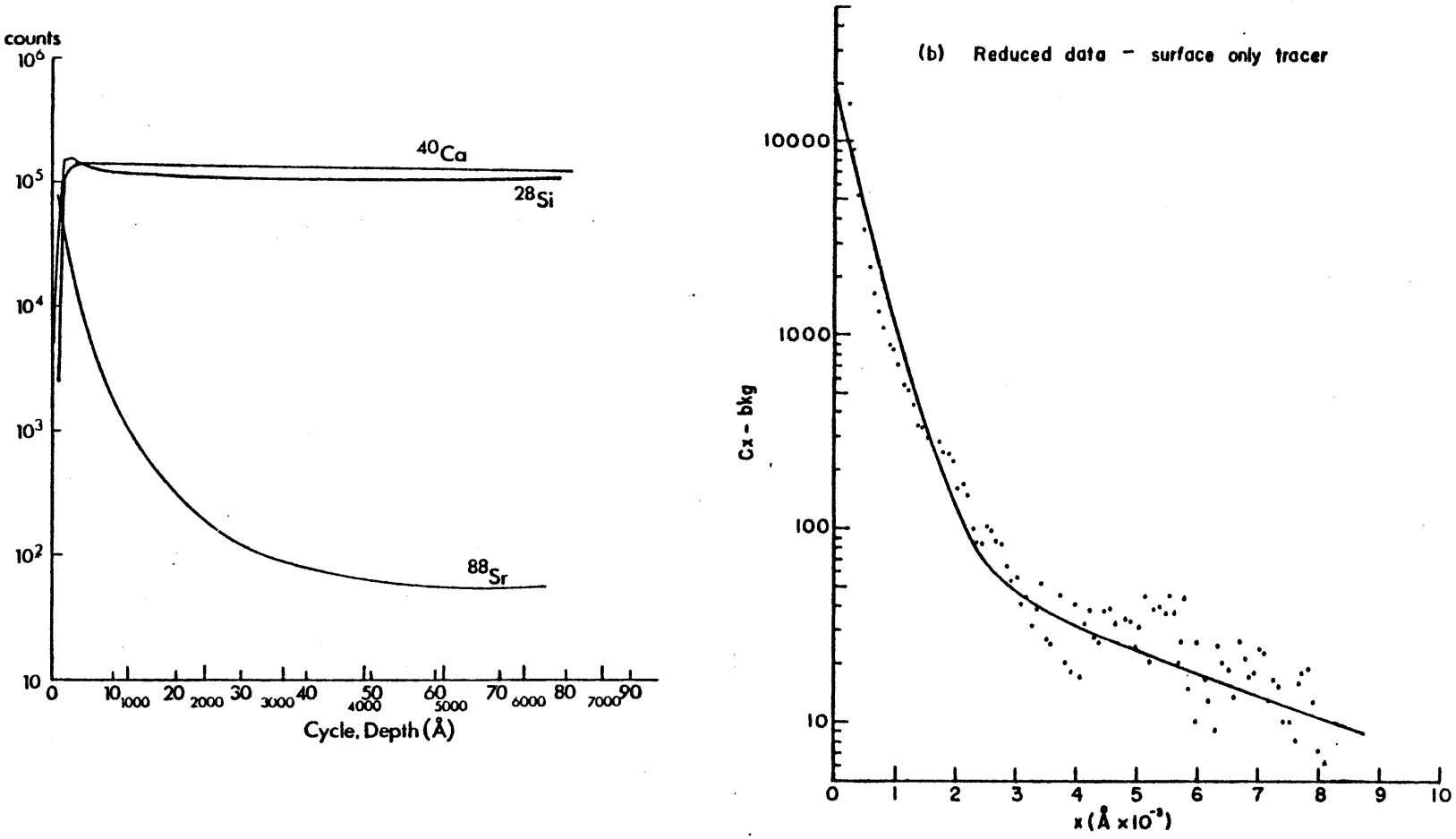

Figure 4-6. Surface only tracer profiles. (a) Curves fit through the raw data showing the apparent background for the ^{88}Sr profile. (b) Reduced ^{88}Sr data showing the tail and near-surface broadening. The solid curve is the sum of exponentials fit to the respective ends of the profile.

best fit of the "tail" (>4000 Å) was determined and this line subtracted from the observed curve. A second exponential was fit to the remainder. The point-by-point sum of these two exponential lines is represented by the solid curve in Figure (4-6b). Other attempts to model the data produced no better fits than that shown. These two exponentials cannot be divided into one for edge effect and one for knock-on because the magnitude of the tail and the depth extension of the front section (fit by the second curve) both vary with the size of the rastered area. This is evidence of an edge contribution to both. The size of the tail is also strongly dependent on the beam shape and focus, and the position of the analysed area within the pit.

Hall and Morabito (1976) developed a formalism for extracting diffusion coefficients from ion probe profiles of diffusion couples. The idea is to measure the profile before and after the diffusion anneal under identical conditions and then "subtract" the initial gradient from the final one. Their justification comes from the fact that a gaussian diffusion process measured by an instrument whose response is gaussian results in an uncorrected profile which is also gaussian. Also, observed broadening can be treated as the square root of the sum of the squares of the diffusion length and the instrument resolution (Lo and Schuele, 1975). Thus, concentration gradients add as reciprocal squares and as long as an effect is gaussian it can be added to this sum. Factors such as instrument resolution, surface roughness, and initial diffusion can be theoretically separated from the diffusion profile. (Initial diffusion is that which occurs during the heat up and cool down periods of an experiment.) Hall and Morabito represent this with the equation:

$$G_{obs}^{-2} = G_{diff}^{-2} + G_{init\ diff}^{-2} + G_{resol}^{-2} + G_{rough}^{-2} \qquad (4\text{-}3)$$

where G is a concentration gradient dc/dx. Since the only difference between the before analysis and the after analysis is the gradiant due to diffusion (G_{diff}), the above can be rewritten:

$$G_{diff}^{-2} = G_{obs}^{-2}]_{t=t} - G_{obs}^{-2}]_{t=0} \qquad (4\text{-}4)$$

Their formula is applicable when the measured profiles can be described by error function complements (erfc), thus giving straight lines on a probability plot. This is true for diffusion couples but not for thin film source experiments. The concentration for couples is given by:

$$C = \frac{C(x,t)}{C(-\infty,t)} = 0.5\text{erfc}(x/2\sqrt{Dt}) \qquad (4\text{-}5)$$

The diffusion gradient G is the derivative of the above.

$$G_{diff} = \frac{dc}{dx} = \frac{1}{2\sqrt{\pi Dt}} e^{-x^2/4Dt} \qquad (4\text{-}6)$$

and at x = 0, gives:

$$G_{diff}^{o} = -(4\pi Dt)^{-1/2} \qquad (4\text{-}7)$$

Substituting this into equation (4-4) and rearranging terms yields:

$$D = [1-(G_t/G_o)^2]/4\ G_t^{\,2}t \qquad (4\text{-}8)$$

The data are plotted on a probability graph (Figure 4-7) and the gradients G_o and G_t are measured. These measurements are accomplished by extrapolating the gradient from x = 0 using the equation:

$$y = Gx + 0.5 \qquad (4\text{-}9)$$

The values where y = 1 and y = 0 are given by:

$$x_o = -0.5/G \quad \text{and} \quad x_1 = 0.5/G \qquad (4\text{-}10)$$

Since $G = -(4\pi Dt)^{-1/2}$ for a diffusion problem, substitution of x_o and x_1 into equation (4-5) gives:

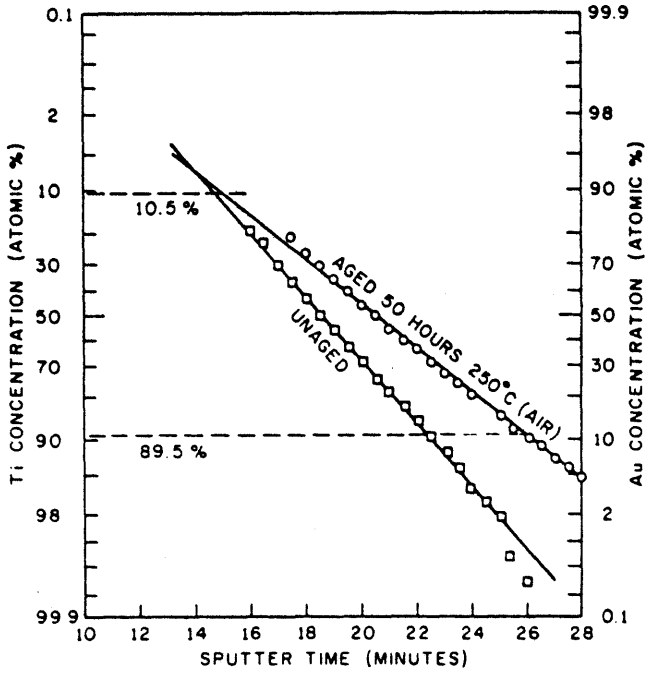

Fig. 1. Probability plot of Auger data for Ti-Au before (unaged) and after (aged) heat treatment at 250°C.

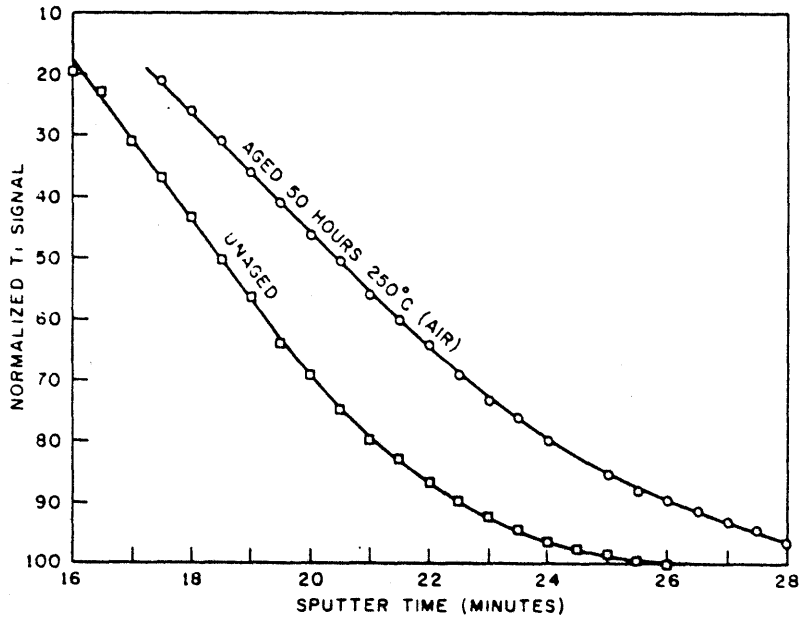

Fig. 2. Linear plot of Auger data for normalized Ti signal before (unaged) and after (aged) heat treatment at 250°C.

Figure 4-7. Plots of Ti-Au interdiffusion shown as an example of Hall and Morabito's (1976) formalism for diffusion couples. The top diagram is a probability plot and the lower graph contains the same concentrations on a linear plot (from Hall and Morabito, 1976).

$$C_{x_o} = 0.5\text{erfc}(\sqrt{\pi}/2) \quad \text{and} \quad C_{x_1} = 0.5\text{erfc}(-\sqrt{\pi}/2) \qquad (4\text{-}11)$$

or:

$$C_{x_o} = 0.105 \quad \text{and} \quad C_{x_1} = 0.895$$

These are the values on the probability plot equivalent to y = 0 and y = 1. x_o is therefore written $x_{0.105}$ and x_1 is written $x_{0.895}$. The gradient (G_o or G_t) can be derived from equations (4-9) and (4-10) and the substitution of $x_{0.105}$ and $x_{0.895}$:

$$G = (x_{0.895} - x_{0.105})^{-1} \qquad (4\text{-}12)$$

Values for x are read from the plot (Figure 4-7) at C = 0.895 and C = 0.105 and G_o and G_t are calculated. These are utilized in equation (4-8) to derive D.

In order to use this formalism with thin film derived profiles, the data must be recalculated in the form of residual diffusant. That is:

$$C_x = \int_x^\infty C(x,t)dx = C_o\text{erfc}(x/2\sqrt{Dt}) \qquad (4\text{-}13)$$

where C_o is the total amount of diffusant applied to the analysed area. $C_x/2C_o$ is plotted on the probability graph and the formalism is applied.

However, a similar formula is derived here which uses concentration data from thin source experiments directly. Machine and initial transport effects are subtracted and diffusion coefficients are calculated. In this case, the solution to Fick's Second Law is:

$$C(x,t) = \frac{C_o}{\sqrt{\pi Dt}} e^{-x^2/4Dt} \qquad (4\text{-}14)$$

At x = 0 the exponential term disappears and:

$$C(0,t) = \frac{C_o}{\sqrt{\pi Dt}} \qquad (4\text{-}15)$$

which is equivalent to Hall and Morabito's C. Differentiation with respect to x results in the gradient due to diffusion.

$$G_{diff} = \frac{dC}{dx} = \frac{x}{2Dt} e^{-x^2/4Dt} \qquad (4\text{-}16)$$

Inspection shows that at $x = 0$, $G_{diff} = 0$, so another point must be chosen at which to measure the gradient. $x = 2\sqrt{Dt}$ is chosen for convenience, yielding:

$$G_{diff} = e^{-1}/\sqrt{Dt} \qquad (4\text{-}17)$$

Substituting this into equation (4-4) and solving for D produces an equation analogous to equation (4-6).

$$D = e^{-2}[1-(G_t/G_o)^2]/G_t{}^2 t \qquad (4\text{-}18)$$

Measurement of the gradients is accomplished by extrapolating from $x = 2\sqrt{Dt}$ using the equation $y = Gx$. At $y = 0$ and $y = 1$, $x = 0$ and $x_1 = 1/G$. These values of x are entered into equation (4-15) to derive the concentrations which correspond to the values of y.

$$C_{x_o} = e^{-0/4Dt} \quad \text{and} \quad C_{x_1} = e^{-(1/G)^2/4Dt} \qquad (4\text{-}19)$$

or:

$$C_{x_o} = 1 \quad \text{and} \quad C_{x_1} = e^{-1.85} = 0.158$$

The data are plotted in the normal fashion for a thin film source, ln C vs x^2, which yields a straight line (Figure 4-8). G is rewritten to include the values of x at C_{x_0} and C_{x_1}:

$$G = (x_{0.158} - x_1)^{-1} \qquad (4\text{-}20)$$

the plot of ln C vs x^2 leads to some modifications in this equation. First, The subscripts of x can be changed to reflect the natural log values of C. Second, the scale on the abscissa is x^2 and therefore the square root of the

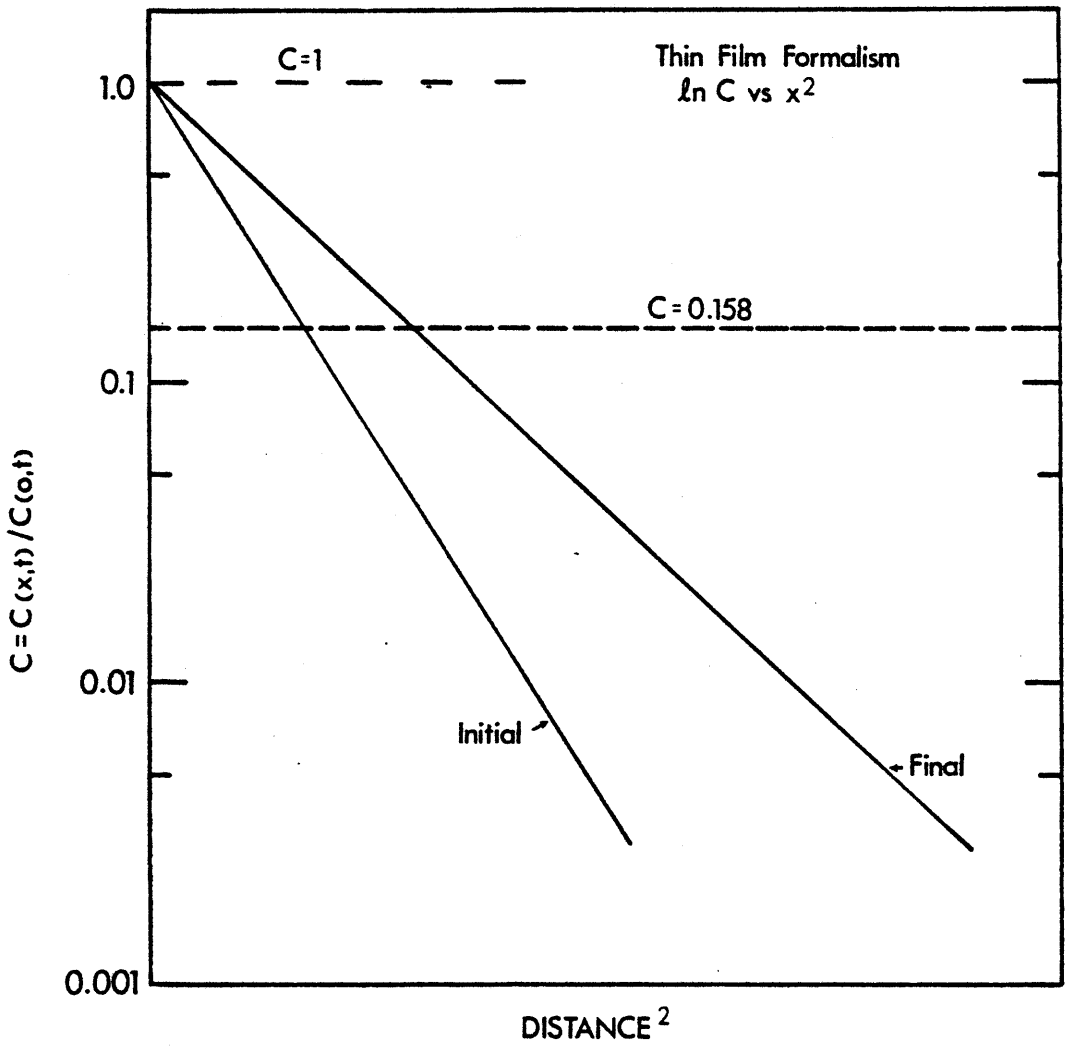

Figure 4-8. Schematic representation of the thin-film formalism (ℓn C vs x^2). Dashed lines are at values of C used to define gradients for calculation of diffusivities.

difference between the two points must be calculated for equation (4-20). The relationship which results is:

$$G = (x^2_{-1.85} - x^2_0)^{-1/2} \qquad (4\text{-}21)$$

The values of G are entered in equation (4-18) and a D is calculated.

It should be noted that the only reason for using the probability plot and the ln C vs x^2 plot is to linearize the data. The formalisms can be applied without that step. It simply indicates how closely the actual curves follow theory.

With these treatments in mind, a sample (B14) was prepared with a surface deposited tracer. It was heated to 1100°C and then immediately cooled at the rate other runs were. This zero time experiment was compared to other B series runs with the same run temperature. All profiles from these samples exhibited obvious tails beyond the diffusion produced curves. These were removed by subtracting the best fit exponential line through the later cycles of each run from the rest of the points. Following this, the gradients were calculated using the thin film source formalism. The zero time gradients were considerably steeper than the others so that G_t/G_o was much less than G_t and equation (4-18) was effectively reduced to:

$$D = e^{-2}/G_t{}^2 t \qquad (4\text{-}22)$$

Therefore, data manipulation for ion probe effects beyond subtraction of the exponential fit to the tail end of the observed profile was not employed for the diffusion coefficients derived in this study.

Theoretical evaluation of such effects as knock-on and edge contributions do not provide much help in extracting the true diffusion curve from observed profiles. However, empirical formulas can eliminate obvious machine-generated

additions, and uncertainties in other aspects of the experiment are large enough to mask further contributions. Thus, ion probe depth profiling can be used to determine diffusion coefficients as long as it is realized that the observed profile has most likely been modified by the analytical process. Sources of these modifications are instrumental uncertainties and the effects of the sputtering process.

V. DATA PRESENTATION

"There are lies, damned lies, and statistics." - Disraeli

Three analytical methods for determination of the diffusion coefficients and two distinct sample types were used in this work. The diffusivities derived from each method will be presented individually in this chapter along with the data reduction procedures. Sources of error will also be examined and conclusions internal to each set, including Arrhenius relations, will be presented. The results of time studies and a representative concentration-dependent solution will be discussed toward the end of the chapter. Comparisons among the three methods will be undertaken in the next chapter.

Radiotracer and sectioning

The original experiments in this study consisted of a radioactive tracer diffused into a piece of natural diopside, with analysis by grinding the doped face of the specimen while counting its residual activity. Additional radiotracer experiments were performed on synthetic crystals to allow comparison with the other methods. All runs were at one atmosphere and those using natural samples were run in nitrogen.

Raw data were in the form of residual activity counts and the change in the weight of the sample. The thickness of the removed layers were calculated from the measured surface area, the density of the material, and the weight difference. Sample activity was normalized using a standard and the background was subtracted.

Count rates dropped very quickly within the first 0.2 to 0.5 microns of the sample and then decreased more slowly thereafter. This was taken to represent a high surface concentration of an undiffused stable compound of Sr. Supporting evidence for this assumption included the fact that the ^{85}Sr tracer was a very small percentage (<5%) of the total strontium present.

In addition a layer of unidentified material was visible on the surface of some samples after the anneal. The experiment was modeled as a diffusion couple consisting of the diopside and a strontium-rich phase with a distribution coefficient such that a constant concentration of Sr was maintained at the surface of the diopside.

The concentration with depth in this case is represented by:

$$C(x,t) = C(0,t)\text{erfc}(x/2\sqrt{Dt}) \qquad (5\text{-}1)$$

Residual activity (residual diffusant) is found by the integration of the above from x to ∞.

$$C_x = \int_x^\infty C(x,t)dx = C(0,t)\sqrt{Dt}\ 2\text{ierfc}(x/2\sqrt{Dt}) \qquad (5\text{-}2)$$

where ierfc is the integrated error function complement defined by:

$$\text{ierfc } x = \int_x^\infty \text{erfc}\eta d\eta = \frac{1}{\sqrt{\pi}} e^{-x^2} - x \text{ erfc } x \qquad (5\text{-}3)$$

Tables of 2 ierfc x are available (Hartlee, 1935). C_0, the total amount of diffusant, can be calculated from equations (5-2) and (5-3):

$$C_0 = 2\ C(0,t)\ \sqrt{Dt}/\sqrt{\pi} \qquad (5\text{-}4)$$

and reinserted into equation (5-2) giving:

$$C_x = 0.886\ C_0\ 2\ \text{ierfc}\ (x/2\sqrt{Dt}) \qquad (5\text{-}5)$$

The value of C_0 was estimated by choosing two points on the profile and solving for the observed ratio C_{x1}/C_{x2} by varying D. The estimate of D was then used to calculate C_0 for both points. The measured values of x which correspond to the calculated C_0's ranged from 0.05 to 0.5 microns and usually occurred at an obvious change in slope on a plot of C vs x (Figure 5-1a). data were plotted on a graph of 2 $\text{ierfc}^{-1}(C_x/0.\text{-}86C_o)$ vs x, where 2 ierfc^{-1} is defined by A = 2 ierfc B. The numbers should plot on a straight line with

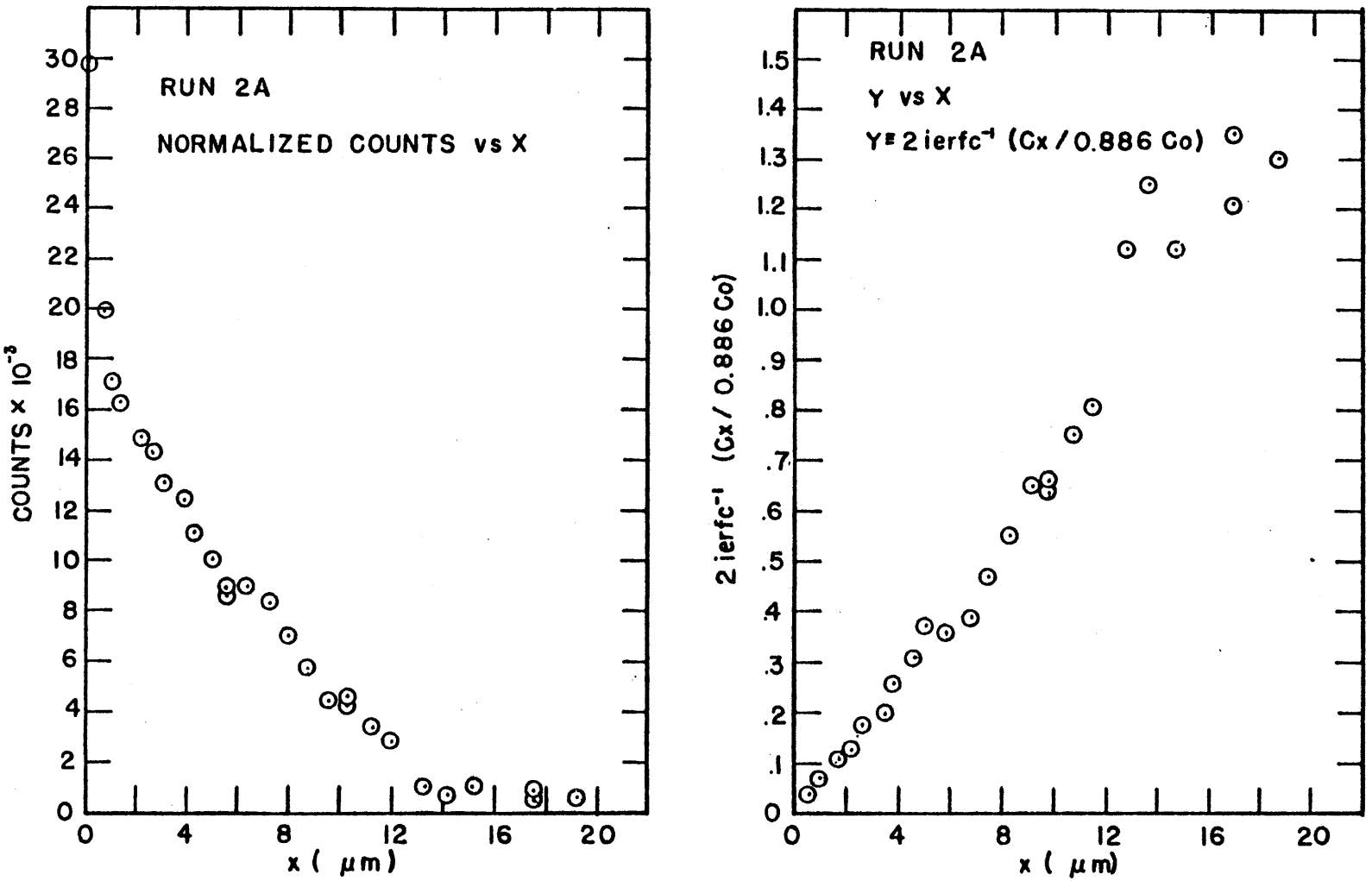

Figure 5-1. RT run #2a (c direction, 1250°C, natural sample). (a) Normalized ^{85}Sr residual activity minus background (C_x) vs cumulative thickness of removed layer (x). (b) Y vs x where $Y = 2\ \text{ierfc}^{-1}(2C_x/\sqrt{\pi}C_0)$.

an intercept of zero (Figure 5-1b). If the fit was not acceptable C_0 was recalculated from two other points and the data replotted. The slope of the best fit stright line (b) was used to calculate D via the relation:

$$D = (4\ b^2\ t)^{-1} \tag{5-6}$$

A variety of sources contribute to the uncertainty in the calculated value of D. Counting statistics predict an error bar for an observed number equal to plus or minus the square root of that number. This was applied to all values generated by the measurement of radioactivity (sample, standard, and background) and to the calculated value of C_0. The uncertainty in the ratio C_x/C_0 is therefore dependent on total counts and was appreciable (>10%) in instances of low count rates. For most points, the value was less than 5%. Replicate weighings of samples from time to time gave an average deviation of ±3 μg. Surface dimensions were measured with a microscope and calibrated grid with a probable error of ±0.1 mm. Maximum uncertainty for any single section was approximately 8%. The variability in a given value of x was found by the following:

$$\sigma_x = \left(\sum_{i=1}^{n} \sigma_{\Delta x}^2\right)^{1/2}/n \tag{5-7}$$

The slope (b) and the intercept (a) of the best fit line were calculated using the equations for the "major axis" (York, 1966).

$$b = \frac{\Sigma V_i^2 - \Sigma U_i^2 + [(\Sigma V_i^2 - \Sigma U_i^2)^2 + 4(\Sigma V_i U_i)^2]^{1/2}}{2\Sigma U_i V_i} \tag{5-8}$$

where:

$$U_i = x_i - \bar{x} \quad \text{and} \quad V_i = y_i - \bar{y},$$

$$a = \bar{y} - b\bar{x} \tag{5-9}$$

$$r = \Sigma U_i V_i / (\Sigma U_i^2 \Sigma V_i^2)^{1/2} \tag{5-10}$$

and:

$$\sigma_b = \frac{b}{r}\left(\frac{1 - r^2}{n}\right)^{1/2} \qquad (5\text{-}11)$$

where r is the correlation coefficient with r = 1 perfect correlation, r = 0 no correlation, and r = -1 perfect negative correlation. This treatment assumes that all points carry equal weight, which was not the case in the present experiments. Individual weighting factors, $\omega(x_i)$ and $\omega(y_i)$, were derived as the reciprocals of the variances ($\sigma_{x_i}^2$ and $\sigma_{y_i}^2$) and York's "least squares cubic" was applied to representative analyses. By elimination of points with large σ_i's (>10%), good agreement between the two methods was achieved for the diffusion coefficient. Thus, the more convenient major axis formulation was accepted for the data reduction.

The uncertainty in the diffusion coefficient was calculated as:

$$\sigma_D = \sqrt{2}\sigma_b / 4b^2 t \qquad (5\text{-}12)$$

and ranged from 2 to 31% for the values used in this portion of the study.

The temperatures, times, crystal directions, and diffusion coefficients are listed in Table (5-1) and the data are plotted on an Arrhenius plot (lnD vs 1/T) in Figure (5-2). The activation energy was calculated for each data set (natural and synthetic) using the equation:

$$\Delta H_a(\text{cal/mole}) = -Rb \qquad (5\text{-}13)$$

where R is the gas constant equal to 1.987 cal/deg mole and b is the slope of the best fit straight line calculated using the least squares cubic (York, 1966).

Comparison between the natural and the synthetic samples shows that while the activation energies are practically the same, the D's at a given temperature differ by two orders of magnitude. A number of factors are likely contributors to the cause of this difference. The dislocation densities of the natural and synthetic samples have been estimated by examination of etch

Table 5-1. Radiotracer and sectioning, Sr, c direction, one atm.

natural

run #	T(°C)	$t \times 10^{-5}$(sec)	D(cm^2/sec)
3	1300	7.76	$1.6 \pm 0.1 \times 10^{-12}$
5A	"	4.12	$1.5 \pm 0.1 \times 10^{-12}$
7	"	4.14	$1.8 \pm 0.2 \times 10^{-12}$
2A	1250	7.99	$6.5 \pm 0.4 \times 10^{-13}$
4A	"	9.22	$3.9 \pm 0.6 \times 10^{-13}$
4B	"	"	$3.6 \pm 0.3 \times 10^{-13}$
6A	"	8.14	$3.6 \pm 0.2 \times 10^{-13}$
8	1200	16.8	$1.1 \pm 0.1 \times 10^{-13}$
10	"	11.9	$4.0 \pm 0.2 \times 10^{-13}$
12	"	15.3	$2.8 \pm 0.1 \times 10^{-13}$

$\Delta H_a = 97 \pm 17$ Kcal/mol

$D_o = 54$ cm^2/sec

synthetic

run #	T(°C)	$t \times 10^{-5}$(sec)	D(cm^2/sec)
18A	1300	5.58	$8.3 \pm 2.6 \times 10^{-15}$
18B	"	"	$1.3 \pm 0.2 \times 10^{-14}$
15A	1250	7.66	$6.9 \pm 1.2 \times 10^{-15}$
15B	"	"	$5.4 \pm 0.8 \times 10^{-15}$
36A	1200	10.4	$1.7 \pm 0.04 \times 10^{-15}$
36B	"	"	$8.9 \pm 1.1 \times 10^{-16}$

$\Delta H_a = 109 \pm 18$ Kcal/mol

$D_o = 24$ cm^2/sec

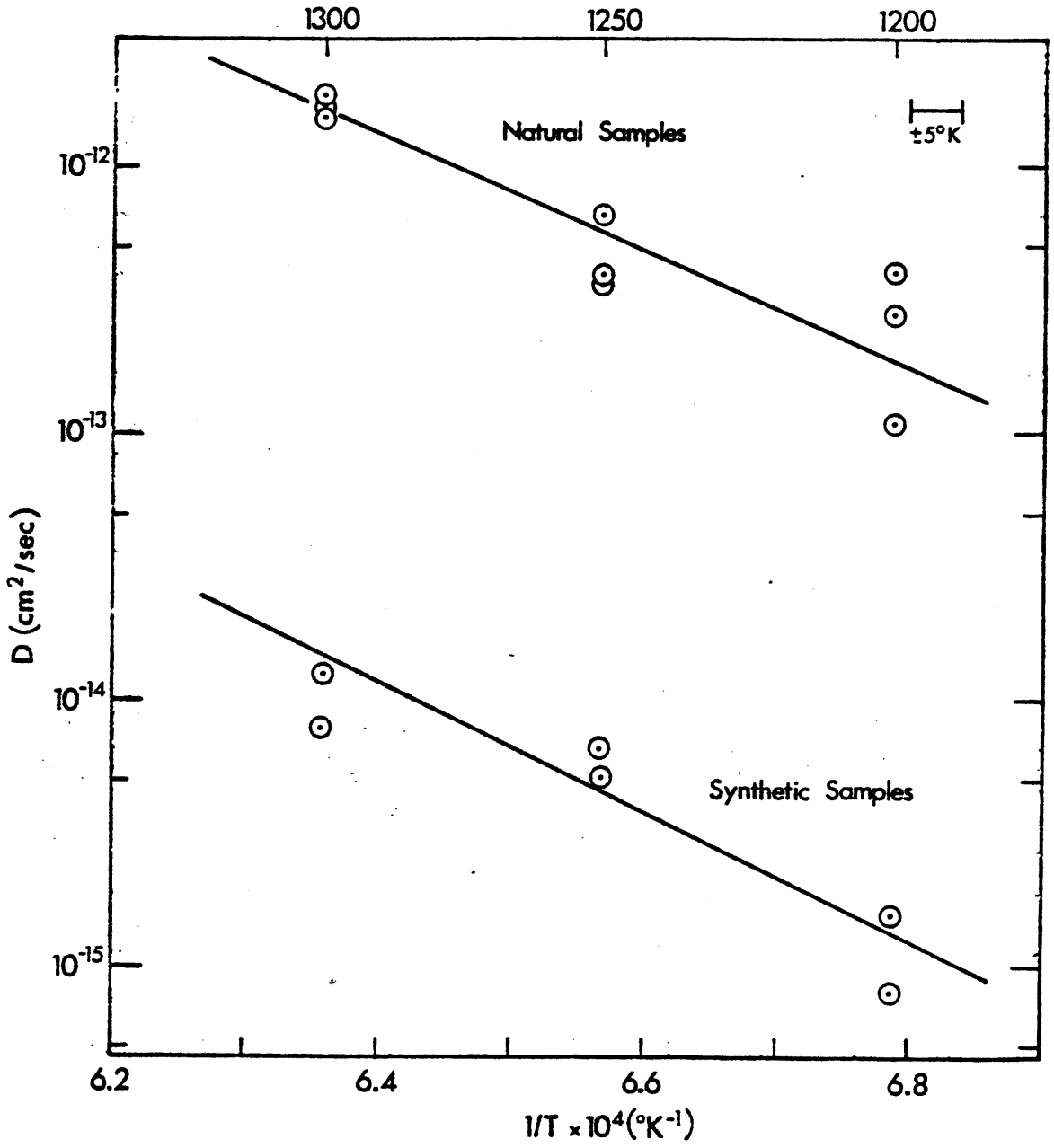

Figure 5-2. Radiotracer and sectioning, ℓn D vs 1/T. Upper line is for the natural samples, ΔH_a = 97 ± 17 Kcal/mol and D_0 = 54 cm^2/sec. Lower line is for the synthetic samples, ΔH_a = 109 ± 18 Kcal/mol and D_0 = 24.5 cm^2/sec. Error bar in upper right-hand corner is equivalent to approximately ±5°K. Uncertainties in D are listed in the tables.

pits and the natural diopside was found to contain roughly two orders of magnitude more of these defects than the laboratory-grown crystals. Buening and Buseck (1973) have demonstrated that Mg-Fe interdiffusion rates increase with increasing oxygen fugacity for iron-bearing olivines. They attributed this to an increased vacancy concentration associated with electron holes needed to balance the charge of Fe^{3+}. A similar effect may occur in this study in that the natural samples contain approximately eight times the Fe in the synthetic specimens. The oxygen fugacities during the diffusion anneals were probably higher than during formation of the natural crystals, resulting in oxidation of the Fe and formation of vacancies. A third factor is the high impurity level of the natural samples, which may also affect the defect concentration. All of these effects would be manifested in the frequency factor of the Arrhenius relation. The activation energy is essentially unchanged becuase defect levels are assumed to be sufficiently high in both materials so that diffusion is controlled by the activation energy of defect movement (extrinsic diffusion). This value, ΔH_m, is independent of the impurity concentration. Quantitation of the various effects on the D_o is not possible in the present study due to the number of contributing parameters. Variation of a single factor while holding all others constant is necessary for such an examination.

Ion probe depth profiling

Samples analysed with the ion probe were divided into three groups; diffusion couples at one atmosphere, surface tracer at one atmosphere, and high pressure diffusion couples. All samples were crystallographically oriented pieces of synthetic crystals. Analysis conditions were the same for the three series and the raw data were in the form of counts vs elapsed time in cycles. After normalization, the count rate is directly proportional

to the diffusant concentration. Since relative concentrations can be used to derive D, the use of normalized counts will give the same diffusivity. D was calculated in the units of cycles^2/sec and then converted to cm^2/sec by measuring the final hole depth and calculating the distance per cycle. This was done by subtracting 200 Å for the thickness of the gold coating and dividing the remainder by the number of cycles minus those used to sputter through the gold. Not all holes were measured. Some depths were estimated from the measured penetration rate of neighboring analyses, which was normally constant for a given ion probe session. Diffusion coefficients derived from estimated holes are indicated in the data tables.

The background attributable to the counting electronics was subtracted from the raw data for both the tracer and the mass to which it was to be normalized. The ratio of the mean of the standard isotope and the counts of the standard for each cycle was used as a multiplier for the point-by-point normalization of the diffusant counts. Sample background was measured for the starting material and normalized in the same way before its average was subtracted from the normalized diffusion profile. A surface value C(0) was chosen by inspection and the data plotted on a graph of ln(C(x)/C(0)) vs x (Figure 5-3a). If there was a noticeable tail, as described in the last chapter, a straight line was fit through it. The curve was then subtracted point-by-point from the data.

The remainder was plotted lnC'(x) vs x^2 (Figure 5-3b) if the experiment was modeled as a thin film source, where $C'(x) = C(x)/C(0) - C_{tail}$. A straight line was fit using the major axis formula (equation 5-8) through the points with values $\geq 0.01C'(0)$. Points less than one percent of the tail-subtracted surface value were eliminated in order that the assumptions regarding weighting factors were not violated. The diffusion coefficients

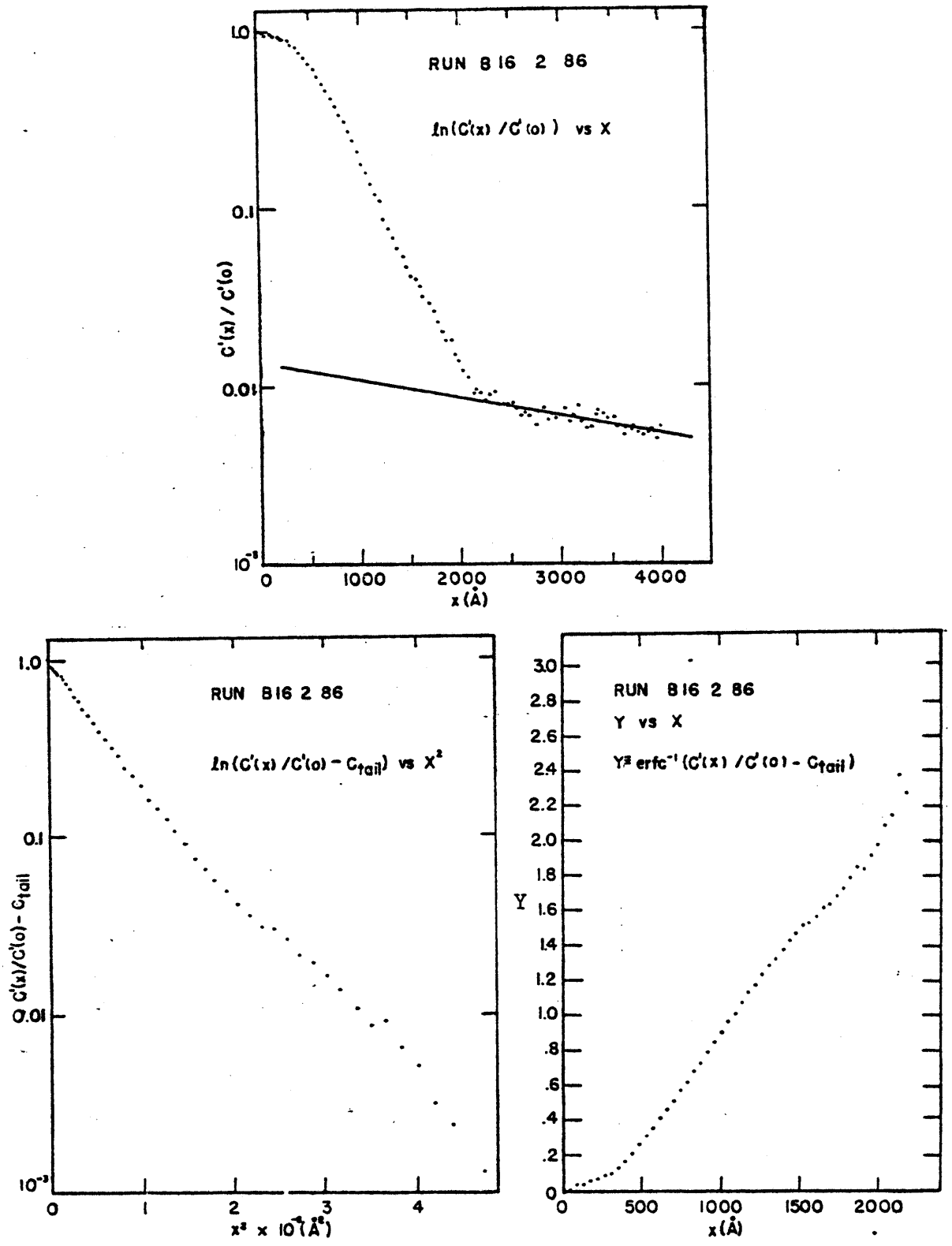

Figure 5-3. IP run #B16 2 86 (c direction, 1100°C, synthetic sample). (a) $\ell n[C'(x)/C'(0)]$ vs depth. C'(x) is the normalized counts at x. Machine-induced tail is evident and the line is the best fit for the data at $x > 2500\text{Å}$. (b) Thin film model, $\ell n[C'(x)/C''(0) - C_{tail}]$ vs x^2. C_{tail} is calculated at each point from the straight line in (a). (c) Y vs x, where $Y = \text{erfc}^{-1}[C'(x)/C'(0) - C_{tail}]$.

were derived from the equation:

$$D^c(\text{cycles/sec}) = -(4bt)^{-1} \qquad (5\text{-}14)$$

When modeled as a constant surface concentration (diffusion couple) a tail-subtracted-value for the surface was either estimated by eye or calculated in a fashion similar to that used in the radiotracer experiments. The relation in this case was:

$$C'(x) = C'(0)\text{erfc}(x/2\sqrt{Dt}) \qquad (5\text{-}15)$$

The data were plotted erfc^{-1} $[C'(x)/C'(0)]$ vs x (Figure 5-3c) and a straight line fit to the portion corresponding to values $C'(x) \geq 0.01\ C'(0)$. D was calculated from:

$$D^c(\text{cycles}^2/\text{sec}) = (4b^2t)^{-1} \qquad (5\text{-}16)$$

Uncertainty in D arises from the scatter of the data about the major axis more than from the deviations within each point. Counting statistics provide probable errors in the raw data which propagate through the normalization procedure to the C(x) values. The line used for subtraction of the tail is another source of error which must be factored into the uncertainty of C'(x). Since both lnC and $\text{erfc}^{-1}C$ are nonlinear, deviations in these values were estimated by calculating the values corresponding to $C + \sigma_c$ and $C - \sigma_c$ and halving the difference. Examination showed that the weighting factor $\omega(y_i)$ decreases with decreasing number of counts. By not using values of $C'(x) < 0.01\ C'(0)$ these factors can be assumed to be constant for the purpose of the calculation of the slope. The x values were assumed to be invariant so that the calculation on the major axis as the best fit to the data was acceptable. The standard deviation σ_{Dc} for the constant surface concentration model is given by equation (5-12) and for the thin film source by:

$$\sigma_D c = \sigma_b/4b^2t \qquad (5\text{-}17)$$

Profilometer traces were assigned an uncertainty of ±100 Å, which comes from the accuracy of reading the strip chart output of the measuring device. This corresponds to an estimated error of less than 5% for the shallowest holes (∿2000 Å). The penetration rate (s) was calculated by dividing by the number of cycles, so that the uncertainty is the same percentage for the conversion factor. Changing the units of D from cycles^2/sec to cm^2/sec incorporates σ_s into σ_D by the relationship:

$$(D^c \pm \sigma_D c)(s \pm \sigma_s)^2 = D \pm D^c s^2 [(\frac{\sigma D^c}{D^c})^2 + 2(\frac{\sigma s}{s})^2]^{1/2} (cm^2/sec) \quad (5\text{-}18)$$

For values of $\sigma_D c/D^c \geq 7$ or 8 times σ_s/s, the term $2(\sigma_s/s)^2$ becomes insignificant and the above reduces to:

$$D \pm \sigma_D = s^2(D^c \pm \sigma_D c) \quad (5\text{-}19)$$

Values of σ_s for estimated hole depths were derived from the calculation of the average penetration rate of the neighboring analyses. These values were larger than those of the measured holes and this is reflected in the uncertainties in the D values.

Strontium data

The data are listed in Tables (5-2) through (5-6) according to experiment type and crystallographic direction. They are also plotted in Figures (5-4) and (5-6). Activation energies are calculated from the least squares cubic fit of lnD vs 1/T. The high pressure data were also plotted on a graph of lnD vs P (Figure 5-7).

The data for the one atmosphere diffusion couples contain a great deal of scatter and in general have significantly lower values than the surface tracer experiments. The most probable cause of this is poor surface contact between the halves of the couple. The experiments were designed to alleviate this problem through finely polished surfaces and the weights on top of the

Table 5-2. Ion probe diffusion couples, Sr, one atm.

run #	T(°C)	t x 10^{-5}(sec)	D(cm^2/sec)
c direction			
25 a 8	1300	6.75	$1.0 \pm 0.4 \times 10^{-17}$
25 b 8	"	"	$1.6 \pm 0.2 \times 10^{-17}$
25 c 8	"	"	$4.1 \pm 1.0 \times 10^{-17}$
27 a 8	"	3.45	$6.9 \pm 0.9 \times 10^{-17}$
24 a 8	1250	4.22	$1.2 \pm 0.1 \times 10^{-17}$
24 c 8	"	"	$4.2 \pm 0.4 \times 10^{-18}$
28 a 8	1200	19.7	$1.7 \pm 0.3 \times 10^{-16}$
28 b 8	"	"	$1.4 \pm 0.1 \times 10^{-16}$
a direction			
35 a 1	1200	31.0	$4.2 \pm 1.3 \times 10^{-18}$
35 b 1	"	"	$1.7 \pm 0.5 \times 10^{-18}$
35 b 2	"	"	$3.0 \pm 0.9 \times 10^{-18}$
b direction			
29 b 8	1300	3.39	$2.0 \pm 0.1 \times 10^{-16}$
29 c 8	"	"	$1.0 \pm 0.2 \times 10^{-16}$
31 a 8	1250	12.0	$5.1 \pm 0.7 \times 10^{-18}$
31 b 8	"	"	$2.6 \pm 0.4 \times 10^{-18}$
30 b 8	1200	7.74	$1.6 \pm 0.4 \times 10^{-17}$
30 c 8	"	"	$8.9 \pm 2.2 \times 10^{-18}$

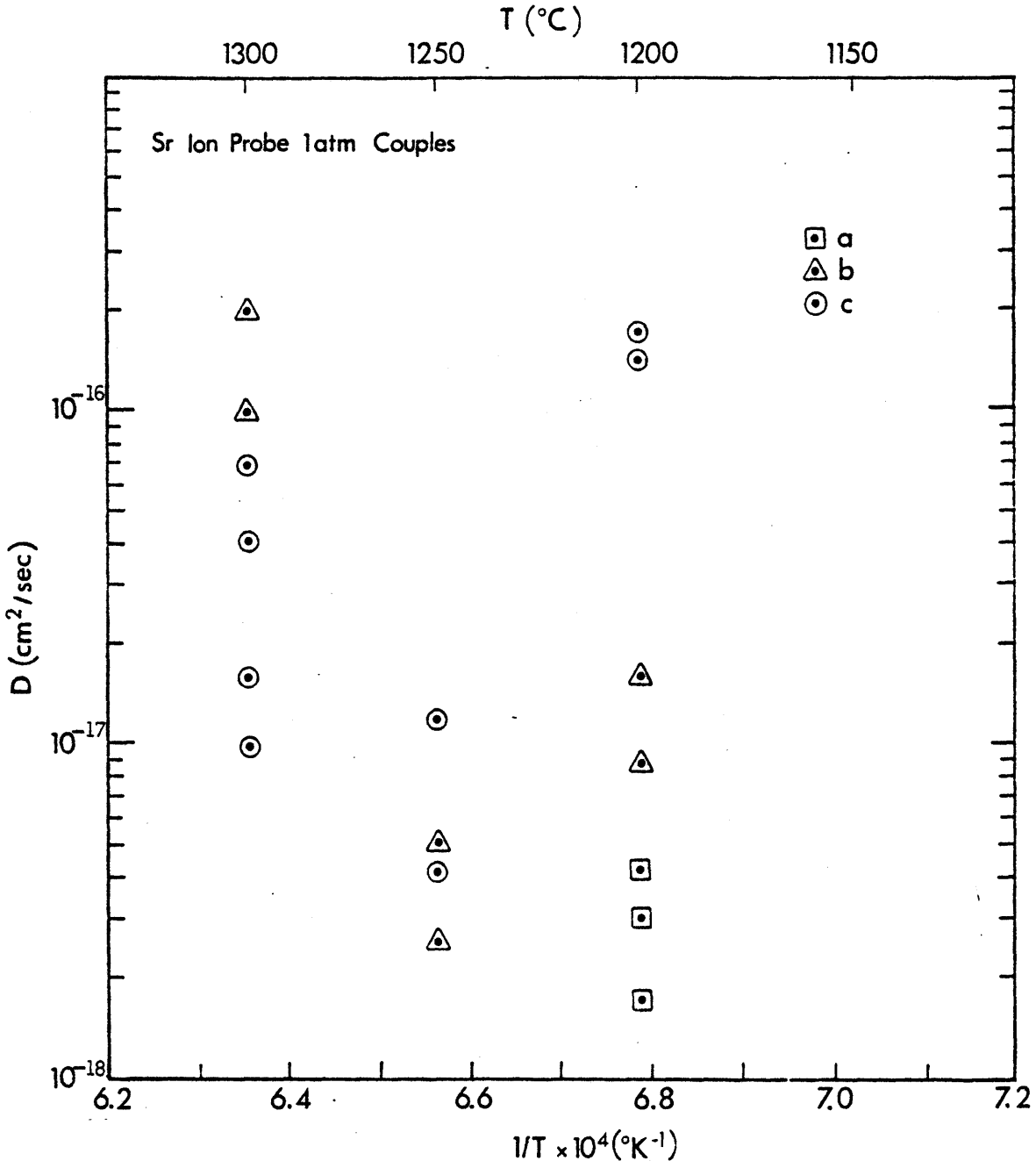

Figure 5-4. Ion probe diffusion couples for Sr at one atm, ℓn D vs 1/T. a direction - squares, b direction - triangles, c direction - circles.

Table 5-3. IP surface tracer experiments, Sr, one atm.

c direction

run #	T(°C)	t(sec)	D(cm^2/sec)
B13 1 88	1250	7200	$2.4 \pm 0.1 \times 10^{-15}$
86	"	"	$2.7 \pm 0.1 \times 10^{-15}$
B13 2 88	"	"	$3.1 \pm 0.1 \times 10^{-15}$
86	"	"	$3.3 \pm 0.1 \times 10^{-15}$
B12 1 88	1200	15300	$7.7 \pm 0.3 \times 10^{-16}$
B12 2 88	"	"	$1.3 \pm 0.1 \times 10^{-15}$
86	"	"	$1.3 \pm 0.1 \times 10^{-15}$
B10 1 88	1100	248000	$3.1 \pm 0.2 \times 10^{-17}$
86	"	"	$3.1 \pm 0.2 \times 10^{-17}$
B10 2 88	"	"	$3.5 \pm 0.2 \times 10^{-17}$
B16 1 88	"	335000	$7.3 \pm 0.5 \times 10^{-17}$
B16 2 88	"	"	$5.1 \pm 0.2 \times 10^{-17}$
86	"	"	$5.1 \pm 0.2 \times 10^{-17}$
B16 4 88	"	"	$2.4 \pm 0.1 \times 10^{-17}$
86	"	"	$2.5 \pm 0.1 \times 10^{-17}$
B17 1 88	"	169000	$9.2 \pm 0.2 \times 10^{-17}$
86	"	"	$9.2 \pm 0.2 \times 10^{-17}$
B17 3 88	"	"	$3.5 \pm 0.2 \times 10^{-17}$
86	"	"	$3.3 \pm 0.2 \times 10^{-17}$
B17 4 88	"	"	$1.8 \pm 0.1 \times 10^{-16}$
B17 5 88	"	"	$1.4 \pm 0.1 \times 10^{-16}$

$\Delta H_a = 122 \pm 7$ Kcal/mol

$D_o = 1200$ cm^2/sec

Table 5-4. IP surface tracer experiments, Sr, one atm.

a direction

run #	T(°C)	t(sec)	D(cm^2/sec)
B21 1 88	1250	43500	$1.6 \pm 0.1 \times 10^{-15}$
86	"	"	$2.0 \pm 0.1 \times 10^{-15}$
B21 2 88	"	"	$1.7 \pm 0.1 \times 10^{-15}$
B18 1 88	1200	79200	$5.4 \pm 0.2 \times 10^{-16}$
B18 2 88	"	"	$4.4 \pm 0.1 \times 10^{-16}$
86	"	"	$4.6 \pm 0.1 \times 10^{-16}$
B19 1 88	1150	173000	$1.6 \pm 0.1 \times 10^{-16}$
86	"	"	$1.5 \pm 0.1 \times 10^{-16}$
B19 2 88	"	"	$9.0 \pm 0.3 \times 10^{-17}$
B19 3 88	"	"	$2.5 \pm 0.1 \times 10^{-16}$
86	"	"	$2.5 \pm 0.1 \times 10^{-16}$

$\Delta H_a = 108 \pm 10$ Kcal/mol

$D_o = 6.4$ cm^2/sec

b direction

B22 1 88	1250	43500	$5.2 \pm 0.4 \times 10^{-15}$
86	"	"	$5.2 \pm 0.4 \times 10^{-15}$
B23 1 88	1200	88200	$9.7 \pm 0.4 \times 10^{-16}$
87	"	"	$9.7 \pm 0.4 \times 10^{-16}$
B23 2 88	"	"	$3.0 \pm 0.1 \times 10^{-15}$
B23 3 88	"	"	$1.4 \pm 0.1 \times 10^{-15}$
86	"	"	$1.4 \pm 0.1 \times 10^{-15}$
B20 1 88	1150	173000	$4.1 \pm 0.1 \times 10^{-16}$
86	"	"	$4.1 \pm 0.1 \times 10^{-16}$
B20 3 88	"	"	$1.4 \pm 0.04 \times 10^{-16}$
86	"	"	$1.4 \pm 0.04 \times 10^{-16}$
B20 5 88	"	"	$2.3 \pm 0.1 \times 10^{-16}$
B20 6 88	"	"	$1.5 \pm 0.04 \times 10^{-16}$
86	"	"	$1.5 \pm 0.03 \times 10^{-16}$

$\Delta H_a = 135 \pm 9$ Kcal/mol

$D_0 = 1.2 \times 10^5$ cm^2/sec

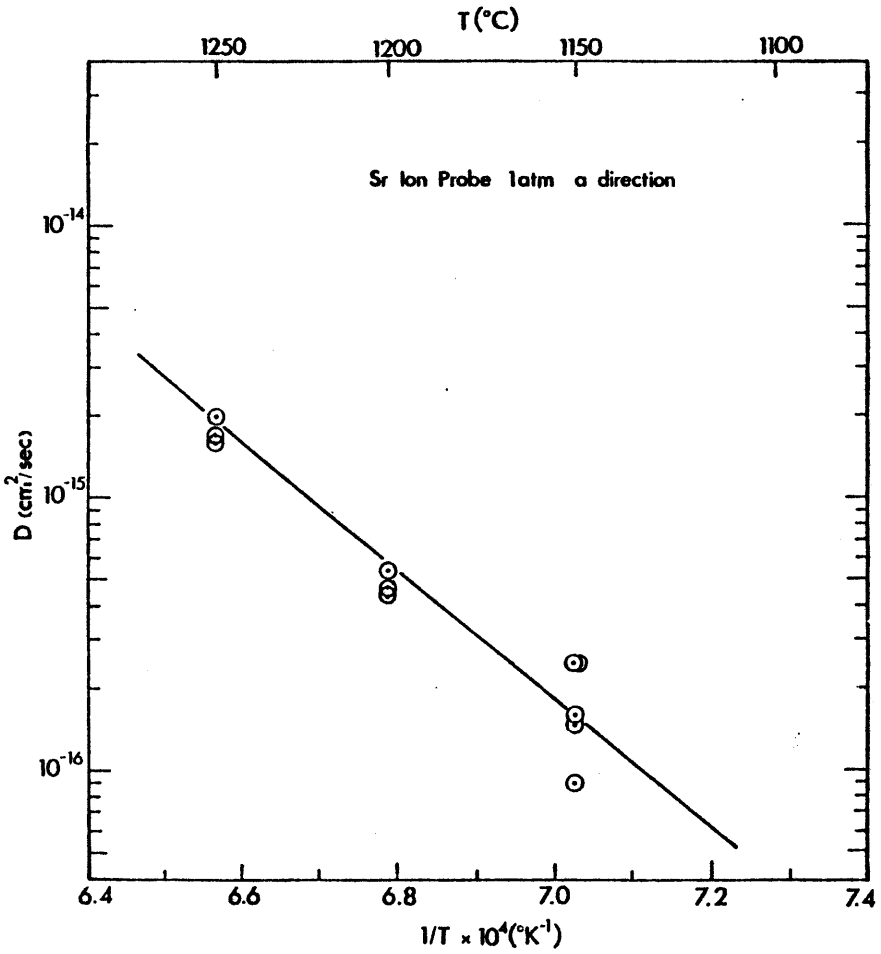
T(°C)
1250
1200
1150
1100
Sr Ion Probe 1atm a direction
10^{-14}
10^{-15}
10^{-16}
D (cm²/sec)
6.4
6.6
6.8
7.0
7.2
7.4
1/T × 10⁴(°K⁻¹)

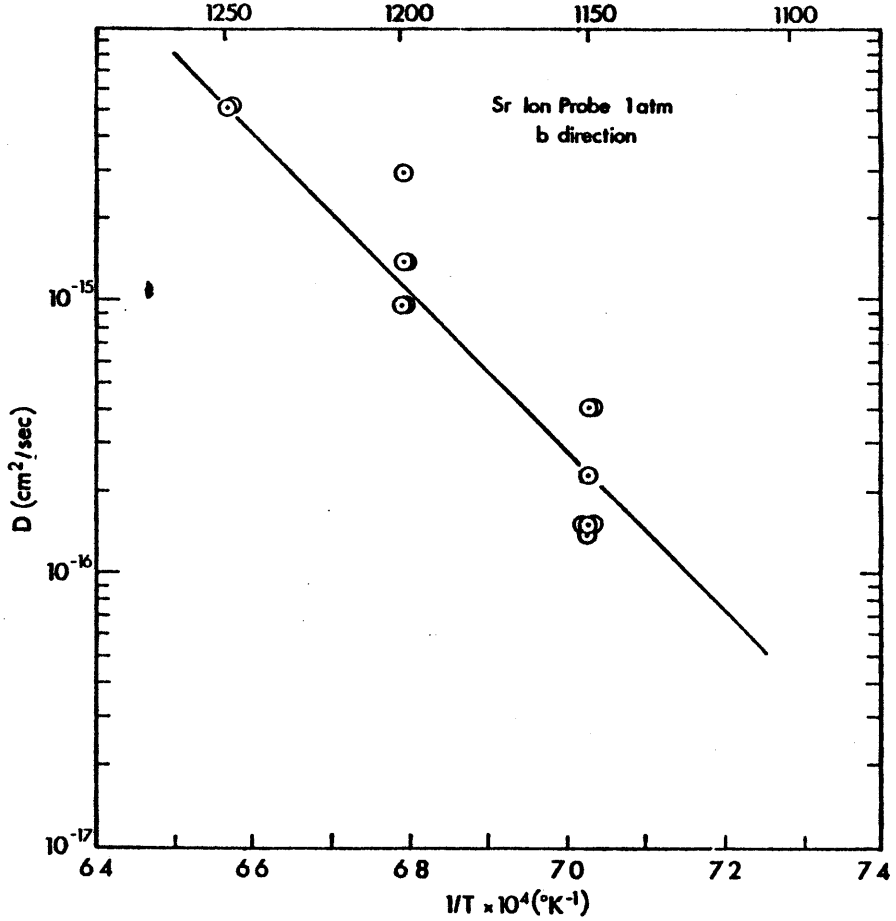
1250
1200
1150
1100
Sr Ion Probe 1atm
b direction
10^{-15}
10^{-16}
10^{-17}
D (cm²/sec)
6.4
6.6
6.8
7.0
7.2
7.4
1/T × 10⁴(°K⁻¹)

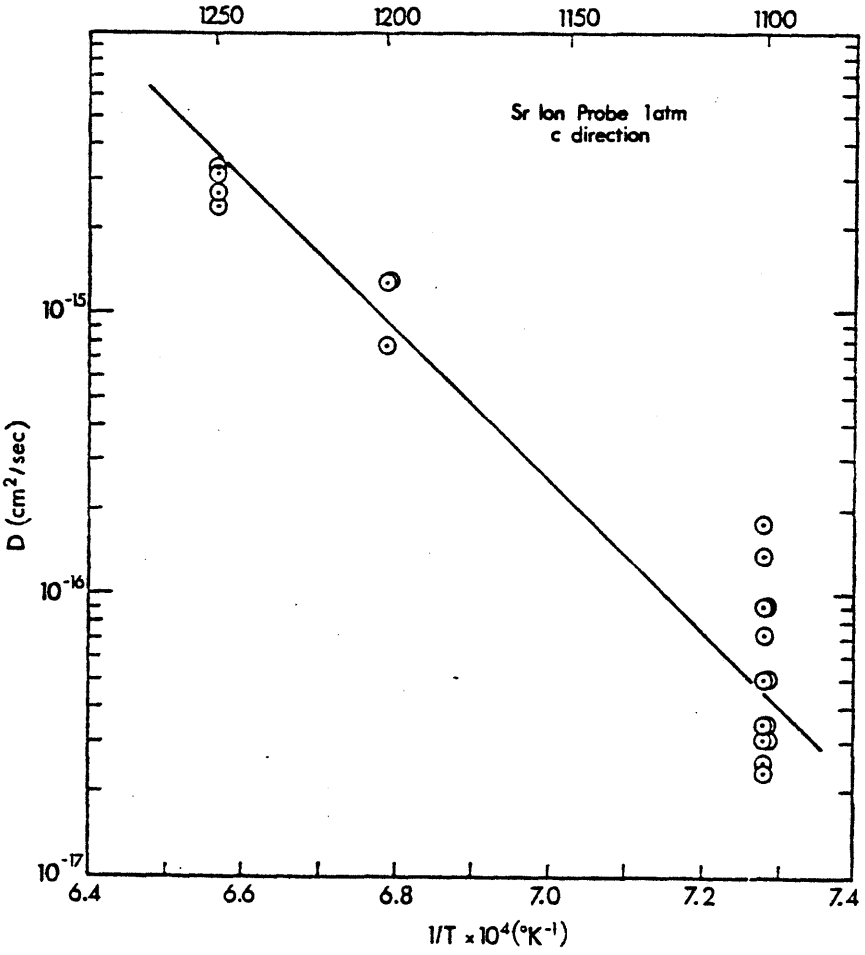

Figure 5-5. IP surface-tracer experiments for Sr at one atm, ℓn D vs 1/T. Temperature uncertainty is the same as for Figure 5-2. (a) a direction, ΔH_a^a = 108 ± 10 Kcal/mol and D_0 = 6.4 cm^2/sec. (b) b direction, ΔH_a^a = 135 ± 9 Kcal/mol and D_0 = 1.2 x 10^5 cm^2/sec. (c) c direction, ΔH_a^a = 122 ± 7 Kcal/mol and D_0 = 1200 cm^2/sec.

Table 5-5. IP diffusion couples, Sr, high pressure.

run #	T(°C)	t(sec)	D(cm^3/sec)
c direction			
P37 2	1250	28800	$1.4 \pm 0.05 \times 10^{-14}$
P22 2*	1200	18000	$4.2 \pm 0.1 \times 10^{-16}$
P22 3	"	"	$2.5 \pm 0.2 \times 10^{-15}$
P38 1*	"	54000	$2.8 \pm 1.1 \times 10^{-15}$
P38 2*	"	"	$2.9 \pm 1.4 \times 10^{-15}$
P38 4*	"	"	$1.7 \pm 0.7 \times 10^{-15}$
P38 5*	"	"	$1.2 \pm 0.3 \times 10^{-15}$
P16 5	1150	86400	$1.1 \pm 0.3 \times 10^{-15}$
P43 2*	1100	173000	$6.5 \pm 2.8 \times 10^{-17}$
P43 3	"	"	$7.8 \pm 1.6 \times 10^{-17}$
P43 4*	"	"	$10.4 \pm 5.4 \times 10^{-17}$
	$\Delta H_a = 145 \pm 8$ Kcal/mol		
	$D_o = 8.7 \times 10^6$ cm^2/sec		
c direction 14 Kbar			
P25 2	1250	21600	$6.9 \pm 0.6 \times 10^{-15}$
P25 3	"	"	$2.0 \pm 0.2 \times 10^{-14}$
P40 3	1200	57600	$1.7 \pm 0.4 \times 10^{-15}$
P40 4	"	"	$8.8 \pm 2.6 \times 10^{-16}$
P39 1	1150	86400	$6.0 \pm 1.5 \times 10^{-16}$
P39 2	"	"	$4.4 \pm 0.9 \times 10^{-16}$
	$\Delta H_a = 174 \pm 32$ Kcal/mol		
	$D_o = 1.2 \times 10^{11}$ cm^2/sec		
c direction 8 Kbar			
P28 1	1250	23400	$8.4 \pm 0.9 \times 10^{-15}$
P28 2	"	"	$3.9 \pm 0.3 \times 10^{-15}$
P41 3	"	28800	$7.0 \pm 1.8 \times 10^{-15}$

* = estimated hole depth

Table 5-6. IP diffusion couples, Sr, high pressure.

a direction 20 Kbar

run #	T(°C)	t(sec)	D(cm^2/sec)
P33 1*	1250	21600	$2.9 \pm 0.6 \times 10^{-14}$
P33 2*	"	"	$1.3 \pm 0.3 \times 10^{-14}$
P33 3*	"	"	$1.5 \pm 0.4 \times 10^{-14}$
P32 1*	1150	28800	$7.0 \pm 1.4 \times 10^{-15}$
P32 3*	"	"	$4.1 \pm 1.2 \times 10^{-15}$
P29 1*	1100	62100	$4.2 \pm 1.5 \times 10^{-15}$
P29 2	"	"	$1.7 \pm 0.1 \times 10^{-15}$
P29 4*	"	"	$6.5 \pm 1.6 \times 10^{-15}$

$\Delta H_a = 62 \pm 12$ Kcal/mol

$D_o = 1.7 \times 10^{-5} cm^2/sec$

b direction 20 Kbar

P34 1	1250	19800	$3.1 \pm 0.3 \times 10^{-14}$
P35 1	1150	37800	$3.4 \pm 1.1 \times 10^{-15}$
P35 2	"	"	$5.5 \pm 0.5 \times 10^{-15}$
P35 3	"	"	$1.2 \pm 0.1 \times 10^{-14}$
P31 1	1100	43200	$1.1 \pm 0.1 \times 10^{-15}$
P31 2	"	"	$4.1 \pm 0.2 \times 10^{-15}$

$\Delta H_a = 91 \pm 20$ Kcal/mol

$D_o = 0.52\ cm^2/sec$

* = estimated hole depth

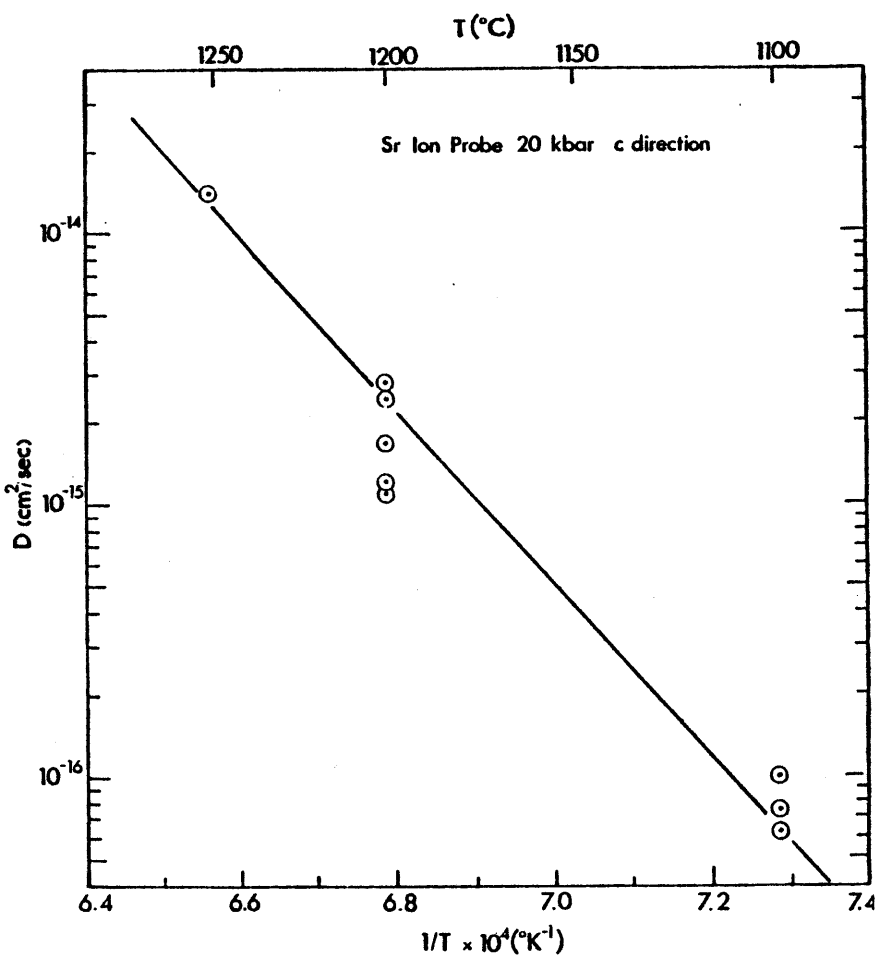
T (°C)
1250
1200
1150
1100
Sr Ion Probe 20 kbar c direction
10^{-14}
10^{-15}
10^{-16}
D (cm²/sec)
6.4
6.6
6.8
7.0
7.2
7.4
1/T × 10^4(°K^{-1})

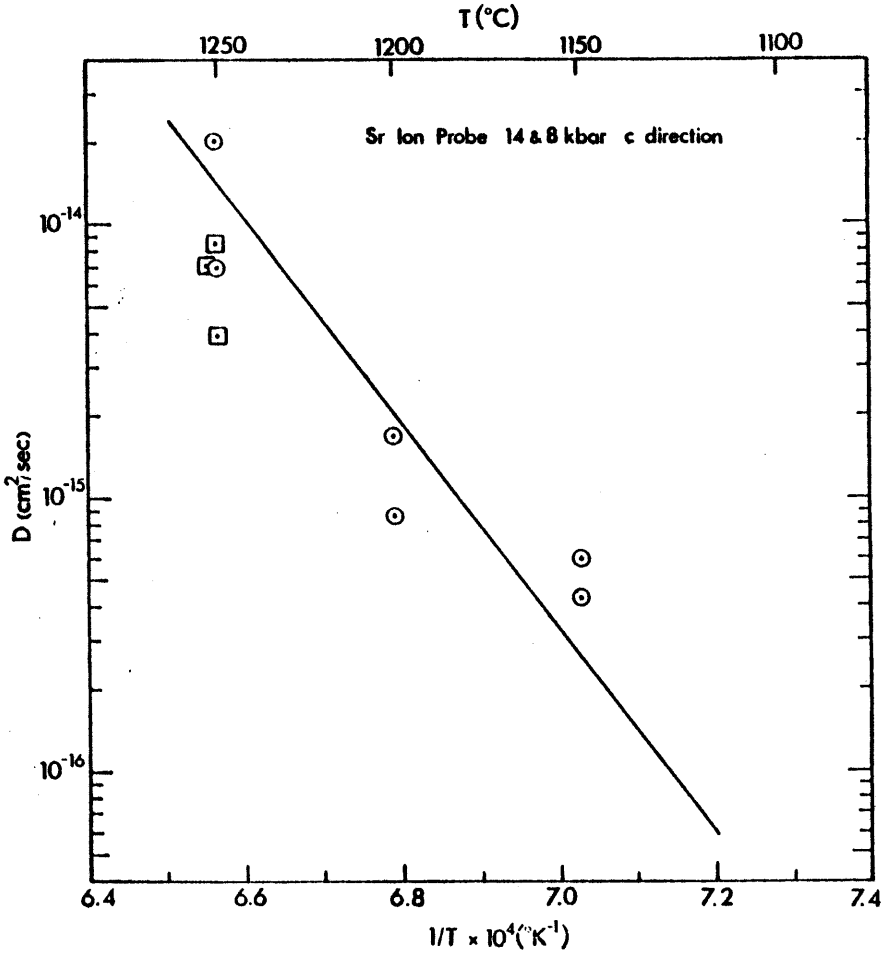
T (°C)
1250
1200
1150
1100
Sr Ion Probe 14 & 8 kbar c direction
10^{-14}
10^{-15}
10^{-16}
D (cm²/sec)
6.4
6.6
6.8
7.0
7.2
7.4
1/T × 10^4(°K^{-1})

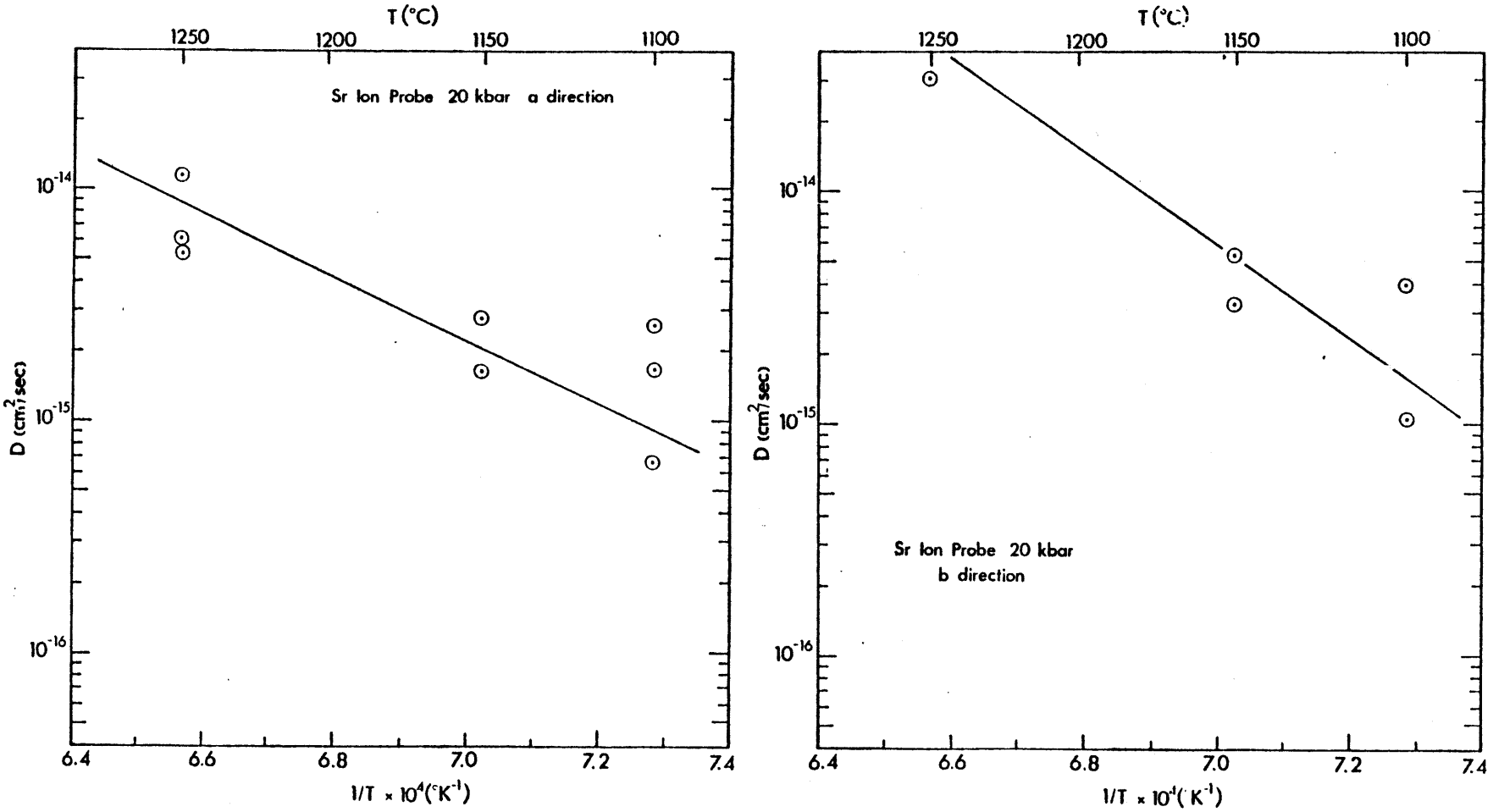

Figure 5-6. IP diffusion couples for Sr at high pressures, ℓn D vs 1/T. Uncertainty in T is ±10°K. All values of ΔH_a are in units of Kcal/mol and D_0's are in units of cm^2/sec. (a) c direction, 20 Kbar, $\Delta H_a = 145 \pm 8$ and $D_0 = 8.7 \times 10^6$. (b) c direction, 14 Kbar (circles) and 8 Kbar (squares); line is for 14 Kbar data, $\Delta H_a = 174 \pm 32$ and $D_0 = 1.2 \times 10^{11}$. (c) a direction, 20 Kbar, $\Delta H_a = 62 \pm 12$ and $D_0 = 1.7 \times 10^{-5}$. (d) b direction, 20 Kbar, $\Delta H_a = 91 \pm 20$ and $D_0 = 0.52$.

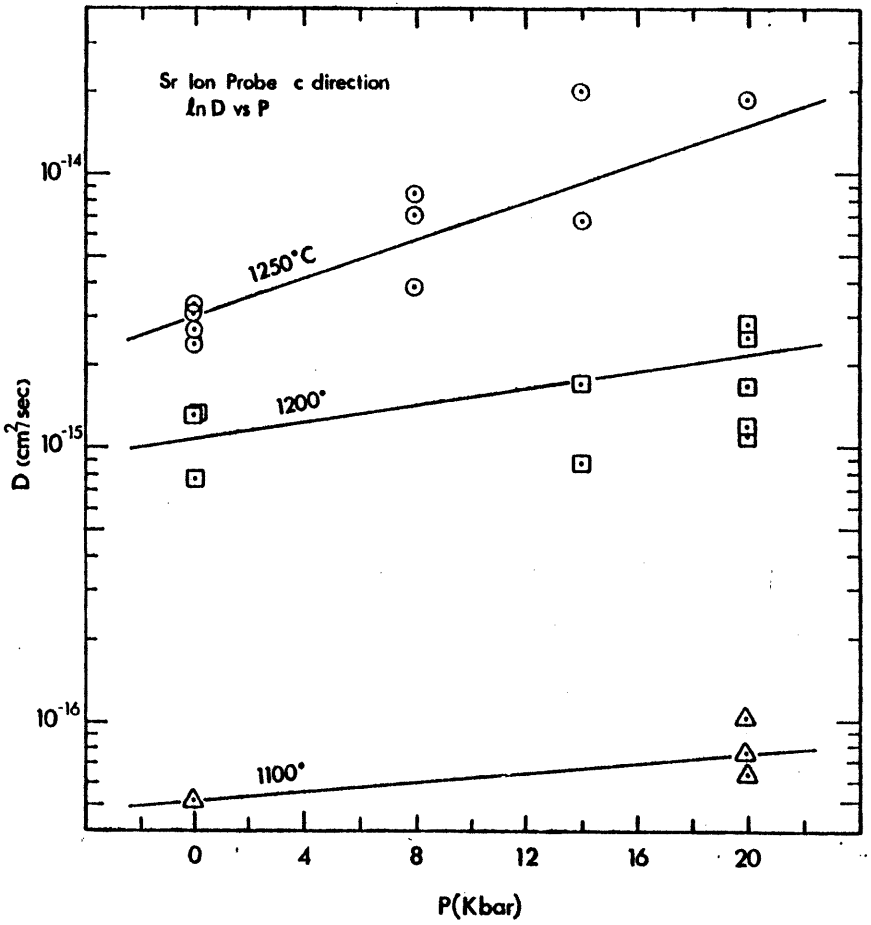
Sr Ion Probe c direction
ℓn D vs P
1250°C
1200°
1100°
10^{-14}
10^{-15}
10^{-16}
D (cm^2/sec)
0
4
8
12
16
20
P(Kbar)

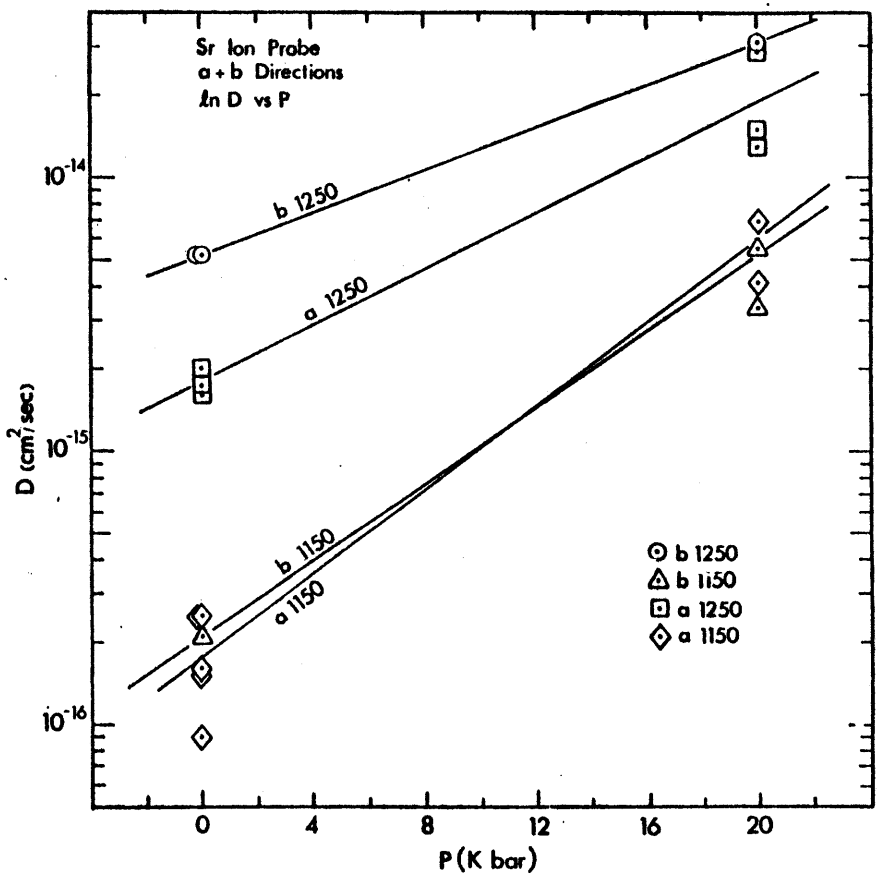
Sr Ion Probe
a + b Directions
ℓn D vs P
b 1250
a 1250
b 1150
a 1150
b 1250
b 1150
a 1250
a 1150
10^{-14}
10^{-15}
10^{-16}
D (cm^2/sec)
0
4
8
12
16
20
P (K bar)

Figure 5-7. IP experiments for Sr, ℓn D vs P. Uncertainty in the high pressure is ±1 Kbar. All values of ΔV_a are in units of cm^3/mol and values of D' are in cm^2/sec. (a) c direction, 1250°C (circles) $\Delta V_a = -10.3 \pm 1.4$ and $D' = 3.0 \times 10^{-15}$, 1200°C (squares) $\Delta V_a = -4.5 \pm 2.5$ and $D' = 1.1 \times 10^{-15}$, 1100°C (triangles) $\Delta V_a = -2.3 \pm 1.7$ and $D' = 5.2 \times 10^{-17}$. The one atm, 1100°C point is an average for those conditions. (b) a and b directions; a direction - 1250°C (squares) $\Delta V_a = -15.0 \pm 0.9$ and $D' = 1.8 \times 10^{-15}$, a direction - 1150°C (diamonds) $\Delta V_a = -20.6 \pm 13.9$ and $D' = 1.8 \times 10^{-16}$, b direction - 1250°C (circles) $\Delta V_a = -11.3 \pm 0.1$ and $D' = 5.2 \times 10^{-15}$, b direction - 1150°C (triangles) $\Delta V_a = -19.2 \pm 3.9$ and $D' = 2.1 \times 10^{-16}$. The one atm, 1150°C value for the b direction is an average value.

couples. Even so, contact over the entire surface could not be guaranteed. Surface kinetics undoubtedly also play an important role. The transfer of ions from one surface to the other may be the rate determining step causing the measured D's to be lower than the actual ones because effective volume diffusion does not occur during the early stages of the experimental anneal. For these reasons, this data set was not used in the discussions which follow. The diffusion equation for samarium will be derived for comparison to the high pressure data although its veracity is questionable.

The surface deposited tracer runs had two important advantages over the diffusion couples. One was the better contact between the dopant and the crystal and the other was the increased count rates due to higher tracer concentrations. The experiments did not behave as true instantaneous thin film sources because count rates at the surface would decrease if the samples were cleaned in boiling H_2O at the end of the anneal. This indicated there was a water-soluble compound such as SrO on the surface throughout the runs. The data were modeled as both thin film and constant-surface concentration experiments with the resultant D's rarely differing by more than a factor of three. The thin-film formulation usually produced a better correlation coefficient, so those are the numbers reported here.

The different lines in Figure (5-8a) are for the three crystallographic directions. The corresponding activation energies are 108 K cal/mole for the a direction, 122 for the c, and 135 for the b. All have appreciable uncertainties such that the values of adjacent numbers overlap and unambiguous ordering of the directions is not possible. However, the indicated progression of the actuation energies of a, c, b is not that which was predicted.

The relationship of the magnitudes of the diffusion coefficients at any temperature in most of the experimental range is the opposite of the ΔH_a

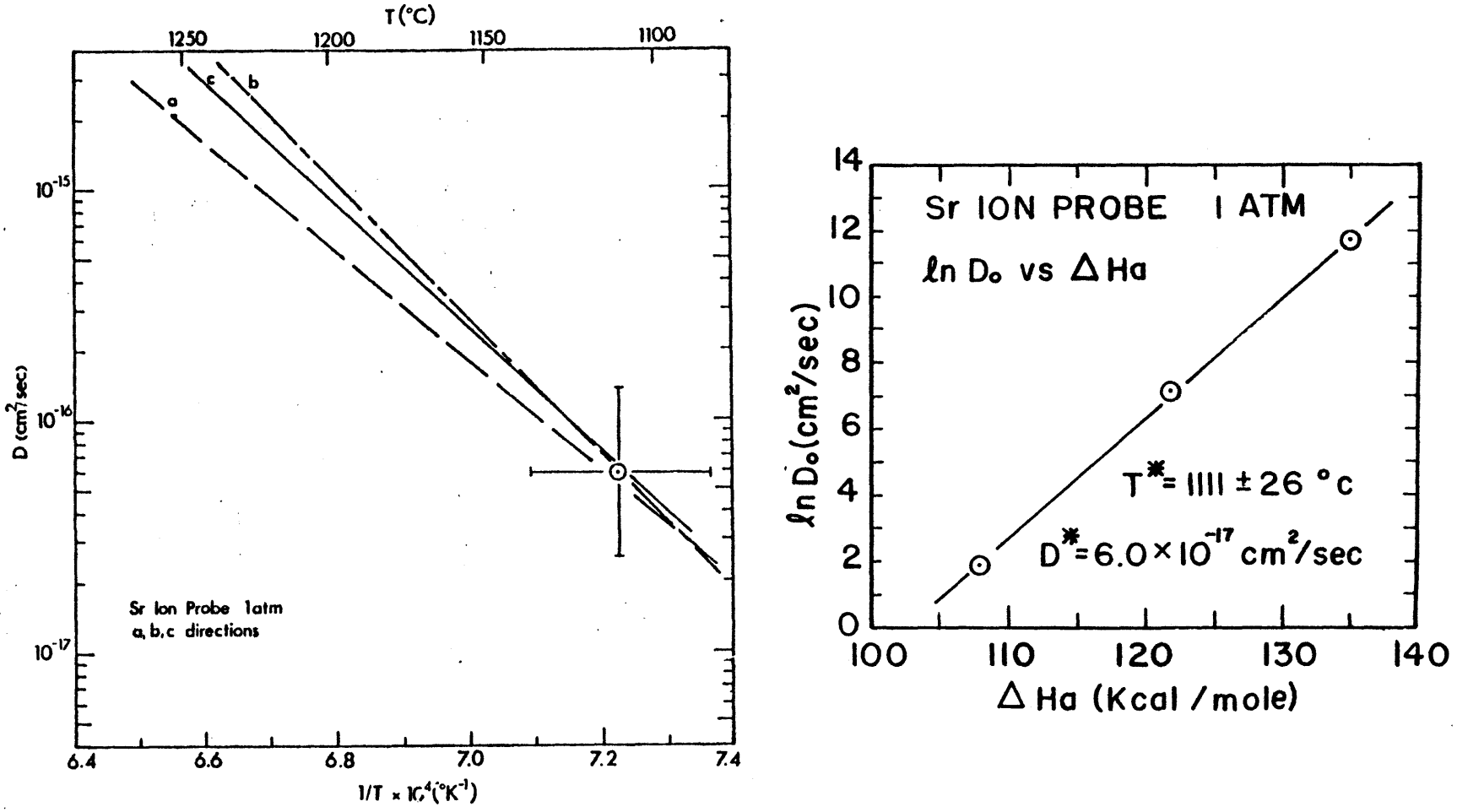

Figure 5-8. IP surface tracer for Sr at one atm, directional compensation. (a) ℓn D vs 1/T showing Arrhenius lines for the three crystallographic directions and the calculated crossover point. (b) compensation diagram, ℓn D_0 vs ΔH_a, T^{cr} = 1111 ± 26°C and D^{cr} = 6.0 x 10^{-17} cm^2/sec.

order with the b direction being the fastest. The three lines cross in the vicinity of 1100°C, giving an internal compensation point. Figure (5-8b) is a compensation diagram of $\ln D_o$ vs ΔH_a. The slope of a straight line on this plot equals $1/RT^{cr}$ where T^{cr} is the crossover temperature and the intercept gives D^{cr}, the crossover diffusion coefficient (Hart, 1981). The calculated values for these data are 1111 ± 26°C and 6.0 (+7.9, - 3.5) x 10^{-17} cm^2/sec. The physical significance of this is that the material behaves isotropically for diffusion at temperatures close to 1100°C and nearly isotropically over the range of many igneous processes. This internal compensation is also evidence that the observed values of ΔH_a and D_o are close to the true values and the relative ordering of the Arrhenius lines is probably correct.

Diffusion in the a direction may be the easiest, but above the crossover temperature it is the slowest due to the number of paths available. D_o is an indication of the total number of jumps which would be available if the activation energy did not limit movement. Examination of the data shows that a has the smallest value of the pre-exponential constant. Whereas ΔH_a defines the slope of the diffusion line on an Arrhenius plot, D_o gives the line's relative position.

The high pressure samples did not suffer from the contact problems that plagued the one-atmosphere couples. However, the pressure had the adverse effects of surface roughening in some cases and cracking of the specimens. The fractures were randomly oriented and probably occurred during pressurization or depressurization when stresses are not always isotropic. The cracked areas could be avoided during analysis to the extent that the imaged area was isolated from the fractures by distances two or more times the diffusion distance $2\sqrt{Dt}$. Surface roughness increased the uncertainty in

the depth for a given concentration and inhibited measurement of some pits. The system of sample preparation and packaging is viable but has a built-in failure rate of about 25%, due mainly to the inability to locate the diffusion surface at the end of the anneal in some samples.

Activation energies and frequency factors have been calculated for data at 20 kilobars in all three crystallographic directions and at 14 Kbar in the c direction only. Comparison of the numbers with those derived at one atmosphere show decreases in the a and b directions of both parameters while maintaining their relative differences (Table 5-7). The c direction data increase to a maximum measured value at 14 Kbar before dropping to a value at 20 Kbar which is higher than the one atmosphere value. The data are plotted on a compensation diagram in Figure (5-9). The 20 Kbar directional compensation point lies at 1286°C and 5.0×10^{-14} cm^2/sec, higher than the low pressure result (Table 5-8). The crossover temperature for compensation on each of the a and b axes was the same, 1525°C. The value for the c direction is 1150°C. When all the data are considered, a good apparent compensation line ($r^2 = 0.992$) can be calculated which gives a T^{cr} of 1284°C and a D^{cr} of 2.2×10^{-14} cm^2/sec. When the data are plotted on an Arrhenius diagram (Figure 5-10) it is seen that the best fit lines through the data do not all intersect in that area. It is possible that the probable values on the compensation diagram are defined by a narrow band which can be seen as a general compensation effect. Interesting features may be present within this band, but with the current analytical uncertainties, unambiguous recognition of them is impossible.

Levien and Prewitt (1981) have determined the diopside structure at pressures up to 53 Kbar. From one atmosphere to 23.6 Kbar, the M(2) site decreased in volume by 2.3% and the average metal-oxygen bond shrank by

Table 5-7. IP activation energies and frequency factors, Sr.

direction	type*	P(Kbar)	ΔH_a(Kcal/mol)	D_o(cm^2/sec)
a	T	0^+	108 ± 10	6.4×10^{0}
b	T	0	135 ± 9	1.2×10^{5}
c	T	0	122 ± 7	1.2×10^{3}
a	C	20	62 ± 12	1.7×10^{-5}
b	C	20	91 ± 20	5.2×10^{-1}
c	C	20	145 ± 8	8.7×10^{6}
c	C	14	174 ± 32	1.2×10^{11}

*experiment type: T = surface tracer, C = diffusion couple

+one atmosphere

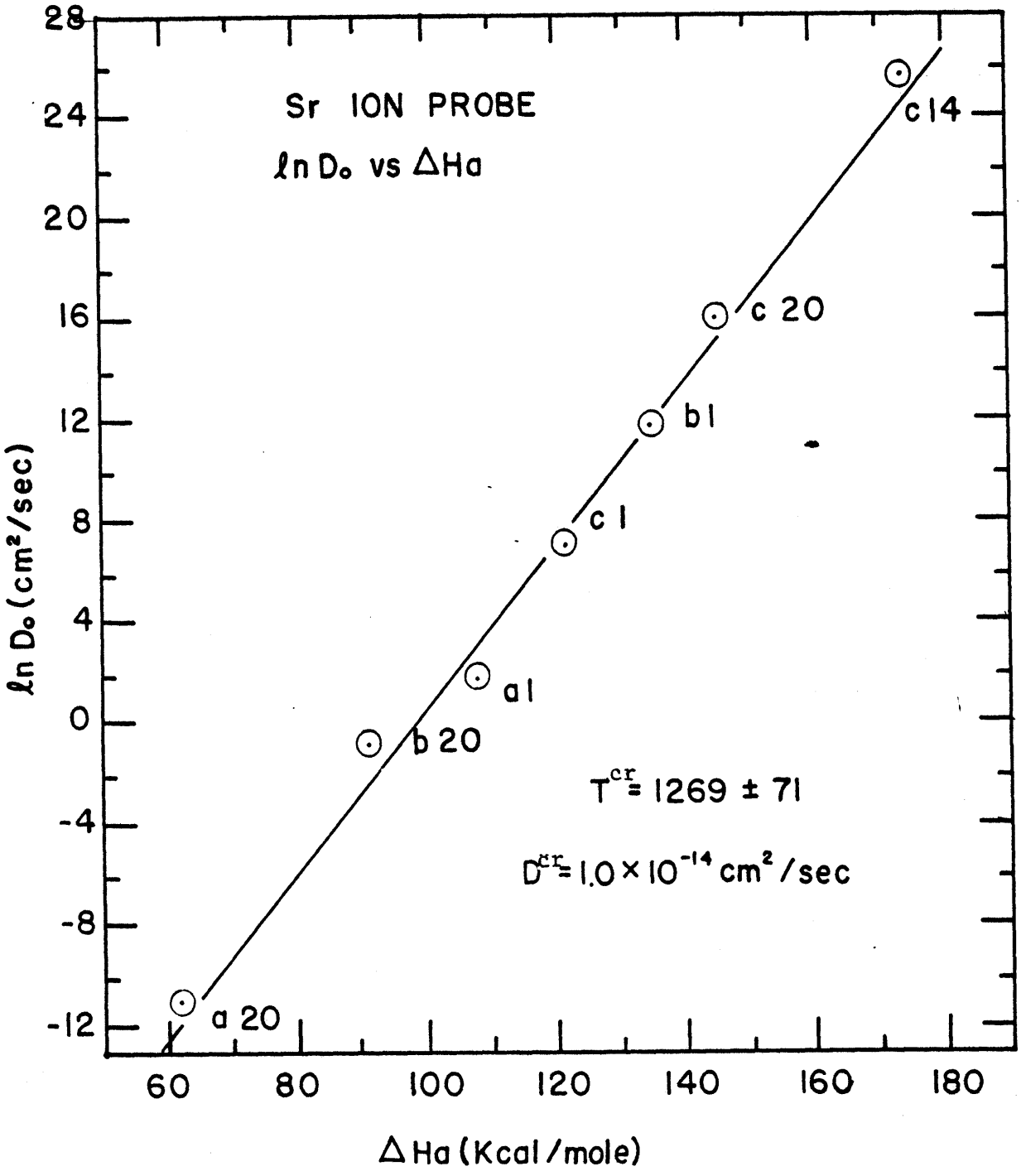

Figure 5-9. IP experiments for Sr, compensation plot, ℓn D vs ΔH_a. Direction and pressure are given with each point. Line is best fit through all data with T^{cr} = 1269 ± 71°C and D^{cr} = 1.0 x 10^{-14} cm^2/sec.

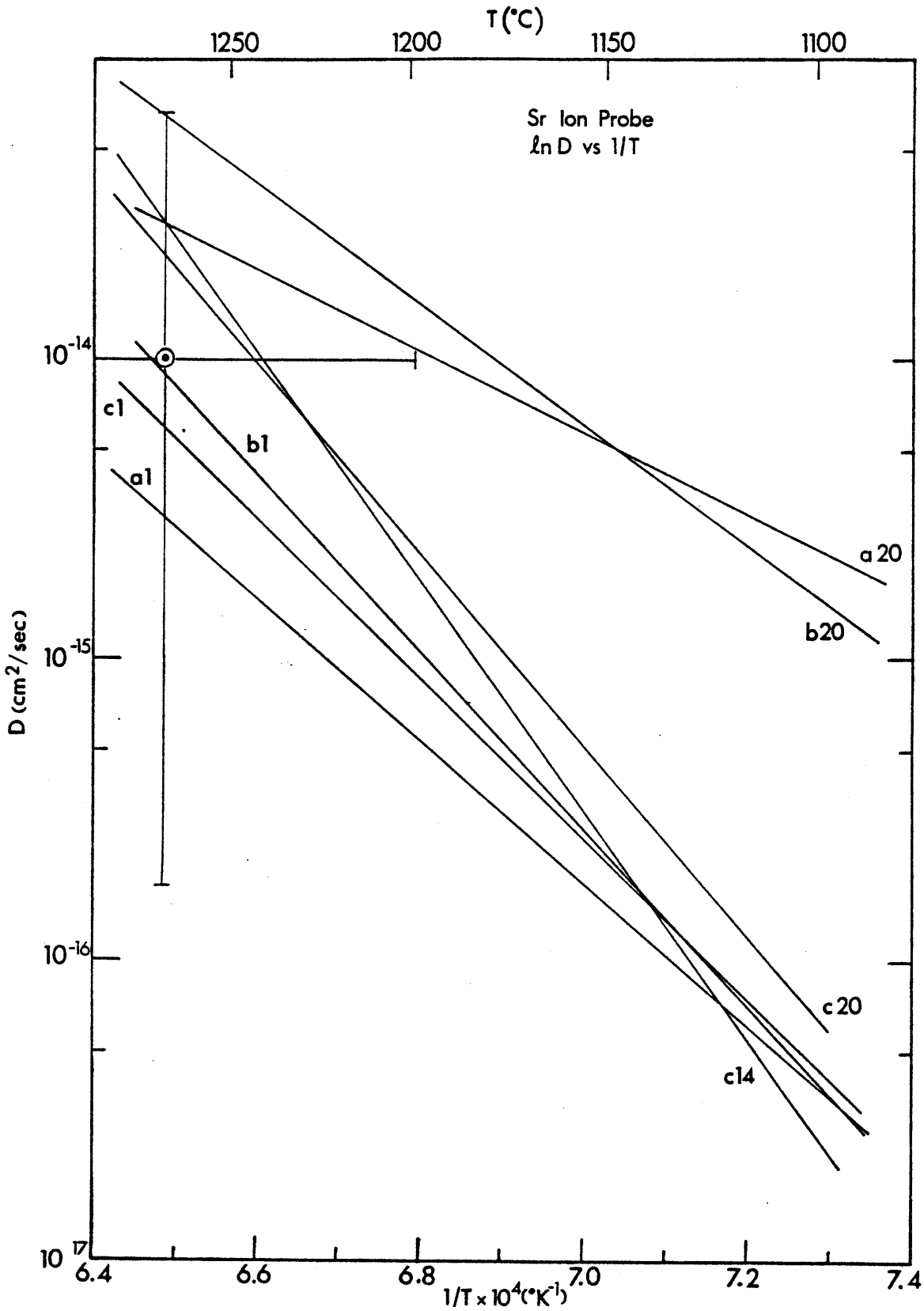

Figure 5-10. IP experiments for Sr, ℓn D vs 1/T, showing all Arrhenius lines and the calculated crossover point with error bars, T^{cr} = 1269 ± 71°C and D^{cr} = 1.0(+5.6, -0.83) x 10^{-14} cm^2/sec. Directions and pressures are given with each line.

Table 5-8. IP Compensation results, Sr.

group	T^{cr}(°C)	ln D^{cr}	D^{cr}(cm^2/sec)
1 atm	1111 ± 26	-37.35 ± 0.84	6.0×10^{-17}
20 Kbar	1284 ± 35	-30.84 ± 0.87	4.0×10^{-14}
a direction	1529 ± 97+	-28.30 ± 1.37	5.1×10^{-13}
b direction	1522 ± 96+	-26.16 ± 1.93	4.3×10^{-12}
c direction	1065 ± 63	-38.74 ± 2.34	1.5×10^{-17}
all	1269 ± 71	-32.19 ± 1.84	1.0×10^{-14}

+uncertainty estimated, only two points for the line

0.8%. However, all M(2)-O bonds do not reduce by the same amount and the shape of the site changes. Most of the compression occurs along the longest bond lengths, the M(2)-O(3C2) and the M(2)-O(3D2) (see Figure 5-11). The SiO_4 tetrahedra compress considerably less than the M(1) and M(2) sites, which leads to kinking of the SiO_3 chains in order to maintain structural integrity. This, in turn, changes the relative positions of the anions, adding an effect to the activation energy which would not be present with simple shrinkage of the structure. Differences in the pressure dependence of the diffusion equations for the three directions could be accounted for by such structural changes. Levien and Prewitt do not calculate all of the O-O distances and the interatomic angles for those anions surrounding the M(2) site. Thus evaluation of constriction or dilation of the saddle points between sites is not directly possible with their data set.

An unexpected result of high pressure experiments is the apparent increase in D with pressure. Activation volumes (ΔV_a) have been calculated for the c direction at 1250, 1200, and 1100°C and show a decrease with increasing temperature (Table 5-9 and Figure 5-7a). The 1250°C value is based on points at four pressures, the 1200°C on three pressures, and the 1100°C number on two pressures. ΔV_a's were also calculated for two temperatures in the a and b directions using points at two pressures for each value (Table 5-9 and Figure 5-7b). The activation volume increases with increasing temperature for these two axes.

The explanation for the higher D's at pressure comes from any one or a combination of a number of factors. The first three are experimental effects. Firstly, there is a possibility that longer diffusion anneals would produce lower values much in the same way as was found with the one atmosphere runs. The longest high-pressure anneal at 1100°C was 48 hours compared to 96 hours

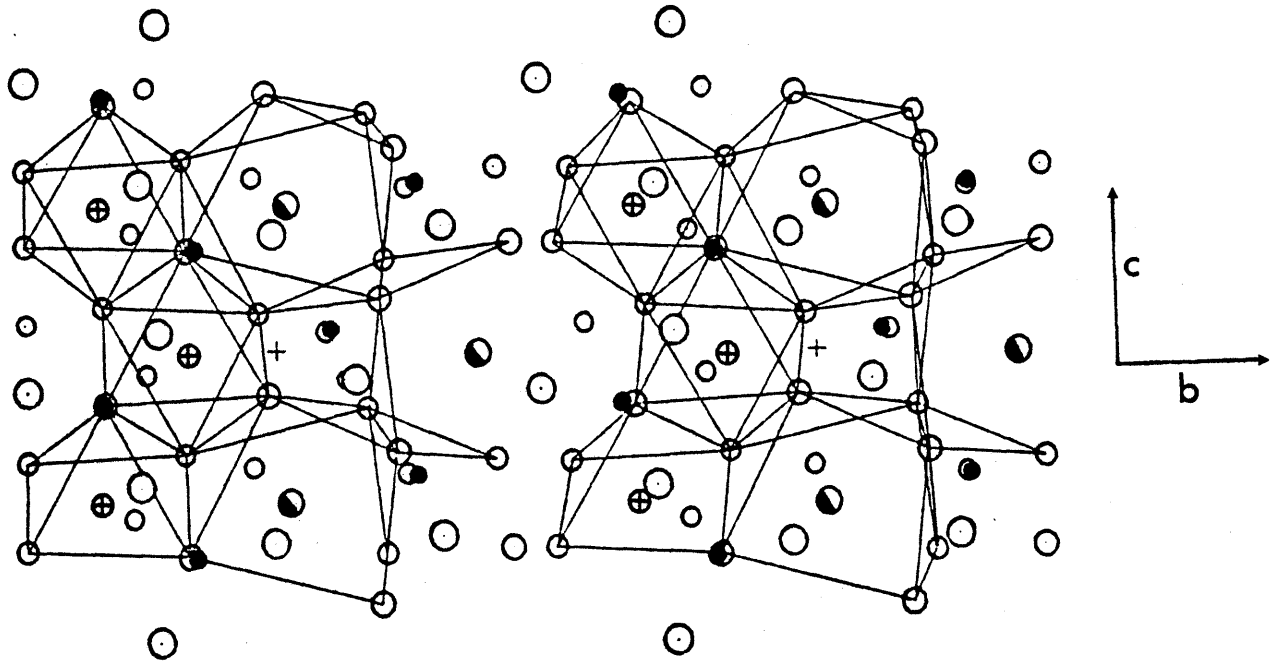

a. Cation polyhedra version

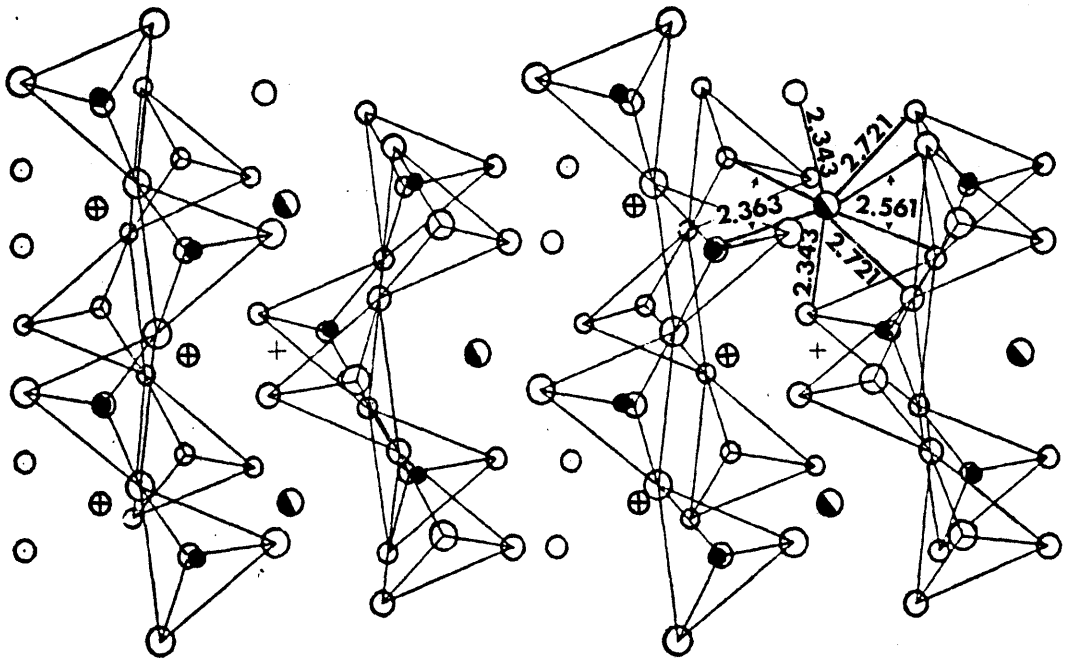

b. Silicate chain version

Figure 5-11. Diopside structure (Matsui, 1973). (a) Outline of cation polyhedra. (b) Outline of silica tetrahedra chains showing M(2)-O bond distances. Values (in Å) are from Levien and Prewitt (1981). Oxygen-open circles, silicon-filled circles, calcium-half filled circles, magnesium-crosses.

Table 5-9. IP activation volumes and D', Sn.

direction	T(°C)	# of P's	ΔV_a (cm^3/mole)	D' (cm^2/sec)
a	1250	2	-15.0 ± 0.9	1.8×10^{-15}
a	1150	2	-20.6 ± 13.9	1.8×10^{-16}
b	1250	2	-11.3 ± 0.1	5.2×10^{-15}
b	1150	2	-19.2 ± 3.9	2.1×10^{-16}
c	1250	4	-10.3 ± 1.4	3.0×10^{-15}
c	1200	3	-4.5 ± 2.5	1.1×10^{-15}
c	1100	2	-2.3 ± 1.7	5.2×10^{-17}

for the same T at one atmosphere. However, the times utilized are believed to have been long enough to avoid short-term transients. Longer runs become less practical because of the increased failure rate inherent with long experiments in the piston-cylinder at these temperatures and pressures. Secondly, there is a better surface contact insured by the pressure between the halves of the couples. Surface deposited tracer experiments should be immune to the poor contact problems evident in the one atmosphere couples. Therefore, this problem should not affect the relative values of D. Another source for the higher D's at pressure is a possible increase in dislocation density caused by non-hydrostatic compression of the sample. The piston-cylinder assembly was designed to minimize this problem, but cracks in run products indicated that there was directional variation in pressure at some time during the experiments. The most likely times for this are during pressurization and depressurization. Large cracks were not a problem because they could be avoided during ion probe analysis. However, smaller defects could account for the increased diffusivities. The fourth factor is the non-homogeneous compressibility of the diopside structure itself. Changes in the configuration of the activated complexes may open up more diffusion paths and make it easier for the ions to move through the lattice. The fact that reasonable straight lines can be fit through the data for 3 or 4 pressures on a lnD vs P plot and that ΔH_a and D_o values lie on the compensation trend are evidence of the negative activation volumes being real. Further support comes from the general observation that geochemical systems appear to approach equilibrium more quickly at high pressure.

Samarium data

Diffusion coefficients were calculated for samarium from data collected from the diffusion couples. Data are listed in Tables (5-10) to (5-12) and

Table 5-10. IP diffusion couples, Sm, one atm.

c direction

run #	T(°C)	t x 10^{-5}(sec)	D(cm^2/sec)
25 a 8	1300	6.75	$5.4 \pm 0.9 \times 10^{-17}$
b 8	"	"	$2.6 \pm 0.5 \times 10^{-16}$
27 a 8	1300	3.45	$5.2 \pm 1.6 \times 10^{-16}$
b 8	"	"	$3.0 \pm 0.3 \times 10^{-16}$
24 a 8	1250	4.22	$6.2 \pm 1.3 \times 10^{-17}$
b 8	"	"	$1.1 \pm 0.2 \times 10^{-17}$
c 8	"	"	$2.2 \pm 0.4 \times 10^{-17}$
28 a 8	1200	19.7	$1.2 \pm 0.1 \times 10^{-17}$
b 8	"	"	$8.2 \pm 1.2 \times 10^{-17}$
26 a 8	1150	19.0	$3.1 \pm 0.7 \times 10^{-18}$
c 8	"	"	$1.1 \pm 0.2 \times 10^{-17}$

$\Delta H_a = 116 \pm 26$ Kcal/mole

$D_o = 2.9 \times 10^{0} cm^2/sec$

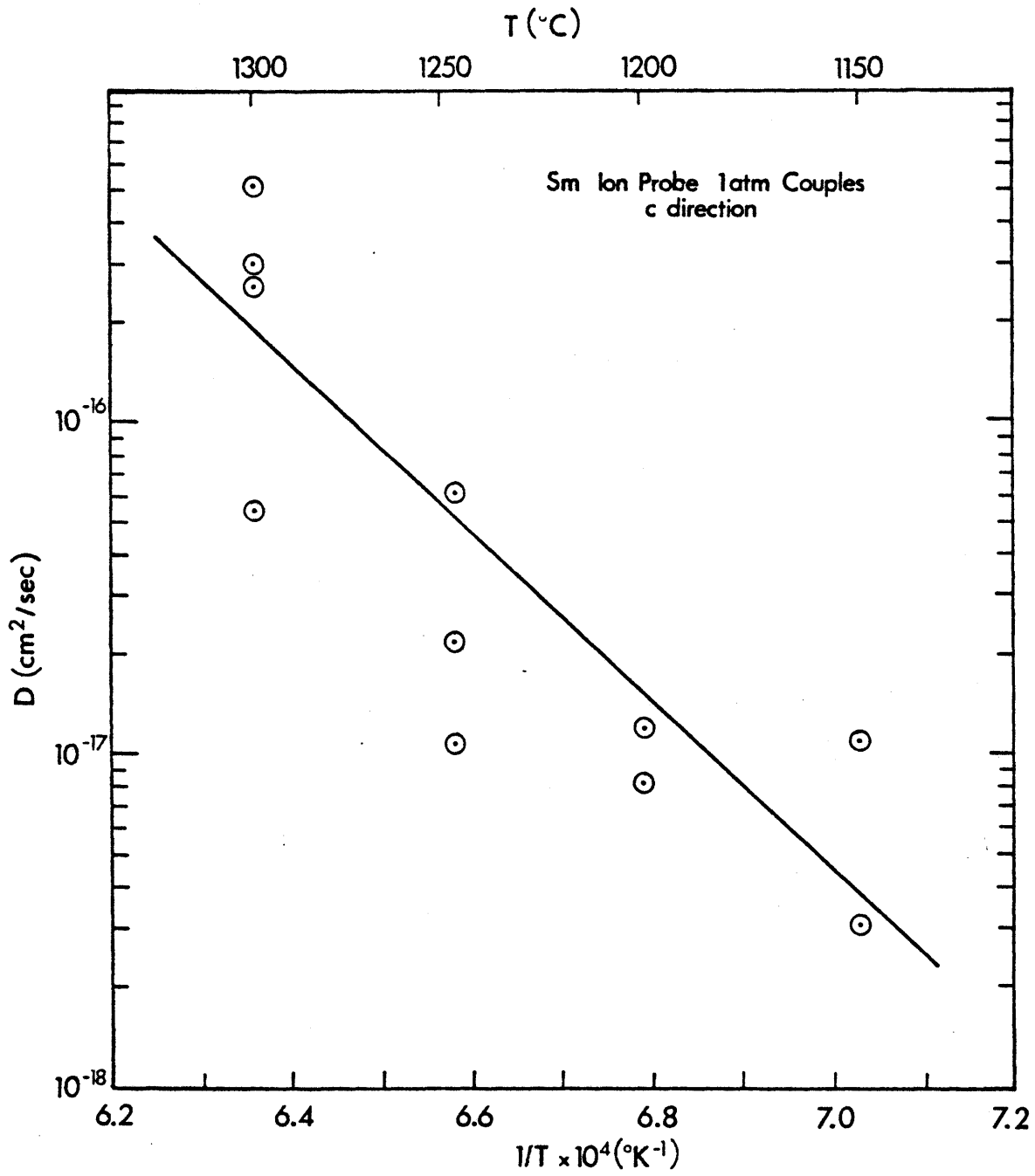

Figure 5-12. IP diffusion couples for Sm at one atm, c direction, ℓn D vs 1/T. Temperature uncertainty is ±5°K; uncertainties in D are given in the data tables. ΔH_a = 116 ± 26 Kcal/mol and D_0 = 2.9 cm^2/sec.

Table 5-11. IP diffusion couples, Sm, high pressure.

c direction	20 Kbar		
run#	T(°C)	t(sec)	D(cm^2/sec)
P37 1*	1250	28800	$1.9 \pm 0.6 \times 10^{-15}$
P37 2	"	"	$2.1 \pm 0.4 \times 10^{-14}$
P38 1*	1200	54000	$8.5 \pm 3.2 \times 10^{-16}$
2*	"	"	$1.1 \pm 0.5 \times 10^{-15}$
4*	"	"	$8.3 \pm 3.2 \times 10^{-16}$
5*	"	"	$1.8 \pm 0.5 \times 10^{-15}$
P43 2*	1100	173000	$9.8 \pm 4.3 \times 10^{-17}$
3	"	"	$1.1 \pm 0.3 \times 10^{-16}$
4*	"	"	$9.1 \pm 4.8 \times 10^{-17}$
	$\Delta H_a = 141 \pm 23$ Kcal/mole		
	$D_o = 1.4 \times 10^{6} cm^2/sec$		
c direction	14 Kbar		
P25 2	1250	21600	$5.3 \pm 1.0 \times 10^{-15}$
3	"	"	$6.9 \pm 0.8 \times 10^{-15}$
P40 3*	1200	57600	$1.6 \pm 0.4 \times 10^{-15}$
4*	"	"	$8.8 \pm 2.5 \times 10^{-16}$
P39 1	1150	86400	$4.0 \pm 1.0 \times 10^{-16}$
2	"	"	$1.4 \pm 0.2 \times 10^{-16}$
	$\Delta H_a = 150 \pm 17$ Kcal/mole		
	$D_o = 2.5 \times 10^{7} cm^2/sec$		
c direction	8 Kbar		
P28 1	1250	23400	$1.3 \pm 0.1 \times 10^{-14}$
3	"	"	$1.5 \pm 0.1 \times 10^{-14}$
P41 1*	"	28800	$5.6 \pm 1.3 \times 10^{-15}$
3*	"	"	$6.2 \pm 1.6 \times 10^{-15}$
P30 1	1150	32400	$4.4 \pm 0.4 \times 10^{-15}$
2	"	"	$4.1 \pm 0.3 \times 10^{-15}$
P26 7*	1100	86400	$1.9 \pm 0.5 \times 10^{-15}$
8*	"	"	$7.9 \pm 2.0 \times 10^{-16}$
	$\Delta H_a = 57 \pm 11$ Kcal/mole		
	$D_o = 1.9 \times 10^{-6} cm^2/sec$		

* estimated hole depth

Table 5-12. IP diffusion couples, Sm, high pressure.

a direction	20 Kbar		
run #	T(°C)	t(sec)	D(cm^2/sec)
P33 1*	1250	21600	$4.3 \pm 1.0 \times 10^{-14}$
2*	"	"	$1.4 \pm 0.3 \times 10^{-14}$
3*	"	"	$1.3 \pm 0.4 \times 10^{-14}$
P32 2*	1150	28800	$1.7 \pm 0.3 \times 10^{-14}$
3*	"	"	$6.2 \pm 1.7 \times 10^{-15}$
P29 1*	1100	62100	$3.1 \pm 1.1 \times 10^{-15}$
2	"	"	$4.4 \pm 0.3 \times 10^{-15}$
4*	"	"	$5.6 \pm 1.4 \times 10^{-15}$

$\Delta H_a = 47 \pm 12$ Kcal/mole

$D_o = 1.2 \times 10^{-7} cm^2/sec$

* estimated hole depth

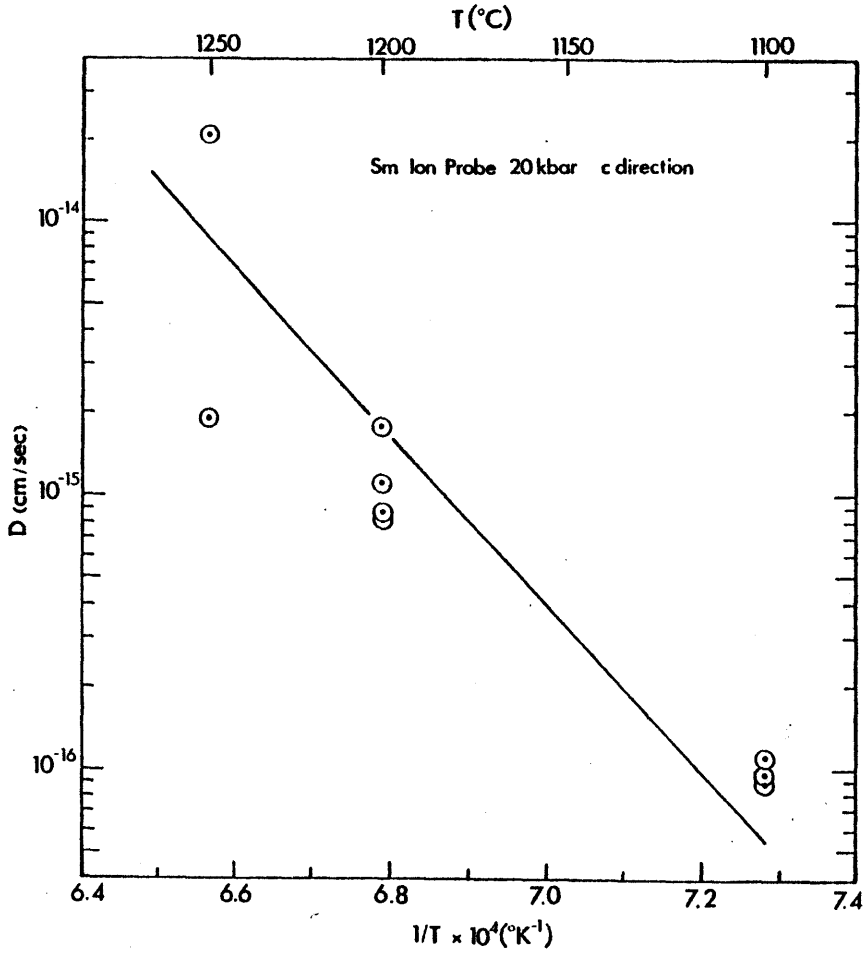
T(°C)
1250
1200
1150
1100
Sm Ion Probe 20 kbar c direction
10^{-14}
10^{-15}
10^{-16}
D (cm/sec)
6.4
6.6
6.8
7.0
7.2
7.4
1/T × 10^4(°K^{-1})

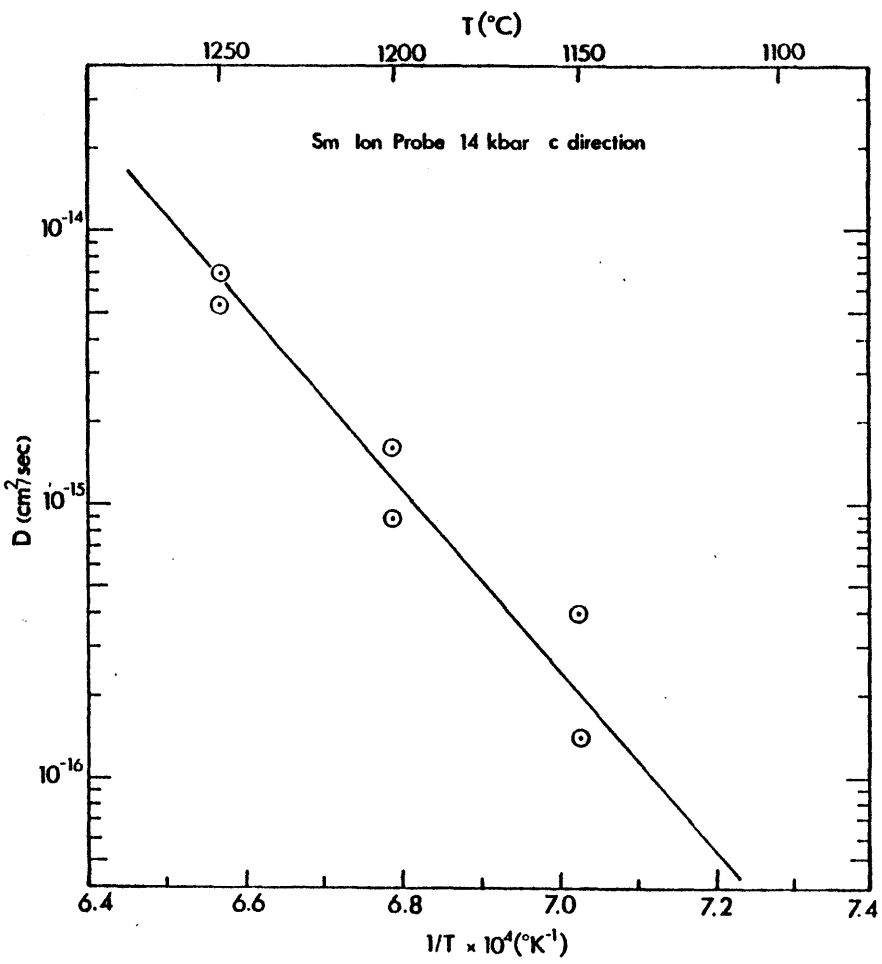
T(°C)
1250
1200
1150
1100
Sm Ion Probe 14 kbar c direction
10^{-14}
10^{-15}
10^{-16}
D (cm^2/sec)
6.4
6.6
6.8
7.0
7.2
7.4
1/T × 10^4(°K^{-1})

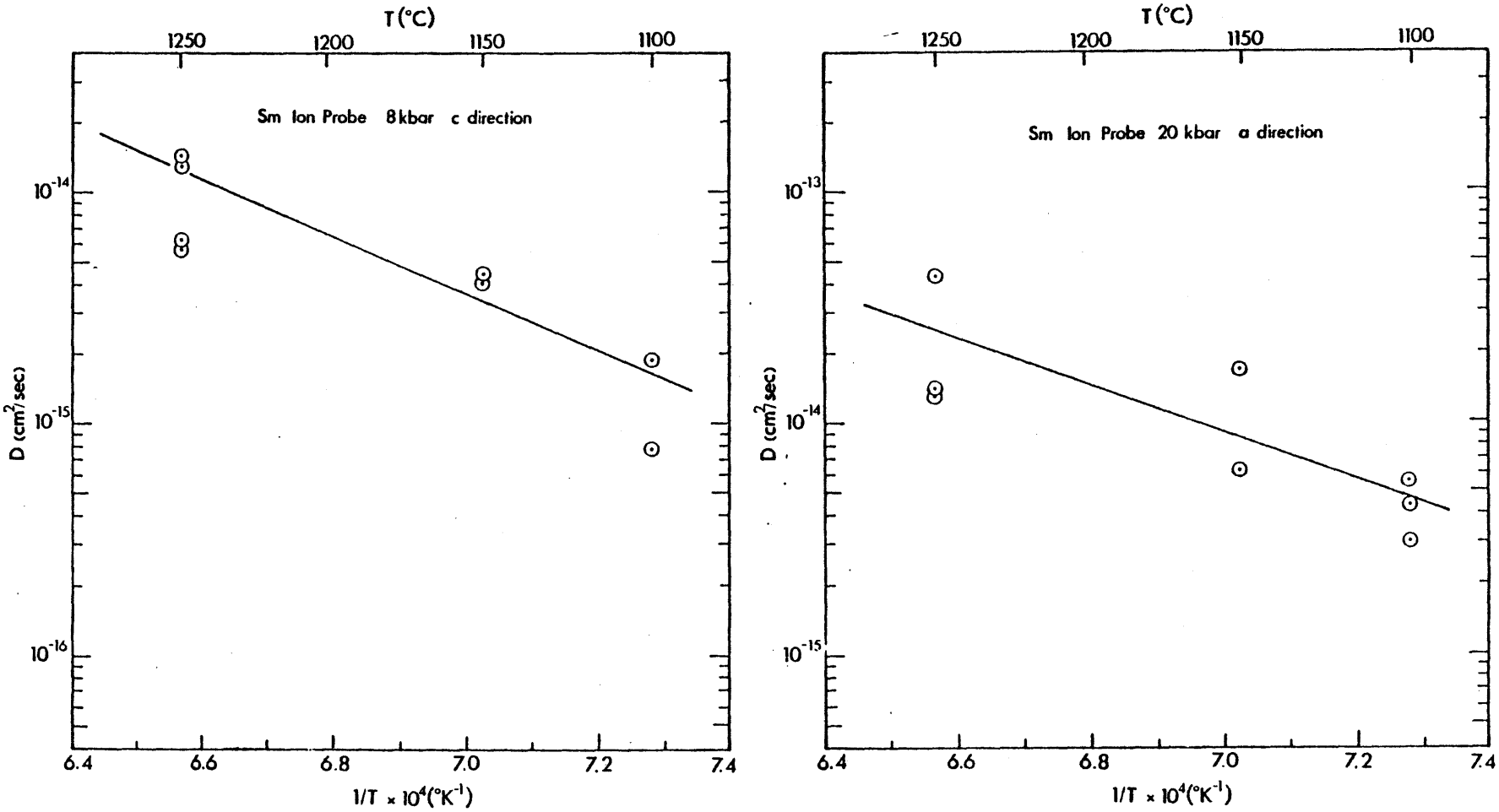

Figure 5-13. IP diffusion couples for Sm at high pressures, ℓn D vs 1/T. Uncertainty in temperature is ±10°K. All values of ΔH_a are in units of Kcal/mol and the D_0's are in units of cm^2/sec. (a) c direction, 20 Kbar, $\Delta H_a^a = 141 \pm 23$ and $D_0 = 1.4 \times 10^6$. (b) c direction, 14 Kbar, $\Delta H_a^a = 150 \pm 17$ and $D_0 = 2.5 \times 10^7$. (c) c direction, 8 Kbar, $\Delta H_a^a = 57 \pm 11$ and $D_0 = 1.9 \times 10^{-6}$. (d) a direction, 20 Kbar, $\Delta H_a^a = 47 \pm 12$ and $D_0 = 1.2 \times 10^{-7}$.

plotted in Figures (5-12) and (5-13). Since the one atmosphere runs gave low strontium values, low samarium values were expected. Activation energies and frequency factors were calculated for the c direction at one atmosphere and 8, 14, and 20 Kbar and for the a direction at 20 Kbars. Examination of the compensation plot (Figure 5-14) shows that the one atmosphere value falls below the trend defined by the four high pressure points. This supports the belief that the one atmosphere values are too low due to some non-diffusion effect. Maintaining the same ΔH_a, a new value of D_o was calculated from the line through the other data. This caused an increase in the D's of slightly more than two orders of magnitude. Such an increase in the Sr data would bring the couple values into agreement with the surface-tracer experiments in the synthetic samples, although the considerable scatter would persist, hindering any attempt to calculate an activation energy.

Activation volumes for the samarium data were calculated at 1250, 1200, 1150, and 1100°C for the c direction (Figure 5-15). The spread in the data and the availability of only two pressures for all but the 1250°C line seriously hamper the accuracy of the values of ΔV_a (Table 5-13). Although all of the numbers are positive, large error bars on the two higher temperature lines and the unrealistic size of the values at 1150 and 1100°C indicate that this apparent sign difference between Sm and Sr is most likely due to uncertainties. The lower temperature ΔV_a's are considered to be large because they are greater than the gram-atomic volume of Sm, 20 cm^2/mole. Due to the large uncertainties, these data will not receive further consideration.

Comparison of the Sr and Sm high pressure data shows very similar activation energies and D_o's at each pressure. Point-by-point examination yields an even closer correspondence in the measured range, suggesting that differences in ΔH_a and D_o are artifacts of the scatter of the data. The compensation

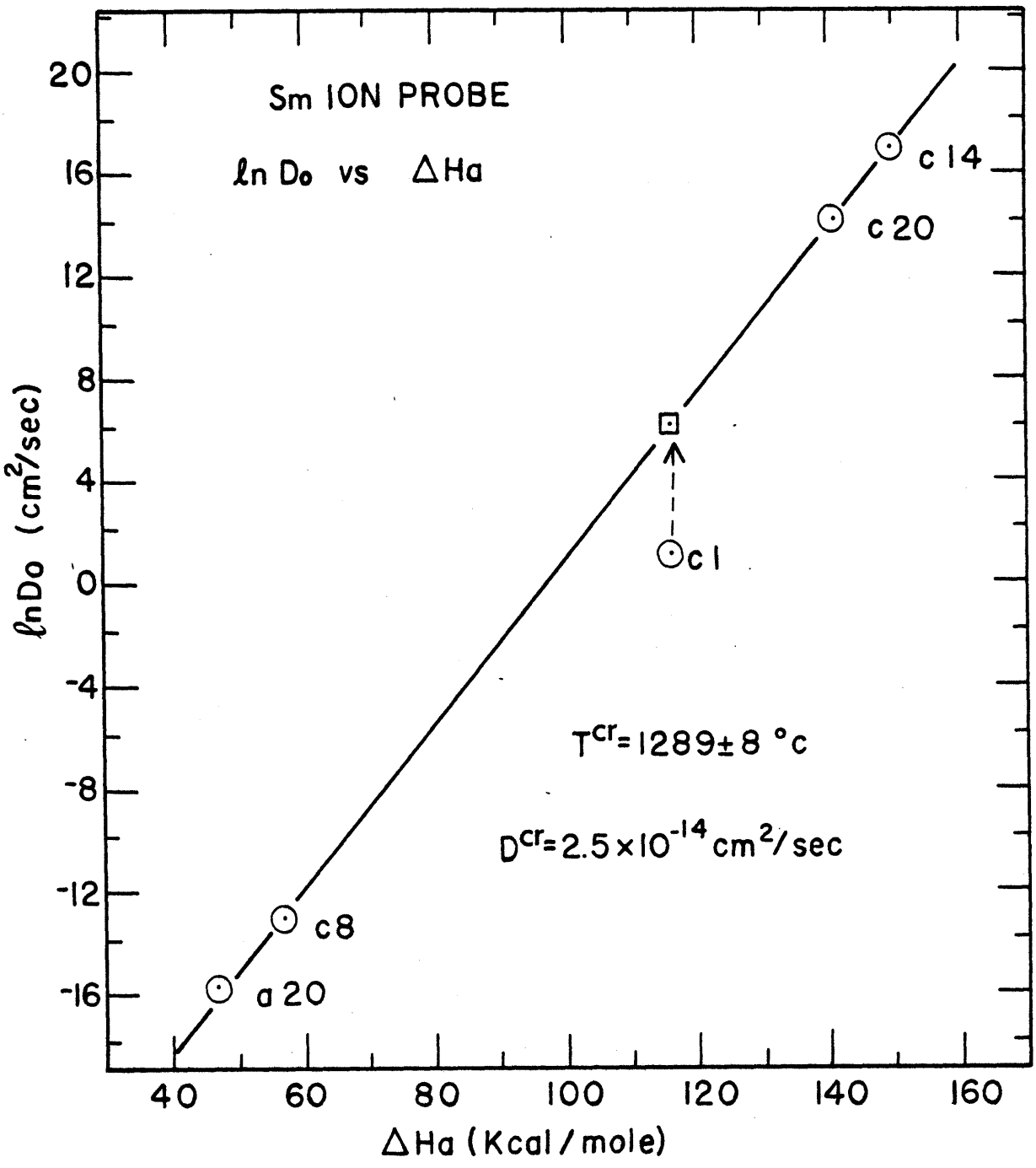

Figure 5-14. IP diffusion couples for Sm , compensation plot, ℓn vs ΔH_a. Direction and pressure are given with each point. Line is the best fit through the high pressure data with T^{cr} = 1289 ± 8°C and D^{cr} = 2.5 x 10^{-14} cm^2/sec. Square is the projection of the one atm point onto the compensation line while holding ΔH_a constant.

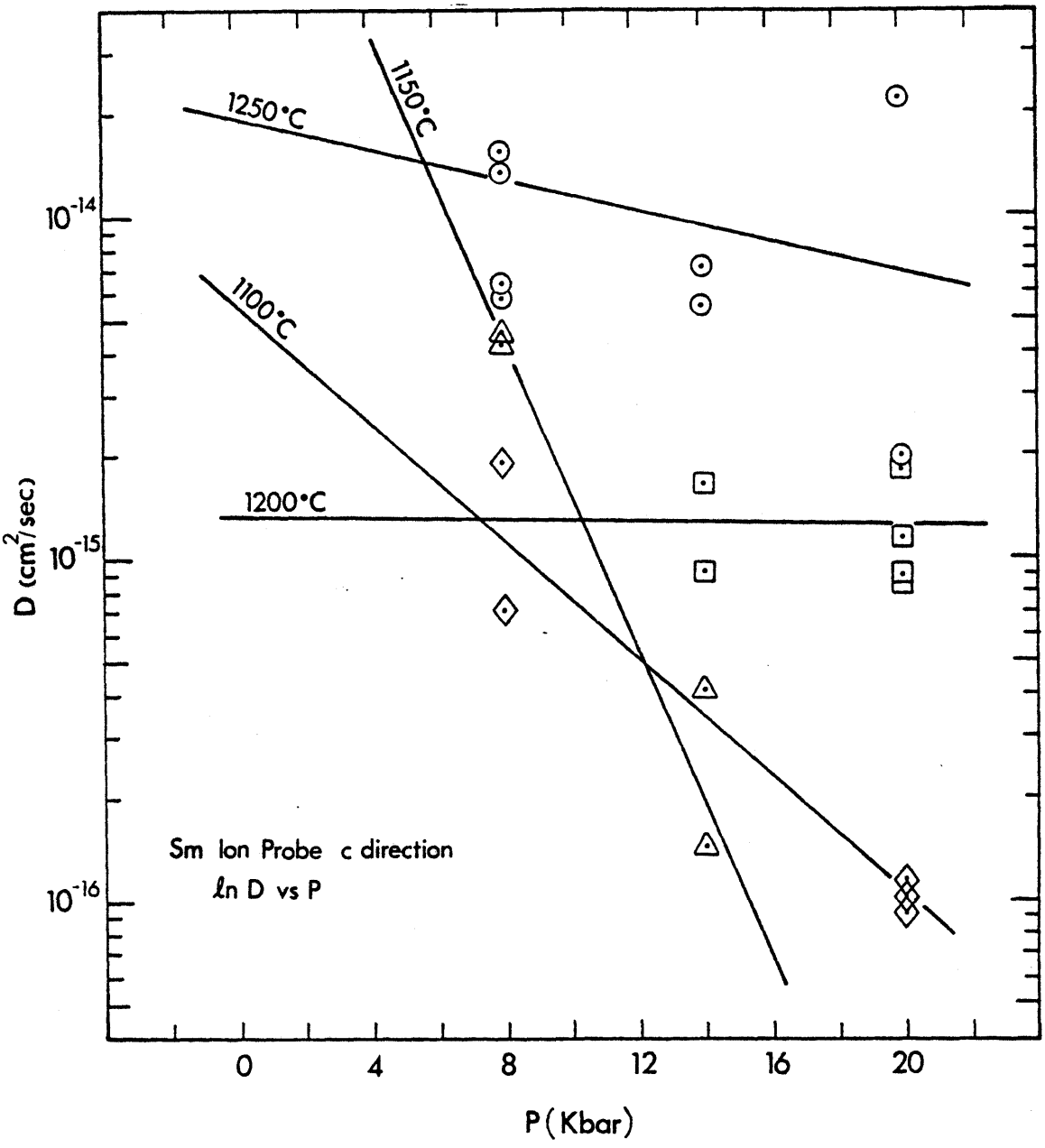

Figure 5-15. IP diffusion couples for Sm at high pressure, c direction, ℓn D vs P. Uncertainty in the pressure is ±1 Kbar. All values of ΔV_a are in units of cm^3/mol and the values of D' are in units of cm^2/sec. 1250°C (circles) ΔV_a = 6.6 ± 6.0 and D' = 1.9 x 10^{-14}, 1200°C (squares) ΔV_a = 0.3 ± 6.6 and D' = 1.3 x 10^{-15}, 1150°C (triangles) ΔV_a = 61.5 ± 8.9 and D' = 2.8 x 10^{-13}, and 1100°C (diamonds) ΔV_a = 23.6 ± 3.7 and D' = 6.4 x 10^{-15}.

Table 5-13. IP activation volumes and D', Sm.

direction	T(°C)	# of P's	ΔV_a (cm^3/mole)	D' (cm^2/sec)
C	1250	3	6.6 ± 6.0	1.9×10^{-14}
C	1200	2	0.3 ± 6.6	1.3×10^{-15}
C	1150	2	61.5 ± 8.9	2.8×10^{-13}
C	1100	2	23.6 ± 3.7	6.4×10^{-15}

Table 5-14. IP compensation comparison.

tracer	group	T^{cr}	ln D^{cr}	D^{cr} (cm^2/sec)
Sr	all	1269 ± 71	-32.19 ± 1.84	1.0×10^{-14}
Sm	all	1289 ± 18	-31.31 ± 0.33	2.5×10^{-14}

lines for the two species are identical (Table 5-14). The fact that two vastly different tracers proceed at the same rate points to the overwhelming control of the diffusion process by the diopside structure and defect levels. It also suggests a similar transport mechanism for both.

A simple empirical expression which combines activation energy and activation volume to give D as a function of temperature and pressure can be derived from the two separate Arrhenius equations for ΔH_a and ΔV_a. Assuming that $D = D'\exp(-P\Delta V_a/RT)$ is the proper expression for the pressure dependence of D, the equation for D(P,T) is:

$$D(P,T) = D_o^o \exp(-\Delta H_a^o/RT)\exp(-P\Delta V_a^T/RT) \qquad (5\text{-}20)$$

where D_o^o and ΔH_a^o are the frequency factor and activation energy at P = 0, and ΔV_a^T is the temperature dependent value of the activation volume. Equation (5-20) is not a rigorous description of the diffusivity, D(P,T), because ΔH_a^o and $P\Delta V_a^T$ can vary as long as their sum remains the same. The values of the activation parameters in a given study are derived empirically from the measured diffusion coefficients by isolating the temperature and pressure effects. Activation energies are calculated at constant pressure, and activation volumes at constant temperature.

In the present study, the Sr c direction ion probe data can be used to evaluate equation (5-20). A variety of regression models were applied to the three ΔV_a values for the c direction in order to calculate the apparent temperature dependence of the activation volume. The best fit ($r^2 = 0.996$) was achieved by the equation:

$$1/\Delta V_a = B/T - A \qquad (5\text{-}21)$$

where A and B are the intercept and the slope of the line through the data. Rearranging terms gives an expression for ΔV_a:

Table 5-15. IP compilation of Arrhenius equations

Sr constant P R = 1.987 cal/deg mole

P	direction	equation
1 atm	a	$D_{Sr} = 6.4 \times 10^{0} \exp[-(108 \pm 10)\ 1000/RT]$
1 atm	b	$D_{Sr} = 1.2 \times 10^{5} \exp[-(135 \pm 9)\ 1000/RT]$
1 atm	c	$D_{Sr} = 1.2 \times 10^{3} \exp[-(122 \pm 7)\ 1000/RT]$
20 Kbar	a	$D_{Sr} = 1.7 \times 10^{-5} \exp[-(62 \pm 12)\ 1000/RT]$
20 Kbar	b	$D_{Sr} = 5.2 \times 10^{-1} \exp[-(91 \pm 20)\ 1000/RT]$
20 Kbar	c	$D_{Sr} = 8.7 \times 10^{6} \exp[-(145 \pm 8)\ 1000/RT]$
14 Kbar	c	$D_{Sr} = 1.2 \times 10^{11} \exp[-(174 \pm 32)\ 1000/RT]$

Sr constant T R = 83.14 cm^3 bar/deg mole

T	direction	equation
1250	a	$D_{Sr} = 1.8 \times 10^{-15} \exp[(15.0 \pm 0.9)P/RT]$
1250	b	$D_{Sr} = 5.2 \times 10^{-15} \exp[(11.3 \pm 0.1)P/RT]$
1250	c	$D_{Sr} = 3.0 \times 10^{-15} \exp[(10.3 \pm 1.4)P/RT]$
1200	c	$D_{Sr} = 1.1 \times 10^{-15} \exp[(4.5 \pm 2.5)P/RT]$
1150	a	$D_{Sr} = 1.8 \times 10^{-16} \exp[(20.6 \pm 13.9)P/RT]$
1150	b	$D_{Sr} = 2.1 \times 10^{-16} \exp[(19.2 \pm 3.9)P/RT]$
1100	c	$D_{Sr} = 5.2 \times 10^{-17} \exp[(2.3 \pm 1.7)P/RT]$

Table 5-15 cont'd.

Sm constant P R = 1.987 cal/deg mole

P	direction	equation
20 Kbar	a	$D_{Sm} = 1.2 \times 10^{-7} \exp[-(47 \pm 12) 1000/RT]$
20 Kbar	c	$D_{Sm} = 1.4 \times 10^{6} \exp[-(141 \pm 23) 1000/RT]$
14 Kbar	c	$D_{Sm} = 2.5 \times 10^{7} \exp[-(150 \pm 17) 1000/RT]$
8 Kbar	c	$D_{Sm} = 1.9 \times 10^{-6} \exp[-(57 \pm 11) 1000/RT]$

Sm constant T R = 83.14 cm^3 bar/deg mole

T	direction	equation
1250	c	$1.9 \times 10^{-14} \exp[-(6.6 \pm 6.0) P/RT]$
1200	c	$1.3 \times 10^{-15} \exp[-(0.3 \pm 6.6) P/RT]$
1150	c	$2.8 \times 10^{-13} \exp[-(61.5 \pm 8.9) P/RT]$
1100	c	$6.4 \times 10^{-15} \exp[-(23.6 \pm 3.7) P/RT]$

$$\Delta V_a = T/(AT - B) \qquad (5\text{-}22)$$

and the values derived for Sr in the synthetic crystals were A = 2.94 moles/cm^3 and B = 4640 moles°K/cm^3. It should be noted that the only basis for using equation (5-21) is the exactness of the fit in the study range. Extrapolation of this formulism of the temperature dependence of ΔV_a beyond the study temperature and pressure ranges may not be warranted. Substitution of equation (5-22) with the derived values of A and B, and D_o and ΔH_a from the one atmosphere ion probe data into equation (5-20) gives:

$$D(P,T) = 1200 \exp(-122{,}000/RT) \exp(-P/2.94T - 4640)R) \qquad (5\text{-}23)$$

Comparison of diffusivities calculated from this equation with the corresponding measured values shows good but not exact agreement. Inclusion of uncertainties in each term results in the overlap of the error bars for the two values.

If it is assumed that the pressure dependence of D is the same for the natural and synthetic samples, substitution of D_o and ΔH_a from the natural specimen radiotracer data into equation (5-23) gives an expression applicable to geologic situations:

$$D(P,T) = 54 \exp (-97{,}000/RT) \exp(-P/(2.94T - 4640)R) \qquad (5\text{-}24)$$

The T dependence of the activation volumes for the a and b directions could not be calculated because only two points were available for each. Also, the Sm data could not be used to develop an expression analogous to equation (5-23) due to the lack of values of D_o^o and ΔH_a^o. Therefore, Table (5-15) is a compilation of ΔH_a's, D_o's, ΔV_a's and values of D' for this work in order to facilitate estimation of diffusivities for conditions similar to those studied.

Rutherford backscattering data

The third analytical method is also an instrumental depth profiling technique. The raw data were in the form of counts per channel with a certain

energy per division (Figure 5-16). The channel to energy conversion factor was calculated by first locating the positions of the individual elemental surface values. The rebound energies are well-defined and a plot of energy vs channel number for these points gives the conversion factor (Figure 5-17). To change this to a distance scale, the energy dissipation of diopside was calculated from first principles using the chemical formula, the measured density, and elemental stopping powers. The result of this calculation is a number in units of KeV/angstroms. Division of the first factor (KeV/channel) by the second gives the channel to distance factor. The calculation was performed for a 2MeV incident beam and a detector located at an angle of 175° from the beam, and gave a value of 34.3 Å/channel. The distance between the fronts for calcium and strontium was 130 channels, or approximately 4450 Å. This was the range over which an entire profile could be seen.

Due to low count rates, a reduction scheme which utilized total counts and surface concentration was used. The problem was modeled as a constant surface concentration and the total amount of diffusant which had entered the sample by time t was:

$$C_o = 2\sqrt{Dt}\ \ C(0,t)/\sqrt{\pi} \qquad (5\text{-}25)$$

Measuring C_o and C(0,t) allows calculation of D by rearrangement of the above:

$$D = \frac{\pi}{4t}\left(\frac{C_o}{C(0,t)}\right)^2 \qquad (5\text{-}26)$$

Uncertainty in this measurement is dominated by the counting statistics of the two measured values. First D was determined with the units of channels^2/sec. The deviation caused by the square roots of C_o and C(0,t) is given by the following:

$$\sigma_D = D\ \left[2\left(\frac{1}{C_o} + \frac{1}{C(0,t)}\right)\right]^{1/2} \qquad (5\text{-}27)$$

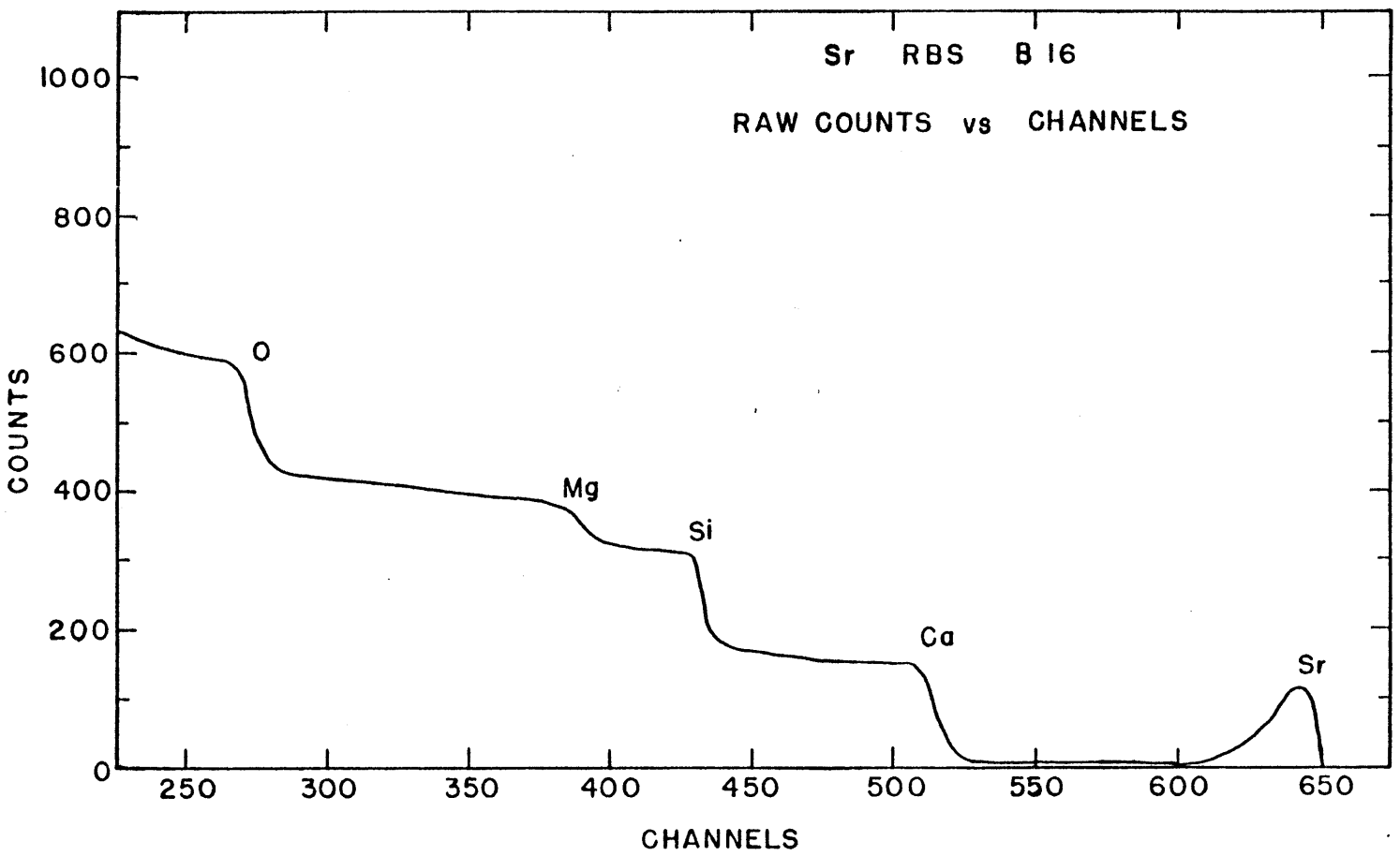

Figure 5-16. Rutherford backscattering spectroscopy profile for Sr in run B16 (1100°C, one atm), raw counts vs analyser channels. Channels can be converted to distance (Å) by multiplying by 34.3 Å/channel. Steep slopes occur at the surface energy values for the species, and relative heights do not directly reflect concentrations because the backscattering cross section varies from element to element. Sr peak shows the diffusion profile.

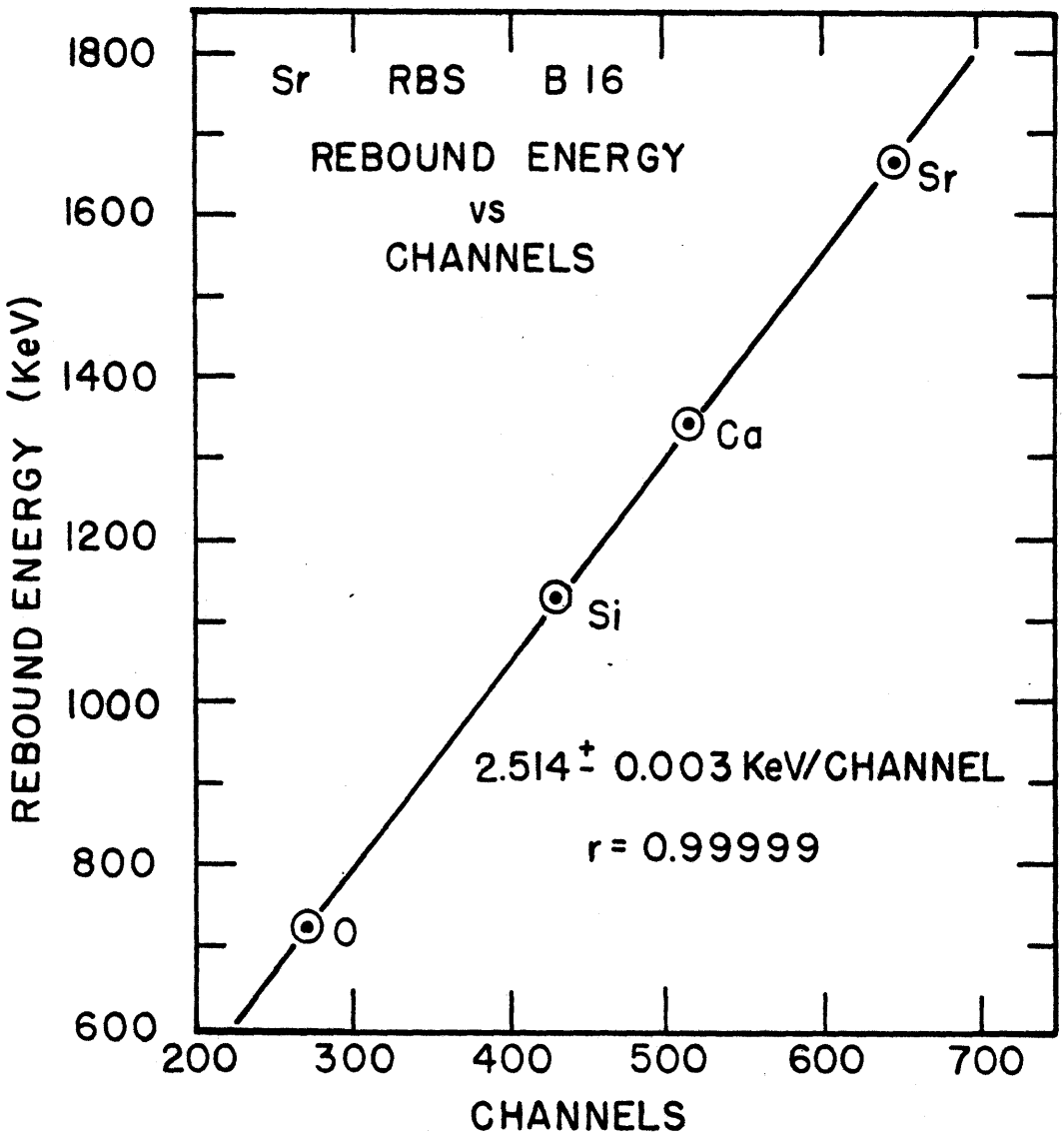

Figure 5-17. RBS channel to energy conversion, rebound energy vs channels. Values of energy depend on the mass, the placement of the detector, and the energy of the incident particles. The line is the best fit through the points with slope = 2.514 ± 0.003 KeV/channel (r = 0.9999).

Table 5-16. RBS surface tracer experiments, Sr, one atm.

c direction

run #	T(°C)	t(sec)	D(cm^2/sec)
B13	1250	7200	$5.5 \pm 0.5 \times 10^{-15}$
B12	1200	15300	$2.0 \pm 0.2 \times 10^{-15}$
B10	1100	248000	$5.9 \pm 0.4 \times 10^{-17}$
B16	1100	335000	$5.8 \pm 0.7 \times 10^{-17}$
B17	1100	169000	$6.6 \pm 0.9 \times 10^{-17}$

$\Delta H_a = 130 \pm 6$ Kcal/mole

$D_o = 3.1 \times 10^4$ cm^2/sec

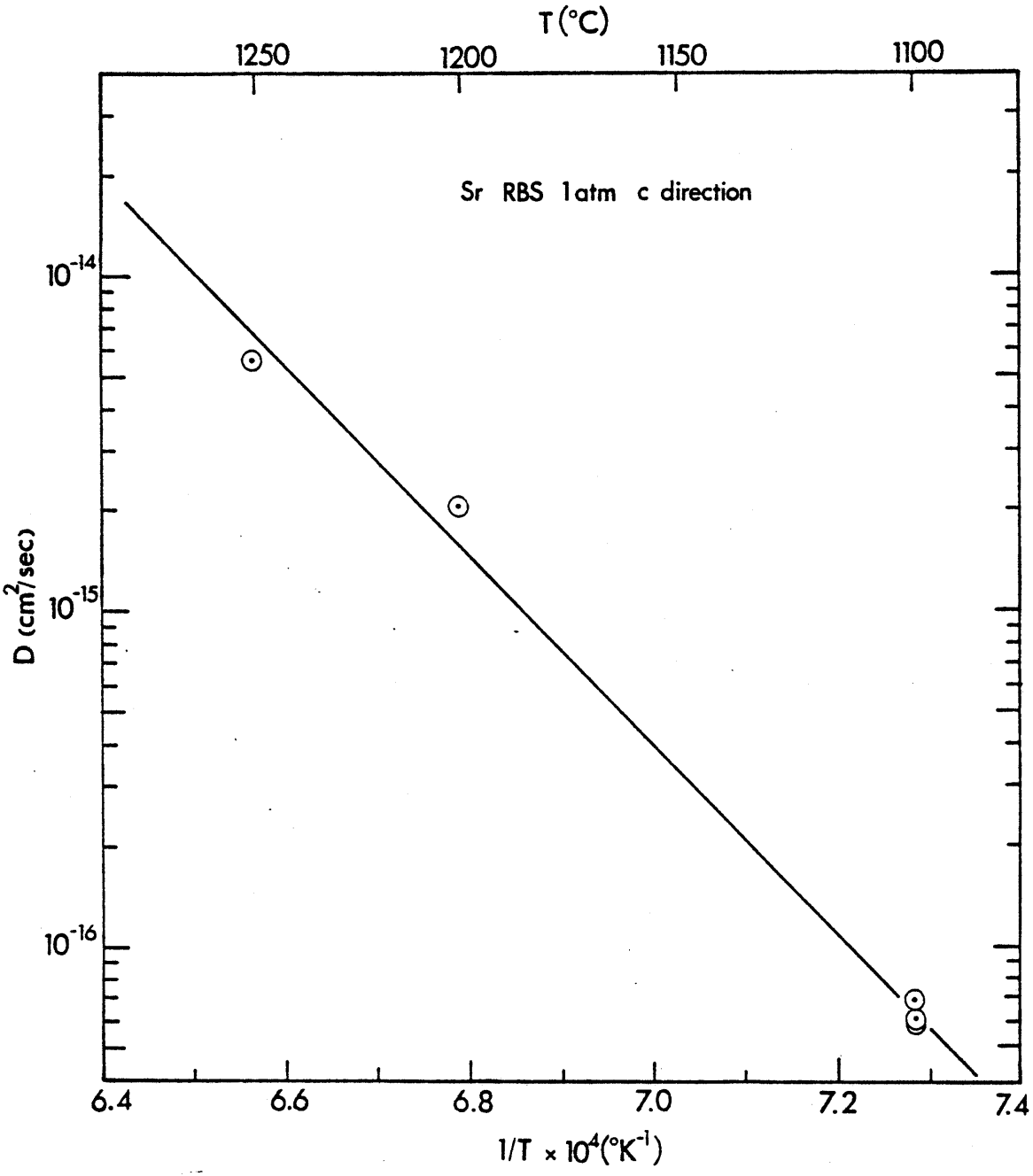

Figure 5-18. RBS experiments for Sr at one atm, ℓn D vs 1/T. Temperature uncertainty is ±5°K and uncertainties in D are given in the data tables. ΔH_a = 130 ± 6 Kcal/mol and D_0 = 3.1 x 10^4 cm^2/sec.

Changing to cm^2/sec brings in the uncertainty of the conversion factor. The points used for the channel to energy step are of equal weight and the slope of the major axis is given as 2.514 ± 0.003 KeV/channel. The diopside stopping factor was calculated as 13.64 ± 0.27 Å/KeV. Combination gives a value of 34.3 ± 0.7 Å/channel. This 2% error bar was usually eclipsed by the value from the counting statistics and could be ignored. Therefore, $\sigma_D(cm^2/sec)$ was equal to $\sigma_D(channels^2/sec)$ times the conversion factor squared.

Data were taken for the c direction at one atmosphere in the synthetic samples only. They are listed in Table (5-16) and plotted on an Arrhenius plot in Figure (5-18). The activation energy and D_o values were calculated and will be compared with the ion probe and radiotracer data in the next chapter.

Time studies

It was mentioned earlier that a number of time studies at single temperatures were undertaken to examine the extent of the initial transient. Their results are presented here. Multiple radiotracer experiments were carried out at three different temperatures. These are listed in Table (5-17) and plotted ln D vs t in Figure (5-19). The 1200°C series shows a trend of decreasing D with time but this variation is assumed to be minor compared to those seen in the ion probe data both in magnitude and duration. The other temperatures show that there was no evidence of a time dependent effect.

Six runs were made at 1100°C, c direction, and one atmosphere for analysis by the ion probe and RBS (Table 5-18). The results (Figure 5-20 and 5-21) clearly show an approximately two order of magnitude decrease in the apparent D from 2 hrs. to 47 hrs. Application of the thin film formalism developed in the last chapter to the IP results reduces this variation for the 2 and

Table 5-17. RT time studies, Sr, one atm.

run #	T(°C)	t x 10^{-5}(sec)	D(cm^2/sec)
5A	1300	4.12	$1.5 \pm 0.1 \times 10^{-12}$
7	"	4.14	$1.8 \pm 0.2 \times 10^{-12}$
3	"	7.76	$1.6 \pm 0.1 \times 10^{-12}$
2A	1250	7.99	$6.5 \pm 0.4 \times 10^{-13}$
6A	"	8.14	$3.6 \pm 0.2 \times 10^{-13}$
4A	"	9.22	$3.9 \pm 0.6 \times 10^{-13}$
4B	"	9.22	$3.6 \pm 0.3 \times 10^{-13}$
10	1200	11.9	$4.0 \pm 0.2 \times 10^{-13}$
12	"	15.3	$2.8 \pm 0.1 \times 10^{-13}$
8	"	16.8	$1.1 \pm 0.1 \times 10^{-13}$

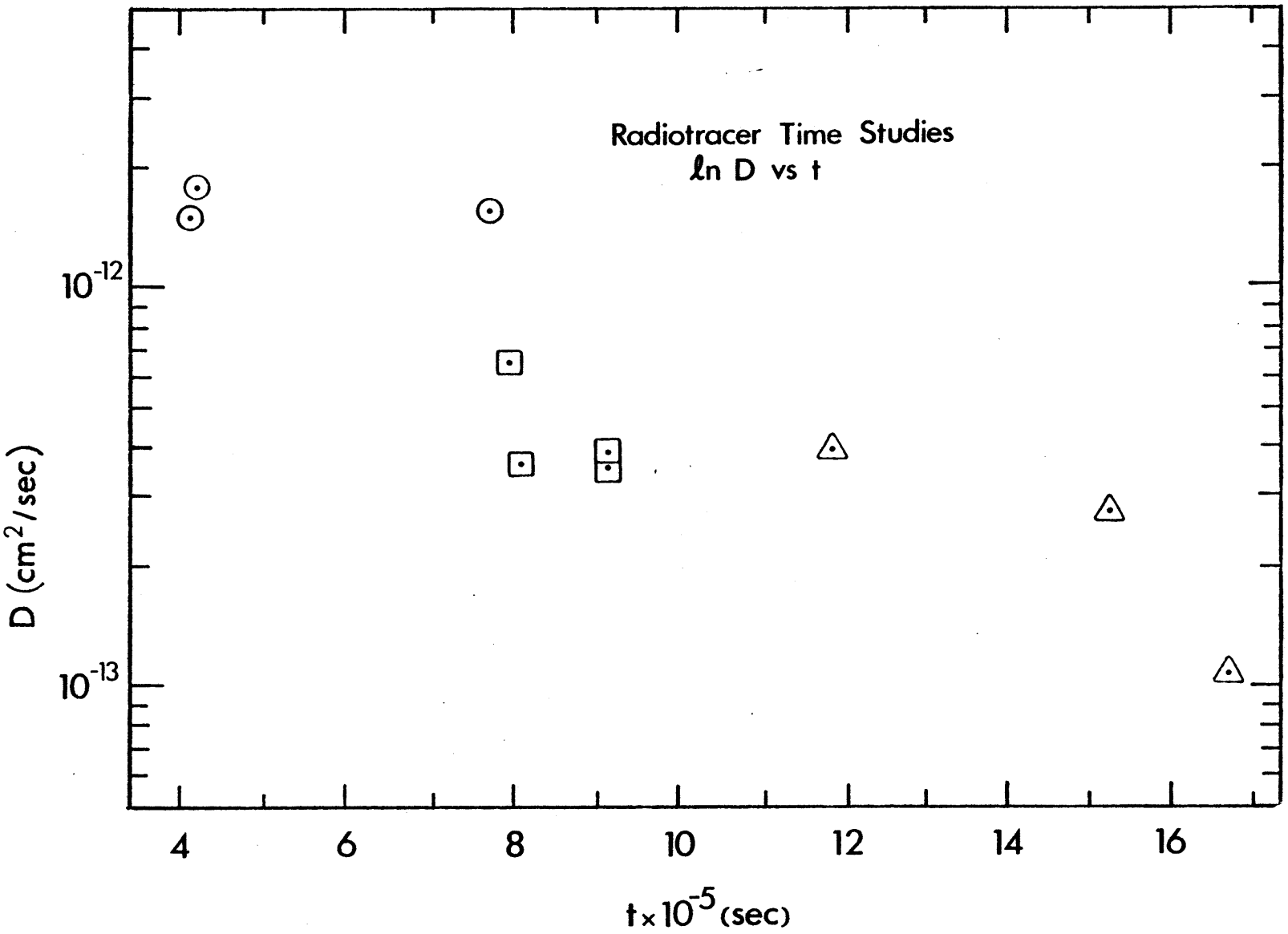

Figure 5-19. Time studies, radiotracer and sectioning in the natural samples, ℓn D vs t. 1300°C (circles), 1250°C (squares), and 1200°C (triangles).

Table 5-18. Time studies, Sr, one atm.

A) IP surface tracer, c direction.

run #	T(°C)	t(sec)	D(cm^2/sec)
B7 1 88	1100	7200	$2.5 \pm 0.2 \times 10^{-15}$
B7 2 88	"	"	$2.6 \pm 0.2 \times 10^{-15}$
86	"	"	$2.4 \pm 0.2 \times 10^{-15}$
B7 7 88	"	"	$1.8 \pm 0.1 \times 10^{-15}$
86	"	"	$1.8 \pm 0.1 \times 10^{-15}$
B6 2 88	1100	82800	$2.1 \pm 0.1 \times 10^{-16}$
86	"	"	$2.3 \pm 0.1 \times 10^{-16}$
B17 1 88	1100	169000	$9.2 \pm 0.2 \times 10^{-17}$
86	"	"	$9.2 \pm 0.2 \times 10^{-17}$
B17 3 88	"	"	$3.5 \pm 0.2 \times 10^{-17}$
86	"	"	$3.3 \pm 0.2 \times 10^{-17}$
B17 4 88	"	"	$1.8 \pm 0.1 \times 10^{-16}$
B17 5 88	"	"	$1.4 \pm 0.1 \times 10^{-16}$
B10 1 88	1100	248000	$3.1 \pm 0.2 \times 10^{-17}$
86	"	"	$3.1 \pm 0.2 \times 10^{-17}$
B10 2 88	"	"	$3.5 \pm 0.2 \times 10^{-17}$
B16 1 88	1100	335000	$7.3 \pm 0.5 \times 10^{-17}$
B16 2 88	"	"	$5.1 \pm 0.2 \times 10^{-17}$
86	"	"	$5.1 \pm 0.2 \times 10^{-17}$
B16 4 88	"	"	$2.4 \pm 0.1 \times 10^{-17}$
86	"	"	$2.5 \pm 0.1 \times 10^{-17}$

B) RBS surface tracer, c direction

run #	T(°C)	t(sec)	D(cm^2/sec)
B7	1100	7200	$3.1 \pm 0.2 \times 10^{-15}$
B6	1100	82800	$6.6 \pm 0.6 \times 10^{-16}$
B17	1100	169000	$6.6 \pm 0.9 \times 10^{-17}$
B10	1100	248000	$5.9 \pm 0.4 \times 10^{-17}$
B16	1100	335000	$5.8 \pm 0.7 \times 10^{-17}$

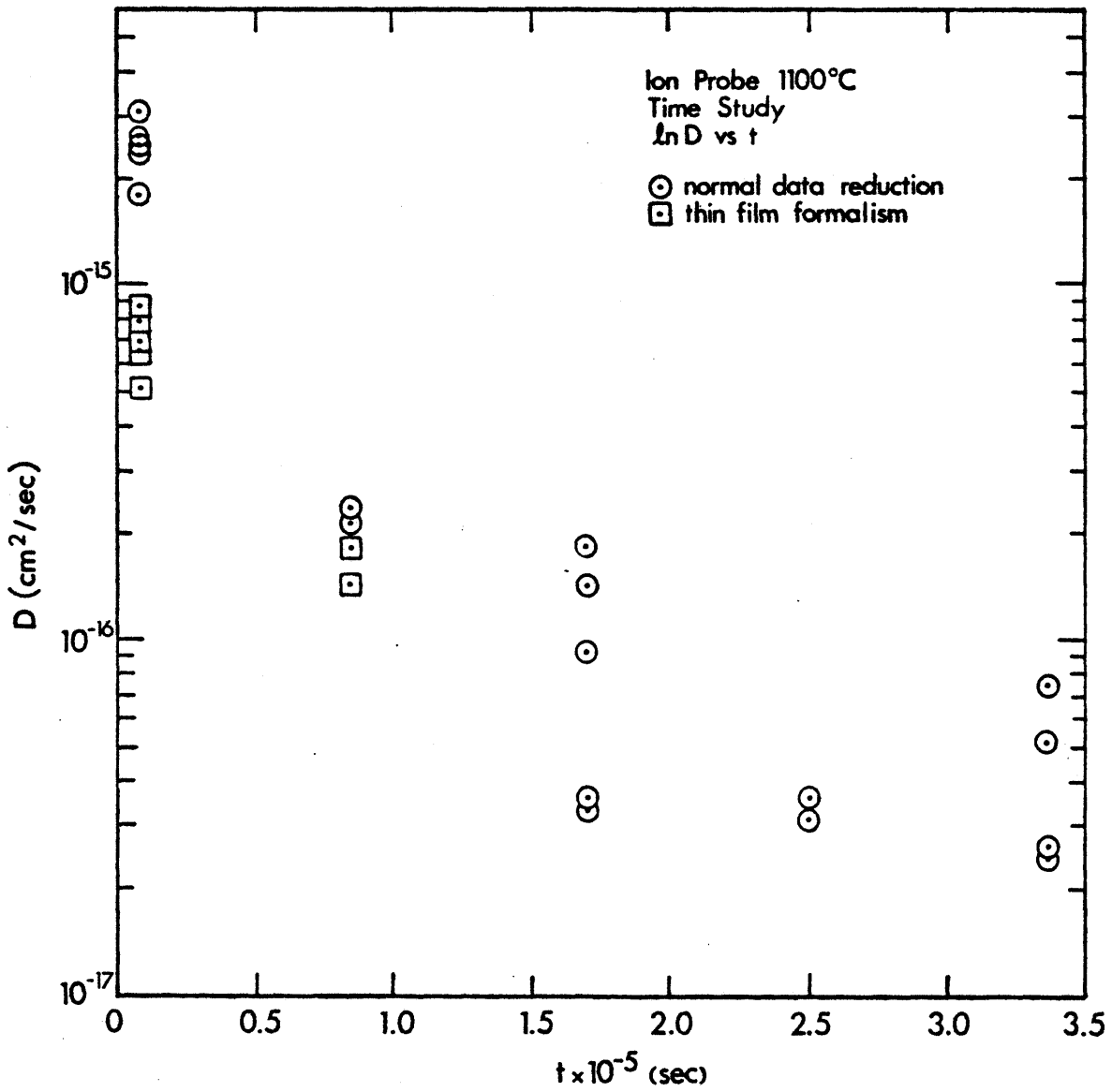

Figure 5-20. Time study, IP surface tracer for Sr, 1100°C, ℓn D vs t. Circles are for the normally calculated diffusivities and squares are for the treatment of the data using the thin film formalism developed in Chapter IV (not shown if coincident with the normal treatment value).

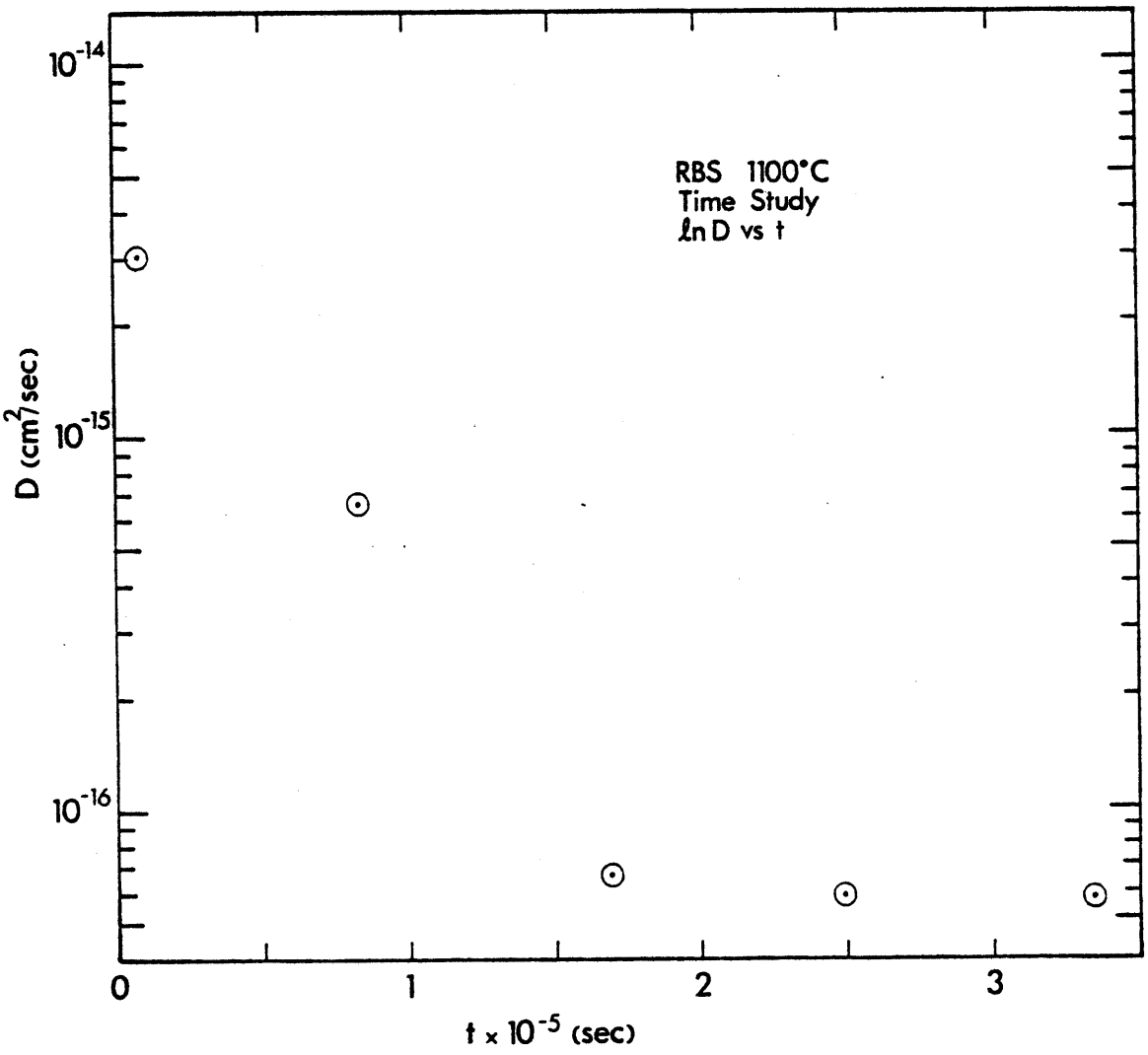

Figure 5-21. Time study, RBS for Sr, 1100°C, ℓn D vs t.

Table 5-19. IP time study, calculation of D via thin film formalism.

1100°C

run #	$D(cm^2/sec)$
B7 1 88	7.0×10^{-16}
B7 2 88	7.8×10^{-16}
86	8.5×10^{-16}
B7 7 88	5.1×10^{-16}
86	6.7×10^{-16}
B6 2 88	1.4×10^{-16}
86	1.8×10^{-16}
B17 1 88	7.5×10^{-17}
86	7.3×10^{-17}
B17 3 88	3.2×10^{-17}
86	3.0×10^{-17}
B17 4 88	1.3×10^{-16}
B17 5 88	7.5×10^{-17}
B10 1 88	3.0×10^{-17}
86	3.0×10^{-17}
B10 2 88	3.4×10^{-17}
B16 1 88	7.0×10^{-17}
B16 2 88	5.0×10^{-17}
86	4.9×10^{-17}
B16 4 88	2.3×10^{-17}
86	2.3×10^{-17}

23 hr points but does not totally remove it. D's calculated by this method are given in Table (5-19). The observed increase in D thus appears to be partially machine-generated and partially a physical attribute of the diffusion anneal. Concentrations of tracer in the near surface area are high for the first part of the experiment and the simple models used do not apply. The easiest way to deal with the problem is to increase the annealing time to avoid the effect. In this study, this increase did not lead to the added complication of concentration gradients too long to be analysed in a reasonable time.

D_{ij} tensor

The compensation effect among the crystallographic directions can be represented by the tensor notation developed in Chapter II. The matrix for D_{ij} for a monoclinic structure like diopside (symmetry axis parallel to b) is:

$$D_{ij} = \begin{bmatrix} D_{11} & 0 & D_{13} \\ 0 & D_{22} & 0 \\ D_{31} & 0 & D_{33} \end{bmatrix} \qquad (5\text{-}28)$$

At the compensation temperature T^{cr}, this reduces to the isometric case:

$$D_{ij} = \begin{bmatrix} D_{11} & 0 & 0 \\ 0 & D_{11} & 0 \\ 0 & 0 & D_{11} \end{bmatrix} \qquad (5\text{-}29)$$

This does not mean that diopside is crystallographically isometric at this point. Crystal symmetry is always the lowest form possible for the structure while physical properties can have higher forms. The fact that the symmetry for diffusion is temperature dependent is not unusual. Numerous properties

vary with temperature and sometimes equivalence between directions occurs.

If the principal axes are chosen so that y coincides with b and z with c, the values of D_{22} and D_{33} become D_b and D_c, respectively. Calculation of the other values requires two more determinations of D in the ac plane to provide three equations for three unknowns.

Boltzmann-Matano calculation

A representative surface tracer experiment (run #B10 1 88) was analysed using the Boltmann-Matano treatment to test the assumption that the diffusion rate is concentration independent. The data had undergone normalization, tail subtraction, and division by 2C(0) before being plotted (Figure 5-22). The B-M interface was taken to be the surface. The D value derived earlier was $3.1 \times 10^{-17} cm^2/sec$. Values for six concentrations are given in Table 20 and are all within a factor of two of the concentration independent number. The large difference on the last point is most likely due to errors in the slope and/or area estimates. The surface concentrations for this run was calculated as 8% Sr (molar), a fairly high value. However, it is evident that the composition dependence of D is slight and the thin film solution is a good representation of the diffusion process.

This chapter has shown that there is a difference in diffusion rates between the natural and synthetic samples which takes the form of a variation in the frequency factor more so than in the activation energy. Compensation among the crystal directions was demonstrated as well as among pressures and between two trace elements in the same structure. The measured D's for Sr and Sm were essentially equivalent, indicating that the host material effectively controls the diffusion process in this case. Measured activation energies did not display a monotomic behavior with pressure although the

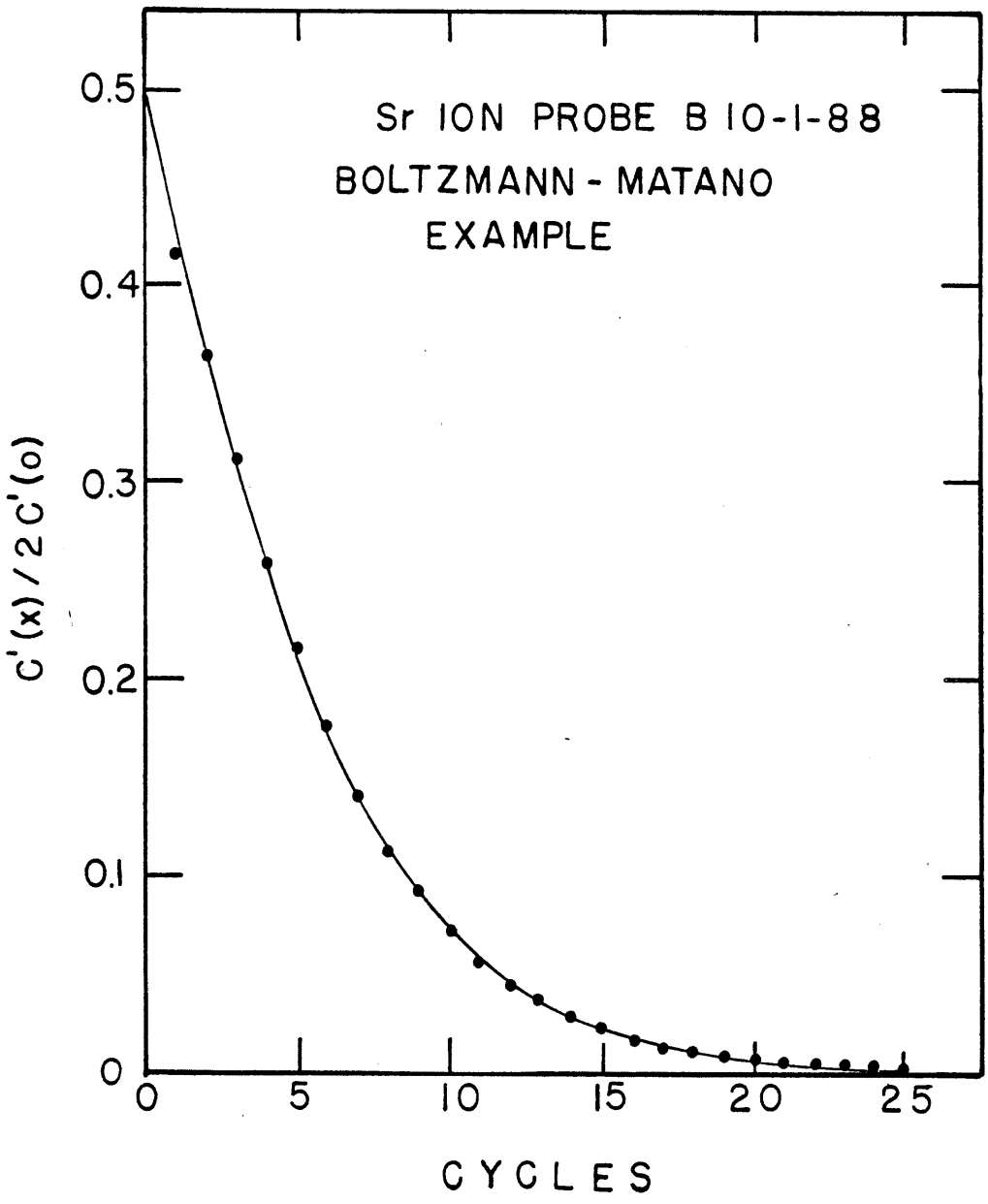

Figure 5-22. Concentraion profile for Boltzmann-Matano example. IP surface tracer for Sr at one atm (run #B10 1 88, 1100°C), C'(x)/2C'(0) vs depth. Boltzmann-Matano zero is assumed to be at the surface of the sample. Results are listed in Table 5-20.

Table 5-20. Boltzmann-Matano calculation for B10-1-88.

$D_{t.f.} = 3.1 \pm 0.2 \times 10^{-17}$ cm^2/sec

c_1*	$\frac{dx}{dc}\left(\frac{\text{Å}}{\#}\right)$	$\int_0^{c_1} x\,dc\,(\text{Å}\#)$	D(cm^2/sec)
0.425	764	132	2.0×10^{-17}
0.310	1020	127	2.6×10^{-17}
0.215	1288	106	2.8×10^{-17}
0.110	2190	72	3.2×10^{-17}
0.055	4247	43	3.7×10^{-17}
0.010	22342	11.2	5.1×10^{-17}

*$c_1 = c'(x)/2c'(0)$

ΔV_a's for strontium did have a temperature dependence. Thus, an empirical equation relating D to both temperature and pressure is not applicable under all conditions. Negative activation volumes were calculated for strontium and non-systematic positive numbers were derived for samarium. Time studies delineated the extent of short time transients which give the lower limit for annealing times that produce meaningful profiles. Only runs which had times greater than this minimum value of t were used in derivation of Arrhenius lines. Finally, the 2nd order tensor D_{ij} was examined briefly and a concentration dependent solution was applied to a representative high dosage tracer run. The results showed that D does not vary appreciably with concentration.

VI. COMPARISON OF THE THREE ANALYTICAL METHODS

"A man with one watch knows what time it is. A man with two is never sure."

--Molnar

A variety of analytical techniques are available with which to study diffusion. Transport rates in crystalline silicates are very slow and therefore difficult to analyse using methods which require long (>50 μm) concentration gradients to extract a D. Instrumental depth profiling procedures such as Rutherford backscattering spectroscopy, Auger electron spectroscopy, and ion probe in-depth analysis are being used more widely as equipment becomes available and the techniques become better known. The advantages of instrumental depth profiling are the ability to analyse short profile lengths (<1 μm), and to use low concentrations and stable isotopes. Each has built-in idiosyncrasies which may not be well understood and which produce an observed curve which is different from the true profile.

This study employed a traditional analytical technique, radiotracer and sectioning (RT), and two instrumental depth profiling schemes; ion microprobe (IP) and Rutherford backscattering spectroscopy (RBS) to determine the Sr diffusion coefficient in diopside. The samples for the c direction comparison were all cut from a single synthetic crystal of diopside grown for the study. The IP and RBS specimens were run as pairs so that experimental conditions were identical. The RT runs required a ^{85}Sr tracer and much longer annealing times to attain measurable profiles and were thus done separately. The data for each method were presented in the preceding chapter.

Radiotracer advantages and disadvantages

Radioactive tracer techniques have been used for most of the previous tracer and self-diffusion experiments in silicates. Many of these have been

autoradiography studies, in which the sample is sectioned lengthwise after annealing and placed in contact with a photo-emulsion. The dopants are beta particle emitters and thus leave tracks on the film. The other commonly-used technique is to section the sample parallel to the diffusion face and count the activity in either the slice or the residual specimen. The tracer is normally a gamma emitter.

This study used ^{85}Sr and a sectioning technique. Descriptions of autoradiographic methods can be found in Mysen and Seitz (1975) or Watson (1979). Considerations in designing an experiment using radioactivity-counting arise from the nature of both the tracer and of the material. The sample will determine the range of diffusion coefficients and thus the annealing time necessary to create a measurable profile. Shorter gradients can be examined in cases where residual activity is counted and very small distances can be measured or estimated.

Tracer half-life becomes a factor in the technique applicability as annealing time approaches $t_{1/2}$. ^{85}Sr decays by electron capture to ^{85}Rb with a half-life of 62.5 days. Long runs will have significantly less Sr at the end compared to the initial amount. This effect will not be drastic if, as in this work, the tracer is a small percentage of the total diffusing element. Carrier-free tracers undergo large changes in concentration and thus their use should be limited to runs of short duration with respect to $t_{1/2}$. Another problem arises from isotopes which decay to radioactive products. An example is ^{90}Sr which decays by beta emission to ^{90}Y, which then decays to ^{90}Zr. The half-life of ^{90}Sr is considerably longer than that of ^{90}Y and after an initial transient, a one to one correspondence in decay events will occur. The two species are chemically dissimilar and would yield a composite profile when counted. Decay energy is also important in that

low energy radiation has higher backgrounds and/or may dissipate before reaching the detector. Equations are available that take into account radiation which does not escape the sample until sectioned (Jambon and Carron, 1976). Examination of these show that this is not a problem for most gamma decays but can be appreciable for beta radiation. The activity of an isotope will at times have a bearing on its applicability. Low count rates can be remedied by increased tracer concentration, as long as it is realized that its behavior may not remain concentration independent. This is compounded for species which are not available without stable isotopes as carriers. Problems sometimes arise concerning the commercial availability of isotopes and the purity and form of those which are obtainable. "Carrier-free" has different meanings to different suppliers and must be investigated before use. It is seen that tracers must be examined for their suitability for the experiment and for their characteristics from a number of aspects.

Tracer introduction is a problem shared with any doping technique. Difficulties unique to radioactive species stem from safety considerations. Evaporation of the tracer during an experiment can contaminate furnaces and possibly the laboratory environment. Sectioning of the sample introduces errors which must be addressed. It is often difficult to maintain a surface which is parallel to the original diffusion surface. Small variations of a few percent of the diffusion distance can be ignored or dealt with analytically (Eisen and Birchenall, 1957). Larger variations will alter the profile appreciably, especially if the skewness is compounded by successive grindings.

An advantage that this technique shares with the ion probe is the possibility of using multiple tracers. The isotopes must possess gamma radiation

of distinct energies and must be counted with either a multichannel analyser or a single channel analyser adjusted to examine one peak at a time. This system could be used to resolve sequential decay patterns if the energies of the conflicting events can be separated. A variation on this is in-situ activation of species by bombarding a portion of the sample with neutrons or other high energy particles (Varshneya et al., 1973; Hofmann and Brown, 1976). This eliminates problems normally associated with interface kinetics.

Possibly the most important advantage of the method is the relative economy of the analytical system. Essential components include an accurate scintillation detection system and a means of measuring small distance differences. This may be a profilometer, a micrometer, a dial gauge, or a microbalance depending on the sample size and the thickness of the step. Other considerations are the means of sectioning and the tracers themselves. Taken in total, the necessary equipment is definitely more available than ion probes or high-energy alpha particle accelerators.

RBS advantages and disadvantages

Rutherford backscattering spectroscopy is an instrumental depth-profiling technique. Like ion probe depth profiling, it can examine short diffusion gradients with a high degree of accuracy. Beyond that, the two sytems are dissimilar in approach. The RBS technique analyses rebounding high-energy α particles to give concentration as a function of depth. The thickness of the analysed layer depends on the incident beam energy and the masses of the target atoms.

Whereas RBS is also an in-situ form of analysis, it is not nearly as subject to the surface roughness problems which can greatly reduce the usefulness of ion probe profiles. First, variable surface height is not seen by the incident beam nor the detector. The energy loss for slighly longer path

lengths through vacuum is minuscule compared to the loss on interaction with the target surface. Second, the process is basically non-destructive. A pit is not formed and surface irregularities are not accentuated as in the sputtering process. Third, physical measurement of the profile length is not necessary. It is calculated from highly-developed theory concerning nuclear interactions. Another advantage of the system is the speed of analysis. A complete profile can be taken in as little as fifteen minutes since counts accumulate for all energies simultaneously. Eight samples were examined in a four-hour session including machine start-up and beam focussing. Relative peak heights can be used to derive sample composition if the nuclear cross-sections of the constituent atoms are known. Small amounts of light elements are hard to distinguish in silicates, due to the large amounts of heavier species like silicon and calcium. Major elements and, in some cases, heavy trace elements can be assigned abundances with little difficulty. The presence of heavy tracers can be easily determined even if their concentration cannot be derived because of interferences. An important consideration in diffusion experiments is the state of the trace isotope. Stable dopants can be used with RBS, thus removing half-life problems from annealing times, profile data reduction, and the synthesis of doped starting materials.

There are a number of short-comings which limit the applications of the technique. One that will be discussed in the next section is instrumental broadening which affects the apparent surface concentration. This is dealt with fairly easily by estimating or calculating the surface value from the rest of the curve. Another form of broadening occurs as a result of energy losses from non-collisional interactions in the sample. This is evidenced

by the increased counts for lower energies in a homogeneous elemental material in which all values are equally probable. A second problem is that profiles for light tracers occur on top of the major element curves. Subtraction of this sample background induces large uncertainties in the diffusion curve. Use of tracers which are considerably heavier than the major species can avoid this. In this work, Sr has twice the mass of Ca so that the peaks are separated by an energy difference equivalent to 4450 Å. Natural samples with their variety of trace elements have fairly complicated spectra onto which the diffusion profile would be superimposed. This can be handled in the data reduction but, once again, uncertainties are introduced which are not present in pure synthetic specimens. Multiple tracer experiments must also take into account spectra overlap. Diffusants of similar mass would be difficult to separate analytically. The technique is best suited to a single high mass dopant in a pure phase.

Both RBS and IP depth profiling (discussed in chapter IV) require specialized equipment which is not readily available. Large linear accelerators like the one utilized by this project are not necessary for RBS. Smaller, dedicated machines exist, although most cannot reach the potentials at which the linear accelerator normally runs. They are in the KeV range which limits the depth of analysis and decreases the differences between surface values for the various elements.

Profile lengths

Since the IP and RBS samples underwent identical diffusion anneals any differences in the concentration profiles will be machine induced. A non-diffusion tail has been recognized in the IP profiles and was removed before comparison with the RBS spectra. Table (6-1) shows the distances at which the concentration equals 10% of the surface value for both the IP and RBS

Table 6-1. Distances to 10% of surface concentration.

run #	Avg. of IP(Å)	RBS(Å)
B 6	1214 ± 34	1934 ± 69*
B 7	855 ± 84	1079 "
B 9	1220 ±258	1600 "
B10	690 ± 85	818 "
B11	1213 ±150	1302 "
B12	1033 ± 94	1488 "
B13	1091 ± 95	1674 "
B16	1023 ±173	1063 "
B17	1037 ±366	892 "

*assigned value of ± 2 channels

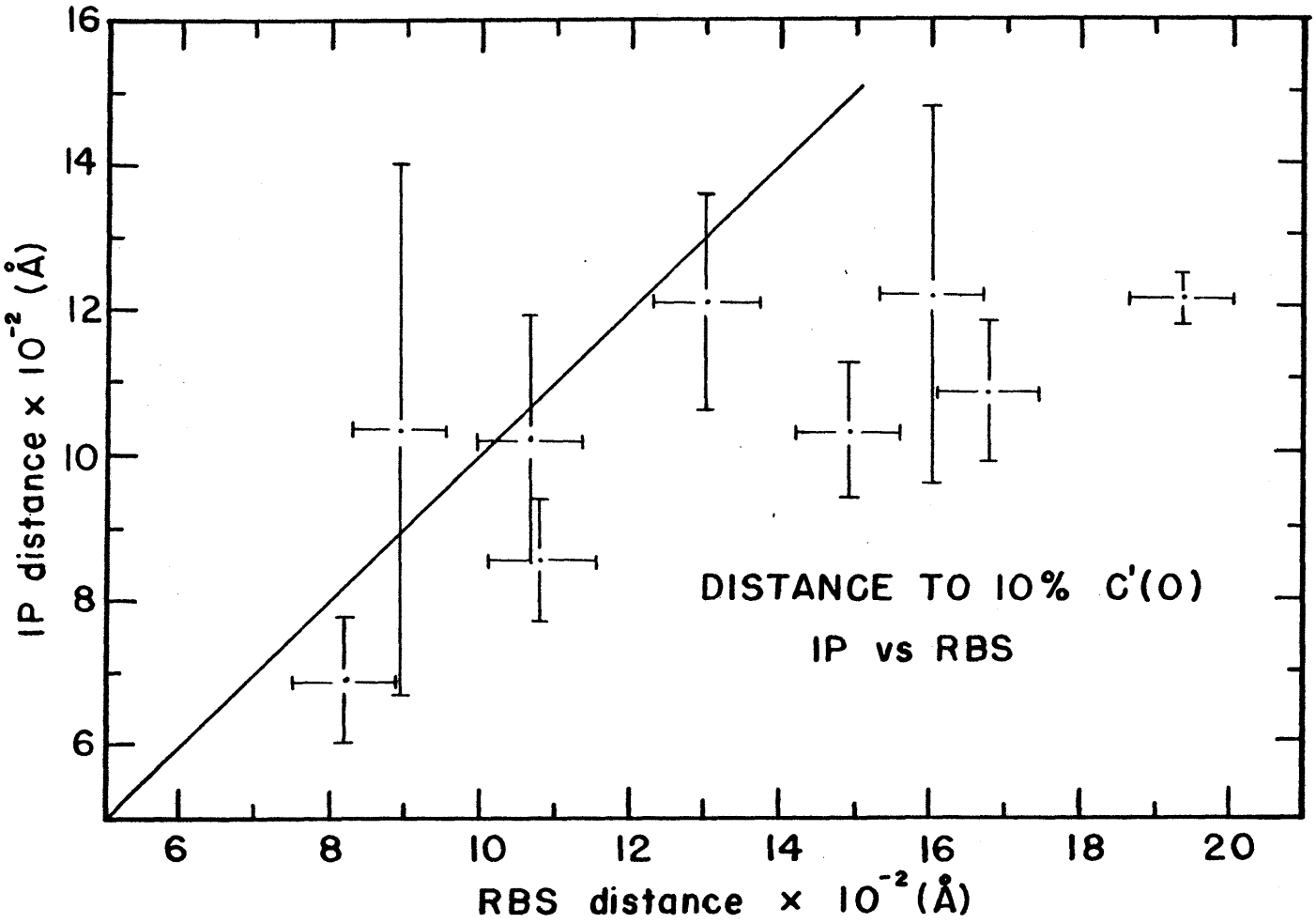

Figure 6-1. Comparison of depths to 0.1 C'(0) for IP and RBS, depth (IP) vs depth (RBS). The straight line has a slope of one. Most values lie to the right of this line, eindicating that the RBS profiles are extended by some machine effect.

analyses. Plotting these numbers on a graph of IP vs RBS (Figure 6-1) should give a line with a slope of one if there isn't any machine-induced broadening. The RBS data were taken during two different sessions with different detectors. Runs B6 to B13 were analysed with one system while B16 and B17 used another. The second set-up produced far less instrumental broadening of the peak due to its greater energy discrimination capabilities. The data show considerable scatter with most of the values lying to the right of the unit slope line in Figure (6-1). This indicates that the RBS profiles are lengthened by some machine effect. Simple instrumental peak broadening, where a mono-energetic signal is measured as a gaussian with the area under the curve equal to the signal's "area", will not lengthen the profile. Figure (6-2) crudely illustrates this by replacing the gaussian with a triangle whose width is defined by the amount of broadening. Selected points of a diffusion curve were drawn as triangles with the corresponding area. These were then summed and the resultant plotted as the observed curve. The true transport curve matches this exactly except near the surface. Therefore, true distance would be derived from such a profile if the surface value is correctly estimated. Actual lengthening requires some other effect such as energy loss due to non-collisional interactions within the sample.

Calculated diffusion coefficients

Comparison of the results of the three methods is shown graphically in Figure (6-3), an Arrhenius plot. There is excellent agreement within the study range with maximum differences of a factor of two in D. Table (6-2) lists the activation energies and frequency factors with standard deviations derived from the "least squares cubic" (York, 1966) of lnD vs 1/T. The values fall very close to the diopside compensation line (Figure 6-4) derived

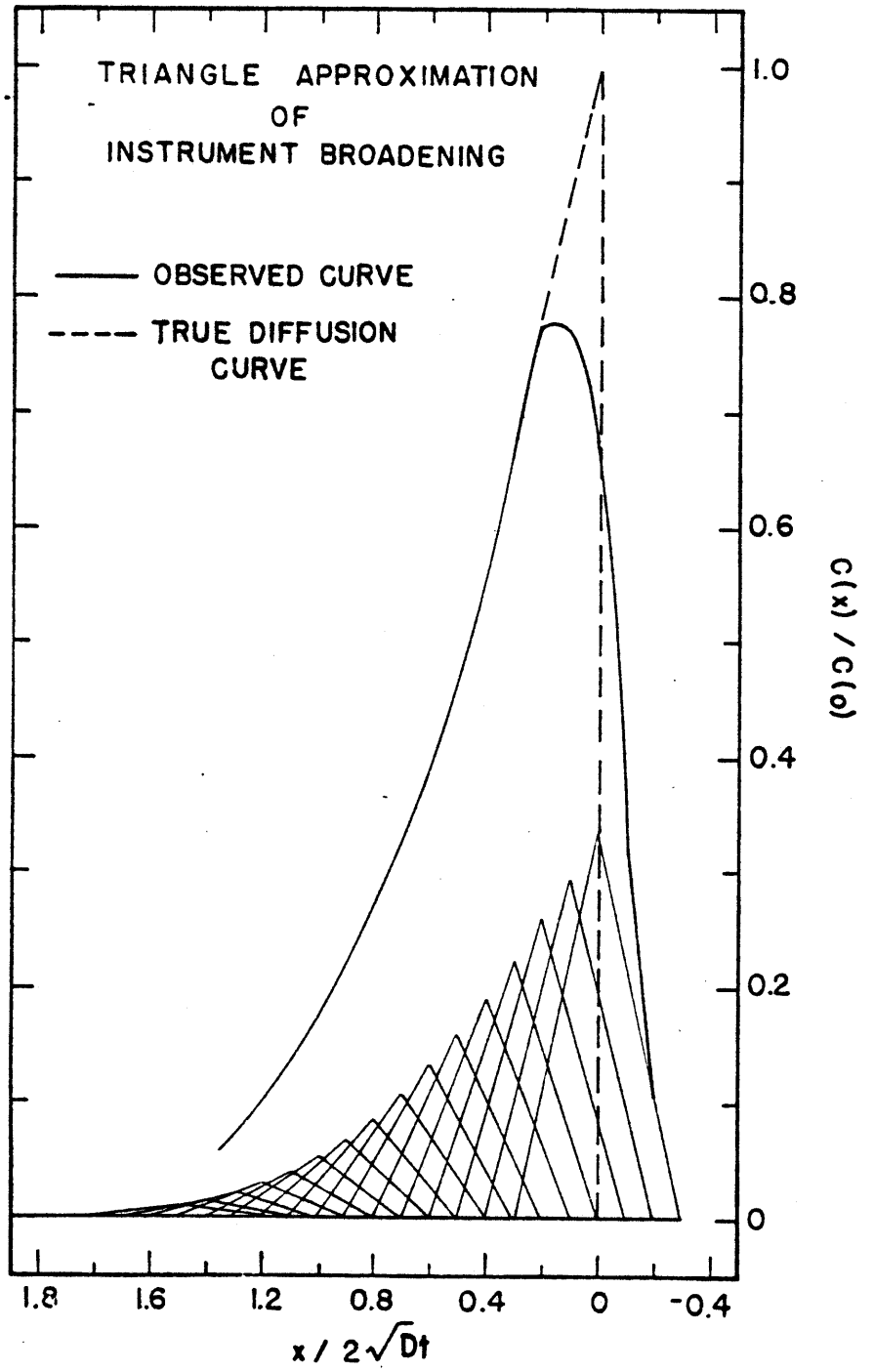

Figure 6-2. Schematic representation of the effect of instrumental peak broadening. Dashed curve is the true diffusion profile and the solid curve is the observed profile calculated by summing the contributions of the triangles intersecting a given value of x. The base of the triangle is fixed and the area is equal to the value of the true diffusion curve at the mid-point of the base. Observed curve coincides with the true profile except near the surface.

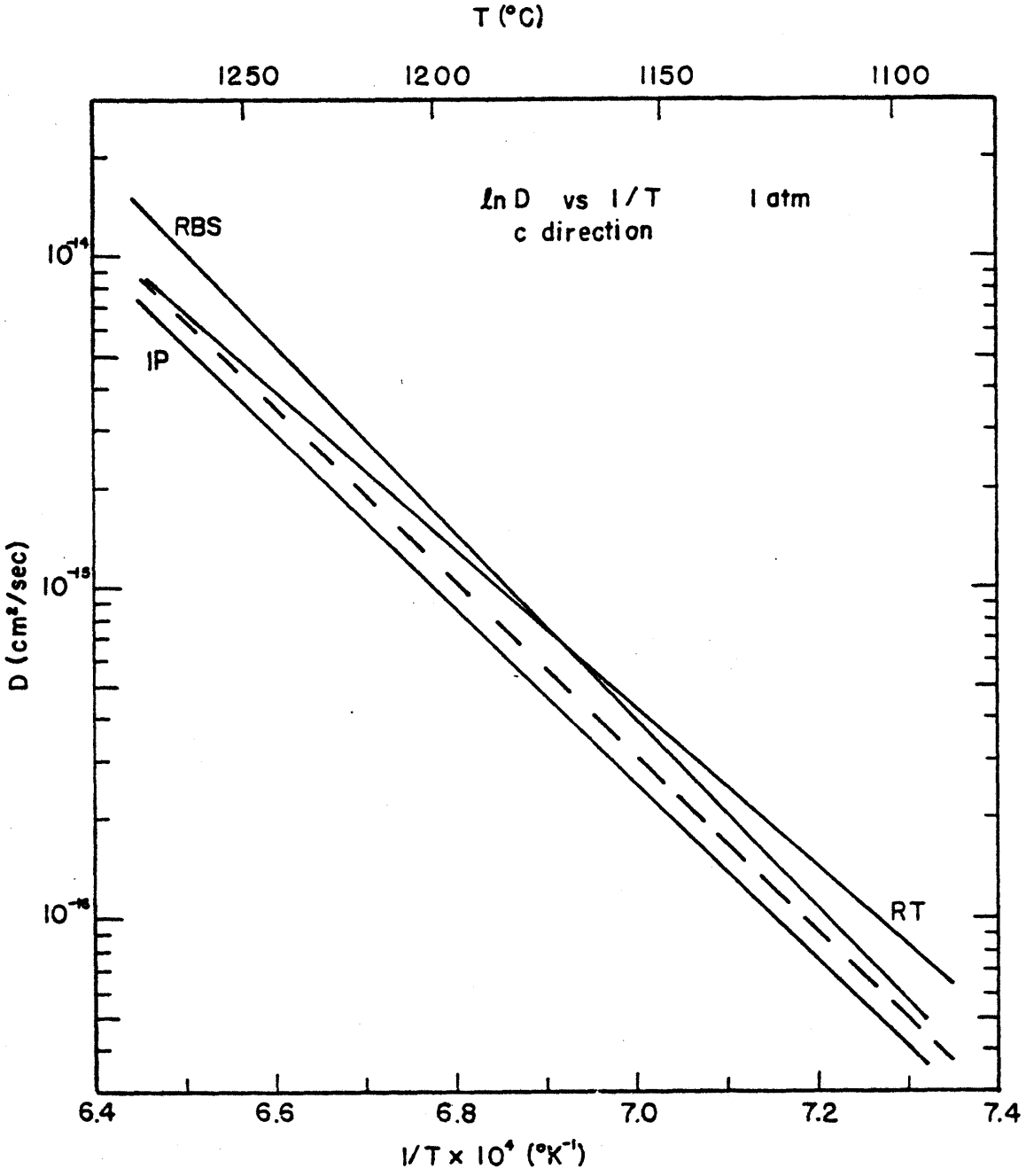

Figure 6-3. Comparison of the three analytical methods for Sr at one atm (synthetic crystal, c direction), ℓn D vs 1/T.
RBS, ΔH_a = 130 ± 6 Kcal/mol and ℓn D_0 = 10.4 ± 2.1 (cm^2/sec).
IP (surface tracer model), ΔH_a = 122 ± 7 Kcal/mol and ℓn D_0 = 7.1 ± 2.5 (cm^2/sec). RT, ΔH_a = 109 ± 18 Kcal/mol and ℓn D_0 = 3.2 ± 5.9 (cm^2/sec).
Dashed line is for a constant surface model of the IP data, ΔH_a = 120 ± 6 Kcal/mol and ℓn D_0 = 6.6 ± 2.0 (cm^2/sec).

Table 6-2. ΔH_a's and D_o's, surface tracer, Sr, one atm.

c direction

method	ΔH_a (Kcal/mole)	ln D_o	D_o
IP	122 ± 7	7.1 ± 2.5	1200
RT	109 ± 18	3.2 ± 5.9	24.5
RBS	130 ± 6	10.4 ± 2.1	32900
IP'*	120 ± 6	6.6 ± 2.0	735

*ion probe data reduced using constant surface concentration model

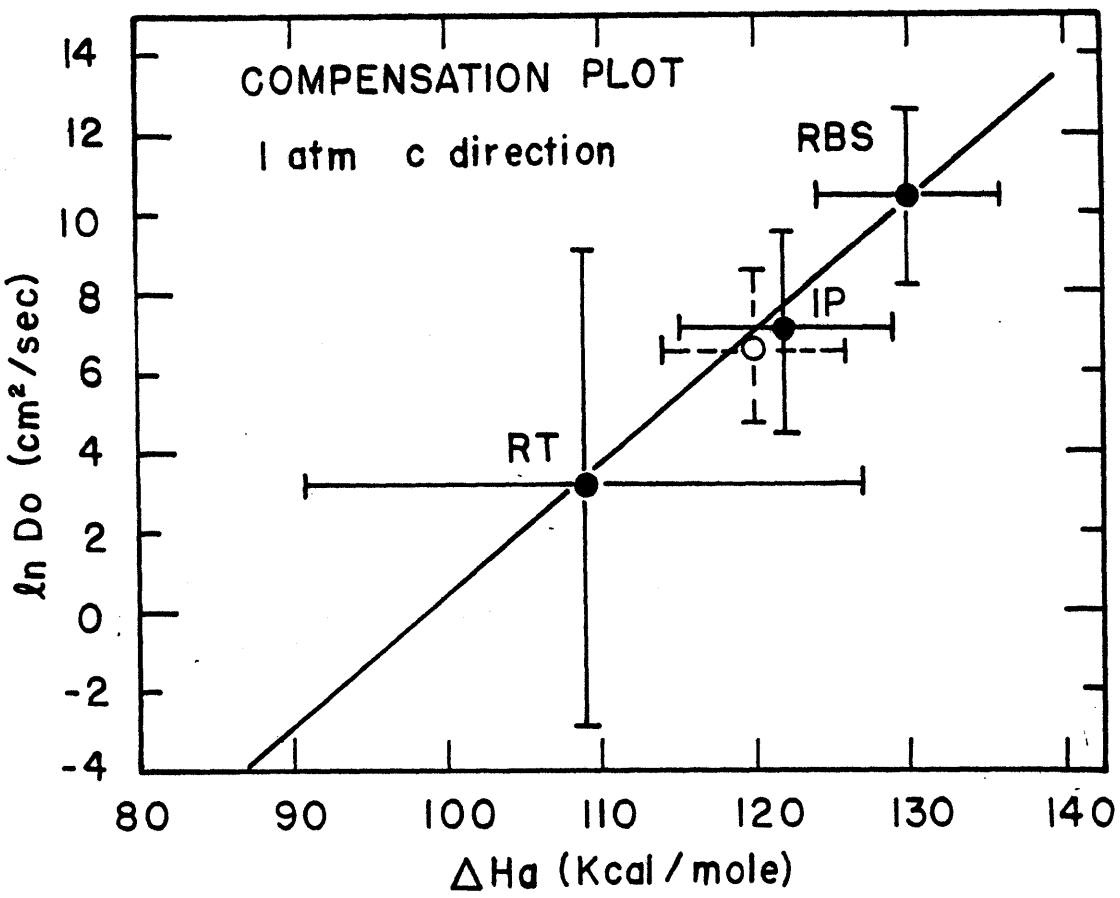

Figure 6-4. Compensation plot for comparison of ΔH_a's and D_0's of the three analytical techniques, ℓn D_0 vs ΔH_a. Open circle is for a constant surface model of the IP data and the straight line is the diopside compensation trend derived in Chapter V. Values of ΔH_a and D_0 for each point are listed in Table 6-2.

earlier, although the large error bars make their exact locations uncertain. Even closer agreement occurs if the ion probe data are treated by the same constant surface concentration model as the RBS and RT values (Table 6-3). The decision was made earlier to use the thin film model for the IP profiles because of better correlation coefficients. Calculation of ΔH_a and D_o for the alternate model for the c direction at one atmosphere is represented by the dashed line in Figure (6-3). The differences in the D's are caused by the models themselves when applied to the non-ideal profile.

The conclusion that can be drawn here is that different analytical methods can provide essentially the same diffusion coefficient if a point is made of dealing with the inherent curve-modifiers present in each system. Ignoring effects such as short-term transients and instrumental broadening can give results which may vary from the true values by more than an order of magnitude. In this respect, a comparison among methods serves to isolate problems which may otherwise go unnoticed. The initially calculated D's for this study were considerably different from the final values for this reason. Internal tests such as time studies eliminated some spurious values while others were not recognized until instrumental cross-comparisons were made.

The three techniques each have difficulties and advantages. The present comparison indicates that all produce essentially the same diffusion coefficients. So, choice of one over the others will be controlled by factors such as sample size and the availability of the analytical equipment. The equivalence of the results also shows that the relatively new method of ion probe depth profiling can be used to derive accurate diffusion rates if machine problems are addressed.

Table 6-3. IP surface tracer experiments, Sr, one atm, diffusion couple model.

c direction

run #	T(°C)	t(sec)	D(cm^2/sec)
B13 1 88	1250	7200	$2.8 \pm 0.2 \times 10^{-15}$
86	"	"	$3.3 \pm 0.2 \times 10^{-15}$
B13 2 88	"	"	$4.2 \pm 0.1 \times 10^{-15}$
86	"	"	$4.5 \pm 0.1 \times 10^{-15}$
B12 1 88	1200	15300	$9.2 \pm 0.3 \times 10^{-16}$
B12 2 88	"	"	$1.7 \pm 0.1 \times 10^{-15}$
86	"	"	$1.7 \pm 0.1 \times 10^{-15}$
B10 1 88	1100	248000	$4.0 \pm 0.3 \times 10^{-17}$
86	"	"	$4.0 \pm 0.3 \times 10^{-17}$
B10 2 88	"	"	$3.8 \pm 0.3 \times 10^{-17}$
B16 1 88	"	335000	$8.2 \pm 0.6 \times 10^{-17}$
B16 2 88	"	"	$5.9 \pm 0.3 \times 10^{-17}$
86	"	"	$6.1 \pm 0.3 \times 10^{-17}$
B17 1 88	"	169000	$9.7 \pm 0.5 \times 10^{-17}$
86	"	"	$10.0 \pm 0.5 \times 10^{-17}$
B17 3 88	"	"	$4.5 \pm 0.3 \times 10^{-17}$
86	"	"	$4.1 \pm 0.2 \times 10^{-17}$

$\Delta H_a = 120 \pm 6$ Kcal/mole

$D_o = 7.5 \times 10^2$ cm^2/sec

VII. PREVIOUS WORK

"Quot homines, tot sententiae." - Latin proverb.

The preceding chapters have dealt almost exclusively with the data derived in this thesis. This section will present a compilation of pertinent volume diffusion information from other sources. These data will be used to examine the effect of pressure on transport and make comparisons between the ion probe and other techniques. The present work will be discussed within the framework of alkaline earth and REE diffusion in silicates in general and, along with other ions, in pyroxenes in particular.

High pressure data

A small percentage of laboratory measurements of diffusion in solids have included the effect of pressure on the system. Many of these have been in metals (e.g., Gilder et al., 1971; Hudson and Hoffman, 1961) with values for the activation volume showing a positive temperature dependence and the diffusion coefficient a negative pressure dependence. Magnitudes of ΔV_a range from a few percent to nearly all of the gram atomic volume of the material. Freer (1980) compiled a list of diffusivity determinations for simple oxides and does not list any for which the effect of pressures was studied.

High pressure studies in silicate liquids and glasses can be divided into two pressure/temperature ranges. The first covers pressures up to a 2 or 3 kilobars and temperatures to 1000°C. These experiments usually utilized a cold-seal bomb apparatus and the pressure was most often a means of maintaining a fluid phase at run conditions. The fluid acts as a reservoir for the tracer and/or controls the water content of the material. Higher pressures and temperatures are achieved in solid media presses or internally heated gas media equipment. This second category covers most studies where

the effect of pressure was examined. Watson (1979, 1981) used a beta track mapping technique to analyse Ca and Cs diffusion in a sodium-calcium-aluminosilicate melt to 30 Kbar. The activation volume for Ca showed a negative temperature dependence while the two temperatures studied for Cs indicate a positive correlation between ΔV_a and T. Ca also exhibited a pressure dependence of the activation energy, which was not the case for Cs. The dissimilar behavior was attributed to a possible structural role for calcium in the melt (Watson, 1981). Fujii (1981) calculated activation energies for Ca-Sr interdiffusion in an albite melt similar to Watson's Ca values but described a complicated pressure effect. For a given temperature, D decreased more rapidly from 0 to 7 Kbar than from 10 to 20 Kbar. This suggested a structural change in the melt of unknown description. He did not report whether a temperature dependence of the pressure effect was observed. Watson's Ca data (Figure 7-1) show compensation with a T^{cr} of about 1450°C. Above this temperature the activation volume is negative, meaning the increased pressure actually causes D to rise. A similar situation was shown in the last chapter for the c direction in diopside, although the magnitude of the ΔH_a for 20 Kbar was between those of the other, lower pressures. The compensation temperature was below the study range, indicating positive values of ΔV_a below 1050°C. Both of these extrapolations of the actual data can be examined experimentally to test the compensation trend. Published results for high pressure studies in melts are shown in Figure (7-2). Except for the extension of the Ca data, the effect of increasing load is to decrease the diffusion coefficient.

Studies in crystalline silicates at pressures greater than two kilobars are sparse. Most determinations of D deal with a single pressure or temperature, making calculations of ΔV_a or its temperature dependence impossible

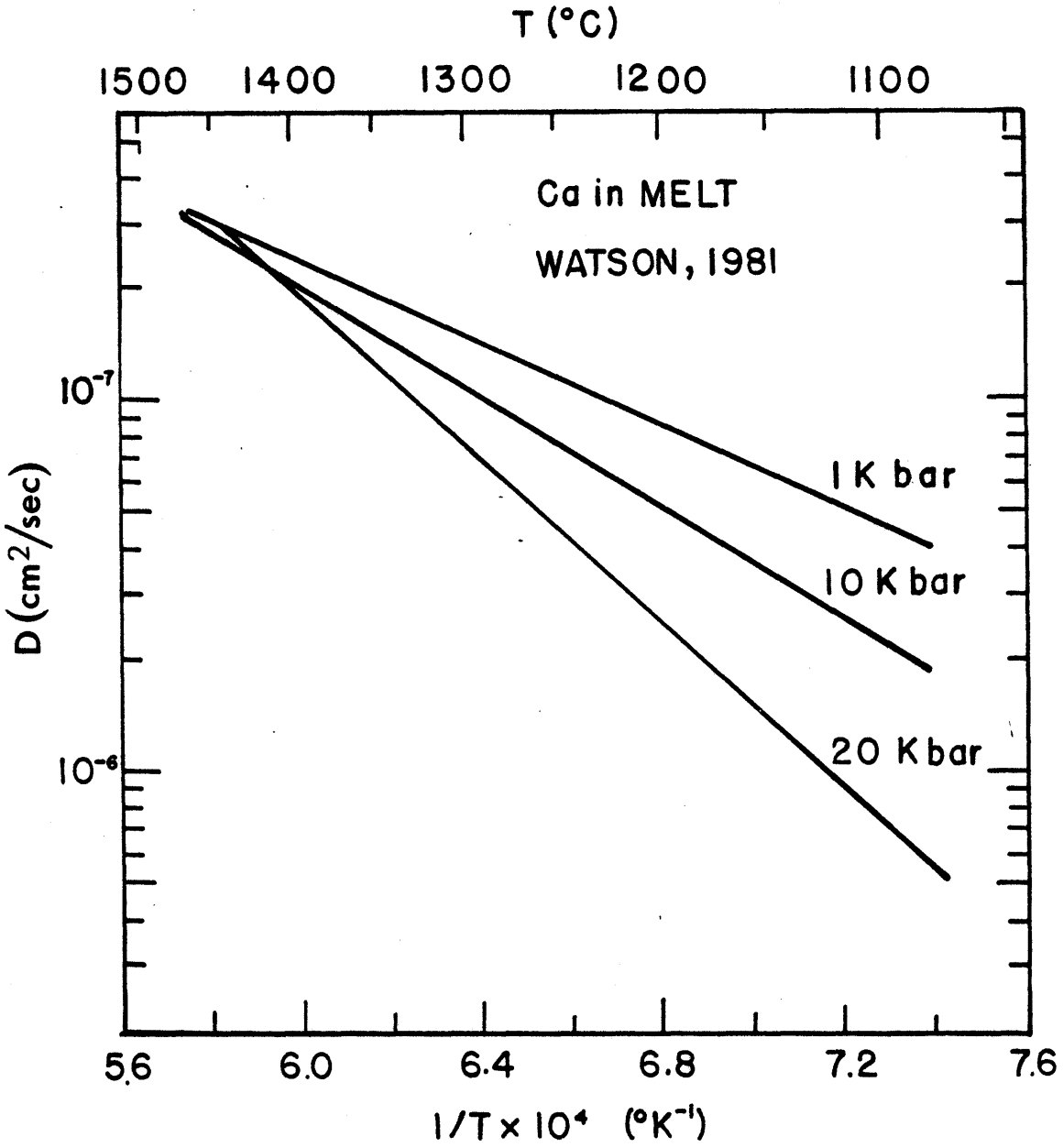

Figure 7-1. Ca diffusion in a sodium-calcium-aluminosilicate melt (Watson, 1981), ℓn D vs 1/T, showing crossover point for compensation among different pressures.

(Figure 7-2). Misener (1974) studied Mg-Fe interdiffusion as a function of temperature, pressure, composition, and crystallographic direction in olivine couples, using an electron microprobe. He did not report ΔH_a at pressures other than one atmosphere, but did calculate ΔV_a as a function of composition at 900 and 1100°C. The activation volume for 1100°C was greater than for 900°C, with the difference decreasing with higher values of the ratio Mg/Mg + Fe. An average value of 5.5 cm^3/mole was recorded in the paper and a positive temperature dependence can be inferred from the plotted values of ΔV_a. Giletti and Tullis (1977) examined Ar diffusion in phlogopite at 15 Kbar and compared it to earlier data at lower pressure. They concluded that pressure had no effect on the diffusion rate outside the scatter of the 2 Kbar numbers. Only two temperatures were examined at 15 Kbar and they formed a line of different slope (different ΔH_a) on an Arrhenius plot. Further experiments at other temperatures are needed to substantiate their conclusion. Yund and Tullis (1980) estimated activation energies of 87.3 ± 7 and 67.2 ± 10 Kcal/mole for albite at one atmosphere and 10 Kbar, respectively, from Al-Si order/disorder experiments. The ordering parameter increases with pressure, and the crossover point for the two Arrhenius lines at different pressures is well above the melting point. This is similar to the behavior of the diffusion coefficients for the a and b directions in this study, although the albite experiments contain water. This in itself may be the explanation of the negative ΔV_a. Yund and Anderson's (1978) values for O diffusion in feldspar (650°C) also show an apparent negative activation volume in the range 125 to 4000 bars, and they interpret this as an effect of the H_2O pressure. They postulate that water, possibly as OH^- or H^+, penetrates the mineral structure and enhances in some way in the oxygen exchange. Thus, what would first appear to be a case similar to this study, is more

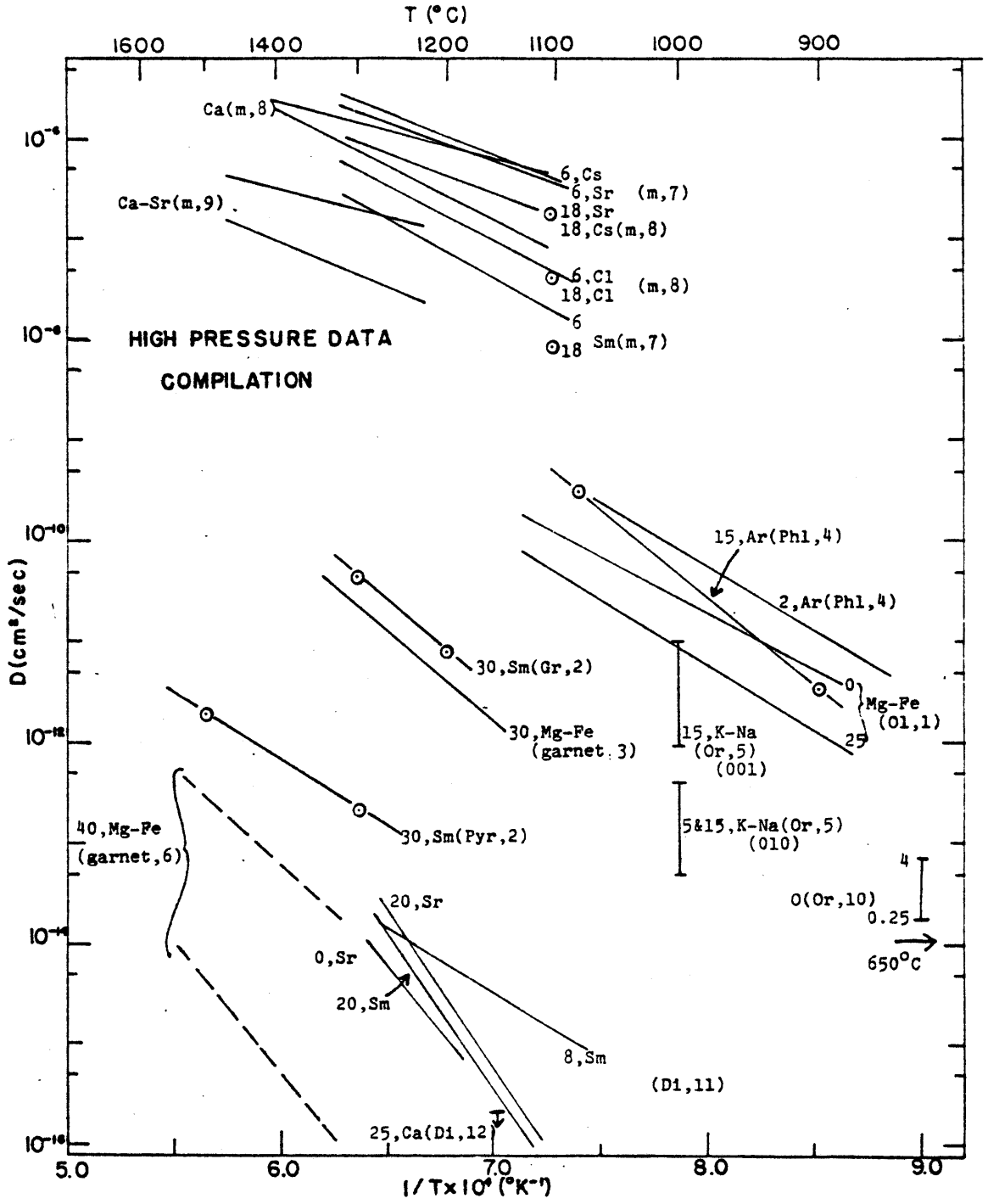
T (°C)
1600
1400
1200
1100
1000
900
Ca(m,8)
6,Cs
6,Sr (m,7)
18,Sr
18,Cs(m,8)
Ca-Sr(m,9)
6,Cl
18,Cl (m,8)
6
18 Sm(m,7)
HIGH PRESSURE DATA
COMPILATION
15,Ar(Phl,4)
2,Ar(Phl,4)
30,Sm(Gr,2)
0
Mg-Fe
(Ol,1)
30,Mg-Fe
(garnet,3)
25
15,K-Na
(Or,5)
(001)
30,Sm(Pyr,2)
5&15,K-Na(Or,5)
(010)
40,Mg-Fe
(garnet,6)
4
0(Or,10)
0.25
650°C
20,Sr
0,Sr
20,Sm
8,Sm
(Di,11)
25,Ca(Di,12)
D(cm²/sec)
10⁻⁶
10⁻⁸
10⁻¹⁰
10⁻¹²
10⁻¹⁴
10⁻¹⁶
5.0
6.0
7.0
8.0
9.0
1/T×10⁴ (°K⁻¹)

Figure 7-2. High-pressure data compilation, ℓn D vs 1/T. The first number in the label or the number on the curve is the pressure in Kbar. The diffusing species is next, followed by the phase and reference number in parentheses.

1. Misener, 1974, Mg-Fe interdiffusion in olivine to 35 Kbar.
2. Harrison and Wood, 1980, Sm in garnet at 30 Kbar.
3. Duckworth and Freer, 1981, Mg-Fe interdiffusion in garnet at 30 Kbar (Freer, 1981).
4. Giletti and Tullis, 1977, Ar in phlogopite at 15 Kbar.
5. Christoffersen, et al., 1981, Na-K interdiffusion in orthoclase at 5 and 15 Kbar.
6. Elphick, et al., 1981, Mg-Fe interdiffusion in garnet at 40 Kbar (range of possible values between dashed lines).
7. Watson and Bender, 1980, Cs, Sm, Sr, Cl in sodium-calcium-aluminosilicate melt at 6 and 18 Kbar.
8. Watson, 1981, Ca in sodium-calcium-aluminosilicate melt to 30 Kbar.
9. Fujii, 1981, Ca-Sr interdiffusion in albite melt to 20 Kbar.
10. Yund and Anderson, 1978, O in orthoclase to 4 Kbar.
11. this study.
12. Brady and McCallister, 1980, Ca in diopside at 25 Kbar (upper limit only, from lamellae homogenization).

likely a result of the wet conditions of the experiments. Christoffersen et al. (1981) measured the Na-K interdiffusion in an alkali feldspar pair as a function of crystal direction at 5 and 15 Kbar, and no pressure effect outside the uncertainties of the individual measurements was observed.

Three recent studies have examined diffusion in garnet at pressures of 30 Kbar or greater. Harrison and Wood (1980) derived D's for Sm in pyrope and grossular at two temperatures (1200 and 1300°C) using equilibration times for partitioning experiments. There is a large difference in activation energies, with the grossular value more than twice that of the pyrope. Besides the uncertainty of a two point determination, the grossular experiments are suspect because of early transient formation of zoisite in the charge. This phase crystallized first and gleens most of the Sm from the fluid. The grossular then precipitates and only accumulates Sm as the zoisite breaks down, releasing the REE. Duckworth and Freer (1981) and Elphick et al. (1981) have reported preliminary data on Fe-Mg interdiffusion in aluminosilicate garnets at 30 and 40 Kbars, respectively. Comparison between the studies is difficult because very few experimental details are included. The fact that D appears to decrease by three orders of magnitude from 30 to 40 Kbar seriously hampers the validity of the comparison.

Figure (7-2) is a compilation of the high pressure diffusion data in silicates. It contains values from the present study as well as a Ca-(Mg,Fe) interdiffusion number derived from pyroxene lamellae homogenization at 1150°C and 25 Kbar (Brady and McCallister, 1980). The authors feel that this value is suspect and is actually measuring some other process besides diffusion because it is considerably lower than one atmosphere tracer data. The D from the homogenization experiment's similarity to the present study is misleading because differences in materials and the measured phenomenon probably

render the agreement a coincidence. No pattern is seen in the high pressure silicate D's which would allow predictions to be made on the behavior of other phases and elements. More determinations are necessary before any generalizations can be drawn.

Ion probe determinations

Ion microprobes are finding increasing use because of their ability to give in-situ trace element concentrations and isotope compositions in the surface analysis mode. Depth profiling applications have been mainly limited to semi-conductor and thin film technologies (Zinner, 1980), but examination of diffusion profiles is slowly expanding as the capabilities and limitations of the systems become known (e.g., Hofmann et al., 1974; Reed and Wuensch, 1980).

One of the major advantages of ion probe depth profiling is the capability to analyse self-diffusion for elements which do not have radioactive isotopes. An example of this in a non-silicate is oxygen self-diffusion in single crystal Al_2O_3 (Reed and Wuensch, 1980). The analytical equipment consisted of an Ar^+ primary beam without rastering capabilities, and a double dual-focusing mass spectrometer. The entire pit was imaged and edge-of-the-hole effects were minimized by defocusing the beam and correcting the data for a theoretical contribution based on the final hole shape. The calculated diffusivities define a straight line on an Arrhenius plot with an activation energy similar to those derived by gas exchange (Oishi and Kingery, 1960) and by proton activation analysis (Reddy and Cooper, 1976, 1978) (Figure 7-3). However, the ion probe Arrhenius line falls approximately two orders of magnitude below these other works. Reed and Wuensch ascribe this to impurity differences in much the same way as interpreted here for the natural and synthetic diopsides. Proton activation analysis of some of their samples yields

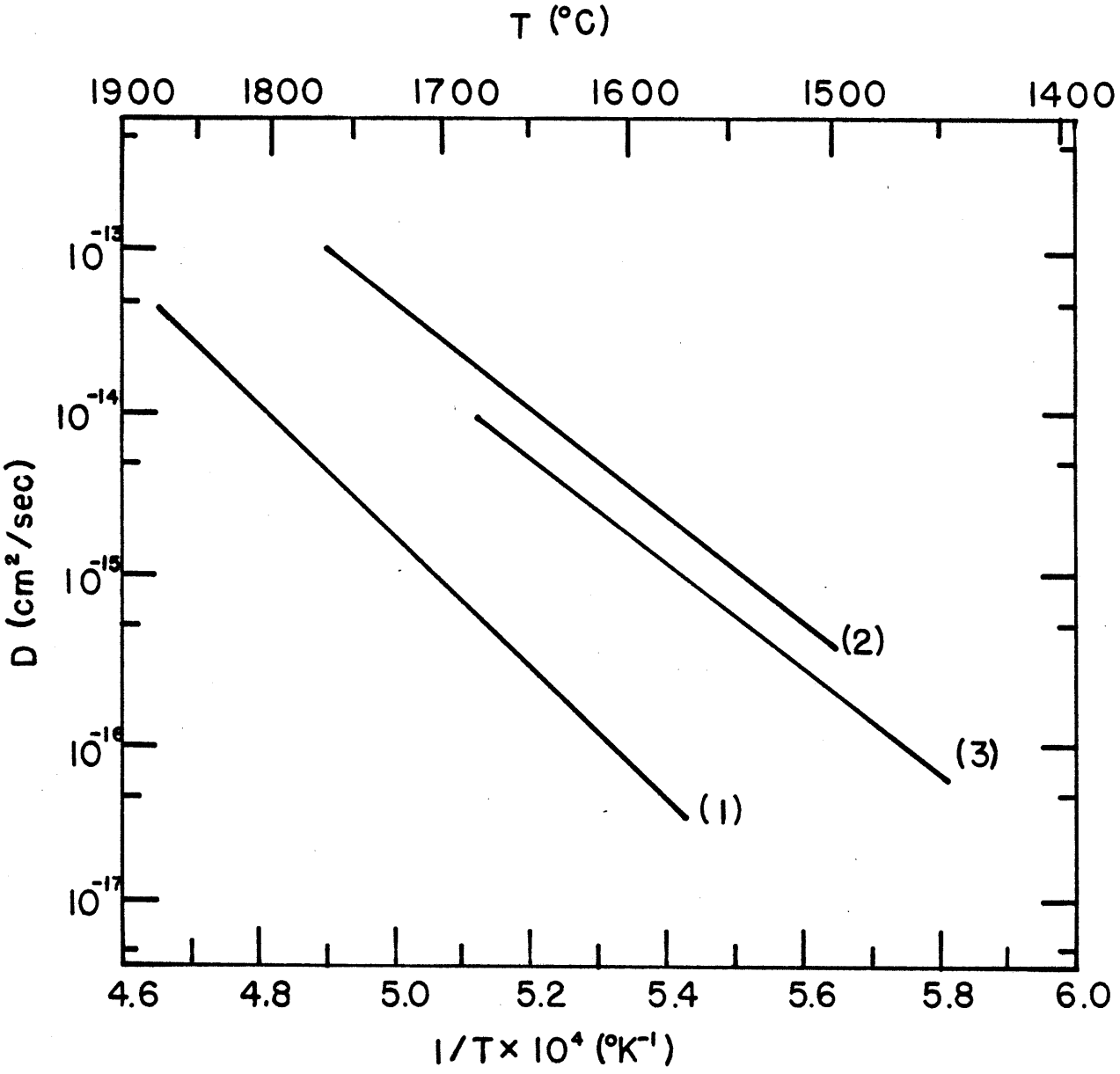

Figure 7-3. Oxygen diffusion in single crystal Al_2O_3, ℓn D vs 1/T.
1. Reed and Wuensch, 1980, ion probe depth profiling.
2. Oishi and Kingery, 1960, bulk isotope exchange
3. Reddy and Cooper, 1976 and 1978, proton activation analysis.

values comparable to the ion probe results. It is evident that even without rastering and a field aperture, it is possible to obtain meaningful diffusion coefficients using data correction procedures. The study also illuminates the danger of comparing experiments in identical phases with different impurity ions and concentrations.

Burns et al. (1979) used a Cameca IMS 300 to examine Ti diffusion in a lithium niobate ($LiNbO_3$) single crystal. The primary ion beam species was $^{32}O_2^+$ and the secondary ions were counted with a scintillation system. They observed high near-surface concentrations of both Li and Ti to apparent depths of 0.2 to 0.3 μm. Beyond this region the Ti profile was best fit by a thin film source model. If the surface values were caused by the formation of a stable Li-Ti-O phase during the anneal as they postulate, Ti diffusion into the crystal should follow a modified constant source model. The fact that the data is well fit by a gaussian in the interior of the sample (0.9 to 5 μm) indicates they may be observing machine effects as well as the diffusion profile.

Other examples of diffusion studies in non-silicates using the ion probe can be found in the abstract volumes "Diffusion and Defect Data" (Wohlbier, 1981). Early studies tended to ignore knock-on and redistribution problems, but, as the sputtering process becomes better understood, they are being addressed analytically and in data reduction.

Most diffusion measurements on silicate glasses and melts which utilized an ion probe have done so in the surface analysis mode. This is mainly because of fast diffusion rates in these phases. Examples are: Li in albite, orthoclase, and obsidian glasses (Jambon and Semet, 1978), Li in albite melt (Lowry et al., 1981), and water in rhyolite glass (Karsten and Delaney, 1980). The ion probe is well suited for the study of tracer or self-diffusion

of lithium, which has only stable isotopes, and of H_2O because of the ability to analyse for hydrogen.

Ion probe depth profiling has been used to study Si self-diffusion in amorphous silica in the range 1110 to 1410°C (Brebec et al., 1980). A Cameca IMS 300 with rastering capabilities and a primary ion beam of O^- was employed to examine concentrations of implanted ^{30}Si after an anneal. The penetration rate was approximately 0.7 Å/sec and pit depths ranged from 1500 to 3500 Å. The authors described a broadening effect for a an undiffused profile which can be ignored in long concentration curves, but which was treated in the data reduction for short annealing times. The Arrhenius relation derived was $D(cm^2/sec) = 328 \exp(139 \text{ Kcal mole}^{-1}/RT)$.

Laursen and Lanford (1978) used a nuclear resonant reaction depth profiling technique to analyse surface hydration of obsidian. The method utilizes a linear accelerator as does Rutherford backscattering spectroscopy, but the incident particles are ^{15}N. At a very specific energy of the nitrogen ions the reaction $^{15}N + {}^{1}H \rightarrow {}^{12}C + {}^{4}He + \gamma$ occurs. Profiles of hydrogen are obtained by counting the gamma radiation while increasing the beam energy so that the reaction takes place at successively deeper levels in the sample. Short profiles (<5 μm) were necessary because the temperature of interest was room temperature. The process was developed as a means of dating archeological artifacts by examining the hydration rind on worked pieces such as arrowheads. Peak broadening effects are similar to RBS, with the controlling factors being the energy distributions of the reactions and the beam. Profile lengths are similar to ion probe depth profiles and a comparison of the two techniques would be useful for analysing machine effects in both for H.

Fast diffusion rates, such as in silicate melts, are best studied by the surface analysis mode on transects perpendicular to the diffusion face.

Otherwise, unreasonably short runs would be needed to stay within the range of depth profiling, which would introduce large effects from heat up and cool down times.

Data derived by the ion probe for crystalline silicates are considerably more abundant than those for liquids. This is directly attributable to the shorter profiles formed by experiments of reasonable duration and temperature. The need for precise measurements of these short profile and the previously mentioned advantage of using stable tracers have attracted geochemists to the depth profiling technique.

The first ion probe study of diffusion in a silicate was that of Hofmann et al. (1974) in which they examined K transport in biotite. A compositional cross section was produced on a single grain by sputtering a series of holes from edge to center. One analysis with a rastered beam was used to evaluate near-surface concentrations. Depths of the pits were estimated from the penetration rate of quartz, and the calculated D for the c direction (normal to the sample surface) was 1×10^{-17} cm^2/sec at 650°C and 2 Kbar. This is two orders of magnitude less than the value derived by bulk isotopic exchange under the same experimental conditions (Hofmann and Giletti, 1970). The difference is partially accounted for by faster diffusion (2 to 4X) in the ab plane, which would raise the bulk number. Also, if the assumed penetration rate is too low, the proper rate would raise the ion probe D closer to the bulk determination. Taking the assumed uncertainty of the probe measurement (a factor of 10) into account results in fairly good agreement between the two dissimilar techniques.

Recently, the ion probe has been used to examine the transport of major elements in olivines, feldspars, and quartz. Three recent studies have looked at ^{18}O diffusion in forsterite. Giletti et al. (1979) reported a single

point at 1100°C and 4 Kbar with the tracer source being an aqueous fluid surrounding the sample. Ion probe and proton activation analysis ($^{18}O(p,\alpha)^{15}N$) data were obtained by Jaoul et al. (1980) from two types of runs. The first used a layer of ^{18}O enriched MgO or Mg_2SiO_4, deposited on the surface by an ion beam, as the source. The second exposed the crystal to an atmosphere into which $H_2{}^{18}O$ was introduced at various p_{O_2}. Data from their two analytical methods, different oxygen fugacities, and both starting configurations gave the same results within the uncertainties. Values of D_o and ΔH_a from Hallwig et al. (1981) are presented in Freer (1981) without detailed description of the experimental procedure. The results of the three different research groups are compared graphically in Figure (7-4). Reddy et al. (1980) derived the diffusion parameters for O in Fo using a dry ^{18}O enriched atmosphere, and the proton activation analysis technique. The results are nearly identical to those of Jaoul et al. in the measured range. The data of Hallwig et al. fall about a factor of ten lower than these two and Giletti et al.'s point is two orders of magnitude higher than the extension of their Arrhenius line. The one atmosphere gas-exchange experiments of Jaoul et al. did not contain water at run temperature, due to dissociation. Thus, the 4 Kbar point is the only wet determination and the difference may be caused by the presence of water. There is good agreement among the one atmosphere studies and between the two techniques.

Cation diffusion in olivine has also been studied by a number of authors. Morioka (1980), using surface analysis, and Hallwig et al. report very similar numbers for Mg self-diffusion which are about two orders of magnitude less than Fe-Mg interdiffusion data from Misener (1974) and Buening and Buseck (1973). Values for Ni, Co, and Mn diffusion extrapolated from Mg interdiffusion data to pure Fo (Morioka, 1981) vary from good agreement with the ion probe

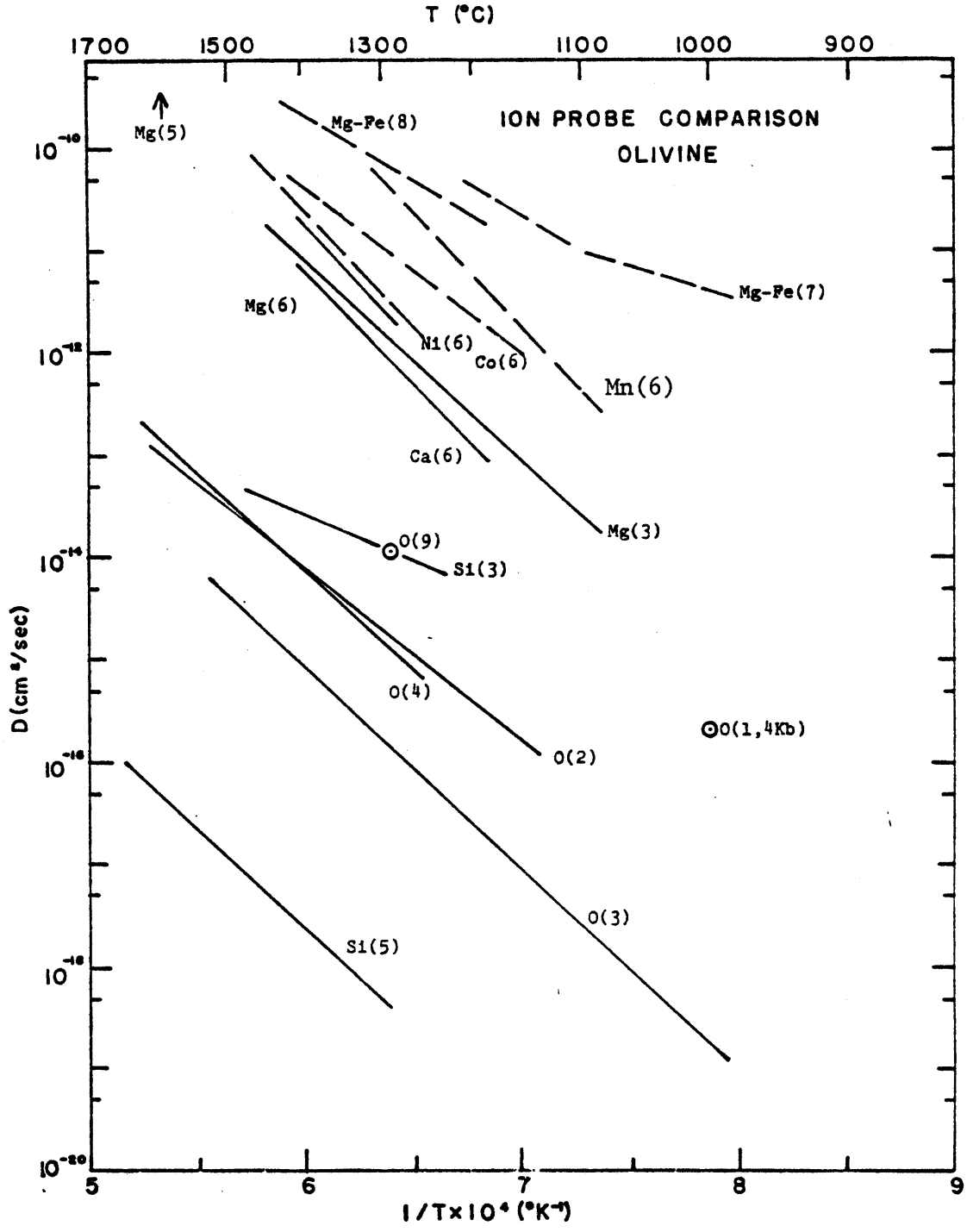
T (°C)
1700
1500
1300
1100
1000
900
ION PROBE COMPARISON
OLIVINE
Mg(5)
Mg-Fe(8)
Mg-Fe(7)
Mg(6)
Ni(6)
Co(6)
Mn(6)
Ca(6)
Mg(3)
O(9)
Si(3)
O(4)
O(2)
⊙O(1,4Kb)
O(3)
Si(5)
D(cm²/sec)
10⁻¹⁰
10⁻¹²
10⁻¹⁴
10⁻¹⁶
10⁻¹⁸
10⁻²⁰
5
6
7
8
9
1/T×10⁴ (°K⁻¹)

Figure 7-4. Olivine data compilation, ion probe and comparable studies, ℓn D vs 1/T. All data are for forsterite except where noted. Solid lines are ion probe determinations and dashed lines are from other methods.

1. Giletti, et al., 1979, O at 4 Kbar by ion probe.
2. Jaoul, et al., 1980, O by ion probe
3. Hallwig, et al., 1981, O by ion probe (Freer, 1981).
4. Reddy, et al., 1980, O by proton activation.
5. Poullemac, et al., 1981, Mg and Si by ion probe.
6. Morioka, 1981, Ca and Mg by ion probe; Ni-, Mn-, and Co-Mg interdiffusion by electron microprobe.
7. Buening and Buseck, 1973, Mg-Fe interdiffusion in olivine (10 wt.% FeO) at $p_{O_2} = 10^{-12}$ atm by electron microprobe.
8. Misener, 1974, Mg-Fe interdiffusion in Fo_{80} at 1 atm by electron microprobe.
9. Muehlenbachs and Kushiro, 1975, O by bulk isotope exchange.

results (Ni) to more than a factor of ten greater (Mn). Calcium was also examined by Morioka with results approximately the same as Mg. The disagreement between the tracer and self-diffusion determinations may be from difference in materials or from the nature of D^* and $\tilde{D}$. The two are related by:

$$\tilde{D} = (D_1^* N_2 + D_2^* N_1)\left(1 + \frac{d\ell n \gamma_1'}{d\ell n N_1}\right) \qquad (7\text{-}1)$$

where N_i is the mole fraction and γ_i' is the activity coefficient of component i. Morioka used synthetic Fo grown by the Czochralski method while the others used natural samples.

Si self-diffusion has been measured by two groups (Hallwig, et al.; Poullemec, et al., 1981) with totally different results. Some of these data have been plotted on a compensation graph by Hart (1981) and the more recent numbers are added to this plot in figure (7-5). The recalculated Co point (Morioka, 1981) and Hallwig, et al.'s Mg value fall very close to the compensation trend. Both of the Si determinations are well below the line and the oxygen number of Hallwig, et al. plots in the vicinity of the other O values. This does not allow a decision as to which, if either, is the more accurate Si equation, but it does show that the compensation trend is limited to cations in the M site. Perhaps analysis of D's for species expected to occupy the tetrahedral site will yield a separate compensation line.

Potassium and oxygen have been analysed in feldspars by ion probe and other methods. Giletti, et al. (1978) determined Arrhenius relations for ^{18}O by depth profiling in adularia (Or_{98}), albite ($Ab_{97,99}$), and anorthite (An_{96}) at 1 Kbar and 350 to 800°C with a Cameca IMS-300. Although the activation energies and D_o's differ somewhat with the bulk exchange method, there is good agreement in the study temperature range (figure (7-6)). Yund and Anderson (1978) showed that an increase of nearly 4 Kbar in fluid pressure

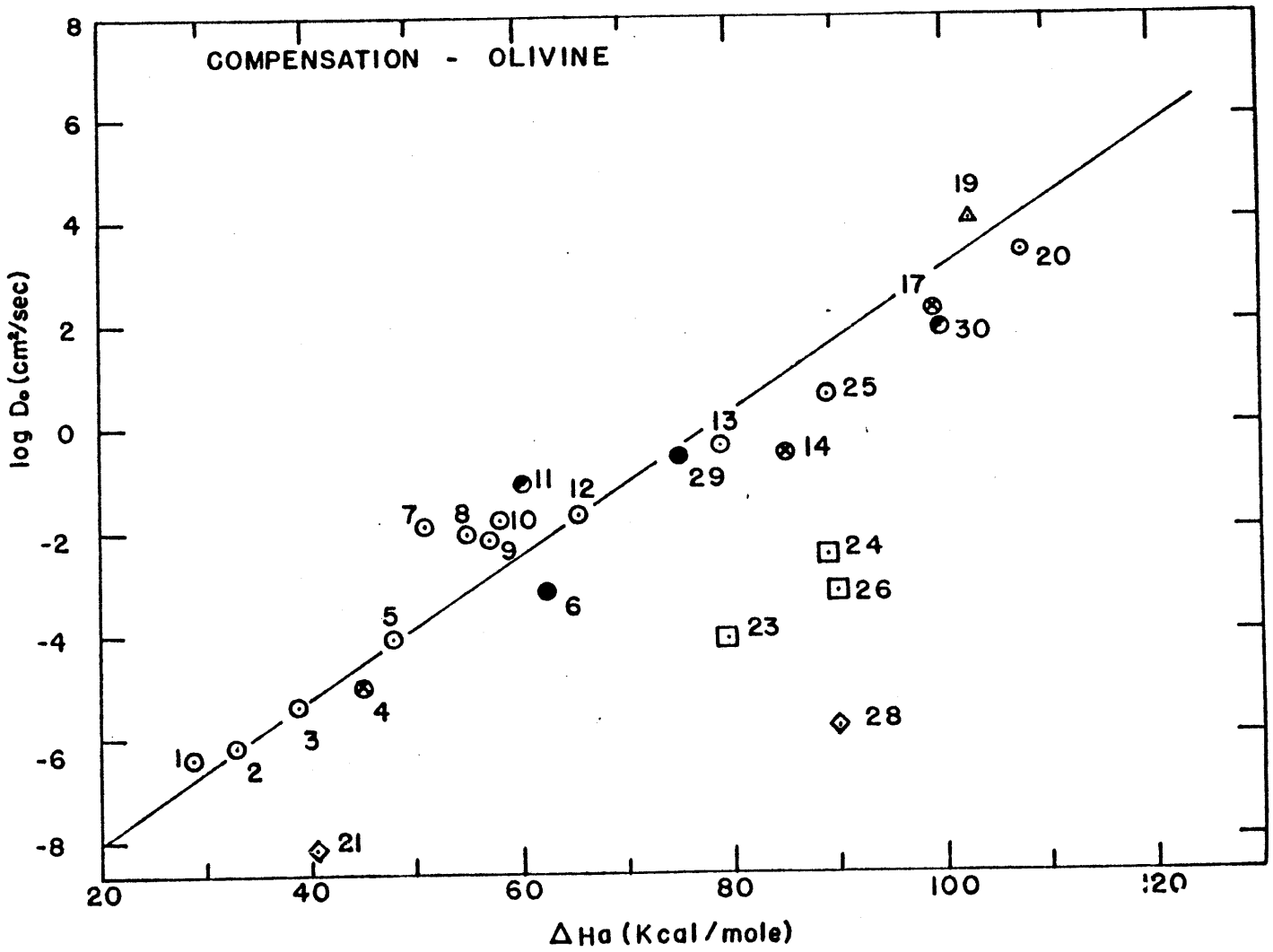
COMPENSATION - OLIVINE
log Do (cm²/sec)
ΔHa (Kcal/mole)
8
6
4
2
0
-2
-4
-6
-8
20
40
60
80
100
120
1
2
3
4
5
6
7
8
9
10
11
12
13
14
17
19
20
21
23
24
25
26
28
29
30

Figure 7-5. Compensation plot for olivine (after Hart, 1981), log D_0 vs ΔH_a. Numbers refer to Hart's Table 2 except 25-30. Line is Hart's "eyeball" fit for compensation trend for olivine.

25. Morioka, 1981, Mg by ion probe.
26. Hallwig, et al., 1981, O by ion probe (Freer, 1981).
27. " " " Si by ion probe (Freer, 1981).
28. Poullemac, et al., 1981, Si by ion probe.
29. Morioka, 1981, Co by electron probe (data from Morioka (1980) refit by a single line, replacing points 15, 16, 21, and 22).
30. Morioka, 1981, Ca by ion probe (replaces point #18).

Fe-Mg, Mg - open circles, Co-Mg - filled circles, Ni-Mg - crossed circles, Mn-Mg - triangles, Ca - half circles, O - squares, Si - diamonds.

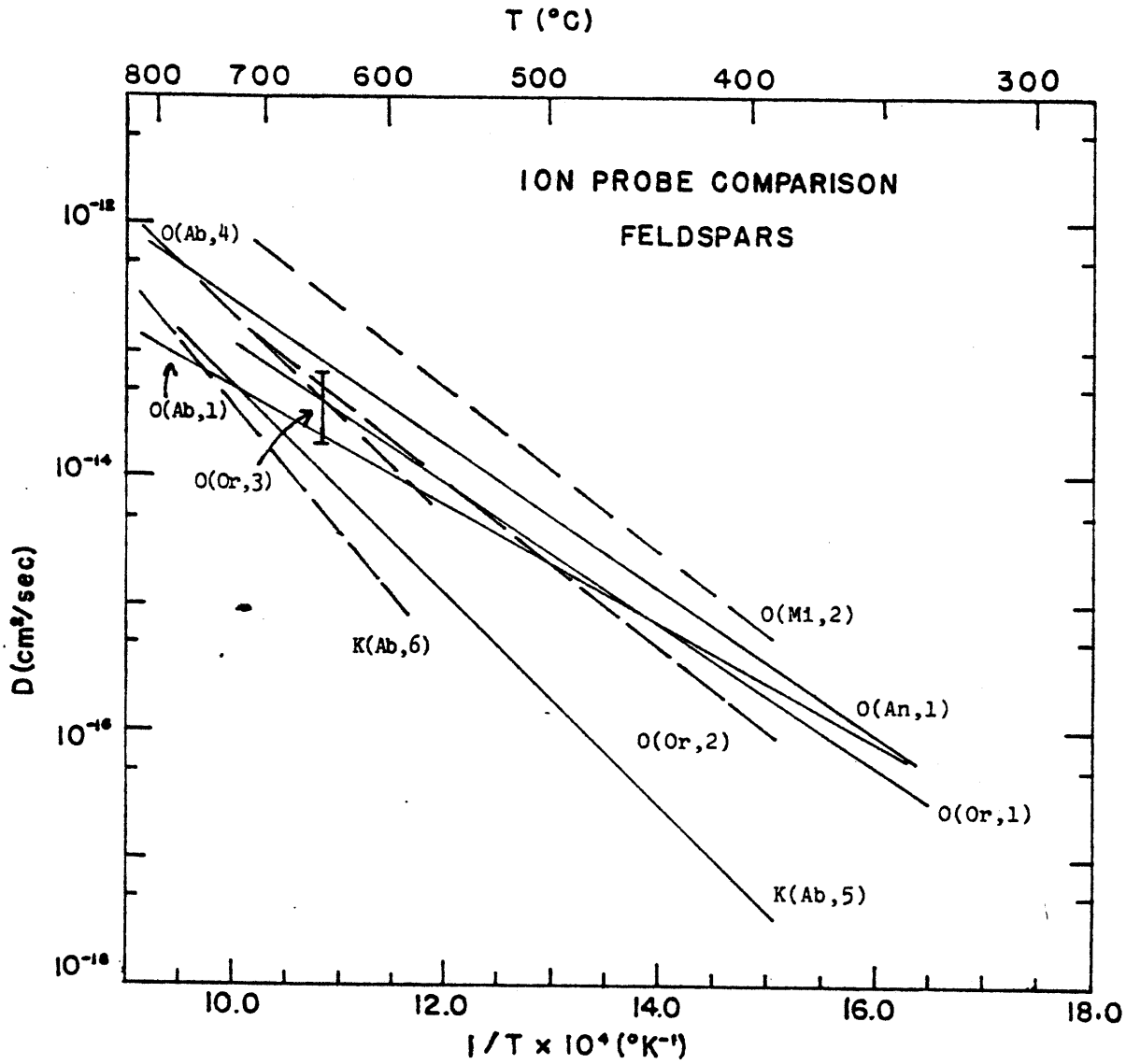

Figure 7-6. Feldspar data compilation, ion probe and comparable studies, ℓn D vs 1/T. Solid lines are for ion probe determinations and dashed lines are for other methods.

1. Giletti, et al., 1978, O in albite, anorthite, and orthoclase by ion probe.
2. Yund and Anderson, 1974, O in orthoclase and microcline by bulk isotope exchange.
3. Yund and Anderson, 1978, O in orthoclase to 4 Kbar by bulk isotope exchange.
4. Anderson and Kasper, 1975, O in albite by bulk isotope exchange.
5. Giletti, et al., 1974, K in albite by ion probe.
6. Kasper, 1974, K in albite by bulk isotope exchange.

increases D by about a factor of 4 at 650°C. Anderson and Kasper (1975) reported an experiment with run conditions similar to those of the ion probe study. The results agree very well with the rest of their data, which were derived from experimental procedures similar to Yund and Anderson. The different experimental procedures and variations in pressure do not significantly change the diffusion coefficient at a given temperature. Therefore, the agreement between the ion probe study and the bulk exchange studies can be assumed to be real, and not the result of off-setting experimental and analytical differences.

Comparison of K diffusion measurements on the same albite shows good agreement within the study temperature range (Giletti, et al., 1974; Kasper, 1974). Hart (1981) showed that all the feldspar data discussed here, cation and anion, fall on a single compensation trend.

Results for ^{18}O transport in quartz are conflicting both within a single method and among various techniques. Data from Dennis (1981) reported by Freer (1981) differ from the diffusivity at 600°C by Gilletti, Semet, and Yund (1976) by 12 orders of magnitude. The experimental and analytical modes appear to be the same: isotope exchange with fluid followed by ion probe depth profiling, although details of Dennis' work are not yet available. Values for proton activation at 667°C are intermediate to these two studies (Choudhury, et al., 1965) and extrapolation of Haul and Dumbgen's (1962) Arrhenius line for bulk exchange to 600°C yields an even lower value than that of Dennis. Clearly, considerable work is needed to determine which, if any, of these are the correct values. Two points for Si self-diffusion are reported by Giletti, Yund, and Semet (1976) and are plotted in figure (7-7).

Ion microprobes are proving to be useful tools to study diffusion, especially at temperatures and with species where profiles generated by reasonable length anneals are short (<5μm). Other depth profiling schemes

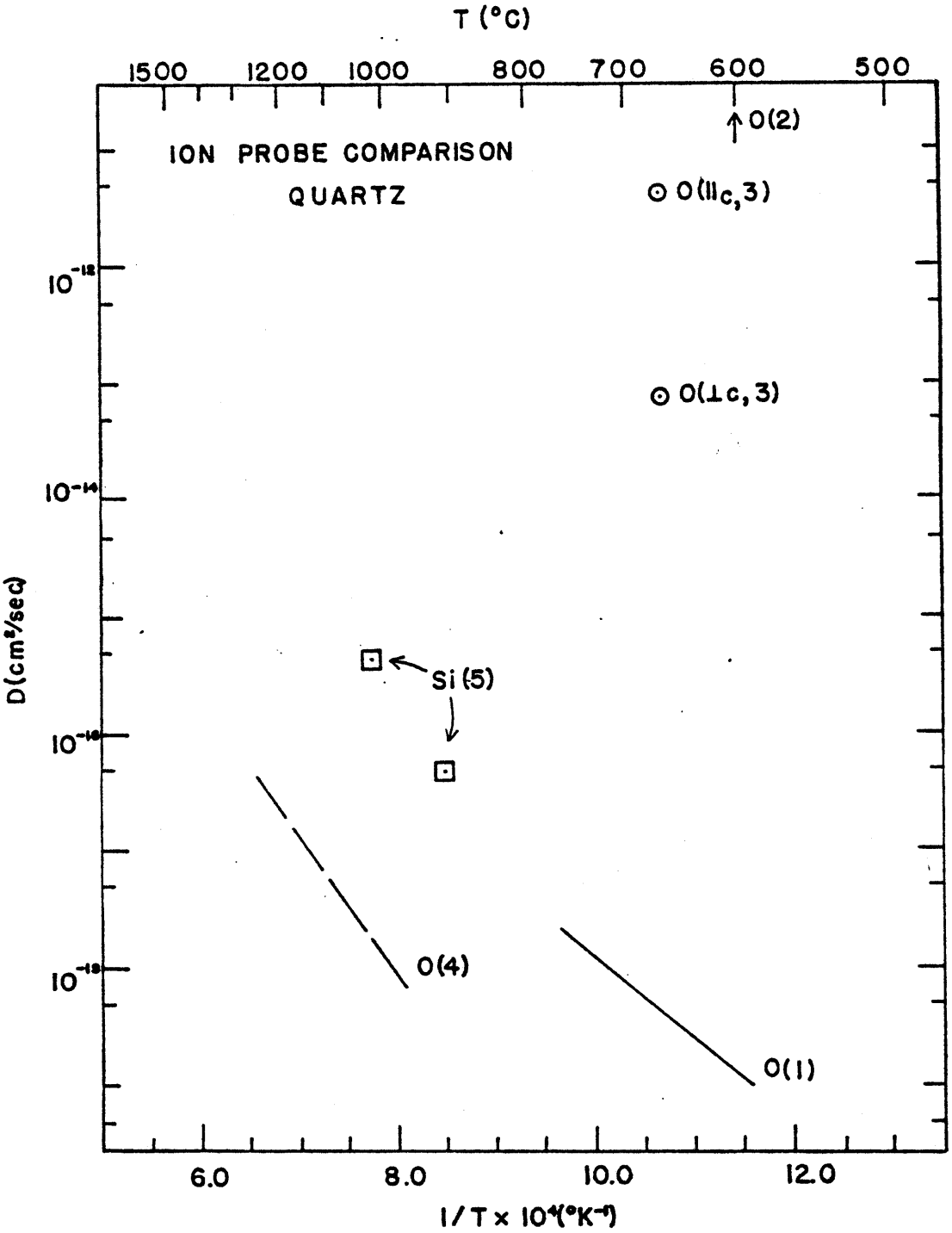

Figure 7-7. Quartz data compilation, ion probe and comparable studies, ℓn D vs 1/T. Solid line is for ion probe determination and dashed line is for bulk isotope exchange experiments.

1. Dennis, 1981, O by ion probe (Freer, 1981).
2. Giletti, Semet, and Yund, 1976, O by ion probe.
3. Choudhury, et al., 1965, O // to and ⊥ to the c direction by bulk isotope exchange.
4. Haul and Dumbgen, 1962, O by bulk isotope exchange.
5. Giletti, Yund, and Semet, 1976, Si by ion probe.

like RBS, proton activation, and nuclear resonant reactions share this advantage, and the combination of all of these methods will greatly enhance the knowledge of solid state transport properties in the full range of geologically interesting temperatures and pressures. This in turn will further the understanding of kinetic mechanisms and chemical structures for these materials.

Directional analysis

Diffusion in silicates has been studied as a function of crystallographic direction by several authors. Buening and Buseck (1973) and Misener (1974) reported that the c direction was the fastest and the b the slowest for Mg-Fe interdiffusion in olivine. Clark and Long (1971) showed similar results for Ni chemical diffusion in olivine, while Reddy, et al. (1980) list b as the fastest direction for oxygen. They caution that the oxygen result may be an effect of impurity levels in samples cut from different crystals. Activation energies and D_o's were estimated for the three directions from Misener's Figure 11, and a good compensation line was formed (figure 7-8) with a D^{cr} of $2 \times 10^{-7} cm^2/sec$ and T^{cr} of 2541°C, well above the melting point. Estimates of ΔH_a and D_o for Ni in the a and b directions were made from Clark and Long's Figure 9 and their reported values of D at 1149°C. These were combined with the reported activation energy and frequency factor for the c axis to give a reasonable compensation trend with the crossover point at 1591°C and 5.3×10^{-11} cm^2/sec, much lower than the results for Mg-Fe interdiffusion. A compensation relation could not be derived from Buening and Buseck's data at $p_{O_2} = 10^{-12}$ and 10% FeO. The ΔH_a's and D_o's are also plotted in figure (7-8). Other studies do not give enough information to attempt a compensation calculation, further testing whether directional coupling is real or an artifact of the data. The studies in olivine give some satisfaction on this point.

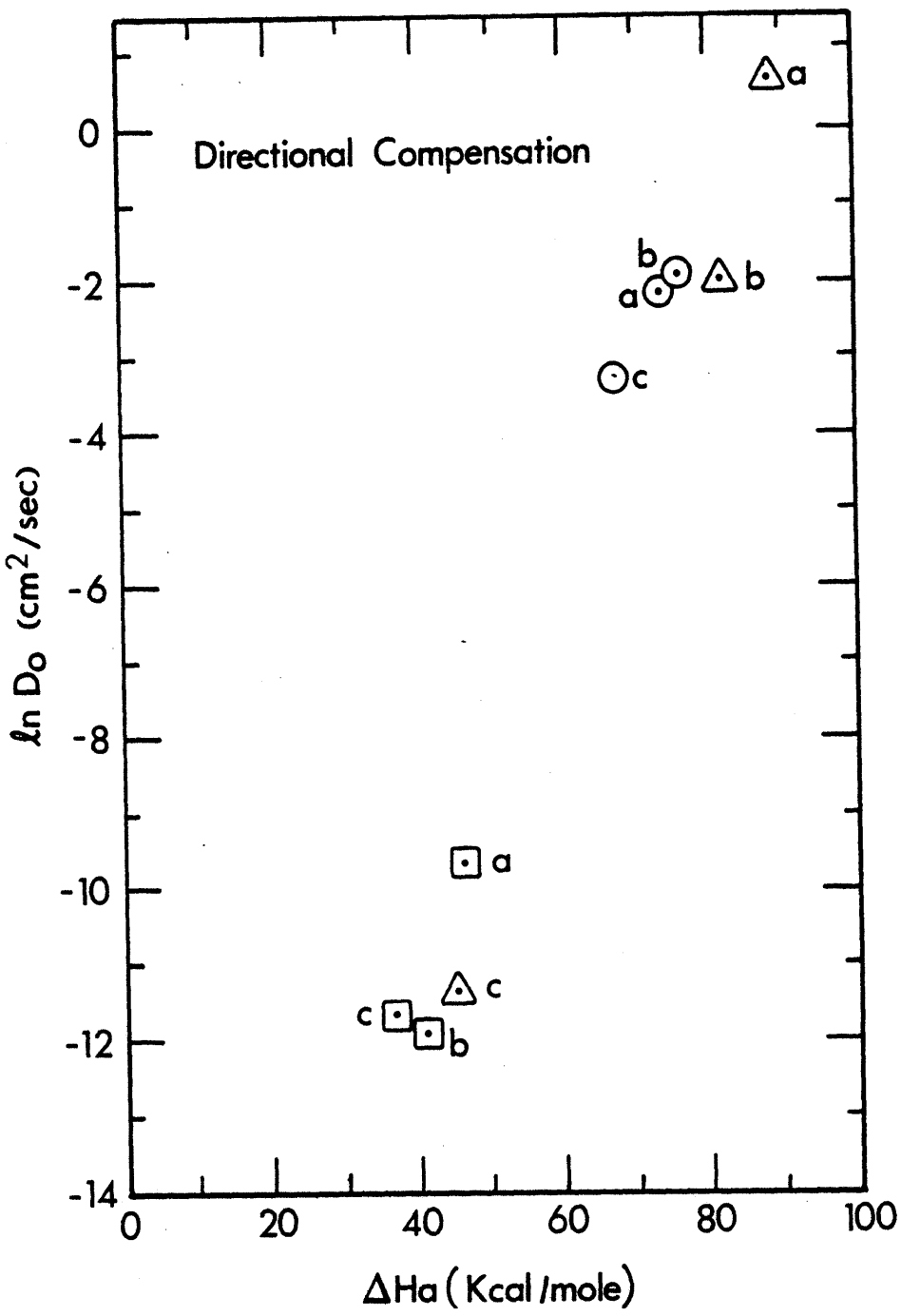

Figure 7-8. Compensation plot for crystallographic directions, $\ell n\ D_0$ vs ΔH_a. Crystal axes are listed next to each point. Misener, 1974, (circles) Fe-Mg interdiffusion in olivine, T^{cr} = 2541°C and $D^{cr} = 2 \times 10^{-7} cm^2/sec$; Buening and Buseck, 1973, (squares) Fe-Mg interdiffusion in olivine; Clark and Long, 1971, (triangles) Ni in olivine, T^{cr} = 1591°C and $D^{cr} = 5.3 \times 10^{-11} cm^2/sec$.

Alkali earth and REE diffusion data

Figure (7-9) is a compilation of published diffusion Arrhenius lines for Ca, Ba, Sr, and REE in two categories; crystalline silicates (excluding pyroxenes) and silicate liquids and glasses. The numbers are drawn from original works wherever possible. Those taken from Freer (1981) are so noted in the figure captions. There do not appear to be correlations in the data with respect to the diffusing species. Rather, data for each phase appear to correlate when more cations are included in the summary. Impurity control of the diffusion process would explain the general grouping and also the scatter within each group. Comparison of the transport rates for different species in a particular mineral must take into account differences in composition. Relative transport rate trends may be evident, but accurate ordering of the diffusion parameters for different ions requires that the experiments use the same starting materials. Compensation plots will normally allow identification of extraordinary samples since their points generally lie off the linear trend. Figure (7-10) shows such a graph for synthetic diopside with the natural RT point included.

Data from Lindner (1955) were obtained from multi-crystalline aggregates by radiotracer and bulk absorption techniques. Some of the gradients were analysed by particle track mapping. Misra and Venkatasubramanian (1977) used a radiotracer and sectioning technique on single crystal samples, counting residual activity. The only ion probe determination listed here is that of Morioka (1981) for calcium in pure Fo.

Pyroxene data comparison

Diffusion in pyroxenes has been measured by three basic methods; tracer, synthetic couples, and natural couples including coarsening or homogenization of exsolution lamellae. For most tracer experiments in natural pyroxenes a general trend is evident (figure 7-11)) when pyroxenoid data is included.

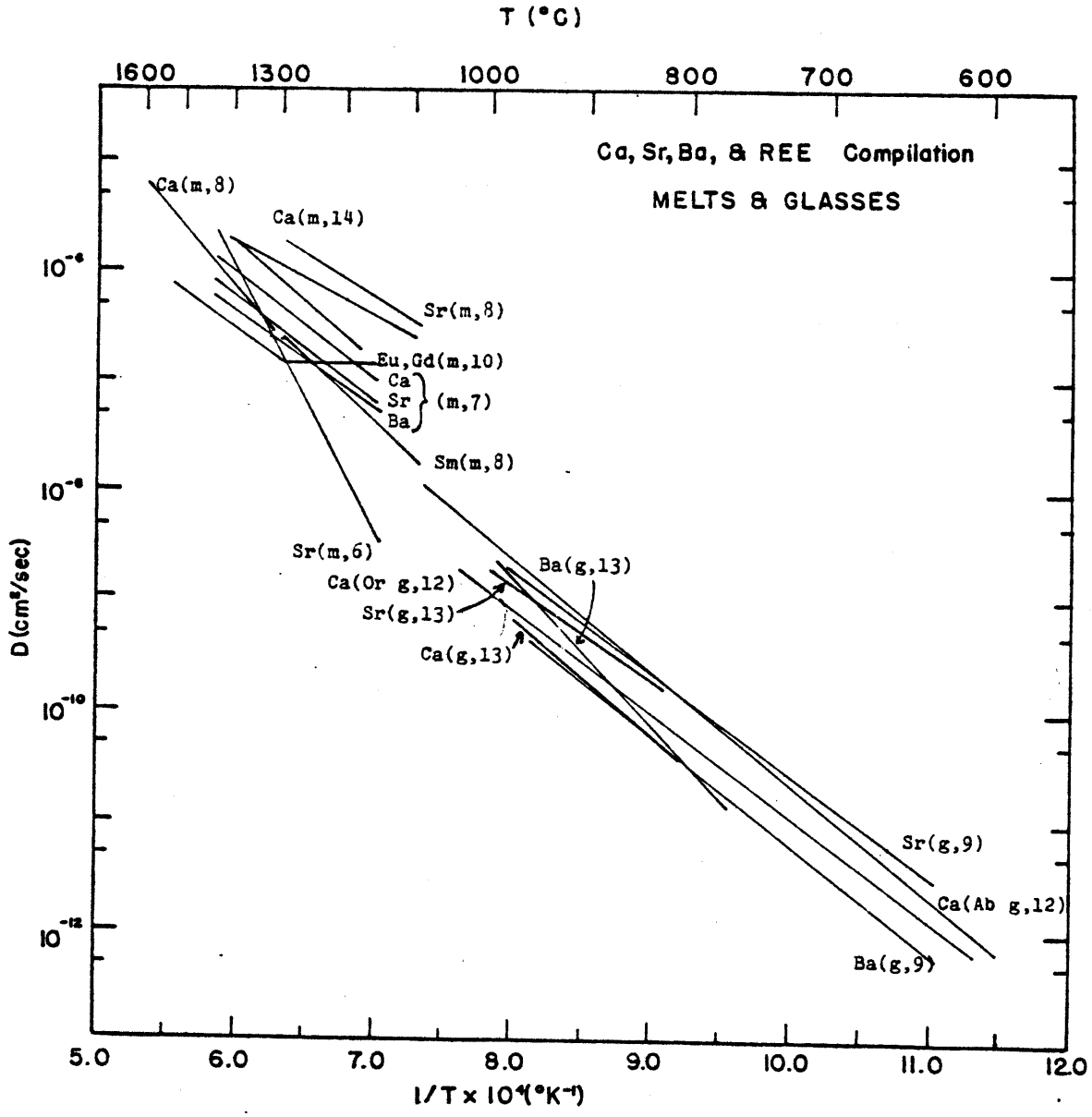
T (°C)
1600
1300
1000
800
700
600
Ca, Sr, Ba, & REE Compilation
MELTS & GLASSES
Ca(m,8)
Ca(m,14)
Sr(m,8)
Eu,Gd(m,10)
Ca
Sr
Ba
(m,7)
Sm(m,8)
Sr(m,6)
Ca(Or g,12)
Sr(g,13)
Ca(g,13)
Ba(g,13)
Sr(g,9)
Ca(Ab g,12)
Ba(g,9)
D(cm²/sec)
10⁻⁶
10⁻⁸
10⁻¹⁰
10⁻¹²
5.0
6.0
7.0
8.0
9.0
10.0
11.0
12.0
1/T x 10⁴(°K⁻¹)

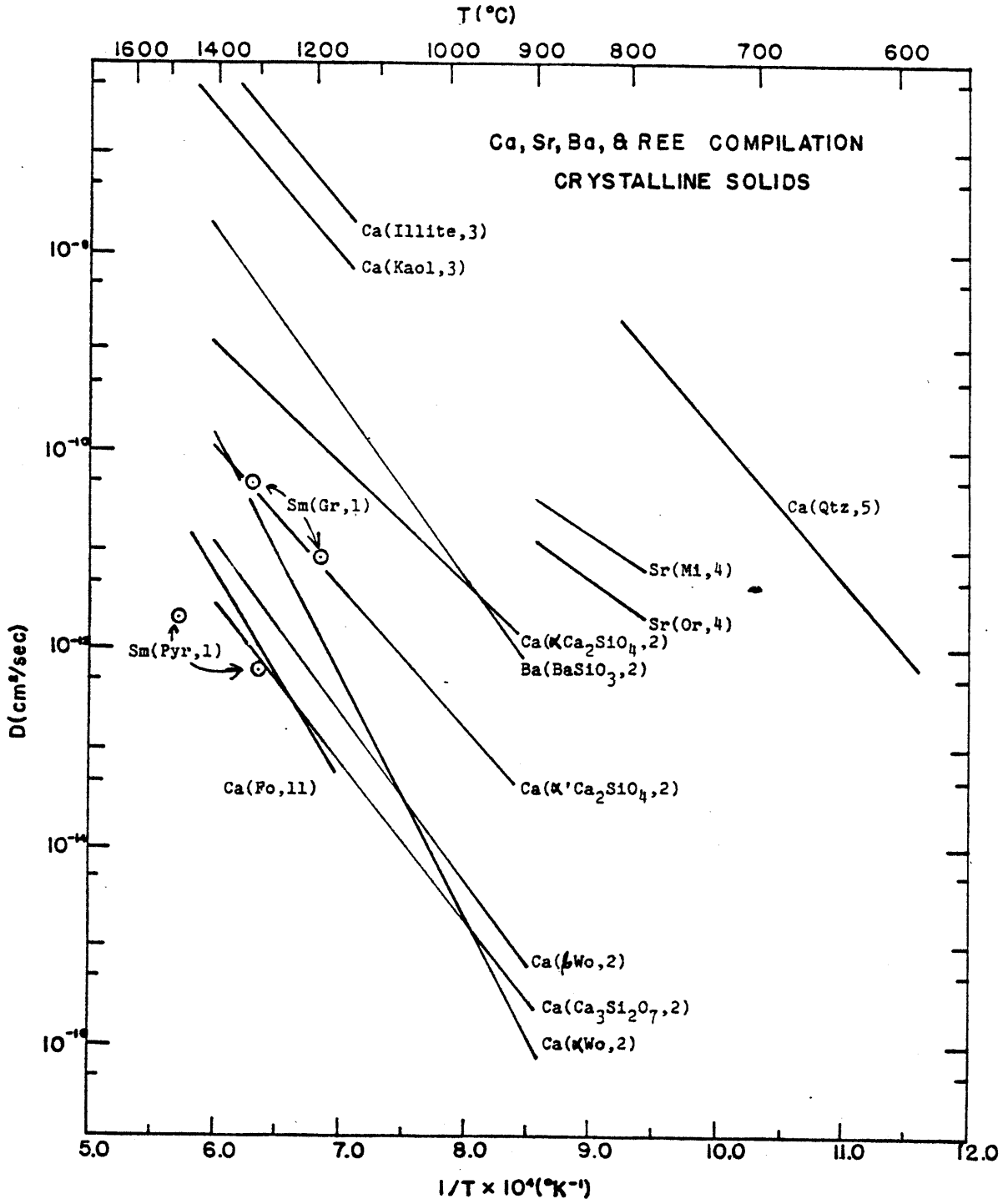
T(°C)
1600 1400 1200 1000 900 800 700 600
Ca, Sr, Ba, & REE COMPILATION
CRYSTALLINE SOLIDS
Ca(Illite,3)
Ca(Kaol,3)
Ca(Qtz,5)
Sm(Gr,1)
Sr(Mi,4)
Sr(Or,4)
Sm(Pyr,1)
Ca(α'Ca2SiO4,2)
Ba(BaSiO3,2)
Ca(Fo,11)
Ca(α'Ca2SiO4,2)
Ca(βWo,2)
Ca(Ca3Si2O7,2)
Ca(αWo,2)
D(cm²/sec)
10⁻⁸
10⁻¹⁰
10⁻¹²
10⁻¹⁴
10⁻¹⁶
5.0 6.0 7.0 8.0 9.0 10.0 11.0 12.0
1/T × 10⁴(°K⁻¹)

Figure 7-9. Alkali earth and rare earth elements in silicates, ℓn D vs 1/T. Pyroxenes are listed separately.
(a) Melts and glasses:

6. Hofmann, 1974, Sr in basalt melt.
7. Hofmann and Magaritz, 1977, Ca, Sr, and Ba in basalt melt.
8. Watson and Bender, 1980, Ca, Sr, and Sm in sodium-calcium-aluminosilicate melt at 6 and 18 Kbar.
9. Magaritz and Hofmann, 1978a, Ba and Sr in obsidian glass.
10. " " " , 1978b, Eu and Gd in basalt melt.
12. Jambon and Delbove, 1977, Ca in albite and orthoclass glasses (Freer, 1981).
13. Jambon and Carron, 1978, Ca, Sr, and Ba in basalt glass (Freer, 1981).
14. Watson ,1981, Ca in sodium-calcium-aluminosilicate melt to 30 Kbar.

(b) Crystalline solids:

1. Harrison and Wood, 1980, Sm in pyrope and grossular at 30 Kbar.
2. Lindner, 1955, Ca in αCa_2SiO_4, $\alpha' Ca_2SiO_4$, Ca_3SiO_7, α-wollastonite, and β-wollastonite; Ba in $BaSiO_3$.
3. Talaber, 1968, Ca in illite and kaolin (Freer, 1981).
4. Misra and Venkatasubramanian, 1977, Sr in orthoclase and microcline.
5. Frischet, 1970, Ca in quartz (Freer, 1981).
11. Morioka, 1981, Ca in forsterite.

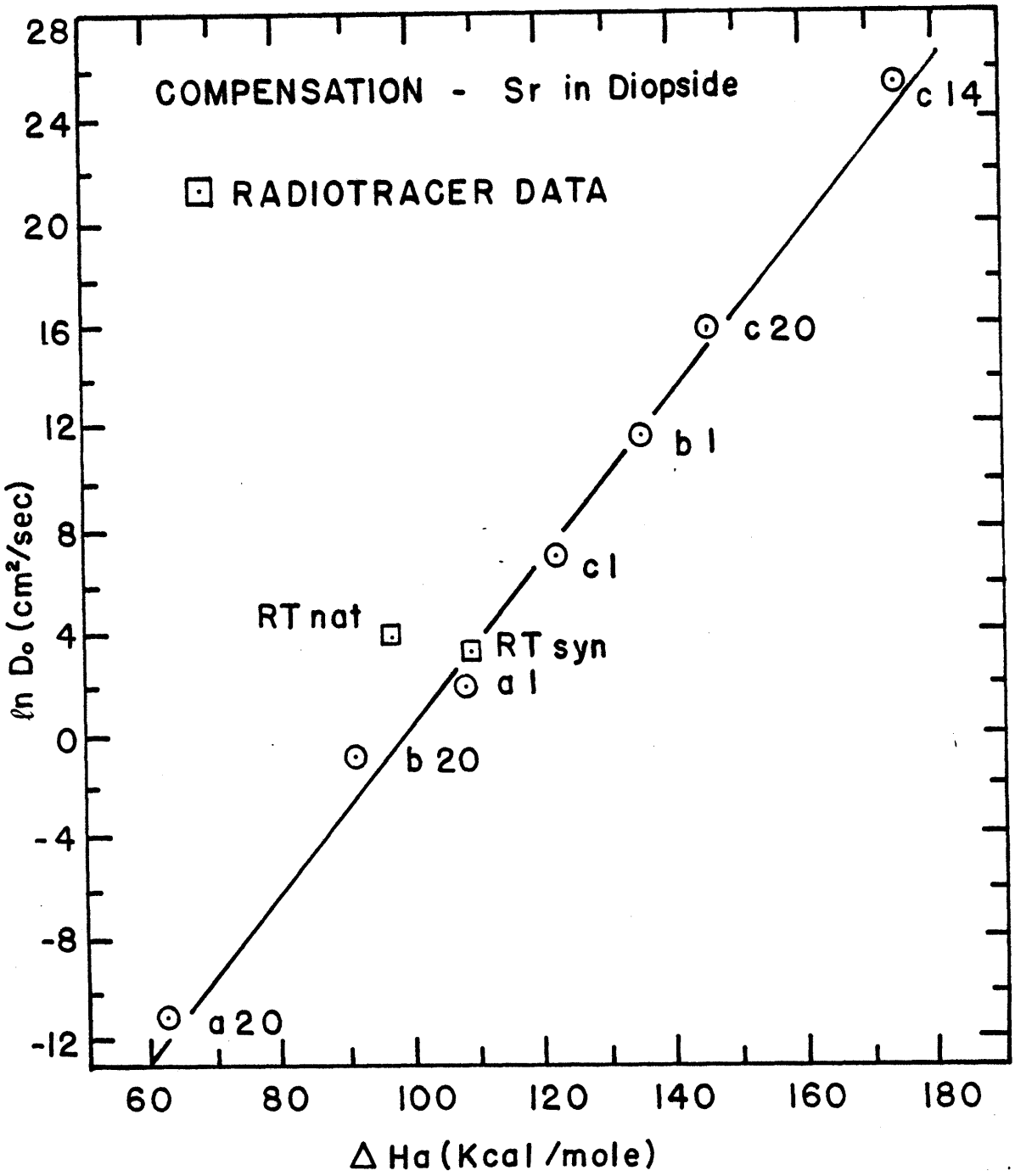

Figure 7-10. Compensation plot for ion probe determinations of Sr in synthetic diopside with radiotracer and sectioning data added, $\ell n\ D_0$ vs ΔH_a. Crystallographic direction and pressure are given with each point for the ion probe data (circles). Radiotracer and sectioning data (squares) show that the value for the natural samples does not fall on the line defined by the ion probe determinations.

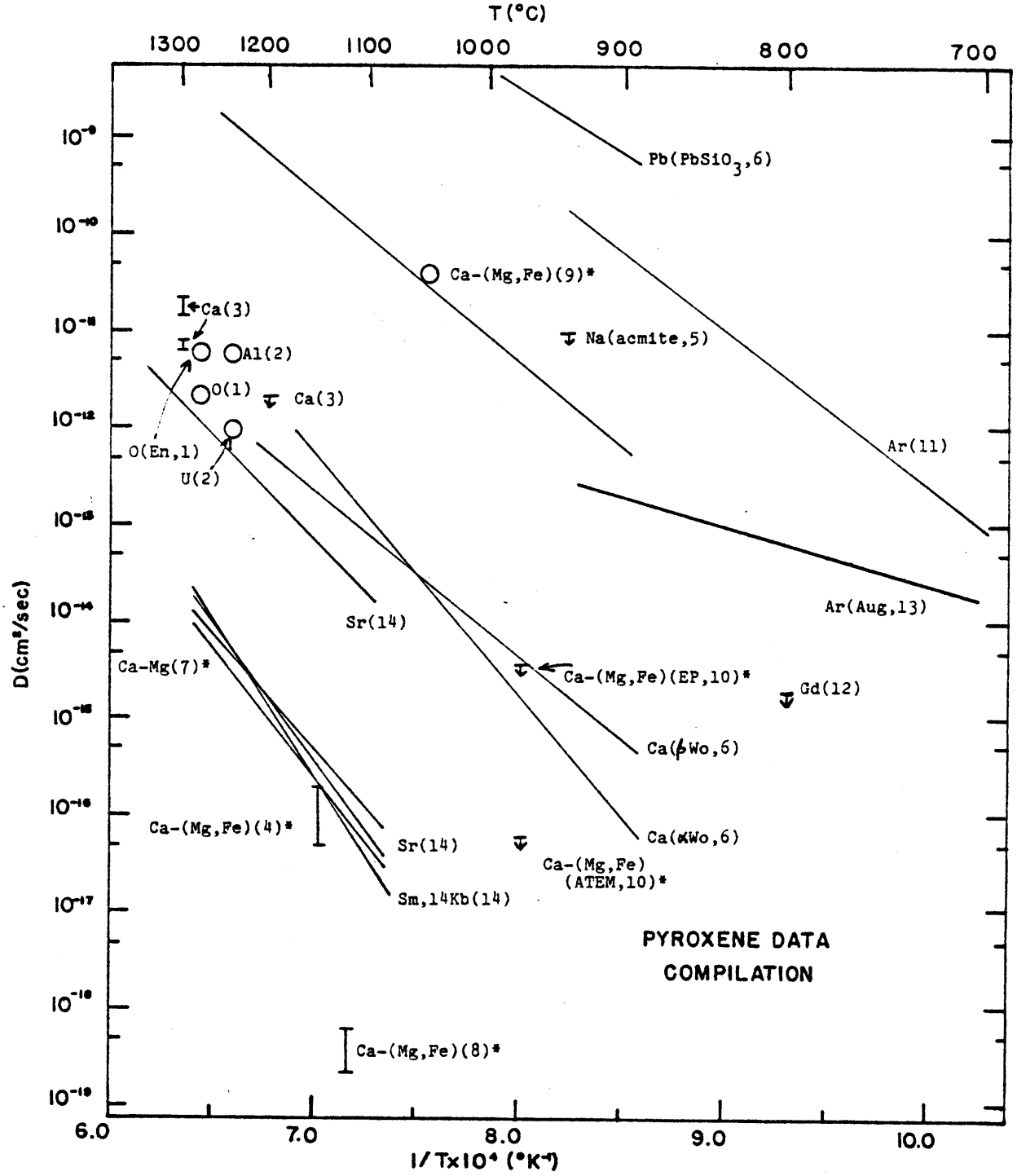
T(°C)
1300
1200
1100
1000
900
800
700
D(cm²/sec)
10⁻⁹
10⁻¹⁰
10⁻¹¹
10⁻¹²
10⁻¹³
10⁻¹⁴
10⁻¹⁵
10⁻¹⁶
10⁻¹⁷
10⁻¹⁸
10⁻¹⁹
Pb(PbSiO3,6)
Ca-(Mg,Fe)(9)*
Ca(3)
Al(2)
O(1)
Ca(3)
Na(acmite,5)
Ar(11)
O(En,1)
U(2)
Sr(14)
Ar(Aug,13)
Ca-Mg(7)*
Ca-(Mg,Fe)(EP,10)*
Gd(12)
Ca(βWo,6)
Ca-(Mg,Fe)(4)*
Sr(14)
Ca(αWo,6)
Ca-(Mg,Fe)
(ATEM,10)*
Sm,14Kb(14)
PYROXENE DATA
COMPILATION
Ca-(Mg,Fe)(8)*
6.0
7.0
8.0
9.0
10.0
1/Tx10⁴ (°K⁻¹)

Figure 7-11. Diffusion data in pyroxenes and pyroxenoids, ℓn D vs 1/T. Downward pointing arrows indicate maximum possible values defined by analytical limitations. True value may be considerably lower. The phase is listed in parentheses with the reference number if different than diopside. Asterisks (*) indicate attempts to measure D with a natural diffusion couple.

1. Muehlenbachs and Kushiro, 1975, O in diopside and enstatite.
2. Seitz, 1973, Al and U in diopside.
3. McCallister, et al., 1979, Ca in diopside.
4. Brady and McCallister, 1980, Ca-(Mg,Fe) interdiffusion in diopside-pigeonite lamellae.
5. Sippel, 1963, Na in acmite.
6. Lindner, 1955, Ca in α-wollastonite and β-wollastonite, Ba in $BaSiO_3$, and Pb in $PbSiO_3$.
7. Huebner, et al., 1975, Ca-Mg interdiffusion in diopside-pigeonite lamellae.
8. Miyamoto and Takeda, 1979, Ca-(Mg,Fe) interdiffusion estimated from lamellar structure.
9. Sanford and Huebner, 1979, Ca-(Mg,Fe) interdiffusion between pigeonite rim and augite core.
10. Huebner and Nord, 1981, Ca-(Mg,Fe) interdiffusion from lamellar coarsening (EP = electron microprobe, ATEM = analytical transmission electron microscope).
11. Amirkhanoff, et al., 1959, Ar is "pyroxene" (Freer, 1981).
12. Zielinski and Frey, 1974, Gd in diopside.
13. Fechtig, et al., 1960, Ar in augite.
14. this study.

Points indicated by a downward arrow are at maximum values of D defined by the detection limits of the analytical systems. For example, the diffusivity of Na in acmite at 940°C (Sippel, 1963) can be anything less than $10^{-11}cm^2/sec$ because no gradient was observed after the anneal. Three tracer experiments fall into this category: Na in acmite; Gd in diopside (Zielinski and Frey, 1974); and Ca in diopside at 1200°C (McCallister, et al., 1979) and do not really destroy the apparent trend.

Diffusion couples are indicated by asterisks(*) in figure (7-11). With the exception of the Ca-(Mg, Fe) interdiffusion point at 1268°C (Sanford and Huebner, 1979) derived from a pigeonite rim on a lunar augite, all lie below the trend defined by tracer experiments in natural samples. The Ca-(Mg, Fe) limit at 985°C for the electron probe (EP) (Huebner and Nord, 1980) is as high as it is because of machine limitations. Analytical transmission electron microscopy (ATEM) of the same sample has an increased spatial resolution, giving a lower D limit for the same concentration profile. These low values point to some other process besides diffusion controlling the exchange between two pyroxenes (Huebner and Nord, 1980). To use lamellar coarsening or coexisting pyroxene values probably greatly underestimates the volume diffusion equation. Data from this study are also shown in figure (7-11). The radiotracer natural sample line lies about one order of magnitude below McCallister et al.'s Ca values. Their experiments utilized a beta mapping technique which was hampered by poor spatial resolution due to long particle ranges and short diffusion profiles. Their 1200°C point was analytically indistinguishable from the zero time profile. Therefore, calculation of an activation energy can only give a lower limit of 50 Kcal/mole. Provided the calcium data are correct, the difference in transport rate between Ca and Sr is not reason for concern, because correlation between defects and the diffusing tracer can easily cause the trace element diffusion to

decrease. Data for Ca in psuedo-wollastonite and α-$CaSiO_3$ (Lindner, 1955) derived from sintered pellets give activation energies of 78 and 112 Kcal/mole respectively, bracketing the Sr in diopside value. Comparison of Di and the $CaSiO_3$ phases is not fully warranted but similarities between them and the lack of other data in pyroxenes justifies their inclusion here. Wollastonite has a triple tetrahedra repeat structure in its silica chains as opposed to the double repeat pattern of pyroxene (figure (7-12)). The synthetic data fall well below the natural trend and close to the maximum values of the natural diffusion-couple studies. This proximity is judged to be a coincidence, as the materials in question are markedly different in their impurity composition. Further, diffusion-couple data for the synthetic crystals at one atmosphere in this study lie below the lines for the tracer experiments, indicating a surface-reaction control of the observed gradients. The conclusion drawn is that the diffusion coefficients derived for the laboratory-grown diopside are correct for that material but do not represent the rates in natural materials. The data from the radiotracer and sectioning natural samples are more representative of the geologic diffusion rates. This examination illustrates some of the pitfalls of direct comparisons of diffusion studies. Three main sources of differences in measured diffusivities can be outlined. Firstly, samples of the same phase may vary widely in defect concentrations which affect diffusion mechanisms and rates. Secondly, experimental conditions can introduce variables such as water or differential stress which alter the transport process. Finally, the analytical system can change the derived D's or can even measure some other process (e.g. surface adsorption of tracer in a bulk exchange experiment). These factors must be taken into account when comparisons among data sets are made. Internal checks such as multiple experimental techniques and two or more analytical methods, will also aid in deciding the validity of particular diffusion studies.

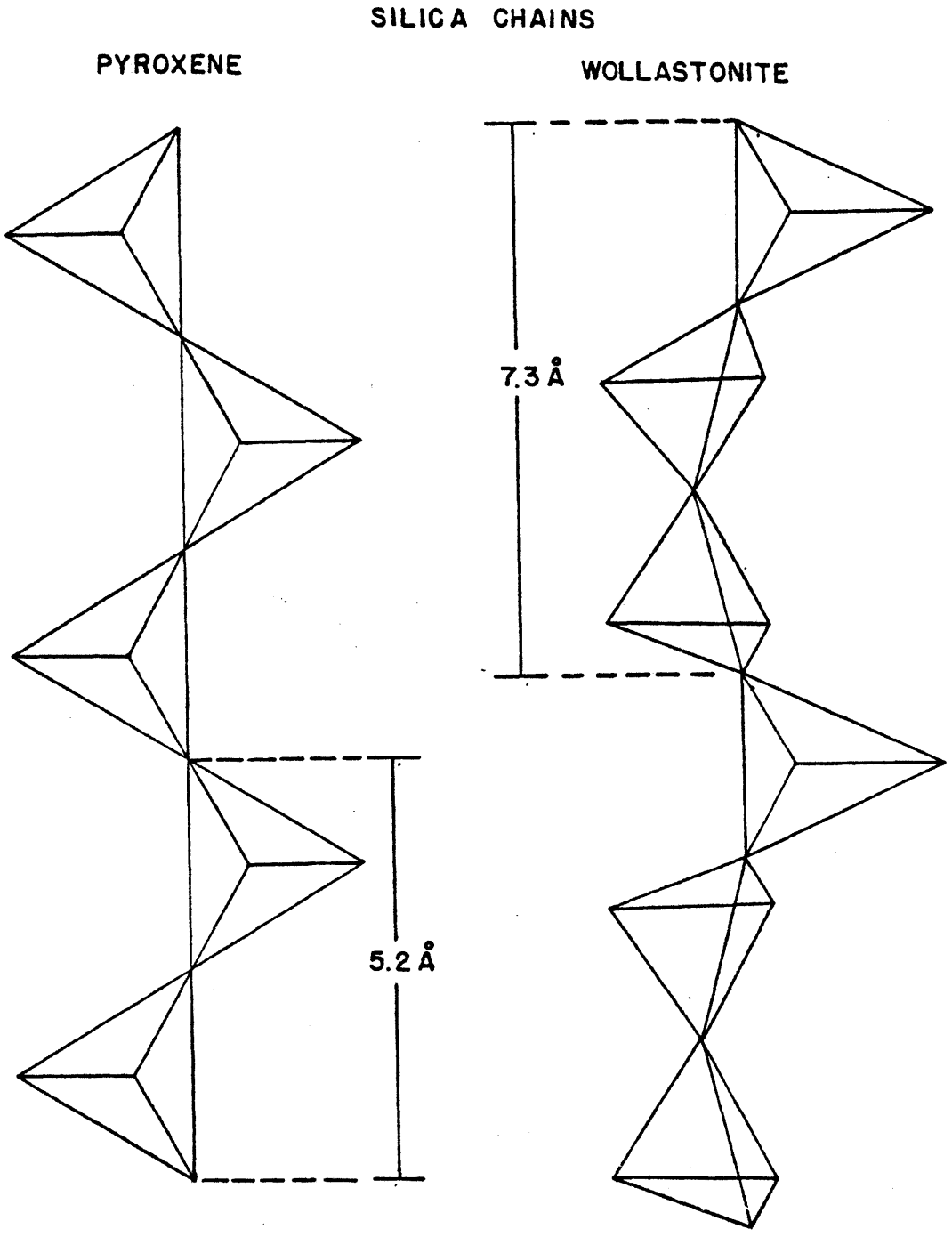

Figure 7-12. Silica chain structure of pyroxene and wollastonite (after Deer, et al., 1966; p. 142). Pyroxene has a double-repeat structure and wollastonite has a triple-repeat pattern.

This chapter has presented pertinent outside information relating to different aspects of this study. The effect of pressure has been seen to generally decrease diffusion rates, giving positive values of ΔV_a. However, a few cases indicate that negative or zero activation volumes are possible. The temperature dependence of this parameter is seen to be both positive and negative, depending on the system. The ion probe was shown to provide values similar to other methods in cases where enough data exists for a meaningful comparison. Compensation trends and the clustering of diffusivities with respect to the material and not the diffusing tracer were demonstrated for silicates in general and pyroxenes in particular. The present study was compared to the pertinent data sets and unusual behavior was only evident in that negative activation volumes were calculated.

VIII. APPLICATIONS OF THE DATA

> Science proceeds more by what it has learned to ignore than by what it takes into account.
>
> --Galileo

Many geochemical theories dealing with the characterization of materials and processes which can't be directly sampled are subject to kinetic effects. In some cases the result of a non-equilibrium situation will be drastically different from that which an equilibrium model would predict. In recent years, significant steps have been taken to include factors such as diffusion and surface kinetics in working hypotheses concerning isotope heterogenenity (e.g. Hofmann and Hart, 1978), crystal growth and zonation (e.g. Albarede and Bottinga, 1972; Shimizu, 1981a, b; and Jambon, 1980), and exsolution (e.g. Huebner and Nord, 1980). The development of even the simplest considerations have been hampered by the lack of applicable diffusion data. In this chapter, diffusion coefficients derived from this study will be applied to various models to extract information on time scales for these problems. Also, the dependence of the electrical conductivity on ionic diffusion will be examined.

A question arises as to the applicability of the diffusion numbers for the synthetic diopside in geologic situations. It is believed here that the natural sample diffusivites are more applicable to the actual situations in nature and are the numbers which should be used by others in model calculations. Both data sets will be employed for calculations involving Sr. Pressure dependence will be simulated for the natural sample determinations by applying ΔV_a's of the laboratory-produced speciments. This is a tenuous assumption which can only be tested by running high pressure experiments on the natural samples. Sm behavior in the natural diopside at one atmosphere will be assumed to be identical to that of strontium, due to the similarity of the data in the synthetic crystals. The cause of this similarity is believed to be the con-

trol of the diffusion process by the defect levels in the different samples. Since the natural diopsides have even greater dislocation densities and iron content, the rate controlling factor is assumed to be the same.

Isotope heterogeneity

The isotope ratio $^{87}Sr/^{86}Sr$ (and $^{143}Nd/^{144}Nd$, which can be modelled by the Sm data) has been used not only in conjunction with geochronology but as a tracer for the origin of the rocks which outcrop at the surface. Mid-ocean ridge basalts (MORB) have 87/86 ratios which generally lie below 0.7030. However, at various locations on the spreading centers there exist anomalous areas with significantly higher values. Values are also greater for the vast majority of oceanic islands. Explanations of this difference between "normal" MORB and the other locations generally fall into two categories. The first is that the source region for the material at the surface is the same for all oceanic basalts but that the processes within the crust vary from place to place. The other is that the source varies and the crustal processes are basically the same everywhere. Both of these require some knowledge of the kinetic behavior of the system. The variable process hypothesis requires assimilation of crustal material by the ascending magma and the effective mixing of the two. Single crystalline phase assimilation experiments (Watson, 1981 and personal communication) are the first step toward understanding the mechanism and time scale of this stoping. The variable source interpretation assumes that heterogeneities, once established, will persist for long geologic times ($\sim 10^9$ years). The scale of these different regions is also the subject of debate. One end-member case is that the source is homogeneous on a regional scale (10 to 1000 km^3 volumes) but heterogeneous on the mineralogical scale (a few cm); the other is its opposite --local equilibrium and regional inhomogeneities.

Hofmann and Hart (1978) addressed this second controversy from a number of standpoints including diffusion in melts and solids. Transport in the liquid phase is considerably faster than in crystalline solids at the same temperature. Even assuming a D of 10^{-6} cm^2/sec for cations in a melt (Hofmann, 1980), the characteristic diffusion distance ($x = 2\sqrt{Dt}$) is only 1.8 km in 10^9 years. This is not an equilibration distance but merely a distance at which the concentration difference is about two-thirds the initial value. So unless there is considerable fine scale mechanical mixing (<1 km) in the mantle, fairly small homogeneous bodies can persist through geologic time. The cause of these blobs is unclear but recently consideration has been given to coherent pieces of subducted material surviving in the lower mantle as a possible source (e.g. Hofmann and White, 1981).

In calculating the time for which mineralogical scale isotopic non-equilibrium could exist, Hofmann and Hart recognized a drawback in that they could only estimate diffusion rates in important source and sink phases for ^{87}Sr. The phase often called upon for the production of large amounts of radiogenic strontium in the mantle is phlogopite (O'Nions and Pankhurst, 1974; Flower, et al., 1975). Reasons for this include its large Rb affinity, its stability at high pressure, and the fact it would be one of the early melting phases during partial fusion. Sr is not well suited to this structure and will diffuse out given sufficient time and an adjacent reservoir. Clinopyroxene is the most likely mantle phase to act as this sink. Based on the observation that high grade metamorphic events invariably equilibrate Sr isotopes in micas, they deduced that diffusion rates in phlogopite are not the rate limiting step for local disequilibrium. A D for Sr in clinopyroxene was assumed based on other cations and similar structures (Lindner, 1955; Sietz, 1973; Huebner et al., 1975). The present study now allows re-calculation of the equilibration scheme used to produce Hofmann and Hart's figure 5.

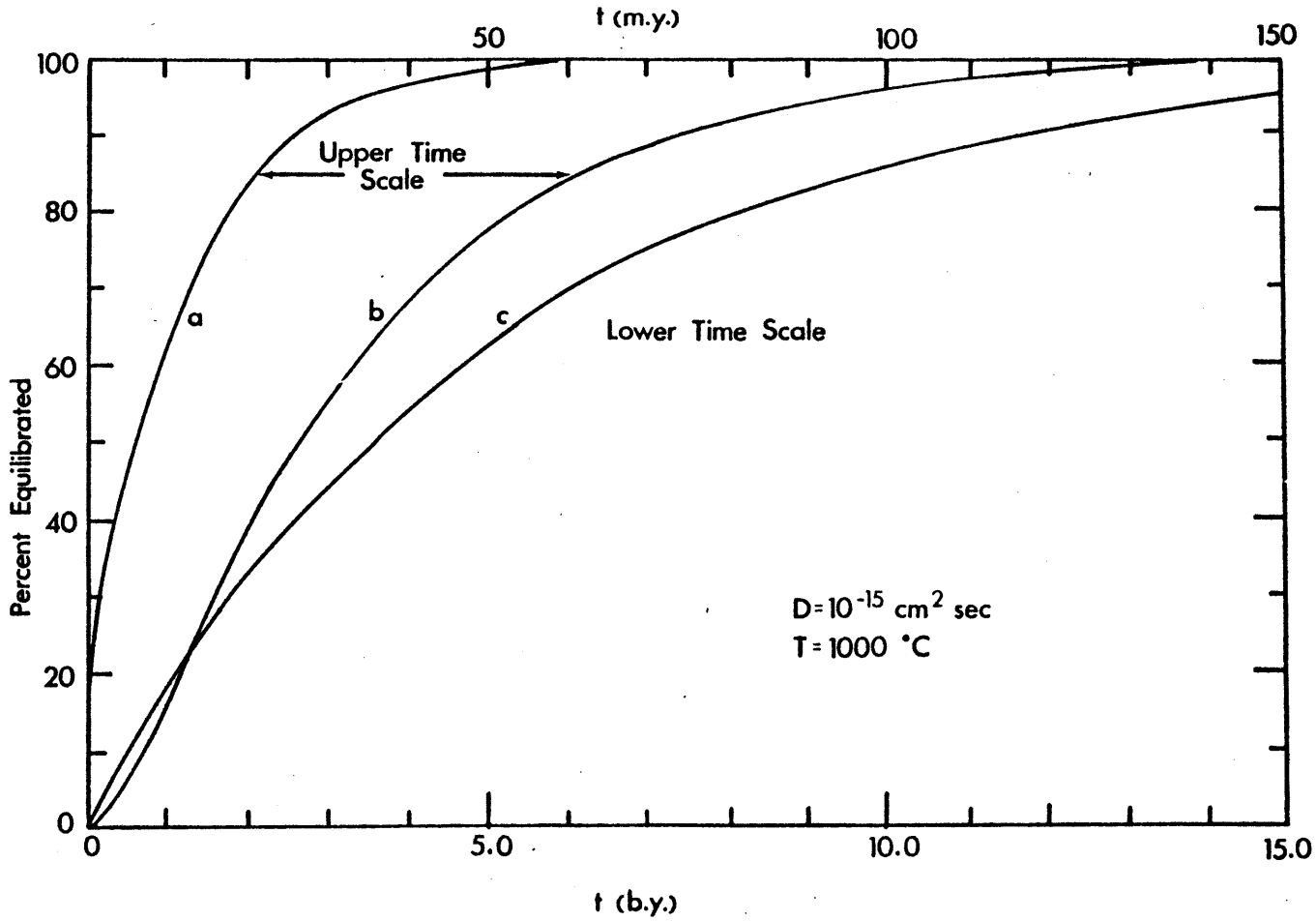

Figure 8-1. Time to mineralogical equilibration for D = 10^{-15} cm^2/sec (after Hofmann and Hart, 1978), percent equilibrated vs time. Case a (upper time scale): two adjacent one cm layers out of equilibrium at t = 0. Case b (upper time scale): 2 one cm layers with an intervening one cm layer; intermediate layer does not restrict flux. Case c (lower time scale): 2 one cm layers (layers one and three) with an intervening one cm layer (layer two) which restricts flow via unfavorable partitioning. Partition coefficients ($C_i/C_j = K_{ij}$) which are used are K_{21} = 0.004 and K_{32} = 500. Curves are calculated using a finite difference method for the appropriate diffusion equation.

The value of the diffusivity which they used was 10^{-13} cm^2/sec at 1000°C. Extrapolation of the one atmosphere natural sample data of this study to that temperature gives approximately $10^{-15} cm^2$/sec. Estimation of the activation volume at 1000°C from the trend of the c direction synthetic determinations gives a value close to zero, meaning a correction for pressure is unnecessary. (A ΔV_a of 1 cm^3/mole would decrease D by approximately 15% at 20 Kbar.) The result of this change in the diffusion coefficient on the finite difference formulation of Hofmann and Hart is merely to change the time scale and not the shape of the curve. The factor of 100 difference in D lengthens the time by a similar amount. Therefore, for their case a, two adjacent 1 cm layers out of equilibrium at t = 0, the time to reach 95% equilibration goes from 0.3 to 30 m.y. The 95% equilibration time increases from 0.9 to 90 m.y. in the example of an intervening but non-interfering layer (case b). When a barrier layer is introduced (case c), only about 50% equilibration is possible in the age of the earth. Data for the synthetic samples increases these times by about three orders of magnitude, making even the fastest example totally impractical. Higher T's and smaller layer thicknesses will significantly reduce equilibration times. At 1250°C, the calculated strontium diffusivity is 6.5×10^{-13} cm^2/sec, which corresponds to a 95% equilibration time of approximately 50,000 years for case a and 23 m.y. for case c. This is believed to be a more reasonable temperature for the upper mantle source of MORB (Stacey, 1977). The presence of a liquid (in which diffusion is much faster) will short-circuit the system and all three possibilities will revert to case a. It is concluded from these calculations that mineralogical scale heterogeneities will exist in moderate temperature (<1100°C) dry regimes for very long times if phases such as phlogopite and pyroxene are not in contact. Introduction of a melt or other fluid will overcome mineralogic separations and destroy the disequilibrium in a relatively short length of

time. O'Nions and Pankhurst (1974) postulated disequilibrium for 20 m.y. to produce the 87/86 ratios seen at the surface in some locations. Under the 1000°C conditions, such times would produce about 80% homogenization which would by necessity prolong the period needed to produce the observed variations. This in turn would allow the system to more closely approximate equilibrium. The calculated diffusion coefficients appear to be just large enough to disallow sufficient build-up of radiogenic strontium in the high rubidium phase to produce the observed ratios. At 1250°C, equilibration occurs much too rapidly to produce the high 87/86 ratios.

The transport rates calculated in this study are compatible with maintaining large scale heterogeneities (and mineralogical scale disequilibrium in some cases) over appreciable geologic time. Presence of a melt or contact between source and sink phases would almost completely destroy small scale variations in periods less than 30 m.y. Therefore, disequilibrium melting models for generation of MORB and oceanic island basalts will not provide the observed variations in the isotopic ratio $^{87}Sr/^{86}Sr$ (or $^{144}Nd/^{143}Nd$).

Another application of this equilibration calculation is the examination of residence times and/or temperatures at depth for lower crustal xenoliths. Richardson et al. (1980) reported perfect $^{87}Sr/^{86}Sr$ and $^{144}Nd/^{143}Nd$ isotopic equilibration between CPX and plagioclase in an orthogneiss nodule from Kilbourne Hole, New Mexico. They estimated a maximum age of 10 m.y. for this inter-mineral equilibrium and postulated that the homogenization was associated with the eruption event, or was the result of storage at granulite-facies conditions related to the opening of the Rio Grande rift. At an eruption temperature of 1100°C, the diffusion coefficient is $2.0 \times 10^{-14} cm^2/sec$ and 95% equilibration occurs in 1.5 m.y. for Hofmann and Hart's case a. This is longer than would be expected for the eruption sequence. Assuming a lower crustal residence temperature of 1000°C, 95% equilibration is achieved in

30 m.y., which is the approximate age for the beginning of the rift's development (Chapin, 1979). Grain sizes for these nodules are on the order of a few millimeters (Richardson, personal communication) and the equilibration time would be considerably less than that predicted by Hofmann and Hart's model which uses one cm layers. It can be concluded that the homogenization of the Sr and Nd isotopes can be achieved easily for lower-crustal residence times pertinent to the age of the Rio Grande rift. However, the diffusion rates during the eruptive sequence appear to be too slow for that to be the source of the homogenization.

A further consequence of these D's is to indicate that there is very little diffusion at lower (<900°C) temperatures in a dry system. Radiogenic isotopes of Sr and Nd will not be redistributed to any great extent and mineral-mineral ages will represent the igneous event. This high closure temperature will be discussed more fully in the section on trace element geothermometry. An implicit assumption in these models of isotopic disequilibrium is that homogenization is controlled by volume diffusion. Metamorphic recrystallization can alter the apparent transport rates by "trapping" slow moving trace elements during growth (provided that the growth rates are fast enough), thus changing the chemical potential gradients and diffusion directions. The effect of a grain boundary fluid will depend on the temperatures reached and the grain sizes. For a T of 850°C, $D = 7 \times 10^{-18} cm^2/sec$. If clinopyroxene grains are modelled as spheres 2 mm in diameter and a fluid rich in a radiogenic isotope totally surrounds them, the time necessary to equilibrate the system depends on the percentage of the total diffusant in the liquid that the sphere will take up (Crank, 1975; p. 95). For an infinite source, the time to 90% equilibration is 8.2 m.y. If the CPX accepts 90% of the available tracer, the time reduces to 0.7 m.y. because there is less diffusant in the fluid. Elemental concentrations may change this quickly, but isotopic

homogenization would continue, eventually resulting in the same radiogenic/stable ratio in all phases. This exchange would follow the infinite source curve. Extending this treatment to metasomatic conditions in the mantle increases D and shortens equilibration times. At 1250°C, D = 6.5 x 10^{-13} cm^2/sec and 90% equilibration is reached in 95 years for the infinite source.

The net effect of a preferential loss of the daughter species by the source and gain by the sink is to rotate the mineral-mineral isochron in a clockwise fashion. The chemical differences between Rb and Sr would be a driving force for this type of rearrangement, because size and charge differences make it unlikely that both elements will be accommodated in the same structure. Chemically similar elements like Sm and Nd would show a more subtle change caused by isotopic homogenization between REE-rich and REE-poor phases. Lower temperatures and larger grain sizes will further limit the re-equilibration which occurs during metamorphism.

Phenocryst zonation and equilibration

Kinetic crystallization models were first applied to trace element partitioning in petrogenesis by Albarede and Bottinga (1972). They showed that solid/liquid distribution coefficients, crystal growth rates, and diffusion in the liquid could cause zoned crystals and affect the bulk partitioning between the melt and the solid phases. Since then, other authors have expanded these models adding further considerations and consequences (e.g. Magaritz and Hofmann, 1978a; Jambon, 1980; Shimizu, 1981b). A basic assumption in all of these treatments is that solid state diffusion can be ignored during the crystallization process. This is true for the non-equilibrium conditions covered by these studies because of the considerable difference between diffusion rates in solids and melts at the same temperature (e.g. ~7 orders of magnitude for the Sr between dropside and basalt at 1100°C). If the crystal growth rate is slow enough that solid state transport continually homogenizes

the grains, diffusion in the liquid will destroy concentration gradients caused by partitioning and equilibrium crystallization will occur.

Diffusion in the solid becomes important after solidification. Zoning which is set up by kinetic processes will leave crystals with bulk compositions not representative of equilibrium partitioning. Shimizu (1981a, 1981b) has indicated the importance of interface kinetics which are often the rate determining step in the up-take of trace elements by a growing crystal. This study has shown that interface problems among crystalline phases are overcome at high pressure for trace elements. However, as discussed in the preceding chapter, major elements appear to be subject to grain boundary kinetics even in cases of perfect surface contact. A higher closure temperature for this interface factor would allow diffusion within the different phases without exchange among them. The zoning in each grain would be destroyed but the total concentration would remain the same non-equilibrium value. For an over-simplified situation of a 3-layer sandwich with the a core of concentration C_o and zero concentration in the outer layers, the problem is symmetric about the center point (x = 0) (figure (8-2)). Reflection at the boundaries x = 0 and x = L (half-width of the crystal) leads to the following equation (Crank, 1975; p. 16):

$$C(x,t) = \frac{1}{2} C_o \sum_{n=-\infty}^{\infty} \left[\operatorname{erf}\left(\frac{h+2nL-x}{2\sqrt{Dt}} \right) + \operatorname{erf}\left(\frac{h-2nL+x}{2\sqrt{Dt}} \right) \right] \qquad (8\text{-}1)$$

where 2h is the thickness of the initial central layer. The average concentration at $t = \infty$ would be $C_\infty = C_o h/L$. For short times, the first three or four terms of the sum in equation (8-1) give a fairly accurate description of the concentration within the boundaries x = -L and x = L. Assuming L = 0.2 cm, h = 0.1 cm, and $D = 10^{-15} cm^2/sec$ (T = 1000°C), 95% equilibration is achieved in 0.5 m.y. (seven terms of the sum were used). At a lower temperature (800°C),

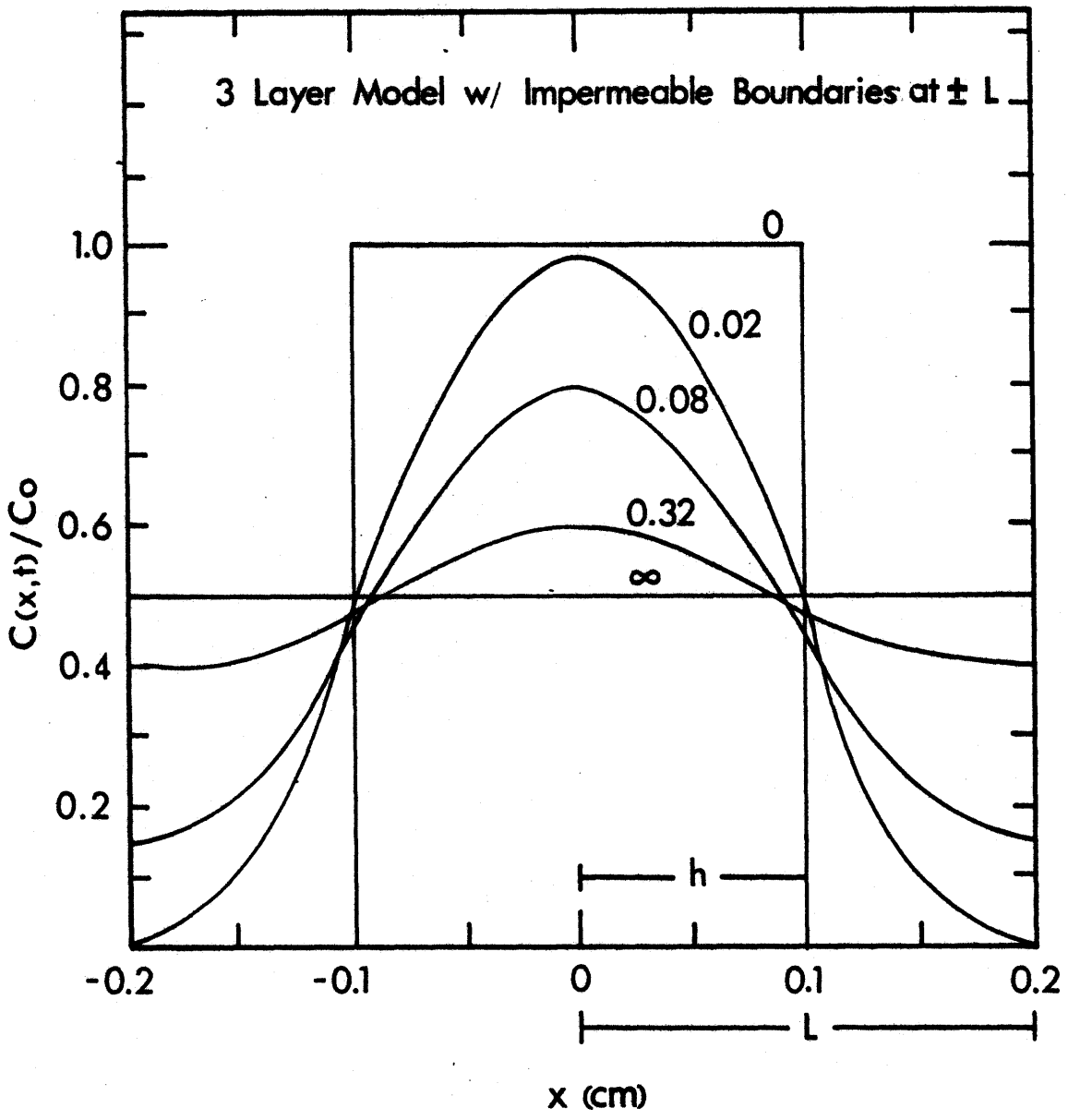

Figure 8-2. Zoned phenocryst model with impermeable boundaries, relative concentration vs distance. In the example, L = 0.2 cm, h = 0.1 cm, and $D = 10^{-15}$ cm^2/sec. Numbers on curves are values of t in units of millions of years.

the extrapolated diffusivity is calculated as $9.4 \times 10^{-19} cm^2/sec$ and the 95% level is reached in 450 m.y., indicating that zoning will persist for geologically pertinent times at lower temperatures. This model for a one dimensional flux provides an upper limit for the problem with spherical or more complicated shapes coming to equilibrium in shorter times. The assumption of an impermeable boundary is also a simplification which can be replaced by transport modified by an interface resistance (Crank; p. 40). This would change C_∞ in the direction of the true equilibrium partitioning value among the solid phases and, in the example, would lengthen the period required to produce a nearly homogeneous crystal.

The many kinetic factors involved in crystallization can skew trace element compositions in phenocrysts away from either total or surface equilibrium with the surrounding melt. Interpretation of zoned crystals must take these into account. Also, diffusion processes in the solid can alter the effects of crystallization kinetics after the fact, further obscuring the true picture of melt composition and the history of the assemblage. At near melt temperatures solid state transport can significantly change apparent zoning and distribution patterns. At lower T's, the action of a fluid is required to seriously alter concentrations as volume diffusion is minimal and crystallization features will remain.

Lamellar processes and geothermometry

Pyroxene mineralogy is marked by subsolidus exsolution between Ca-rich and Ca-poor members. Natural lamellar structures have been used as starting materials for interdiffusion investigations with unconvincing, very slow results (Huebner, et al., 1975; Huebner and Nord, 1980; Brady and McCallister, 1980). It has been assumed that these experiments did not measure volume diffusion but some interface phenomenon. A number of attempts have been made to use thickness of lamellae to estimate cooling histories for the pyroxenes

in which they formed (e.g. Dunham et al., 1972; Huebner et al., 1975; Miyamoto and Takeda, 1977). A major assumption of these examples, which would appear in doubt due to the experimental evidence, is that volume interdiffusion is the rate controlling step. When the rates calculated from the laboratory studies are applied to observed lamellae, unreasonably long geologic times result. Much more believable cooling periods are derived when D's are estimated from tracer experiments in similar phases.

McCallister et al. (1979) have determined the tracer diffusivity of Ca in diopside at 1300°C. Using this and the activation energy of the natural sample RT experiments a D of $5 \times 10^{-18} cm^2/sec$ is calculated for 800°C. Huebner et al. (1975) used a rate of 10^{-19} to assign a cooling time of 30,000 years to a lunar breccia sample with 30 μm augite lamellae in a pigeonite. Substitution of 5×10^{-18} into their figure 4 (reproduced here, figure (8-3)) gives a cooling time of approximately 600 years. This has ramifications on the assumed depth of burial of the pyroxene. Huebner et al. give a 2.75 km depth for their cooling time of 30,000 yrs in an anorthosite crust. The much shorter time translates to a more shallow burial or transport to the surface after 600 yrs at a deeper depth. Miyamoto and Takeda (1977) estimated the diffusion equation for Ca in augite to be $1.1 \times 10^{-14} (cm^2/sec)$ exp (-28 (Kcal/mole)/RT) from the activation energy of enstatite exsolution from supersaturated diopside (McCallister, 1974), and values of D from lamellar exsolution and dissolution at 1125°C. This corresponds to a D_{Ca} of $3.8 \times 10^{-19} cm^2/sec$ at 1100°C. They applied their calculated transport relation to a cooling model which used lamellar thicknesses to estimate the depth of formation of eucrites in a parent body. The diffusion parameters derived here would greatly reduce the depths if all other factors remained unchanged because the rates are so much faster. Dunham et al. (1972) assumed a D of 10^{-14} at 1000°C in calculating cooling rates of pyroxenes at different levels

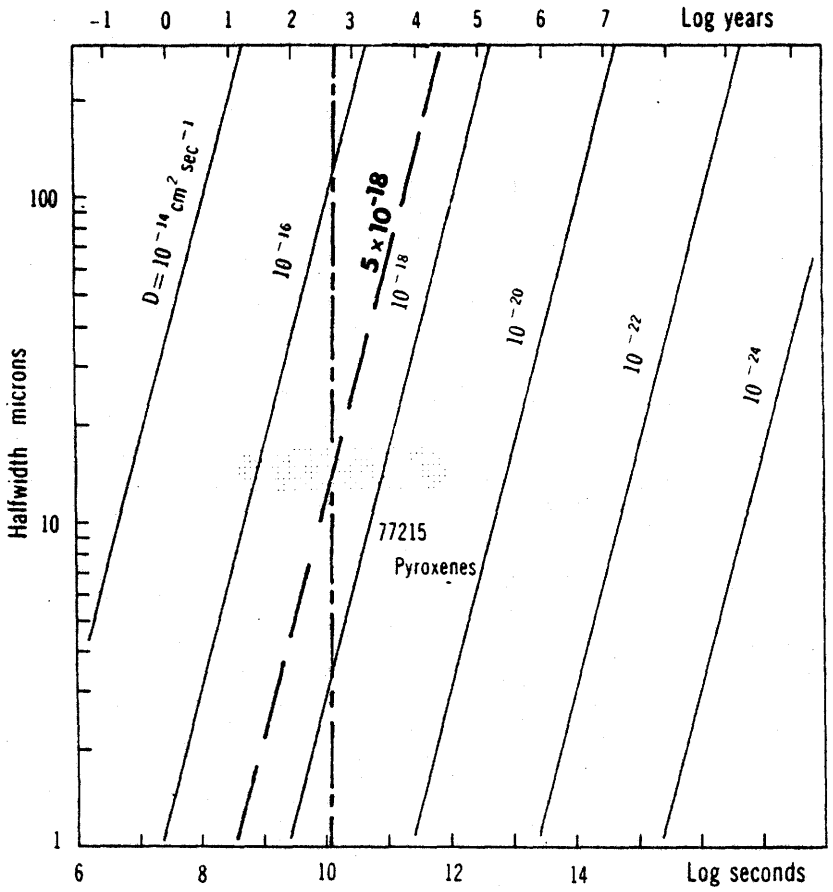

Fig. 4. Solution of the equation for the growth of planar pyroxene lamellae in 77215, in terms of half-width, time, and diffusivity. Assuming a D of $\leq 10^{-18}$ cm^2 sec^{-1}, 30-μm lamellae could grow in $\leq$ 30,000 yr.

Figure 8-3. Lamellar thickness as a function of cooling time (from Huebner, et al., 1975), log half-width vs log time and contoured for diffusivities. Dashed line is at D = 5 x 10^{-18} and dot/dash line is at t = 600 years.

in a dolerite sill. This is not substantially different from the value of 6×10^{-15} for the same T calculated from the present data. Their conclusions would be basically unchanged.

Laboratory measurements of lamellar growth and breakdown and their interpretation as diffusion controlled processes appear to be at odds with the same processes in natural settings. Extrapolation of Ca tracer data using an activation energy from this study give reasonable results for the timing of the production of the observed features. Questions which remain are fourfold. 1) If the interdiffusion experiments are not measuring diffusion, what are they measuring? 2) Why is the same process not evident in natural situations? 3) Are the use of tracer diffusion values truly justified? And 4) Does the calcium transport have an activation energy similar to that of strontium? Further tracer experiments can resolve the last point, while the others require study of the exsolution process with interface kinetics in mind.

A direct application of the trace element diffusion data is in the area of geothermometry. Shimizu (1981c) has suggested the use of partitioning of REE between coexisting garnet and clinopyroxene as a geothermometer. The advantage of such a scheme is that elements in the same abundance range, if not the exact same species, could give both temperature and age determinations. This eliminates questions of whether or not major and trace elements respond similarly to the same conditions and on the same time scale. The ion probe is capable of analysing the trace constituents in the phases and Shimizu has calibrated the geothermometer at one temperature and composition with an experimental charge of known temperature history.

The temperature that a geothermometer measures is the closure temperature, which is the apparent T at which diffusion stops. Hart (1981) examined the closure temperature formulation for spherical geometry and a hyperbolic

cooling rate ($T \propto 1/t$). The equation which describes this was given in chapter II (equation 2-51):

$$T_c = \frac{\Delta H_a/R}{\ln\left(\frac{-ART_c^2 D_o/a^2}{\Delta H_a dT/dt}\right)} \qquad (8\text{-}2)$$

with A, the geometric factor, = 55 for a sphere. The presence of ΔH_a and D_o in the equation allows the compensation plot to be contoured for T_c at a given cooling rate and grain size. Modification of the $\log D_o$ vs. ΔH_a graph to $\log\left(\frac{1000}{dT/dt} D_o\right)$ vs. ΔH_a results in the same set of closure temperature curves being applicable to any cooling rate. (Hart's figure 6 is mislabelled). The compensation line on a simple plot becomes a family of lines with the same slope and the intercept dependent on the cooling rate.

Figure (8-4) is a modified compensation diagram with T_c contours for a 4 mm diameter grain size (a = 0.2 cm) and a family of curves for the synthetic diopside samples. The dashed line is an estimated line through the natural RT point with the same crossover temperature as the synthetics and a 10^5°C/m.y. cooling rate. The observed effect is approximately the same as decreasing the cooling rate two orders of magnitude. It is evident that closure for both Sr and Sm occurs at relatively high temperatures for this grain size, even in the case of slow cooling rates. A plot of closure temperature vs. cooling rate for the natural samples (figure 8-5) illustrates the same point. A cooling rate of 10°C/m.y. gives a T_c of 856°C for the size and shape parameters given above. The compensation lines on figure (8-4) are sub-parallel to the closure isotherms, indicating a very small range of blocking temperatures for Sr and Sm at the various experimental conditions. Smaller crystal sizes would result in lower T_c's with lamellar structures 30 μm wide having a closure temperature of 910°C for the natural sample ΔH_a and D_o,

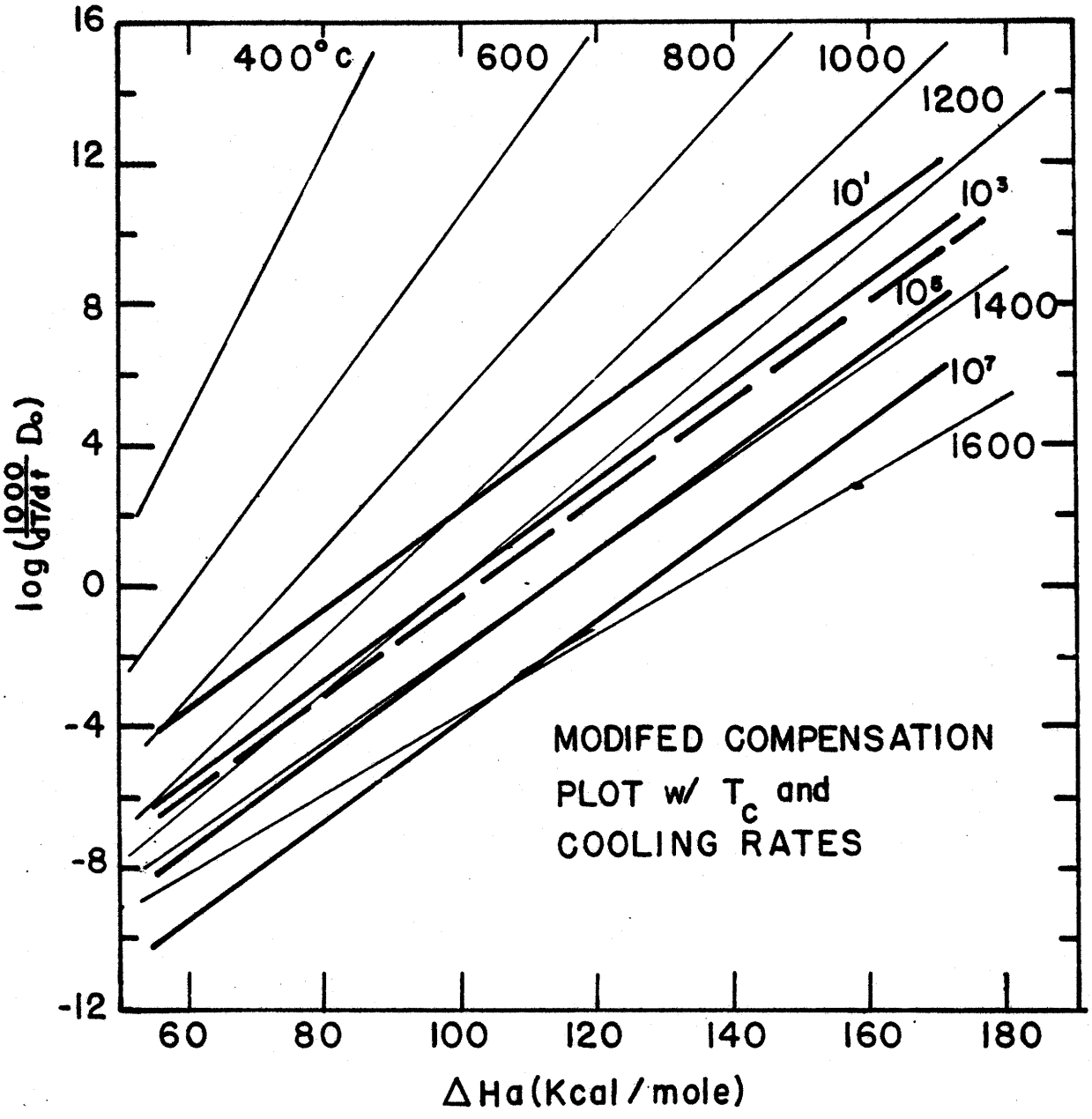

Figure 8-4. Modified compensation diagram showing closure temperature (T_c) contours and compensation trends for diopside at various cooling rates (after Hart, 1981), $\log[(1000/dT/dt)D_0]$ vs ΔH_a. Normalizing the ordinate to dT/dt allows a single set of T_c curves to serve for all cooling rates. Heavy solid lines are the synthetic diopside compensation lines for the indicated cooling rates (°C/m. y.). Dashed line is estimated compensation trend for natural samples and dT/dt = 10^5 °C/m. y. When sample trend coincides with T_c line, all diffusing species close at the same temperature.

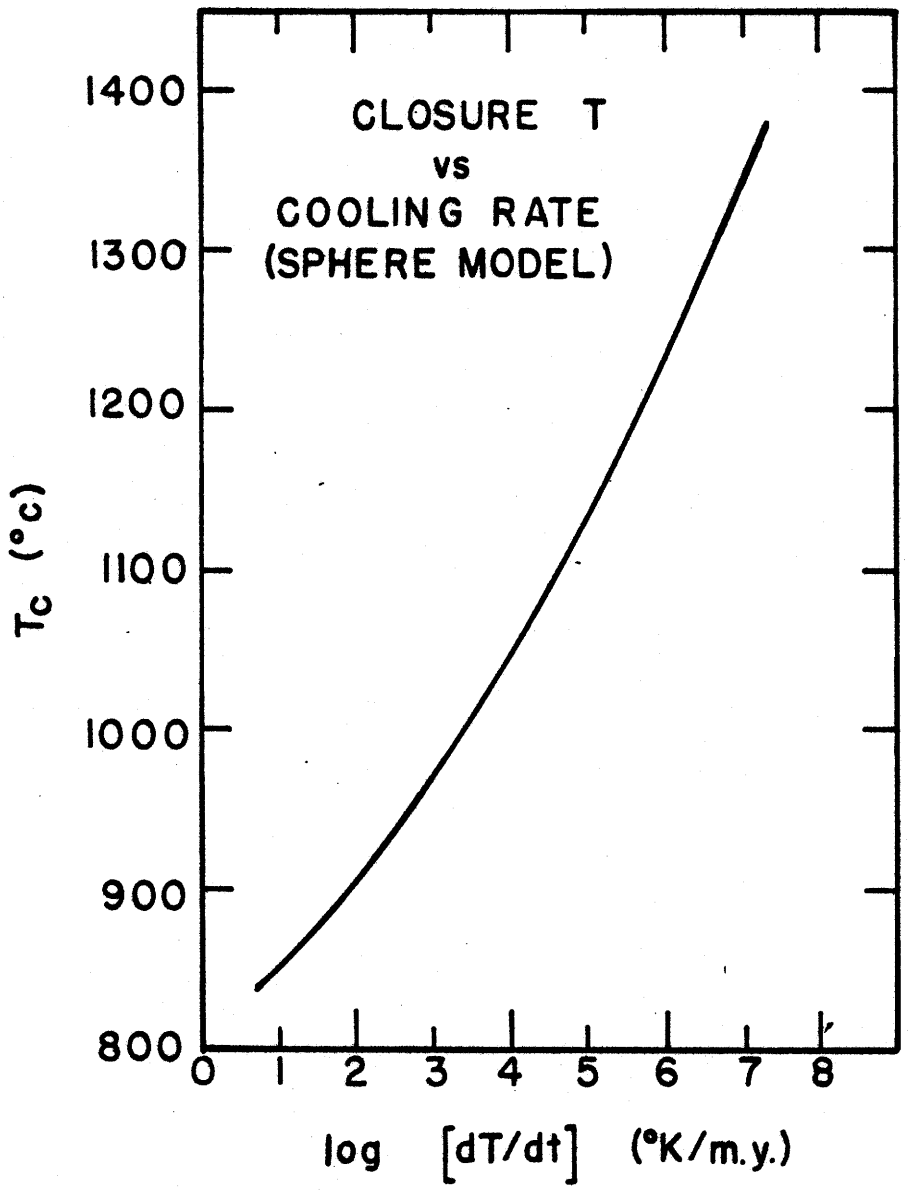

Figure 8-5. Closure temperature (T_c) for the natural sample ΔH_a and D_0, T_c vs log(dT/dt). Closure temperature calculated using equation (8-2) with A = 55 (spherical geometry) and a = 0.2 cm. Diopside closes at relatively high temperatures for most reasonable cooling rates.

and a cooling rate of 10^5°C/m.y.

Earlier, the effect of closure on mineral-mineral isochrons was discussed. With the presentation of the closure expression (equation 8-2), it is now possible to evaluate an example quantitatively. DePaolo and Wasserburg (1979) determined a mineral Sm-Nd age for the Stillwater complex of 2701 $\pm$ 8 m.y. on a sample consisting of bronzite, augite, and plagioclase. Assuming that the Sr natural sample diffusivities apply to the rare earth elements (a reasonable assumption in light of the similarity of the D's in the synthetic samples), a cooling rate for a large batholith of 10^4°C/m.y. (Hart, 1981), and a maximum grain size of one cm, closure for Sm and Nd is expected by 1215°C. Thus, the age which DePaolo and Wasserburg measured is that of the crystallization event. Rb-Sr systematics in the same rocks have been seriously disturbed since emplacement and the authors suggest that this is a result of fluid circulation at lower temperatures. If the disturbance was caused by exceeding the closure temperature for Sr but not that of Nd, the above assumption regarding similar diffusivities would be invalidated.

Pressure/temperature conditions for equilibration of garnet peridotites from the Kao kimberlite pipe have been determined using two-pyroxene geothermometry and the solubility of alumina in orthopyroxene (MacGregor, 1979). The data define a trend on P,T plot with all but three points falling below 1400°C and 60 Kbars (figure (8-6)). The lack of determinations above this point has two possible explanations. Firstly, the kimberlite did not bring any nodules to the surface directly from depths greater than 180 km (60 Kbar), or secondly, unrealistic cooling rates are required in order to have closure above 1400°C. The second case can be tested by using the Arrhenius equation derived from the 1300°C point of McCallister et al. (1979) and the activation energy for Sr in the natural samples (D_{Ca} = 300 exp[-97,000/RT]cm^2/sec). A T_c of 1400°C gives a cooling rate of 5.3 x 10^5°C/m.y. and this value can be

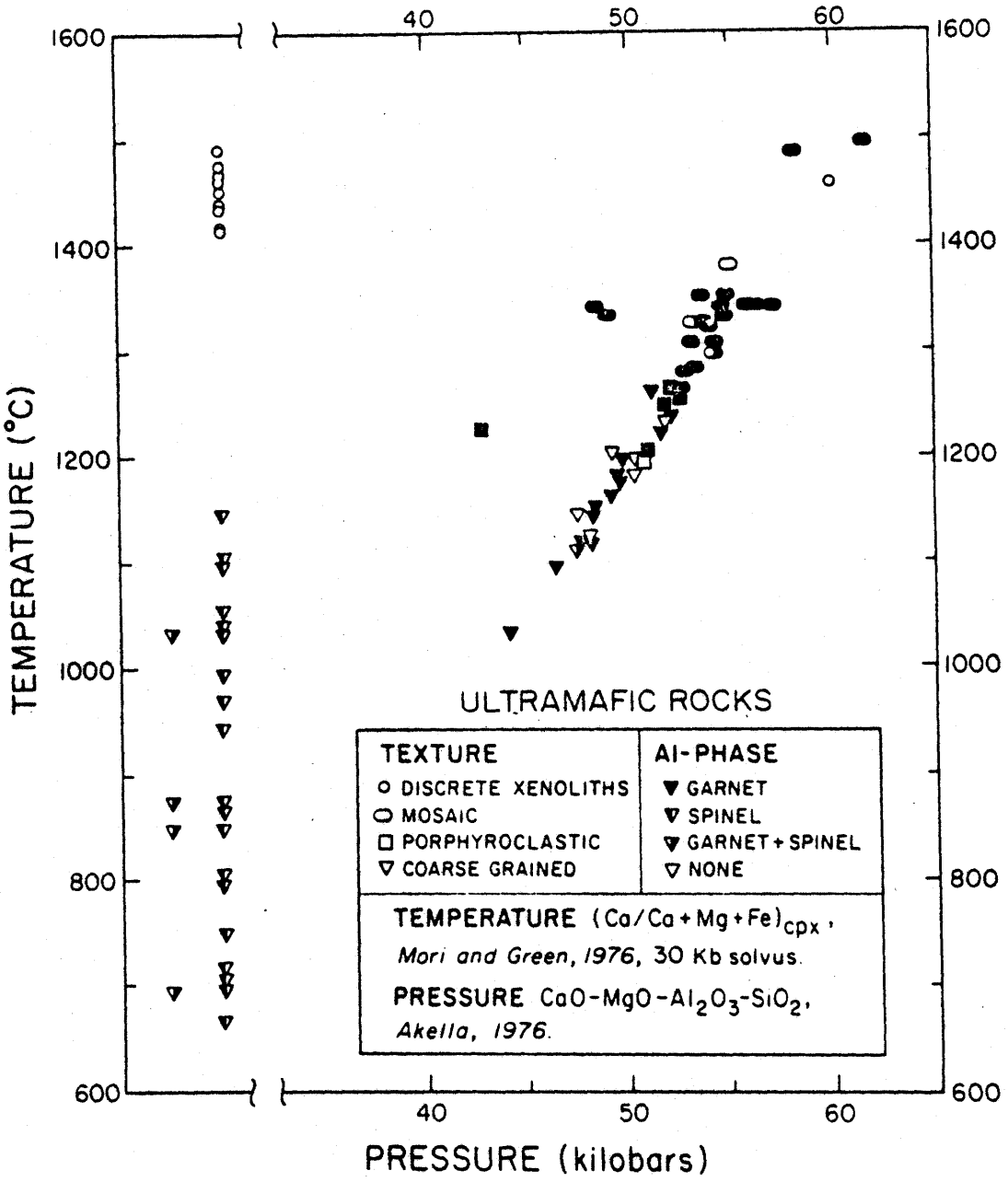

Figure 8-6. Temperatures and pressures of equilibration for ultramafic xenoliths (from MacGregor, 1979), T vs P. Temperatures calculated using a two pyroxene geothermometer and pressure estimated from Al content of OPX coexisting with garnet. Note scarcity of samples above 1400°C.

employed to determine the minimum eruption velocity which will give closure in the system. Assuming a travel distance of 180 km and temperature drop of 250°C, a minimum velocity of 0.38 km/yr was calculated from the following equation:

$$(dT/dt)(\Delta x/\Delta T) = dx/dt. \qquad (8\text{-}3)$$

This velocity is well below accepted values for kimberlite eruption, and leads to the conclusion that this pipe does not directly sample material at temperatures greater than 1400°C. An ascent rate of 10 cm/yr was assumed for non-eruptive transport and MacGregor's garnet peridotite trend was used for dT/dx. These gave a cooling rate of 10^3°C/m.y. and a closure temperature of 932°C, which means that assemblages will continue to re-equilibrate as they rise before eruption. Changes in the diffusivities of an order of magnitude will not alter the conclusions developed here.

Diffusion rates in pyroxenes appear to be slow enough that trace element composition will not change significantly after crystallization. Disequilibrium partitioning will also be "frozen in" so that application of the geothermometer may be subject to errors arising from kinetic factors. Slow cooling bodies with slow crystal growth rates will yield equilibrium assemblages which will close soon after solidification and remain immobile during dry metamorphic conditions. Calculation of T_c supports earlier observations that little diffusion of radiogenic isotopes of Sr and Nd will occur and mineral-mineral isochrons will give true igneous dates. Thus, pyroxenes are good candidates for trace element methods for the extraction of information regarding initial rock-forming events.

Electrical conductivity

Electrical conduction in insulators at high temperatures is most likely ionic in nature (Shankland, 1969). Charge is carried by the diffusing ions and conductivity and diffusivity are related by the Nernst-Einstein equation:

$$\sigma/D = (ez)^2 C/RT \qquad (8\text{-}4)$$

where σ is the conductivity ($ohm^{-1}cm^{-1}$), ez and C are the charge and the concentration of the migrating species, k is Boltzmann's constant, and T is in °K. Misener (1974) used this equation to calculate conductivities from his diffusion data which he compared with directly measured values. Good agreement was observed in the range 1200 to 1400°C, indicating that electrical conduction is a manifestation of the diffusion process.

A similar calculation was undertaken for diopside using the natural sample data. Two cases were computed, one for Sr with a mole fraction of 0.001/mole (estimated from applied dose of tracer) and another for Ca using an Arrhenius line anchored at McCallister et al.'s (1979) 1300°C point with the slope (activation energy) of the Sr data and a mole fraction of 0.1/mole. These are presented in figure (8-7) along with some measured values of the conductivity for pyroxenes. There is no correlation between the two processes which leads to one of two conclusions. One, the M(2) site cations are not the charge carriers in pyroxene. Or two, ionic processes do not control conduction in the range of the electrical measurements. Shankland (1969) recognized three different slopes on the Arrhenius conduction plot for olivine and interpreted them as impurity-controlled conduction (T<800°C), intrinsic semi-conduction (800 to 1200°C), and ionic conduction (T>1200°C). The measurements of conductivity for pyroxene all fall at temperatures below the diffusion study. However, if a different slope segment does exist at high temperatures, it should connect up with the other data, putting it well above the diffusion-derived numbers. This would indicate that the first conclusion is more likely.

In either case, the lack of similarity does not allow use of the data to estimate temperature at depth in the earth similar to the application by Misener (1974). He used an iterative process and independent conductivity

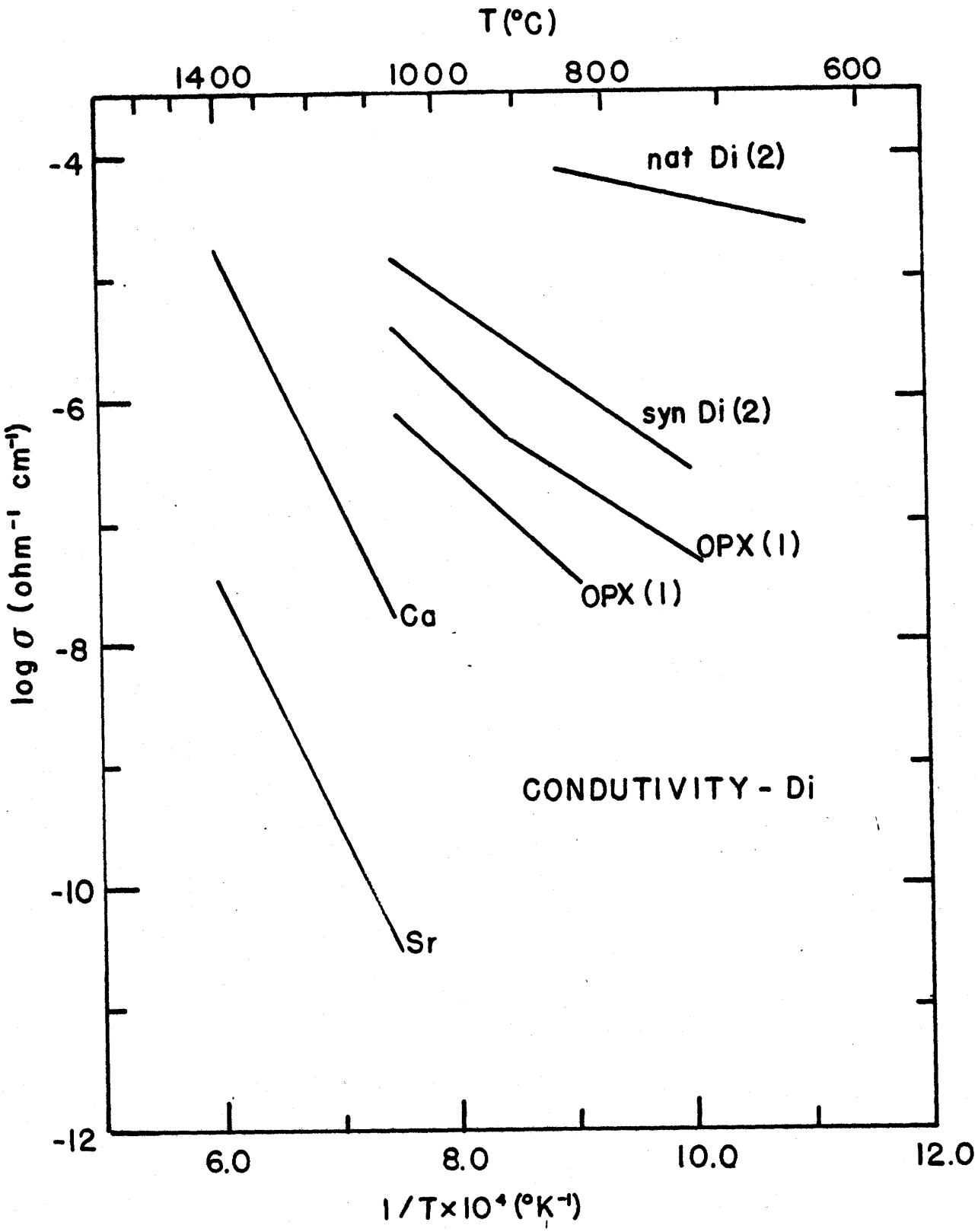

Figure 8-7. Electrical conductivity (σ) of pyroxenes as a function of temperature, logσ vs 1/T. Ca and Sr lines are calculated from diffusion data in this study, using the Nernst-Einstein expression (equation 8-4). Measured conductivities from (1) Duba, et al., 1973 and (2) Hinze, et al., 1981.

estimates for different depths to extract a temperature from equation (8-4) for comparison with model geotherms. Measurement of conductivity in the experimental range of this study, preferably in the same material, would yield a more accurate comparison. Also, diffusion measurements of the major cations would decrease the large uncertainty caused by extrapolation from trace species and possibly help identify the charge-carrying element.

The examples discussed in this chapter have mainly utilized the diffusion coefficients derived for Sr in the natural diopside. The basic result has been that solid-state transport of trace elements does not play a major role in most petrogenetic processes. Exceptions to this are when phases out of equilibrium are adjacent or connected by a liquid at high temperatures without interfering surface kinetics. Closure for Sr and Sm occurs at temperatures above 1000°C for all but the slowest of cooling rates. If the derived compensation line holds up for other cations in CPX, the range of T_c will be small in diopside and different geochronology schemes should give approximately the same age. The same is true for geothermometry/geobarometry. Applications of the high pressure estimates were limited to temperatures where ΔV_a appears to be near zero. High pressure experiments in the natural samples are needed to either confirm the trends of the synthetic samples or establish the correct ones for these specimens. Data from the laboratory-grown crystals most likely do not have applicability to geologic problems, but have been most useful for examining the various diffusion techniques.

IX. CONLCUSIONS

> "Contrariwise," continued Tweedledee, "if it was so, it might be; and if it were so, it would be; but as it isn't, it ain't. That's logic."
>
> --Carroll

This thesis contains a variety of information on the diffusion rates of two geologically important trace elements and on the mechanics of diffusion studies in general. These data provide the basis for investigation and comparison of experimental and analytical techniques and of starting materials. They also provide measured values to be used in geochemical applications which had previously depended on estimated diffusivities. A single empirical equation for D_{Sr} which incorporated both temperature and pressure effects was derived for the synthetic diopsides in the c direction:

$$D(P,T) = 1200(cm^2/sec)\ \exp[-122{,}000(cal/mole)/RT(°K)]\ \exp[-P(bars)/(2.94T(°K) - 4640)R] \qquad (9\text{-}1)$$

Assuming a similar pressure dependence in the natural samples, the above equation can be modified by substituting the ΔH_a and D_o from the radiotracer experiments in the natural diopsides:

$$D(P,T) = 54(cm^2/sec)\ \exp[-97{,}000/RT]\ \exp[-P/(2.94T - 4640)R] \qquad (9\text{-}2)$$

Data for Sr in other directions and the Sm data were not extensive enough to allow development of similar overall equations, but their individual Arrhenius relations are listed in chapter V, table 5-15. The conclusions of the different aspects of the study are presented here.

Comparison of techniques and materials

Three analytical techniques were applied to diffusion profiles in the same material, a synthetic diopside. Radiotracer and sectioning, ion microprobe depth profiling, and Rutherford backscattering spectroscopy gave nearly

identical diffusivities (within a factor of two) in the study temperature range after data reduction had removed recognizable method-generated effects. Ignoring these modifications of the true diffusion profile can result in errors of more than two orders of magnitude in D. Differences in the activation energies and frequency factors found in this study can be attributed to scatter in the data for each technique.

The major reason for undertaking the comparison of analytical systems was to investigate the suitability of ion probe depth profiling as a diffusion study tool. Although the action of the primary beam on the sample is not fully understood, empirical treatments combined with proper adjustment of machine parameters made it possible to extract concentration curves which represented the diffusion process. The use of the ion probe provides the experimentalist a number of advantages. Stable isotopes can be used for tracer and self-diffusion studies. Small samples and short profile lengths can be utilized, thus alleviating problems which particularly affect high pressure experiments. Finally, multiple tracers can be analysed in a single specimen, reducing material consumption and the number of runs necessary. Diffusion in two significantly different diopsides was examined by the radiotracer and sectioning technique. Results showed comparable activation energies but an absolute difference in D of two orders of magnitude between measurements at a given temperature. The faster diffusion rate in the natural samples was attributed to their higher impurity and dislocation densities. The iron content was measured by electron microprobe at 1.5 wt.% FeO as opposed to trace levels (0.1%) for the synthetic crystals. Dislocation densities were estimated by the etch pit method and gave a difference of about a factor of 100. These effects and trace element concentrations will change impurity levels which will increase or decrease the frequency factor. Diffusion in both samples was interpreted as extrinsic because extremely low defect

concentrations are necessary to observe intrinsic transport at the temperatures studied. Postulated intrinsic behavior in silicates in other studies is believed to be in error (Buening and Buseck, 1973; Morioka, 1981).

Effects of species, P, T, and crystallographic direction

Diffusivities were measured as a function of temperature, pressure, and crystallographic direction in the synthetic samples. Data for Sr were collected at four pressures for the c direction and two pressures for the a and b directions. Sm diffusion coefficients were derived from runs at three pressures for the c axis and at 20 Kbar for the a direction. Nearly identical compensation trends were defined for the two data sets (Sr and Sm) and values of D at the same temperature and pressure were usually comparable. Thus, despite differences in charge and ionic size between these two elements, diffusion of the two species appears to proceed at the same rate, if not by the same mechanism.

At one atmosphere, uncertainties in the Sr data caused overlap in the activation energies and measured diffusivities for the three directions, obscuring the relative ordering of the transport rates. Compensation was observed among them with the cross-over point at 1111 $\pm$ 26°C and 6.0(+7.9,-3.5) x 10^{-17} cm^2/sec. As a result of this, and of the similarity of the ΔH_a's, diopside behaves nearly isotropically for diffusion of Sr between 1000 and 1200°C.

High pressure runs were made at 8, 14, and 20 Kbar for the c axis and at 20 Kbar for the a and b directions. Negative activation volumes were calculated for one cation with values for Sr increasing with decreasing temperature. ΔV_a equals -10.3 $\pm$1.4 cm^3/mole at 1250°C, -4.5 $\pm$2.5 at 1200°C, and -2.3 $\pm$1.7 at 1100°C for strontium in the c direction. The effect of pressure at any temperature is to increase the diffusion coefficient. This was interpreted as a result of changes in the shape of the M(2) site and

possible rearrangement of the anions around the saddle points. Other explanations connected with possible experimental irregularities were addressed by duplicate runs and longer annealing times, with the results indicating that the negative ΔV_a's are real.

All data for strontium in the synthetic samples, including that of the Rutherford backscattering spectroscopy and the radiotracer and sectioning, plot on a compensation trend with an apparent cross-over temperature of 1269 $\pm$ 71°C and a diffusion coefficient of 1.0(+5.6, -0.8) x 10^{-14} cm^2/sec. Sm data give very similar values of T^{cr} and D^{cr}, suggesting that this is the compensation trend for all cations in diopside. This can be tested by determining diffusion rates of other species in the same material.

Applications

Due to the purity of the synthetic diopside, use of its diffusivities in models of geochemical processes was deemed to be inappropriate. The radiotracer data for natural samples were employed in the examination of various problems. Pressure effects were assumed to be similar to those of the laboratory-grown specimens.

The re-equilibration calculation of Hofmann and Hart (1978) was modified by using a D from this study, leading to an increase of a factor of 100 in the times to 95% equilibration at 1000°C. This makes it more likely that disequilibrium melting could account for variations in the $^{87}Sr/^{86}Sr$ ratio for oceanic rocks. However, cases of source/sink contact or the presence of a fluid will still destroy mineralogical scale heterogeneities before sufficient decay of ^{87}Rb can occur to significantly alter the 87/86 ratios of the melt fractions.

The compensation line for Sr in synthetic samples was plotted on a log D_o vs. ΔH_a graph which had been contoured for closure temperatures. Closure was seen to occur at temperatures above 1000°C for all but the

slowest cooling rates. Substitution of a line of similar slope through the RT natural sample point gave temperatures which were 100 to 200°C less than for the synthetic crystals at the same cooling rate. The physical significance of this high blocking T is that trace element and isotopic concentrations will reflect values present at the time of solidification. Dating techniques will give igneous ages and geothermometers/geobarometers will give temperatures and pressures of the crystallization event. Crystal zonation and non-equilibrium partitioning will persist throughout the rock's history. Exceptions to this would be in cases of long term high-grade metamorphism or the presence of a fluid at temperatures approaching the closure point.

Generation of pyroxene exsolution lamellae has been used by a number of authors to calculate cooling times for igneous bodies. The assumption that volume diffusion controls the growth rate used by these models is suspect in that transport experiments using lamellae as the starting material give diffusivities well below those of tracer studies. Numbers used in different models were replaced with values derived from this study which significantly changes the results in cases of depth of burial for a lunar sample (Huebner et al., 1975) and meteorites in a parent planetoid (Miyamoto and Takeda, 1977). Further studies including major elements are needed to more accurately assess the role of diffusion in exsolution processes.

This is also true in the application of the diffusion data to conductivity measurements in the earth. Values of σ ($ohm^{-1}cm^{-1}$) were calculated from the present data via the Nernst-Einstein equation and were compared with directly measured values for pyroxenes. No agreement was observed, indicating either that the M(2) site ions are not the charge carriers in ionic conduction or that conduction is not ionically controlled in the temperature range of the electrical and/or transport measurements.

Expansion of the study

It appears to be true that every question answered leads to two more questions. Further study of diffusion in clinopyroxene is needed to examine some apparent trends exposed by this thesis and to corroborate evidence presented here. High pressure experiments in the natural starting materials would show whether or not the negative activation volumes derived from the synthetic samples are representative of all diopsides. The apparent order-of-magnitude difference between Ca and Sr transport should be checked by completion of the calcium tracer study in a natural sample and determination of its diffusivities in the synthetic material. The latter would also provide a test of the compensation trend evident in the Sr and Sm data.

The effect of impurities, especially Fe, can be examined by the growth of crystals with specific trace element signatures. In this way different defect factors can be isolated and quantified. Iron is important because of its variable oxidation state and its ready substitution for Mg.

Once material behavior has been reasonably well established, other cations which are representative of groups of elements or which have important geochemical ramifications should be studied. Examples of the first category are tri-valent and quadra-valent transition elements and alkalies, while Al, Si, Mg, and O would represent the second. These will not only answer specific questions about transport of these species but offer some predictive capabilities for the behavior of other elements.

Transport data are extremely lacking for all silicates, with the possible exception of forsterite. Comprehensive programs of diffusion study such as outlined above for important minerals would greatly aid the application of kinetic theories to geologic situations. This study has taken some steps in that direction, but perhaps more importantly has demonstrated the feasibility of a relatively new powerful analytical tool, the ion microprobe. Proper

use of this and other rarely-utilized stable tracer techniques will greatly expand the data base for sophisticated modelling of petrogenetic processes, and increase the understanding of those regions of the earth and other bodies which cannot be directly sampled.

REFERENCES

Albarede, F., and Y. Bottinga, 1972, Kinetic disequilibrium in trace-element partitioning between phenocrysts and host lava. Geochim. Cosmochim. Acta, 36, 141-156.

Amirkhanoff, Khl., E. N. Bartnitsky, S. B. Brandt, G. V. Voitkevitch, 1959. Dokl Akad Nauk SSSR, Earth Sci. Sect., 126, 394-395. (see Freer, 1981)

Anderson, D. E., 1981, Diffusion in electrolyte mixtures. In: A. C. Lasaga and R. J. Kirkpatrick (eds), Reviews in Minerology, Vol. 8: Kinetics of Geochemical Processes, Mineralogical Society of America, Washington, 211-260.

Anderson, T. F., and R. B. Kasper, 1975, Oxygen self-diffusion in albite under hydrothermal conditions (abst). EOS, 56, 459.

Boltzmann, L., 1894, Integration der diffusionsgleichung bei variabeln diffusionscoefficienten. Annln. Phys., 53, 959-964.

Boyd, F. R., and J. L. England, 1960, Apparatus for phase-equilibrium measurements at pressures up to 50 kilobars and temperatures up to 1750°C. Jour. Geophysical Research, 65, 741-748.

Brady, J. B., 1975, Reference frames and diffusion coefficients. Amer. Jour. Sci., 275, 954-983.

Brady, J. B., and R. H. McCallister, 1980, Diffusion kinetics of homogenization and coarsening of pigeonite lamellae in subcalcic diopside (abst.). GSA Abstracts with Programs, 12, 391.

Brebec, G., R. Seguin, C. Sella, J. Bevenot, and J. C. Martin, 1980, Diffusion du silicium dans la silice amorphe. Acta Metallurgica, 28, 327-333.

Buening, D. K., and P. R. Buseck, 1973, Fe-Mg lattice diffusion in olivine. Jour. Geophysical Research, 78, 6852-6862.

Burns, W. K., P. H. Klein, E. J. West, and E. Plew, 1979, Ti diffsuion in Ti:$LiNbO_3$ planer and channel optical waveguides. Jour. Applied Physics, 50, 6175-6182.

Chapin, C. E., 1979, Evolution of the Rio Grande Rift - a summary. In: R. E. Riecker (ed), Rio Grande Rift: Tectonics and Magmatism, American Geophysical Union, Washington, 1-5.

Choudhury, A., D. W. Palmer, G. Amsel, H. Curien, and P. Baruch, 1965, Study of oxygen diffusion in quartz using the nuclear reaction $^{18}O(p,\alpha)^{15}N$. Solid State Communications, 3, 119-122.

Christoffersen, R., J. Tullis, and R. A. Yund, 1981, K-Na interdiffusion in alkali feldspar: effect of crystallographic anisotropy and pressure (abst). EOS, 62, 411.

Chu, W. -K., J. W. Mayer, and M. -A. Nicolet, 1978, Backscattering Spectroscopy, Academic Press, New York, 384 pp.

Clark, A. M., J. V. P. Long, 1971, The anisotropic diffusion of nickel in olivine. In: J. N. Sherwood, A. V. Chadwick, W. M. Muir, and F. L. Swinton (eds), Proceedings of the Thomas Graham Memorial Symposium, Gordon and Breach, London, 511-521.

Cooper, A. R., 1968, The use and limitation of the concept of an effective binary diffusion coefficient for multi-component diffusion. In: J. B. Wachtman, Jr. and A. D. Franklin (eds), Mass Transport in Oxides, Natl. Bur. Stds. Special Publication 296, 79-84.

Crank, J., 1975, The Mathematics of Diffusion, Oxford University Press, London, 414 pp.

Darkin, L. S., 1948, Diffusion, mobility and their interrelation through free energy in binary metallic systems. Trans. AIME, 175, 189-201.

Deer, W. A., R. A. Howie, and J. Zussmann, 1966, An Introduction to Rock-forming Minerals, Longman Group, Ltd., London, 528 pp.

Dennis, P., 1981, work in progress. (see Freer, 1981)

DePaolo, D. J., and G. J. Wasserburg, 1979, Sm-Nd age of the Stillwater complex and the mantle evolution curve for neodymium. Geochim. Cosmchim. Acta, 43, 999-1008.

Dodson, M. H., 1973, Closure temperature in cooling geochronological and petrological systems. Contr. Mineral. Petrol., 40, 259-274.

Duba, A., J. N. Boland, and A. E. Ringwood, 1973, The electrical conductivity of pyroxene. Jour. Geology, 81, 727-735.

Duckworth and Freer, 1981, Work in progress. (see Freer, 1981)

Dunham, A. C., P. A. Copley, and V. H. Strasser-King, 1972, Submicroscopic exsolution lamellae in pyroxenes in the Whin sill, Northern England. Contr. Mineral. Petrol., 37, 211-220.

Eisen, F. H., and C. E. Birchenell, 1959, Self-diffusion in indium antimonide and gallium antimonide. Acta Metallurgica, 5, 265-274.

Elphick, S. C., J. Ganguly, and T. P. Loomis, 1981, Experimental study of Fe-Mg interdiffusion in aluminosilicate garnet (abst). EOS, 62, 411.

Fechtig, H., W. Gentner, and J. Zähringer, 1960, Argonbestimmungen an kaliummineralien - VII: diffusionverluste von argon in mineralien und ihre auswirkung auf die kalium-argon-altersbestimmung. Geochim. Cosmochim. Acta, 19, 70-79.

Flower, M. F. J., H. U. Shmincke, and R. N. Thompson, 1975, Phlogopite stability and the $^{87}Sr/^{86}Sr$ step in basalts along the Reykjanes Ridge. Nature, 254, 404-406.

Freer, R., 1980, Bibliography: self-diffusion and impurity diffusion in oxides. Jour. Materials Sci., 15, 803-824.

Freer, R., 1981, Diffusion in silicate minerals and glasses: a data digest and guide to the literature. Contr. Mineral. Petrol., 76, 440-454.

Frischtat, G. H., 1970, Ber Dtsch Keram Ges, 47, 364-368. (see Freer, 1981)

Fujii, T., 1981, Ca-Sr chemical diffusion in melt of albite at high temperature and pressure (abst). EOS, 62, 428.

Gilder, H. M., B. J. Buescher, and L. Chhabildas, 1971, Activation volumes in zinc and cadmium. In: A. Lodding and T. Lagerwell (eds), Atomic Transport in Solids and Liquids, Verlag der Zeitschrift für Naturforschung, Tübingen, 331-335.

Giletti, B. J., and T. F. Anderson, 1975, Studies in diffusion, II. Oxygen in phlogopite mica. Earth Planet. Sci. Letters, 28, 225-233.

Giletti, B. J., J. H. Hickey, and T. E. Tullis, 1979, Oxygen diffusion in olivine under hydrous conditions (abst.). EOS, 60, 370.

Giletti, B. J., and K. L. Nagy, 1981, Grain boundary diffusion of oxygen along lamellar boundaries in perthitic feldspars (abst). EOS, 62, 428.

Giletti, B. J., M. P. Semet, and R. B. Kasper, 1974, Self-diffusion of potassium in low albite using an ion microprobe (abst). GSA Abstracts with Programs, 6, 754.

Giletti, B. J., M. P. Semet, and R. A. Yund, 1976, Oxygen self-diffusion measured in silicates using an ion microprobe (abst). EOS, 57, 350.

Giletti, B. J., M. P. Semet, and R. A. Yund, 1978, Studies in diffusion - III. Oxygen in feldspars: an ion microprobe determination. Geochim. Cosmochem. Acta, 42, 45-57.

Giletti, B. J., and J. Tullis, 1977, Studies in diffusion, IV. Pressure dependence of Ar diffusion in phlogopite mica. Earth Planet. Sci. Letters, 35, 180-183.

Giletti, B. J., R. A. Yund, and M. Semet, 1976, Silicon diffusion in quartz (abst). GSA Abstracts with Programs, 8, 884.

Hall, P. M., and J. M. Morabito, 1976, A formalism for extracting diffusion coefficients from concentration profiles. Surface Sci., 54, 79-90.

Hallwig, D., R. Schactner, and H. G, Sockel, 1981, in: K. Dyrek, J. Haber, and J. Nowotny (eds), Proceedings 9th International Symposium on the Reactivity of Solids, Elsevier (in press). (see Freer, 1981)

Harrison, W. J., and B. J. Wood, 1980, An experimental investigation of the partioning of REE between garnet and liquid with reference to the role of defect equilibria. Contr. Mineral. Petrol., 72, 145-155.

Hart, S. R., 1981, Diffusion compensation in natural silicates. Geochim. Cosmochim. Acta, 45, 279-291.

Hart, S. R., N. Shimizu, and D. Sverjensky, 1981, Lead isotope zoning in galena: an ion microprobe study of galena from the Buick Mine, S. E. Missouri (abst). EOS, 62, 429.

Hartree, D. R., 1935, Repeated intergrals of the error function. Mem. Proc. Manchester Lit. and Phil. Soc., 80, 85-102.

Haul, Von R., and G. Dumbgen, 1962, Untesuchung der saurstoffbeglichkeit in titandioxyd, quarz, und quzrzglas mit hiffe des heterogen isotopenaustausches, Z. für Elektrochemie, 66, 636-641.

Herzog, R. F. K., W. P. Poschenrieder, and F. G. Stakiewicz, 1973, Observation of clusters in a sputtering ion source. Radiation Effects, 18, 199-205.

Hinze, E., G. Will, and L. Cemic, 1981, Electrical conductivity measurements on synthetic olivines and an olivine, enstatite and diopside from Dreiser Weiher, Eifel (Germany) under defined thermodynamic activities as a function of temperature and pressure. Physics Earth Planet. Interiors, 25, 245-254.

Hofmann, A. W., 1974, Strontium diffusion in a basalt melt and implications for Sr isotope geochemistry and geochronology. Carnegie Inst. Wash. Yearbook, 73, 935-941.

Hofmann, A. W., 1980, Diffusion in natural silicate melts: a critical review. In: R.B. Hargraves (ed.), Physics of Magmatic Processes, Princeton University Press, Princeton, 385-418.

Hofmann, A. W., and L. Brown, 1976, Diffusion measurements using fast deuterons for in situ production of radioactive tracers. Carnegie Inst. Wash. Yearbook, 75, 259-262.

Hofmann, A. W., and B. J. Giletti, 1970, Diffusion of geochronologically important nuclides in minerals under hydrothermal conditions. Ecologae Geol. Helv., 63, 141-150.

Hofmann, A. W., B. J. Giletti, J. R. Hinthorne, C. A. Andersen, and D. Comaford, 1974, Ion microprobe analysis of a potassium self-diffusion experiment in biotite. Earth Planet. Sci. Letters, 24, 48-52.

Hofmann, A. W., and S. R. Hart, 1978, An assessment of local and regional isotopic equilibrium in the mantle. Earth Planet. Sci. Letters, 38, 44-62.

Hofmann, A. W., and M. Magaritz, 1977, Diffusion of Ca, Sr, Ba, and Co in a basalt melt: implications for the geochemistry of the mantle. Jour. Geophysical Research, 82, 5432-5440.

Hofmann, A. W., and W. M. White, 1981, Mantle plumes from subducted oceanic crust (abst.). EOS, 62, 424.

Huebner, J. S., and G. L. Nord, Jr., 1981, Assessment of diffusion in pyroxenes: What we do and do not know. Lunar and Planetary Sci., 12, 479-481.

Huebner, J. S., M. Ross, and N. Hickling, 1975, Significance of exsolved pyroxenes from lunar breccia 77215. Proc. Lunar Sci. Conf., 6th, 529-546.

Hudson, J. B., and R. E. Hoffman, 1961, The effect of hydrostatic pressure on self-diffusion in lead. Trans. Metallurgical Soc. AIME, 221, 761-768.

Huneke, J. C., J. T. Armstrong, and G. J. Wasserburg, 1981, ^{41}K and ^{26}Mg in Allende inclusions and a hint of ^{41}Ca in the early solar system. Lunar Planet. Sci., XII, 482-484.

Ishitani, T., and R. Shimizu, 1975, Computer simulation of atomic mixing during ion bombardment. Applied Physics, 6, 241-248.

Jambon, A., 1980, Isotope fractionation: a kinetic model for crystals growing from magmatic melts. Geochim. Cosmochim. Acta, 44, 1373-1380.

Jambon, A., and J.-P. Carron, 1976, Diffusion of Na, K, Rb, and Cs in glasses of albite and orthoclase composition. Geochim. Cosmochim. Acta, 40, 897-903.

Jambon, A., and J.-P. Carron, 1978, Bull. Mineral., 101, 22-26, (in French), (see Freer, 1981).

Jambon, A., and F. Delbove, 1977, C. R. Acad. Sci. Ser. D (Paris), 284, 2191-2194, (in French) (see Freer, 1981).

Jambon, A., and M. Semet, 1978, Lithium diffusion in silicate glasses of albite, orthoclase, and obsidian composition: an ion microprobe determination. Earth Planet. Sci. Letters, 37, 445-450.

Jaoul, O., C. Froidevaux, W. B. Durham, and M. Michaut, 1980, Oxygen self-diffusion in forsterite: implications for the high-temperature creep mechanism. Earth Planet. Sci. Letters, 47, 391-397.

Karsten, J. L., and J. R. Delaney, 1980, A new calculation of water diffusivity in rhyolite glass (abst.). EOS, 61, 398.

Kasper, R. B., 1974, Cation diffusion in a low albite (abst.). GSA Abstracts with Programs, 6, 815.

Kirkaldy, J. S., 1970, Isothermal diffusion in multi-component systems. In: H. Herman (ed.), Advances in Materials Res., 4, 55-100.

Lasaga, A. C., 1981, The atomistic basis of kinetics: defects in minerals. In: A. C. Lasaga and R. J. Kirkpatrick (eds.), Reviews in Mineralogy, Vol. 8: Kinetics of Geochemical Processes, Mineralogical Society of America, Washington, 261-319.

Lasaga, A. G., and R. J. Kirkpatrick, 1981, Reviews in Mineralogy, Volume 8: Kinetics of Geochemical Processes, Mineralogical Society of America, Washington, 398 pp.

Laursen, T., and W. A. Lanford, 1978, Hydration of obsidian. Nature, 276, 153-156.

Levien, L., and C. T. Prewitt, 1981, High-pressure structural study of diopside. Amer. Mineralogist, 66, 315-323.

Lindner, R., 1955, Studies of solid state reactions with radiotracers, Jour. Chemical Physics, 23, 410-411.

Lo, C. C., and D. E. Schuele, 1975, Beam-diameter correction of x-ray intensity profile over small diffusion zones. Jour. Applied Physics, 46, 5004-5009.

Lowry, R. K., S. J. B. Reed, J. Nolan, P. Henderson, and J. V. P. Long, 1981, Lithium tracer-diffusion in an alkali-basaltic melt--an ion-microprobe determination. Earth Planet. Sci. Letters, 53, 36-40.

MacGregor, I. D., 1979, Mafic and ultramafic xenoliths from the Kao kimberlite pipe. In: F. R. Boyd and H. O. A. Meyer (eds.), The Mantle Sample: Inclusions in Kimberlites and Other Volcanics, American Geophysical Union, Washington, 156-172.

Magaritz, M., and A. W. Hofmann, 1978a, Diffusion of Sr, Ba and Na in obsidian. Geochim. Cosmochim. Acta, 42, 595-605.

Magaritz, M., and A. W. Hofamnn, 1978b, Diffusion of Eu and Gd in basalt and obsidian. Geochim. Cosmochim. Acta, 42, 847-858.

Matano, C., 1933, On the relationship between the diffusion coefficients and concentrations of solid metals. Japanese Jour. Physics, 8, 109-133.

Matsui, Y., 1973, Stereochemistry of the structure of minerals stable under high pressures. In: N. Onuma and A. Masada (eds.), The distribution of elements in rock-forming processes, 31-64, (in Japanese).

McCallister, R. H., 1974, Kinetics of enstatite exsolution from supersaturated diopsides. In: A. W. Hofmann, B. J. Giletti, H. S. Yoder, Jr., and R. A. Yund (eds.), Geochemical Transport and Kinetics, Carnegie Inst. Wash., Washington, 195-204.

McCallister, R. H., 1980, Determination of major cation diffusion constants in pyroxenes (abst.). GSA Abstracts with programs, 12, 479.

McCallister, R. H., and J. B. Brady, 1979, Self-diffusion of calcium in diopside (abst.). GSA Abstracts with Programs, 11, 474.

McCallister, R. H., J. B. Brady, and B. O. Mysen, 1979, Self-diffusion of Ca in diopside. Carnegie Inst. Wash. Yearbook, 78, 574-577.

Medford, G. A., 1973, Calcium diffusion in a mugearite melt. Canadian Jour. Earth Sci., 10, 394-402.

Misener, D. J., 1974, Cationic diffusion in olivine to 1400°C and 35 Kbar. In: A. W. Hofmann, B. J. Giletti, H. S. Yoder, Jr., and R. A. Yund (eds.), Geochemical Transport and Kinetics, Carnegie Inst. Wash., 117-130.

Misra, N. K., and V. S. Venkatasubramanian, 1977, Strontium diffusion in feldspars--a laboratory study. Geochim. Cosmochim. Acta, 41, 837-838.

Miyamoto, M., and H. Takeda, 1977, Evaluation of a crust model of eucrites from the width of exsolved pyroxene. Geochemical Jour., 11, 161-169.

Morioka, M., 1980, Cation diffusion in olivine-I. Cobalt and magnesium. Geochim. Cosmochim. Acta, 44, 759-762.

Morioka, M., 1981, Cation diffusion in olivine-II. Ni-Mg, Mn-Mg, Mg and Ca. Geochim. Cosmochim. Acta, 45, 1573-1580.

Muehlenbachs, K., and I. Kushiro, 1974, Oxygen isotope exchange and equilibrium of silicates with CO_2 and O_2. Carnegie Inst. Wash. Yearbook, 73, 232-236.

Muehlenbachs, K., and I. Kushiro, 1975, Measurements of oxygen diffusion in silicates (abst.). AOS, 56, 459.

Mysen, B. O., and M. G. Seitz, 1975, Trace element partitioning determined by beta track mapping: an experimental study using carbon and samarium as examples. Jour. Geophysical Research, 80, 2627-2635.

Nord, G. L., Jr., 1980, Decomposition kinetics in clinopyroxenes (abst.). GSA Abstracts with Programs, 12, 492.

Oishi, Y, and W. D. Kingery, 1960, Self-diffusion of oxygen in single crystal and polycrystalline aluminum oxide. Jour. Chemical Physics, 33, 480-486.

O'Nions, R. K., and R. J. Pankhurst, 1974, Petrogenetic significance of isotope and trace element variation in volcanic rocks from the Mid-Atlantic. Jour. Petrology, 15, 603-634.

Onsager, L., 1945, Theories and problems of liquid diffusion. Ann. New York Acad. Sci., 46, 241-265.

Poumellac, M., O. Jaoul, C. Froidevaux, and A. Havette, 1981, Silicon diffusion in forsterite: a new constraint for understanding mantle deformation. (In press.)

Ray, G. L., 1980, An ion microprobe study of trace element partitioning between clinopyroxene and liquid in the diopside ($CaMgSn_2O_6$)- albite ($NaAlSi_3O_8$)-anorthite ($CaAl_2Si_2O_8$) system. Ph.D. thesis, MIT, 142 pp.

Reddy, K. P. R., and A. R. Cooper, 1976, Diffusion of oxygen in sapphire (abst.). Amer. Ceramic Soc. Bull., 55, 402.

Reddy, K. P. R., and A. R. Cooper, 1978, Oxygen diffusion in single and polycrystalline alumina (abst.). Amer. Ceramic Soc. Bull., 57, 306.

Reddy, K. P. R., S. M. Oh, L. D. Major, Jr., and A. R. Cooper, 1980, Oxygen diffusion in forsterite. Jour. Geophysical Research, 85, 322-326.

Reed, D. J., and B. J. Wuensch, 1980, Ion-probe measurement of oxygen self-diffusion in single-crystal Al_2O_3. Jour. Amer. Ceramic Soc., 63, 88-92.

Rice, S. A., and N. H. Nachtrieb, 1959, On the dynamical theory of diffusion in crystals. II. Pressure dependence of the self-diffusion constant. Jour. Chemical Physics, 31, 139-145.

Richardson, S. H., E. R. Padovani, and S. R. Hart, 1980, The gneiss syndrome: Nd- and Sr-isotopic relationships in lower crustal granulite xenoliths, Kilbourne Hole, New Mexico (abst.). EOS, 61, 338.

Rüetschi, P., 1958, The relation between frequency factor and activation energy (compensation law). Z. für Physikalische Chemie Neue Folge, 14, 277-291.

Sanford, R. F., and J. S. Huebner, 1979, Reexamination of diffusion processes in 77115 and 77215. Lunar and Planetary Sci., 10, 1052-1054.

Seitz, M. G., 1973, Uranium and thorium diffusion in diopside and fluorapatite. Carnegie Inst. Wash. Yearbook, 72, 586-588.

Shankland, T. J., 1969, Transport properties of olivine. In: S. K. Runcorn (ed.), The Application of Modern Physics to the Earth and Planetary Interiors, Interscience, New York, 175-190.

Shewmon, P. G., 1963, Diffusion in Solids, McGraw-Hill Book Company, New York, 203 pp.

Shimizu, N., 1981a, Trace element incorporation into growing augite phenocryst. Nature, 289, 575-577.

Shimizu, N., 1981b, A kinetic model of trace element partitioning between crystal and magma. (In preparation.)

Shimizu, N., 1981c, REE partitioning between garnet and clinopyroxene: a possible geothermometer. (In preparation.)

Shimizu, N., and S. R. Hart, 1981a, Applications of secondary ion mass spectrometry to geochemistry and cosmochemistry. In: Annual Review of Earth and Planetary Sciences, Vol. 10, Annual Review, Palo Alto, (in press).

Shimizu, N., and S. R. Hart, 1981b, Isotope fractionation in secondary ion mass spectrometry. Jour. Applied Physics, (in press).

Shimizu, N., M. P. Semet, and C. J. Allegre, 1978, Geochemical applications of quantitative ion-microprobe analysis. Geochim. Cosmochim. Acta, 42, 1321-1334.

Sippel, R. F., 1963, Sodium diffusion in natural minerals. Geochim. Cosmochim. Acta, 27, 107-120.

Stacey, F. D., 1977, A thermal model of the Earth. Physics Earth Planet. Interiors, 15, 341-348.

Steele, I. M., R. L. Hervig, I. D. Hutcheon, and J. V. Smith, 1981, Ion microprobe techniques and analyses of olivine and low-Ca pyroxene. Amer. Mineralogist, 66, 526-546.

Talabar, J., 1968, Proc. Conf. Silicate, Budapest, 9th, 171-177, (see Freer, 1981).

Towers, H., and J. Chipman, 1957, Diffusion of calcium and silicon in a lime-alumina-silica slag. Jour. of Metals, Transactions AIME, 204, 769-773.

Varshneya, A. K., A. R. Cooper, R. B. Diegle, and S. A. Chin, 1973, Measurement of self-diffusion in solids by neutron activation of masked samples. Jour. Amer. Ceramic Soc., 56, 245-247.

Watson, E. Bruce, 1979, Calcium diffusion in a simple silicate melt to 30 Kbar. Geochim. Cosmochim. Acta, 43, 313-322.

Watson, E. Bruce, 1981, Diffusion in magmas at depth in the Earth: the effects of pressure and dissolved H_2O. Earth Planet. Sci. Letters, 52, 291-301.

Watson, E. B., and J. F. Bender, 1980, Diffusion of cesium, samarium, strontium, and chlorine in molten silicate at high temperatures and pressures (abst.). GSA Abstracts with Programs, 12, 545.

Winchell, P., 1969, The compensation law for diffusion in silicates. High Temperature Sci., 1, 200-215.

Winchell, P., and J. H. Norman, 1969, A study of the diffusion of radioactive nuclides in molten silicates at high temperatures. In: High Temperature Technology, 3rd Inter. Symp., Asilomar, 479-492.

Wohlbien, 1981, Diffusion and Defect Data (yearly abstracts volumes), Diffusion Information Center, Cleveland.

York, D., 1966, Least-squares fitting of a straight line. Canadian Jour. Physics, 44, 1079-1086.

Yund, R. A., and T. F. Anderson, 1974, Oxygen isotope exchange between potassium feldspar and KCl solution. In: A. W. Hofmann, B. J. Giletti, W. S. Yoder, Jr., and R. A. Yund (eds.), Geochemical Transport and Kinetics,

Carnegie Inst. Wash., Washington, 99-105.

Yund, R. A., and T. F. Anderson, 1978, The effect of fluid pressure on oxygen isotope exchange between feldspar and water. Geochim. Cosmochim. Acta, 42, 235-239.

Yund, R. A., and J. Tulles, 1980, The effect of water, pressure, and strain on Al/Si order-disorder kinetics in feldspar. Contr. Mineral. Petrol., 72, 297-302.

Zielinski, R. A., and F. A. Frey, 1974, An experimental study of the partitioning of a rare earth element (Gd) in the system diopside-aqueous vapor. Geochim. Cosmochim. Acta, 38, 545-565.

Zinner, E., 1978, The effect of preferential sputtering on ion microprobe depth profiles in minerals. Proc. 13th Annual Conf. of the Microbeam Analysis Soc., 32A-32D.

Zinner, E., 1980, Depth profiling by secondary ion mass spectrometry. Scanning, 3, 57-78.

ACKNOWLEDGEMENTS

Many people have contributed to this thesis in one way or another. Most will probably deny their guilt, but their assistance has been greatly appreciated.

Various and sundry equipment has been made available for my use by a number of sources to whom I am grateful: the M. I. T. Microelectronics Laboratory, Mr. Andy Holik (General Electric R and D Center, Schenectady, New York), John Dickey, Fred Frey, Ed Boyle, the R. P. I. Geology Department, and the glass science group (Department of Materials Engineering, R. P. I.). The Rutherford backscattering analyses were performed with Bill Lanford and Chandra Burman (Physics Department, SUNY Albany) and their interest and help are appreciated. I have benefited greatly from the crystal growing expertise of Woldy Belruss, David Gabbe, and others from the Crystal Physics Lab at M. I. T. and thank them for their guidance and encouragement. Special thanks go to Ken Burrhus, without whom the entire ion probe facility would grind (arc?) to a halt. His experience and his patience with inquisitive amateurs are gratefully acknowledged.

I thank the professors, staff, and fellow students (especially Scott Cameron, Karleen Davis, and the Reverend S. Movie Jones) who have assisted in numerous, not always academic, ways. I appreciate the brothers and the haven of Phi Beta Epsilon, both during my undergraduate years and while commuting from Albany to Boston. I am especially grateful to Bob Lambe for getting me interested in geochemistry in the first place, and to John Dickey for his enthusiasm and early guidance.

The typing of this thesis was masterfully handled by Theresa Miele with timely assistance from Kathy Thurmond. The figures were beautifully

drafted by Donna Hall with help from Steve Fortini. I truly appreciate the time and effort they invested in this manuscript. Dealing long-distance with the M. I. T. bureaucracy for two-and-a-half years was helped greatly by Debby Roecker (and her predecessor, Debby Gillett).

Much appreciation goes to my thesis committee, Bill Brace, Fred Frey, Stan Hart, Nobu Shimizu, and Bruce Watson. I have enjoyed working with Nobu Shimizu and have benefited immensely from his ion probe expertise and appreciation of the complexities of geochemical systems. I thank Bruce Watson for inviting me to work in his lab at R. P. I. He's taught me many things and hopefully some of his flair for simple yet important experiments has rubbed off during our association. Stan Hart has been a very good advisor for me, allowing me to work things out on my own but always having the answer or a helpful suggestion when I went to him. I've deeply appreciated the opportunity to be his student.

My parents are largely responsible for my being who I am today and I thank them for the values and support they have given over the years. Finally, I dedicate this thesis to my wife, Maggie. She has supported and encouraged me throughout my work, often carrying more than her share of responsibilities. Her love and understanding have made this task easier.

And I'm not dead yet.

APPENDIX 1: Crystal Growth.

Top-seeded solution growth (TSSG) is a method developed by Von Hippel and co-workers at the Laboratory for Insulation Research at M. I. T. to obtain large strain-free crystals. The process is capable of this due to its nearly isothermal nature. A heavily insulated furnace provides uniform heating of the melt while sufficient cooling of the seed to induce growth is obtained through the seed rod. The crystal is grown from solution by the gradual lowering of the temperature of the system.

This approach offers a number of advantages over other techniques. Materials whose melting points may be beyond the capability of the furnace and apparatus can be grown at lower temperatures from a solution. Also, if there is an interfering high temperature polymorph or phase change, it can be avoided. One of the earliest materials synthesized by TSSG, $BaTiO_3$, is an example of both these traits (Belruss, et al., 1971). By crystallizing from a liquid containing approximately 64 mole percent TiO_2 (Figure A1-1), cubic $BaTiO_3$ is grown beginning at about 1460°C. The operating temperature is reduced from the melting point of 1618°C and the hexagonal $BaTiO_3$ field is avoided. Another advantage is that the lack of large temperature gradients necessary in other methods allows the growth of practically dislocation free specimens. Small gradients are present and necessary because the crystal must be slightly cooler than the melt in order to avoid nucleation and growth elsewhere in the crucible.

There are some drawbacks to TSSG. A suitable solvent must be found which does not enter substitutionally into the lattice and is not overly volatile. Inclusions of solvent are sometimes observed due to their "capture" by the growing crystal. Finally, equilibrium growth rates are usually slower than in other processes.

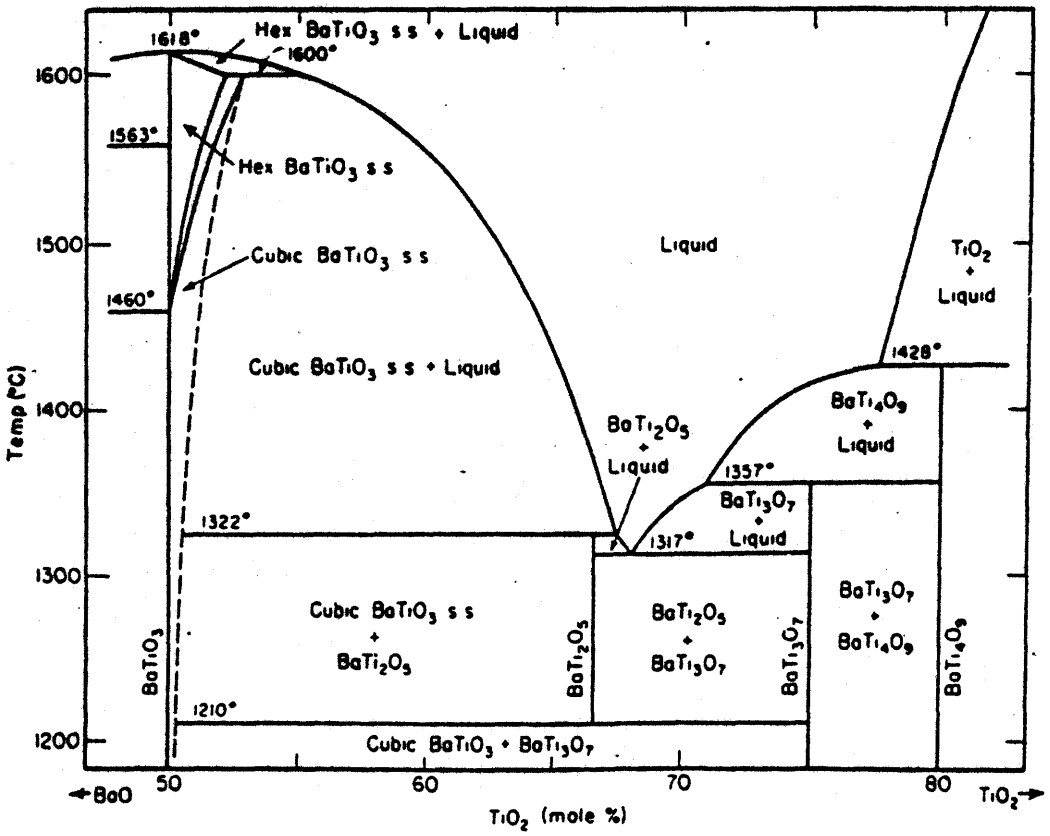

Figure A1-1. Phase diagram of $BaO-TiO_2$ system, after Rase and Roy (1955), showing the advantages of TSSG for growth of $BaTiO_3$.

The furnace and growth apparatus are shown schematically in figure A1-2. The furnace itself is constructed of alumina fire bricks for insulation and silicon carbide heating elements arranged vertically around the central work area. Entrance to the area is by removal of the closing bricks in the top. With these bricks in place, there must be access for control and measurement thermocouples, the seed rod, and two ports - one for viewing the run and the other for a light source to provide visibility in the furnace. The measurement thermocouple should be as close as possible to the melt to provide accurate information on the temperature near the crystal during the run. Temperature control is achieved with a proportional controller, and automatic temperature lowering and rise are accomplished with clock motors and percentage timers attached to the set point potentiometers. Rates from less than 0.1°C/hr to 75°C/hr were available on the system used.

The seed is attached to a double-walled Pt10%Rh tube with a soft Pt spring mounted at the closed or bottom end. Cooling air travels down the center of the tube and then back up through the outer tube (Figure A1-3). The spring insures good thermal contact between the rod and the seed. The Pt seed rod attaches to an air source and rotation motor outside the furnace. Rotation acts to homogenize the growth of the crystal and to stir the melt to a certain extent, thus avoiding concentration gradients in the liquid. The system used in this study had variable rotation speed of 0 to 80 rpm with most growth runs using a rate of 30 to 40 rpm. The seed rod and rotation motor are attached to the pulling apparatus which consists of a screw and half-nut assembly, a variable speed motor, and a gearbox. Growth occurs below the surface of the melt, therefore pulling is not necessary in the sense that it is for Czochralski growth where

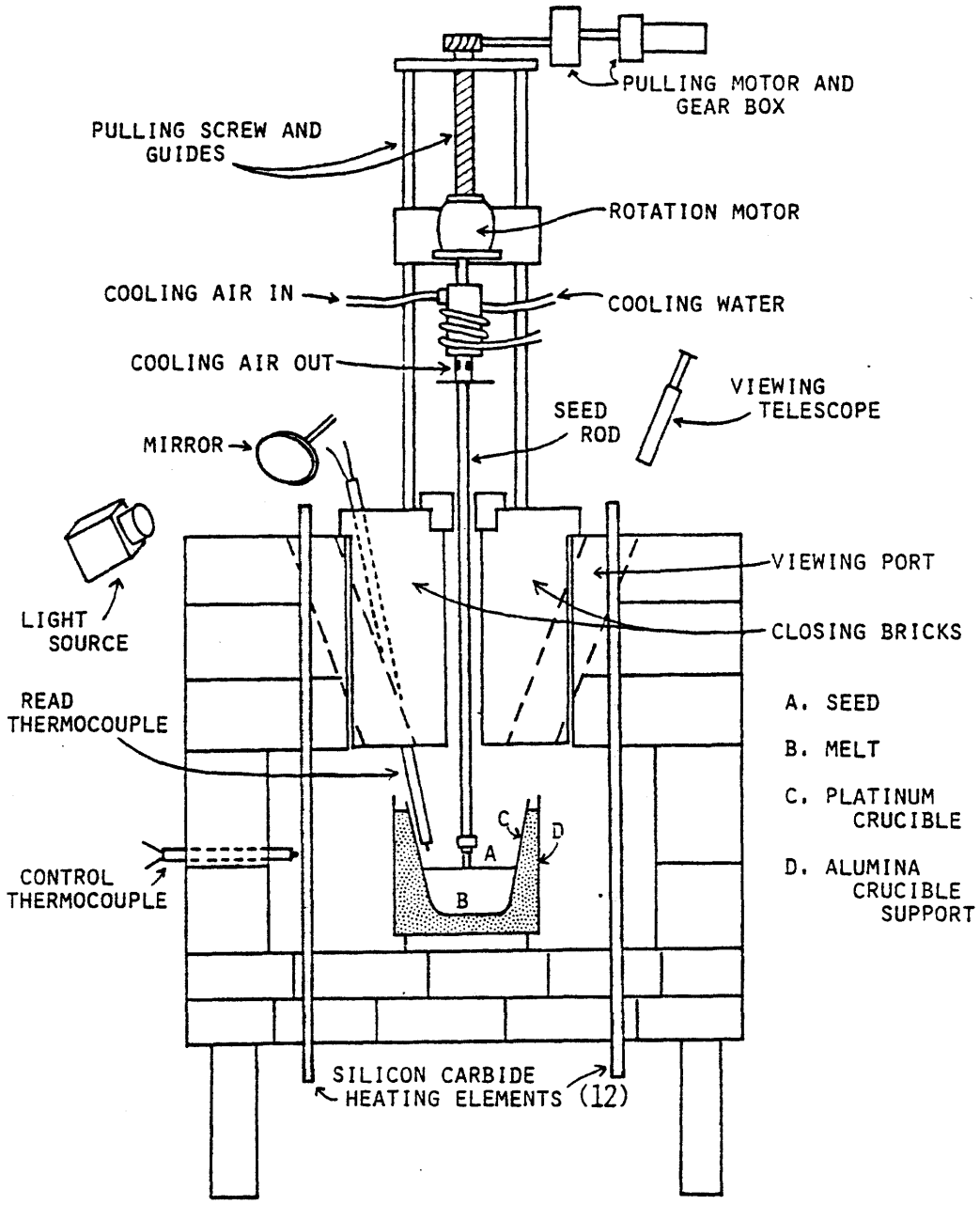

Figure A1-2. Top-seeded solution growth furnace and crystal pulling apparatus. Different elements of the drawing are not to scale.

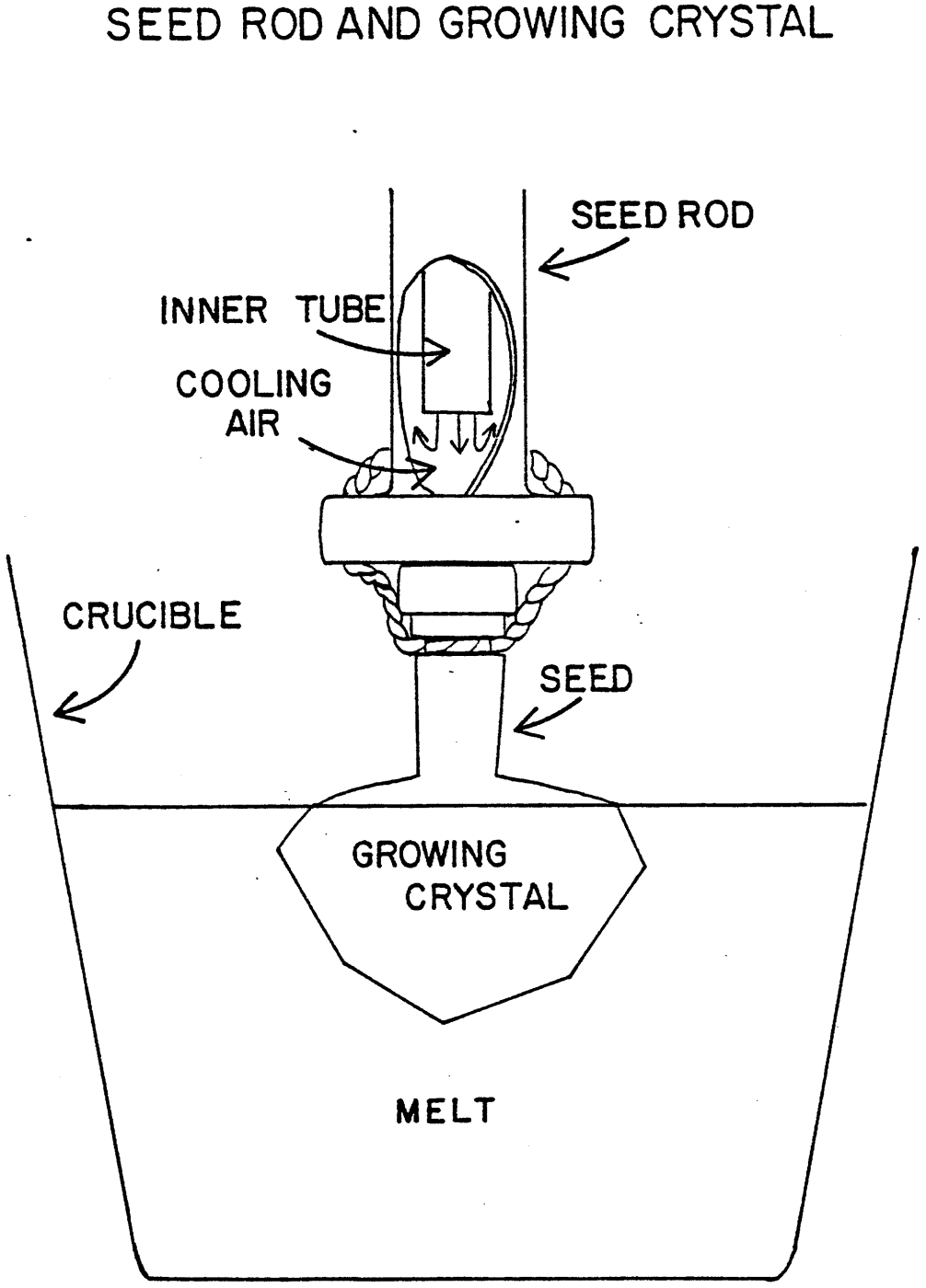

Figure A1-3. Seed rod and growing crystal, showing cut-away of the inner tube. Seed is attached to the rod by Pt wires placed in a notch cut around the seed and then through notches in the button end of the rod. Pt spring is between the crystal and the button.

crystallization occurs at the melt-air interface. In TSSG pulling is used to control the radial size of the crystal and also help to avoid hitting the bottom of the crucible with the growing specimen. Pulling rates of the M. I. T. apparatus varied from less than 0.1 mm/hr to 30 cm/hr.

Several exploratory runs were performed to decide on a starting composition for seeded growth runs. These included simple temperature lowering of various compositions without seeding to determine if diopside would crystallize from a nearly stoichiometric melt. In addition, two compositions were seeded with a platinum wire attached to the end of the seed rod. The composition for which diopside could be effectively grown is listed in Table A1-1. Silicic acid ($SiO_2 \cdot nH_2O$) was heated to 1100°C until weight loss between weighings was negligible (approximately 24 hrs). SiO_2 was then weighed as the oxide, and CaO and MgO were weighed as carbonates. MgF_2 was used as a flux to reduce viscosity in the melt and therefore remove some undercooling problems which occured in early attempts with a Pt wire seed. At run temperature the fluoride breaks down and is lost over the course of a week. It was assumed that MgF_2 simply goes to the oxide MgO when it breaks down. If none of the fluoride is lost, the starting composition used lies within the diopside field on the ternary phase diagram SiO_2-CaO-MgO when projected through the MgF_2 end-member of the quaternary system. If all of the fluoride goes to oxide, the resulting composition is stoichiometric diopside.

One hundred and fifty-five grams of starting material were melted in a 100 ml Pt crucible by raising the temperature to about 1410°C at a rate of 75°C/hr to avoid violent break down of the carbonates. Because diopside seeds were not available, initial runs were seeded with a twisted Pt

Table A1-1. Melt composition (GR 2) with and without MgF_2.

	starting composition		all $MgF_2 \rightarrow MgO$	
	mole %	wt %	mole %	wt %
SiO_2	50.2	53.7	50.2	55.5
CaO	24.9	25.1	24.9	25.9
MgO	16.6	12.0	24.9	18.6
MgF_2	8.3	9.3	0.0	0.0

wire lowered one mm into the melt which had soaked at 1410°C for 6 to 8 hours. Introduction of the cooled seed rod caused the measured temperature to drop about 6°C. The furnace was brought to 1395°C and temperature lowering was then set at 0.1°C/hr. The runs (GR 2 and GR 3) were allowed to proceed for two days and GR 3 produced a mass of diopside approximately 4 cm in diameter and 1 cm thick. About one-third of this was a single crystal which was sectioned for use as seed material in subsequent runs.

Most diopside seeded experiments utilized the same quantity of the starting composition and were seeded at 1394°C (temperature after seed rod introduction). The seed crystal was brought just to the contact with the melt and was not immersed as the wire had been. At the introduction temperature a small amount of the crystal melted, which is desirable in that it produces a fresh surface. Temperature was slowly lowered ($\sim$5°C/hr) until dissolution stopped and then held for a few hours at that point. Slight temperature lowering (<0.1°C/hr) was then used to encourage growth. After three days and a loss of about 5°C crystals were large enough to terminate the runs. This was done by pulling the crystal from the melt quickly (30 cm/hr) but keeping it within the hot zone of the furnace. The system was then cooled at a rate of 25°C/hr to about 200°C at which time power was shut off. Crystals were removed when the measured temperature was less than 150°C. Runs GR 4 and GR 5 produced large single crystal diopsides which exhibited well developed faces. Faceting occurs in many TSSG products due to the fact that growth is slow and takes place below the surface of the melt. Information regarding run conditions and results for all experiments are given in Table A1-2.

During runs GR 7 to GR 10 a dense smoke developed in the furnace, impairing visibility and attacking the seeds before they even reached the

Table A1-2. Compilation of crystal growth runs.

run #	GR 1	GR 2	GR 3	GR 4	GR 5	GR 6	GR 7	GR 8	GR 9	GR 10	GR 11	GR 12
starting composition (mole %)												
SiO_2	43.2	50.2	50.2	50.2	50.2	49.7	49.7	49.6	50.2	50.2	50.0	50.0
CaO	21.6	24.9	24.9	24.9	24.9	24.9	24.9	24.8	24.9	24.9	25.0	25.0
MgO	23.5	16.6	16.6	16.6	16.6	16.8	16.8	16.5	16.6	16.6	16.7	16.7
MgF_2	11.7	8.3	8.3	8.3	8.3	8.4	8.4	8.3	8.3	8.3	8.3	8.3
SrO	-	-	-	-	-	0.3	0.3	0.6	-	-	-	-
Sm_2O_3	-	-	-	-	-	0.03	0.01[1]	0.2	-	-	-	-
seed	wire	wire	wire	Di	Di	Di	Di	Di	wire	Di	Di	Di
direction	-	-	-	⊥ ab plane	// a	// b	// c	⊥ ab plane	-	⊥ ab plane	⊥ ab plane	// c
product	M[2] Fo	M Di	M Di	S Di	S Di	M Di	M Di	M Di	M Di	none	M Di	S Di
size (cm)			U[3]	3.5x 2.5x 2.0	2.5x 2.0x 2.0	U	U	U	U		U	2.5x 1.0x 1.0

[1] all Sm as ^{152}Sm

[2] M = multicrystalline mass, S = single crystal

[3] U = usable single crystal areas at least 4 x 4 mm

melt. The exact nature of the vapor was not determined although qualitative spectroscopic analysis indicated the presence of Si and Ca. The problem disappeared when the growth operation was transfered to another furnace with new fire bricks for runs GR 11 and GR 12. It is postulated that the vapor is a fluoride of some description which is adsorbed by the alumina bricks which eventually become saturated. Subsequent runs are therefore hampered by the presence of the smoke. The effect of the vaporization on the melt composition was not measured.

X-ray diffraction patterns of powdered samples of run products gave values in excellent agreement with published results for diopside (eg. GR 4 in Table A1-3). Electron microprobe analyses of the various run products are given in Table A1-4 and generally show a trend of Mg enrichment in comparison with end-member diopside. The cause of this is not apparent and may stem from changes in melt composition due to vaporization or from the thermodynamics of pyroxene crystallization. Ion microprobe analysis of minor and trace elements show approximately 0.1 wt% FeO in runs GR 4 to GR 6, and 450 ppm Sr and 250 ppm Sm in GR 6.

Top-seeded solution growth has been shown to be a viable means of producing high quality diopside crystals of large size. These synthetic crystals have numerous uses ranging from studies of physical properties to controlled variation of individual elemental compositions for geochemical applications. Further experiments should be undertaken to examine the introduction of various elements into diopside and the feasibility of growing other phases by the TSSG method.

Table A1-3. X-ray diffraction data for GR 4 and diopside.

GR 4		diopside	
d	I	d	I
3.233	51	3.231	28
2.993	100	2.992	100
2.950	61	2.951	32
2.897	41	2.894	42
2.566	33	2.566	25
2.517	60	2.524 2.518	64
1.624	53	1.624 1.617	33

unit cell		
a	9.77 Å	9.748 Å
b	8.94 Å	8.926 Å
c	5.22 Å	5.250 Å
β	105.98°	105.86°

Table A1-4. Electron microprobe analyses - average compositions.

	GR 3	GR 4	GR 5	GR 6	GR 7	GR 8	GR 9	GR 11
wt % oxide								
SiO_2	56.02	55.56	56.05	55.63	55.78	56.22	56.01	55.37
Al_2O_3	0.00	0.00	0.00	0.00	0.00	0.00	0.00	0.00
CaO	24.07	24.44	24.11	24.11	24.10	23.68	24.32	24.17
MgO	20.53	20.30	20.57	20.24	20.44	20.76	20.45	20.62
FeO	0.03	0.06	0.02	0.02	0.06	0.06	0.06	0.03
Total	100.65	100.37	100.76	100.00	100.37	100.71	100.84	100.19
cations								
Si	1.995	1.989	1.995	1.995	1.993	1.998	1.993	1.985
Al	0.000	0.000	0.000	0.000	0.000	0.000	0.000	0.000
Ca	0.919	0.938	0.919	0.927	0.923	0.902	0.927	0.928
Mg	1.090	1.083	1.091	1.082	1.089	1.100	1.085	1.101
Fe	0.001	0.002	0.001	0.001	0.002	0.002	0.002	0.001
Total	4.005	4.011	4.005	4.005	4.007	4.002	4.007	4.015
# of pts. in avg.	5	5	5	5	5	5	5	5

References, appendix 1.

Belruss, V., J. Kalnajs, and A. Linz, 1971, Top-seeded solution growth of oxide crystals from non-stoichiometric melts. Maeteral Research Bull., 6, 899-906.

Rase, D. E., and R. Roy, 1955, Phase equilibria on the system $BaO-TiO_2$. Jour. Amer. Ceramic Soc., 38, 102-113.

APPENDIX 2: Description of Apparatuses.

Ion microprobe

The ion probe used in this study is a Cameca IMS 3f which is controlled by an HP 9825A computer. It is located in the Department of Earth and Planetary Sciences, M. I. T. and is administered by a consortium of M. I. T., Harvard University, and Brown University. A basic description is given here while a much more complete treatment can be found in Lepareur and Gourgout (1979).

The primary beam of O^- ions (Ar and N also available) is achieved by first introducing O_2 gas at low pressure ($\sim 10^{-5}$ torr) into a duoplasmatron, where it is ionized and contained as a plasma. The negative particles are accelerated toward the sample by maintaining this unit at high voltage (10 KV) and the extraction electrode at ground potential. The primary beam is focused and the spot size adjusted by means of a series of electrostatic lenses and mechanical apertures. There is also an electrostatic deflector which when activated, moves the beam off the sample and into a Faraday cup which can measure the beam current. Other deflectors at the sample end of the primary gun provide the beam movement for the rastering mode.

The sample stage will accept polished specimens up to one inch in diameter. Location of a specific area of the sample surface under the primary beam is effected by x and y translation which can be motor controlled, and a reflecting light microscope. The stepping motors can be addressed by the computer, giving the capability of automatic step-scan analysis. Access to the sample chamber is through an airlock so that the rest of the system can be maintained at high vacuum ($\sim 10^{-8}$ torr), thus shortening sample-change time.

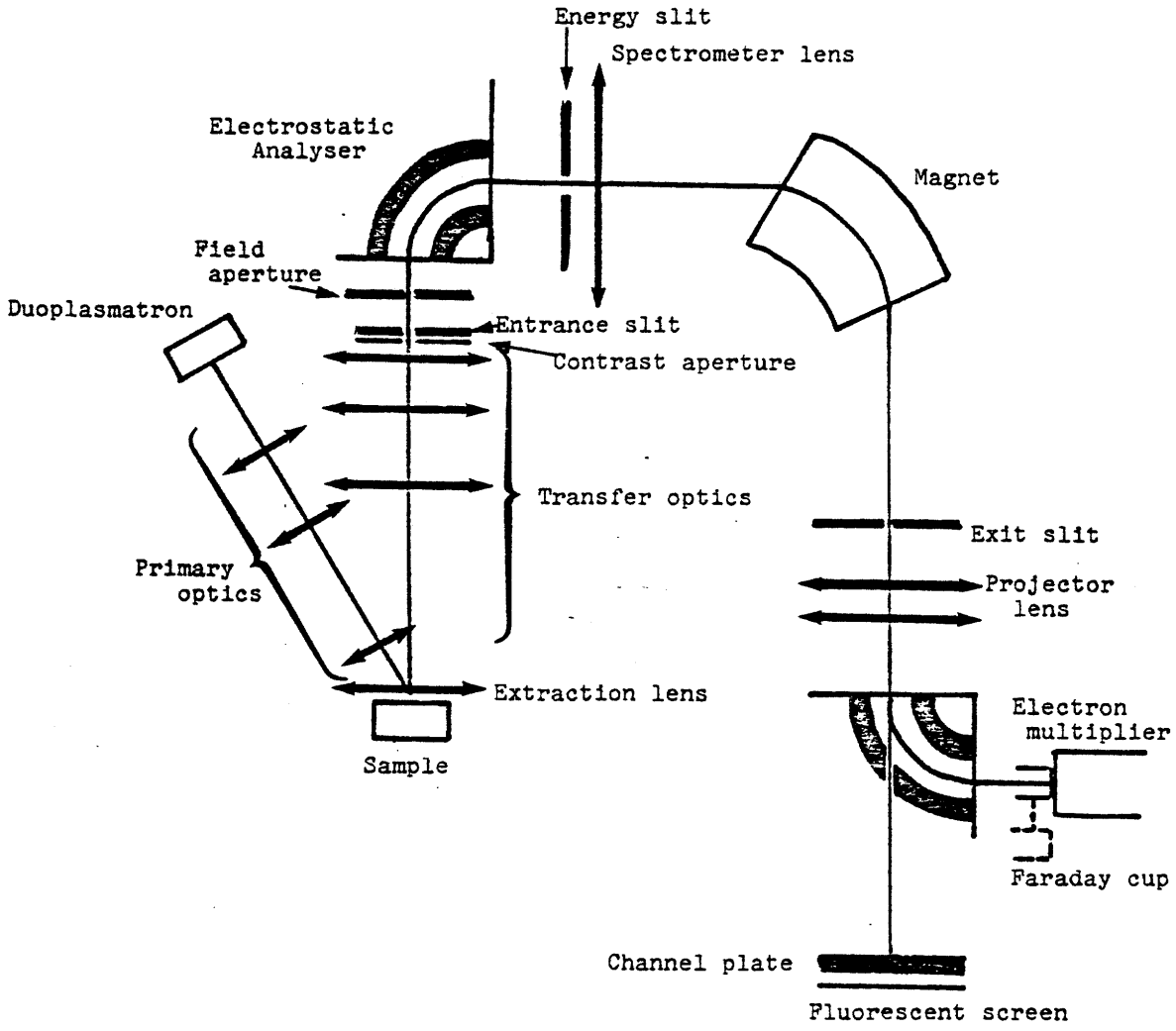

Figure A2-1. Schematic diagram of the Cameca IMS 3f showing components described in the text of this appendix.

The primary beam impinges on the sample surface, dislodging secondary ions. Positive secondary ions are accelerated into the analysis system by maintaining an extraction plate with a centered hole at 4500 V. After passing through the extraction lens the particles enter the transfer optics which are capable of accepting a secondary beam from one of three sizes of imaged field (maximum diameter = 30, 140, and 364 μm) and focusing it on the entrance slit. The extraction and transfer optics operate in such a way as to maintain, in the beam, the relative positions of particles from each point in the imaged area of the sample surface, focusing the beam to a corresponding point image at the entrance slit. Beyond this crossover point the image is inverted. Immediately in front of the slit is the contrast aperture, consisting of four selectable mechanical apertures which eliminate the diffuse edges of the gaussian shaped beam. Adjustment of the entrance slit controls the amount of ions reaching the mass spectrometer and the mass resolution. A narrow slit gives low count rates but higher mass resolution. After this slit is the field aperture which can be adjusted to one of three settings to mask part of the sample beam so that areas smaller than the entire imaged area can be examined. In the case of this study, the transfer optics were set for a 25 μm in diameter image field and field aperture #2 was used to eliminate all but the center 13 μm in diameter area.

The secondary beam passing the field aperture enters a 90° electrostatic analyser (ESA) which disperses the beam with respect to energy. The energy range to be studied is then selected by the placement and width of a slit after the ESA. Further selection is possible by offsetting the extraction voltage from the normal 4500 V, changing the range of energies seen by the ESA. The ions passing the energy slit are then focused on the

magnetic sector by the spectrometer lens. The magnet disperses the beam according to mass and a particular mass is focused on the exit slit by adjusting the magnetic field.

The mass-analysed image carried through the exit slit is re-inverted and magnified by the projector lens, giving the actual image of the selected mass. This image can be detected in one of three modes. It can be allowed to impinge on a channel plate, causing the emission of electrons which are then multiplied by a micro-electron multiplier. These electrons strike a fluorescent screen and the final image is observed through a binocular microscope, showing the spatial distribution of the element in the imaged area of the sample. The secondary ions can be measured quantitatively by engaging a second ESA which bends the beam into the measurement apparatus, consisting of a Faraday cup (replaced on the M. I. T. machine by a vibrating reed electrometer (VRE)) and an electron multiplier (EM). One of these two modes is selected depending on the count rate. The EM is more sensitive to low count rates, but its first diode deteriorates rapidly when exposed to high fluxes of particles. Selection is achieved by physical movement of the VRE into or out of the beam path.

Many of the machine parameters such as extraction voltage offset and magnetic field intensity which can be adjusted manually can also be controlled through the HP 9825A computer. This unit is programmed to handle machine adjustments during normal analytical procedures as well as collect and store data from the counting systems. Programs and data can be stored on magnetic tape cassettes, and data can also be output through a paper tape printer and/or an x,y plotter.

Piston-cylinder high pressure apparatus

This type of solid-media press was first described by Boyd and England (1960) and the R. P. I. equipment is basically the same except for a number of design modifications which allow the use of interchangeable parts.

A large press (100 tons) with a six-inch in diameter ram was used to contain the high pressure system consisting of a stack of various components. With the set-up in place, the large press is pressurized to keep the components from being forced apart when the sample assembly is pressurized (Figure A2-2). On the bottom of the stack, resting on the large ram, is a steel cylindrical block used as a spacer. Next is the unit containing the three-inch ram which provides the sample pressure. On top of this housing is a cylindrical bridge through which the small ram advances upwards toward the sample chamber. Within the space in the center of the bridge a one-inch in diameter hardened steel plug is placed on the three-inch ram (Figure A2-3). The sample piston rests on this plug and is centered in the bridge and on the ram by an attached collar. This system allows the use of different diameter sample chambers and pistons with the same ram. The R. P. I. facility presently has the capability to run sample assemblies of 1/2" and 3/4" diameter. A second collar fits in place at the top of the bridge to close the air-space and provide electrical contact between the bridge and the piston. The top of the bridge contains a depression through which cooling water is circulated during the experiment and a groove near the edge with a rubber O-ring. The need for these will be discussed shortly.

The sample plate rests on the bridge and consists of concentric bands of steel around a carbide steel cylinder which has an inside diameter of

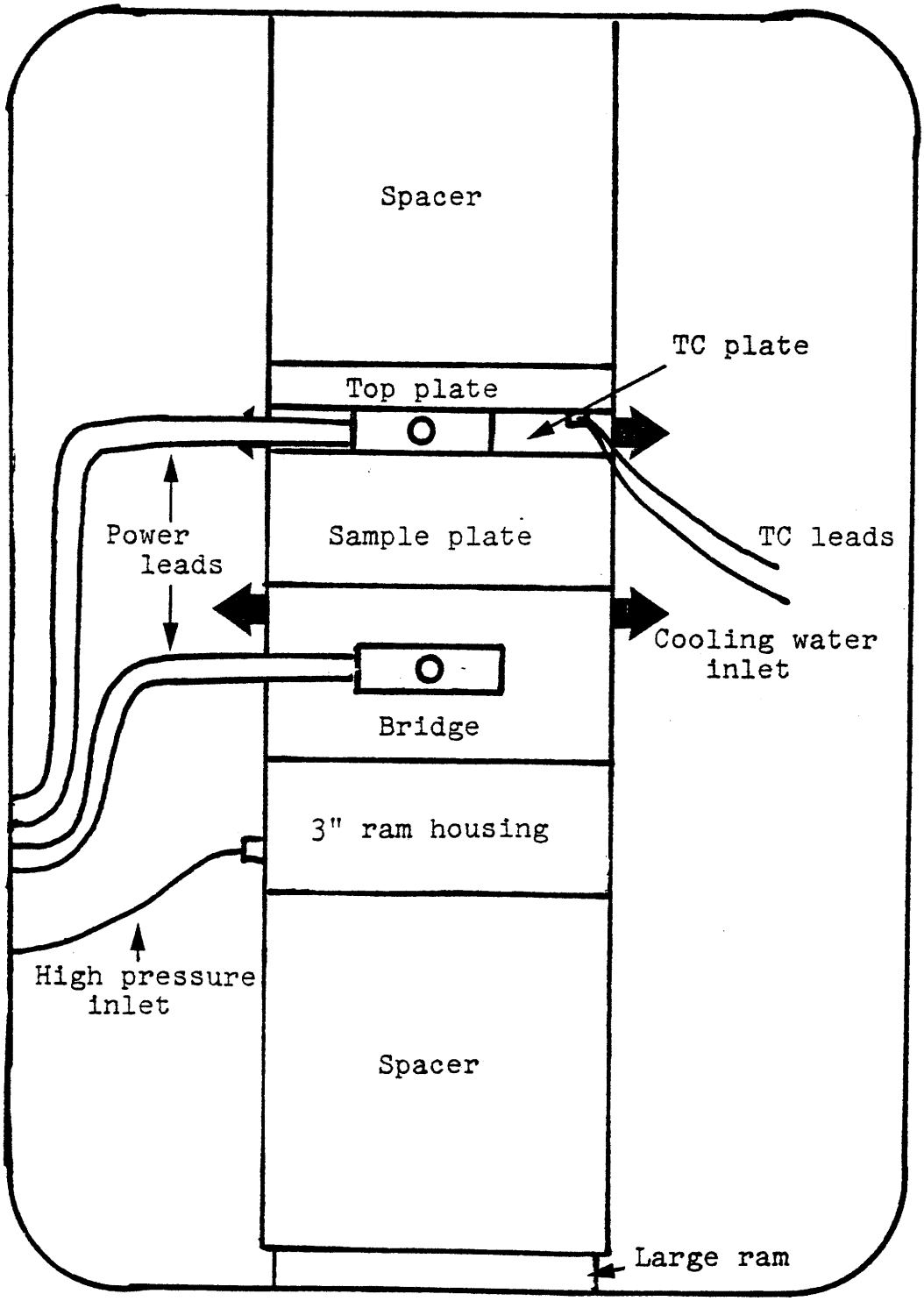

Figure A2-2. Schematic diagram of the R. P. I. piston-cylinder stack. Drawing is not to scale.

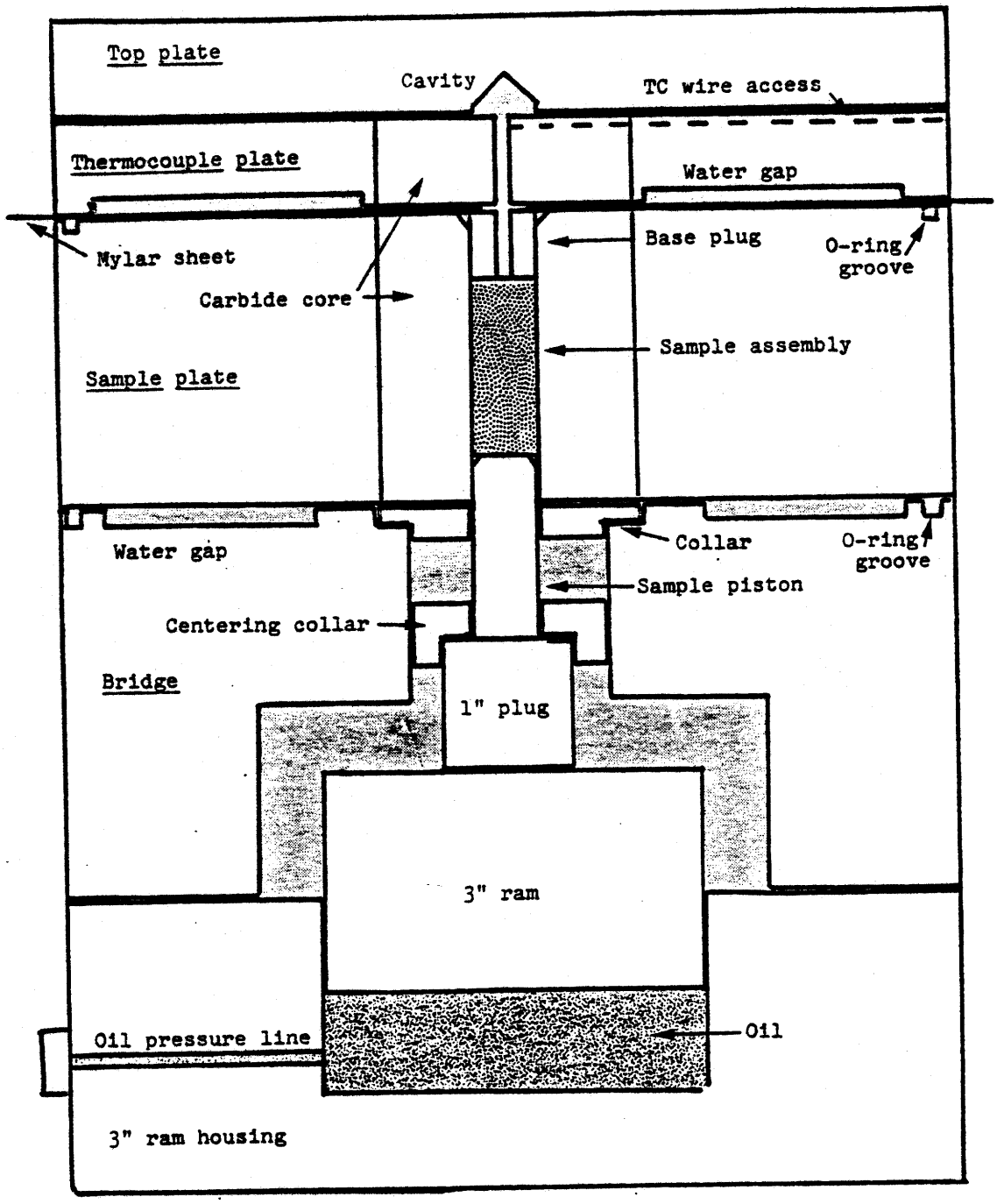

Figure A2-3. Cross section of of the piston cylinder components (except for spacers) showing the relative positions of the internal components. Drawing is not strictly to scale.

1/2" or 3/4", depending on which plate is used. The small piston pushes up into this chamber from below. The sample assembly described in the text is loaded into this cylinder and a steel plug with a pyrophyllite sleeve is loaded on top of it. This plug has a centered hole for introduction of the thermocouple (TC) into the assembly. The top of the sample plate cavity has a conical cross section and a fitted pyrophllite washer is used to fill this space. There is also a groove and O-ring near the edge of this piece.

The next unit is the thermocouple plate which has a carbide core with a hole for the TC. A radial groove in the top surface of the plate allows access for the TC wires, and a depression in the bottom side is used for cooling water circulation. A sheet of mylar with a hole the size of the sample assembly diameter is placed between the sample plate and the TC plate for electrical insulation. The TC plate acts as the back-stop for the force applied by the small ram except for the area of the thermocouple. Friction between the TC ceramic holder and the crushable alumina cylinder in the sample assembly prevents extrusion of the TC at high pressure. The uni-directional load of the sample piston on the assembly is transformed by the pressure medium (talc or NaCl) to a hydrostatic load on the sample itself.

A steel plate with a small cavity in the bottom (over the TC hole) is placed on top of the TC plate. This allows minor extrusion of the thermocouple, which occasionally happens, without allowing the TC wires to short to the apparatus. A mylar sheet is placed on top of this plate for electrical insulation and a second cylindrical block completes the stack.

After pressurization of the large ram, pressure is applied to the sample by pushing in the small ram. The oil used as the pressure medium

behind the rams is pressurized with an air-driven intensifier which is presently the limiting factor on the maximum obtainable sample pressure (∿35 Kbar for 1/2", ∿18 Kbar for 3/4"). Sample pressure during the run is estimated from the oil pressure on the three-inch ram and a conversion factor involving the cross sectional area of it and the sample piston.

Heating of the sample is achieved by passing a low-voltage, high-amperage current through the graphite cylinder in the sample assembly. This current is carried through electrical connections made through the TC plate and the bridge. The mylar sheets insure that the current passes through the graphite and not the apparatus. Temperature is controlled by a solid state system which compares the thermocouple voltage with a set point and adjusts the current to the furnace to eliminate deviations (Hadidiacos, 1972). The TC voltage is also displayed on a digital voltmeter. The R. P. I. system is set up with W25%Re/W3%Re thermocouples, but can be used with any appropriate TC. Tungsten-Rhenium has been shown to have only a slight dependence in output voltage with regard to pressure, and it is used for that reason as well as for its stability at temperatures to 2000°C.

Cooling water is circulated above and below the sample chamber so that the high temperatures generated in the sample assembly are dissipated and do not ruin the pressure plates. The relationship in mass between the cooled plate and the small furnace induces large temperature gradients in the sample assembly, therefore severely limiting the size of the isothermal hot zone. This must be considered when choosing a sample size and thermocouple location. The R. P. I. apparatus has been run to temperatures of 1550°C and is capable of higher temperatures, depending on the sample assembly materials.

References, appendix 2

Boyd, F. R., and J. L. England, 1960, Apparatus for phase-equilibrium measurements at pressures up to 50 kilobars and temperatures up to 1750°C. Jour. Geophysical Research, 65, 741-748.

Hadidiacos, C., 1972, Temperature controller for high-pressure apparatus. Carnegie Inst. Wash. Yearbook, 72, 620-622.

Lepareur, M., and J. M. Gourpout, 1979, Cameca ion microprobe IMS 3f physical principles (translated from the French by N. Shimizu). Cameca information circular.

APPENDIX 3: Data Reduction Programs.

A) HP 9825A and decwriter III using data for four isotopes stored on single files of HP cassette tapes.

Certain symbols on the 9825A are not available on the decwriter and automatic substitution of other symbols occurs. The substitutions are:

9825A		decwriter
$\sqrt{\ }$	=	\
↑	=	^
→	=	}
π	=	{

B) HP 25 using data for two or three isotopes stored on paper tape.

Code entries refer to key position on the calculator with the first digit being the row and the second being the position in that row (except for numerals, which are designated 0,n).

C) HP 25 York (1966) major axis least-squares straight line fit. All points carry the same weight.

D) HP 25 York (1966) "least-squares cubic" straight line fit. Each value of x and y is assigned a weight equal to the inverse of its variance.

References, appendix 3

York, D., 1966, Least-squares fitting of a straight line. Canadian Jour. Physics, 44, 1079-1086.

A) HP 9825A and decwriter data reduction.

```
0: "DATAMASHER (8/17/81),tape3/trk0/file6";
1: dim P[10,7],A$[32],D[500],B$[1],A[1],Z$[30,7],M[100,2],B[4],H[4]
2: fmt 0,c7,"FILE",f3.0;fmt 1,"MASS",f5.0;fmt 2,c60,/;fmt 4,c20,f8.0,/
3: fmt 3,f12.0,f12.0,f12.0,f12.0,f12.0;fmt 9,c20,e12.3;fmt 8,f12.0,f12.3
4: fmt 5,f12.0,f12.2,f12.0,e12.1;fmt 6,e9.1,f6.2;fmt 7,f12.0,e12.1
5: dsp "INSERT DATA TAPE and CONT.";stp ;fxd 0
6: ent "TRACK NUMBER (0 or 1)",r0;prt "TRACK",r0;spc
7: trk r0;ldf 0,A[*],Z$
8: for I=1 to A[1];wrt 16,Z$[I,1,7],I;next I;spc 2
9: ent "FILE NAME (6 CHARS,SPACES TOO!)",A$
10: for I=1 to A[1];if A$[1,6]=Z$[I,1,6];I}r23;num(Z$[I,7])}r22;jmp 2
11: next I
12: ldf r23,P[*],A$,D[*];P[10,2]}N;P[10,3]}C
13: wrt 10.2,A$;prt A$;spc 2
14: ent "PRINT RAW DATA?",B$;if B$#"y";sto "PROC"
15: wrt 10.3,0,P[1,1],P[2,1],P[3,1],P[4,1];fmt 0,/;wrt 10
16: for I=0 to C-1;wrt 10.3,I+1,D[4I+1],D[4I+2],D[4I+3],D[4I+4]
17: next I;wrt 10
18: "PROC":prt "RECORDED MASSES";0}B[1]}B[2]}B[3]}B[4]
19: for I=1 to N;wrt 16.1,P[I,1];10}P[I,4]
20: next I;spc 2
21: ent "REFERENCE MASS",M;wrt 10.4,"REFERENCE MASS",M;if M=0;sto "DISP"
22: for I=1 to N;if M#P[I,1];next I
23: I}M;ent "MACHINE B.G.?",B[M];0}B;N4+M}L
24: ent "CALCULATE MEAN",B$;if B$#"y";ent "MEAN?",B;jmp 3
25: for I=5 to C-1;D[L]+B}B;L+N}L
26: next I;B/(C-5)-B[M]}B
27: wrt 10.4,"MEAN",B
28: "DISP":cfs 7;sfs 8;ent "MASS ON DISPLAY",D;if D=0;sto "END"
29: wrt 10.4,"MASS ON DISPLAY",D
30: for I=1 to N;if D#P[I,1];next I
31: ent "PRINT NORMALIZED DATA?",B$;if B$#"y";cfs 8
32: I}D;ent "MACHINE B.G.",B[D];ent "SAMPLE B.G.",V
33: wrt 10.4,"MACHINE B.G.",B[D];wrt 10.4,"SAMPLE B.G.",V;if M=0;sto "C0"
34: M}L;D}S;for I=0 to 9;B/D[L]}H;if fls8;wrt 10.5,I+1,H,H(D[S]-B[D]-V),0
35: L+N}L;S+N}S;next I;wrt 10
36: "C0":ent "STARTING CYCLE?",0;wrt 10.4,"STARTING CYCLE",0;0N+M}L;0N+D}S
37: ent "C0 VALUE?",Z;wrt 10.4,"C0 VALUE",Z
38: if fls8;wrt 10.2,"X    NORM. FACTOR  C(NORM) C(NORM)/C0            "
39: for I=0 to C-1;1}H;if M#0;B/D[L]}H
40: H(D[S]-B[D]-V)}A;I+1}X;A/Z}Y;if fls8;wrt 10.5,X,H,A,Y
41: if Y<=0;1}Y
42: L+N}L;S+N}S;ln(Y)}Y;I}r16;ssb "STO"
43: next I;wrt 10
44: "TAIL":ent "SUBTRACT TAIL?",B$;if B$#"y";sto "FURT"
45: wrt 10.2,"CALCULATION OF TAIL END                    ";ssb "SLOP"
46: wrt 10.2,"TAIL END SUBTRACTED                        "
47: r1}R;exp(r4)}W;ent "LAST CYCLE TO TREAT",Q
48: for I=0+1 to Q;exp(M[I,2])-W*exp(IR)}Y;if fls8;wrt 10.7,I,Y
49: if Y<=0;1}Y
50: ln(Y)}Y;I}X;I-1}r16;ssb "STO"
*32046
```

```
51: next I;wrt 10
52: "FURT":ent "FURTHER TREATMENT?",B$;if B$#"y";sto "DISP"
53: ent "ANGSTROMS/CYCLE?",U;wrt 10.4,"ANGSTROMS/CYCLE",U
54: ent "TREATMENT? THIN FILM=1, COUPLE=2",Z;Jmp Z
55: wrt 10.2,"THIN FILM";sfs 7;sto "THIN"
56: "COUP":wrt 10.2,"DIFFUSION COUPLE";fxd 0
57: ent "CALCULATE C(0)?",B$;if B$#"y";sto "CONC"
58: enp "TIME(sec)",r8
59: enp "FIRST CYCLE NO.",r1
60: exp(M[r1,2])}r2;prt "FIRST C(X)",r2;r1-0}r1
61: enp "SECOND CYCLE NO.",r3
62: exp(M[r3,2])}r4;prt "SECOND C(X)",r4;r3-0}r3
63: r2/r4}A;fxd 2;prt "C(1)/C(2)=",A;fxd 0;ent "D?",r9
64: r1/2\(r9r8)}X;ssb "ERF"
65: S}r5;r3/2\(r9r8)}X;ssb "ERF"
66: S}r6;r5/r6}r10;wrt 16.6,r9,r10;ent "NEXT D?",r9;if r9#0;Jmp -2
67: fxd 5;prt "C(01)=",r2/r5;prt "C(02)=",r4/r6;fxd 2;spc 2
68: ent "RESULT SATISFACTORY?",B$;if B$#"y";Jmp -9
69: "CONC":ent "CONC. AT ZERO",E;wrt 10.9,"CONC. AT ZERO",E
70: 2.515517}r1;.802853}r2;.010328}r3;1.432788}r4;.189269}r5;.001308}r6
71: 0}P;ent "LAST CYCLE TO TREAT",Q
72: for I=0+1 to Q;P+U}P;exp(M[I,2])/E}K
73: ln(4/KK)}K;if K<0;Jmp 3
74: \K}K;(K-(r1+r2K+r3KK)/(1+r4K+r5KK+r6K^3))/\2}Y
75: wrt 10.8,P}X,Y;I-1}r16;ssb "STO"
76: next I;wrt 10;ent "CALCULATE SLOPE?",B$;if B$="y";ssb "SLOP"
77: ent "ANOTHER MASS?",B$;if B$="y";sto "DISP"
78: sto "END"
79: "END":ent "ANOTHER FILE?",B$;if B$="y";sto 2
80: dsp "INSERT PROGRAM TAPE & CONT.";stp
81: trk 0;cfs ;ldf 0
82: "STO":r16+1}r16;X}M[r16,1];Y}M[r16,2];ret
83: "SLOP":0}r11}r12}r13}r14}r15}r17}r18}r20
84: wrt 10.2,"SLOPE CALCULATION, POINTS NOT USED            "
85: ent "FIRST CYCLE",G;ent "LAST CYCLE",Q;G-1}r19;fxd 3
86: wrt 10.4,"FIRST CYCLE",G;wrt 10.4,"LAST CYCLE",Q;fmt 1,f8.0,f8.3
87: for I=G to Q;wrt 16.1,M[I,1],M[I,2];ent "USE?",B$
88: if B$="y";1+r15}r15;1+r19}r19;M[I,1]}M[r19,1];M[I,2]}M[r19,2]
89: if B$#"y";wrt 10.8,M[I,1],M[I,2]
90: next I;spc 2
91: for I=G to r19;M[I,1]+r11}r11;M[I,2]+r12}r12
92: M[I,1]^2+r17}r17;M[I,2]^2+r18}r18;next I
93: for I=G to r19;(M[I,1]-r11/r15)^2+r13}r13
94: (M[I,2]-r12/r15)^2+r14}r14
95: (M[I,1]-r11/r15)(M[I,2]-r12/r15)+r20}r20;next I
96: (r14-r13+\((r14-r13)^2+4r20^2))/2r20}r1;r20/\(r13r14)}r2
97: r1\((1-r2r2)/r15)/r2}r3;(r12-r1r11)/r15}r4
98: \(r13/(r15-1))}r5;\(r14/(r15-1))}r6;abs(r2)}r16
99: (r6-r5r1)^2/r15+(1-r16)r1(2r5r6+r11r1(1+r16)/r16r16r15)}r7
100: if r7<0;0}r7
*955
```

```
101: if r7>0;\r7}r7
102: wrt 10.9,"SLOPE",r1;wrt 10.9,"+/-",r3;wrt 10.9,"INTERCEPT",r4
103: wrt 10.9,"+/-",r7;wrt 10.9,"CORRELATION COEF",r2;wrt 10
104: ent "CALCULATE D?",B$;if B$#"y";jmp 6
105: ent "TIME(sec)?",r8;wrt 10.4,"TIME (SEC)",r8;fmt 3,c20,e12.1
106: if fls7;wrt 10.3,"DIFFUSION COEF.",-1/4e16r1r8
107: if fls7;wrt 10.3,"+/-",abs(r3/4e16r1r1r8)
108: if not fls7;wrt 10.3,"DIFFUSION COEF.",1/4e16r1r1r8
109: if not fls7;wrt 10.3,"+/-",abs(r3/2e16r1^3r8)
110: wrt 10;ret
111: "ERF":exp(-XX)/\{}A;if X>2;sto "ERFC"
112: 2XA}A;A}S;.5}r10
113: AXX/(r10+1)}A;S+A}S;r10+1}r10
114: if A>1e-10;jmp -1
115: 1-S}S;jmp 4
116: "ERFC":8}r10;X}S
117: X+r10/S}S;r10-.5}r10;if r10>0;jmp 0
118: A/S}S
119: ret
120: "THIN":0}P;ent "LAST CYCLE TO TREAT?",Q
121: for I=0+1 to Q;P+U}P;M[I,2]}Y;wrt 10.8,PP}X,Y;I-1}r16;gsb "STO"
122: next I;wrt 10;ent "CALCULATE SLOPE?",B$;if B$="y";gsb "SLOP"
123: ent "ANOTHER MASS?",B$;if B$="y";sto "DISP"
124: sto "END"
*17312
```

B) HP 25 data reduction, first step.

Switch calculator to PRGM, press f PRGM, then key in program.

line #	key entry	line #	key entry	registers	
01	RCL 1	21	f FIX 0	R_0	$m.b._{88}$
02	-	22	R/S	R_1	$m.b._{152}$
03	x⇄y	23	RCL 6	R_2	$m.b._{40}$
04	RCL 0	24	÷	R_3	M
05	-	25	R↓	R_4	bkg_{88}
06	R↓	26	x	R_5	bkg_{152}
07	R↓	27	x⇄y	R_6	88_0
08	R↓	28	CLx	R_7	152_0
09	RCL 2	29	RCL 5		
10	-	30	-		
11	g 1/x	31	R/S		
12	RCL 3	32	RCL 7		
13	x	33	÷		
14	f FIX 2	34	x⇄y		
15	R/S	35	f SCI 1		
16	↑	36	R/S		
17	R↓	37	R↓		
18	x	38	GTO 00		
19	RCL 4				
20	-				

Switch to RUN, press f PRGM.

Input constants into registers.

Input data: 40, ↑, 88, ↑, 152, R/S.

Output results: normalization factor, R/S, 88_n, R/S, 152_n, R/S,

$88_n/88_0$, R/S, $152_n/152_0$.

Repeat last two lines (input data, output data) until all data has been reduced.

B) HP 25 data reduction, second step.

Calculate best fit line through tail end of normalized data to give

$C_t = ae^{bx}$ where C_t is the value of the tail at a given x.

Switch calculator to PRGM, press f PRGM, then key in program.

line #	key entry	registers	
01	$x \rightleftarrows y$	R_0	x
02	RCL 3	R_1	b
03	-	R_2	a
04	STO 0	R_3	x_0
05	RCL 1		
06	x		
07	g e^x		
08	RCL 2		
09	x		
10	-		
11	RCL 0		
12	g x^2		
13	R/S		
14	$x \rightleftarrows y$		
15	GTO 00		

Switch to RUN, press f PRGM.

Input constants (a, b, x_0) into proper registers.

Input data: cycle no., ↑, $88_n/88_0$, R/S.

Output results: x^2, R/S, $88_n/88_0 - C_t$.

Repeat last two lines until all data have been reduced.

C) HP 25 major axis, step one.

Calculate $\bar{x}$ and $\bar{y}$ with error bars.

Switch the calculator to PRGM, press f PRGM, then key in program.

line #	key entry	line #	key entry	registers	
01	RCL 0	26	x	R_0	$\bar{y}$
02	-	27	÷	R_1	$\bar{x}$
03	↑	28	R/S	R_2	ΣV_i^2
04	g x^2	29	RCL 5	R_3	n
05	STO + 2	30	RCL 6	R_4	ΣV_i
06	R↓	31	RCL 2	R_5	$\Sigma U_i V_{i_2 i}$
07	x⇄y	32	x	R_6	ΣU_i^2
08	RCL 1	33	f $\sqrt{x}$	R_7	ΣU_i, r
09	-	34	÷		
10	+	35	STO 7		
11	GTO 00	36	R/S		
12	RCL 2	37	÷		
13	RCL 6	38	1		
14	-	39	RCL 7		
15	↑	40	g x^2		
16	g x^2	41	-		
17	RCL 5	42	RCL 3		
18	g x^2	43	÷		
19	4	44	f $\sqrt{x}$		
20	x	45	x		
21	+	46	R/S		
22	f $\sqrt{x}$	47	R↓		
23	+	48	RCL 1		
24	RCL 5	49	x		
25	2				

Switch to RUN, press f PRGM, f REG.

Input constants ($\bar{x}$, $\bar{y}$) into proper registers.

Input data: x_i, ↑, y_i, R/S

Repeat until all data entered.

Press GTO 12, R/S.

Output results: slope, R/S, correlation coef. (r), R/S, σ_{slope}, R/S.

Finish calculation: CHS, RCL 0, +, intercept.

C) HP 25 major axis, step two.

Switch calculator to PRGM, press f PRGM, then key in program.

line #	key entry	line #	key entry	registers	
01	RCL 4	21	-	R_0	n
02	RCL 1	22	x	R_1	$\bar{x}$
03	x	23	RCL 3	R_2	σ_x
04	1	24	RCL 2	R_3	σ_y
05	RCL 6	25	RCL 4	R_4	slope
06	+	26	x	R_5	σ_{slope}
07	x	27	-	R_6	r
08	RCL 6	28	g x^2	R_7	
09	g x^2	29	RCL 0		
10	÷	30	÷		
11	2	31	+		
12	RCL 3	32	f $\sqrt{\bar{x}}$		
13	x	33	GTO 00		
14	RCL 2				
15	x				
16	+				
17	RCL 4				
18	x				
19	1				
20	RCL 6				

Switch to RUN, press f PRGM.

Input constants into registers.

Press R/S, $\sigma_{intercept}$.

D) HP 25 "least-squares cubic", step one.

Make an estimate of the slope (b).

Switch to PRGM, press f PRGM, then key in program.

line #	key entry	line #	key entry	registers	
01	g x^2	26	RCL 1	R_0	b^2
02	g 1/x	27	RCL 3	R_1	$\omega(Y_i)$, W_i
03	STO 1	28	x	R_2	$\omega(X_i)$
04	R↓	29	STO + 7	R_3	Y_i
05	STO 3	30	RCL 1	R_4	ΣW_i
06	R↓	31	GTO 00	R_5	$\Sigma W_i X_i{}_2$
07	g x^2	32	RCL 5	R_6	$\Sigma W_i X_i$
08	g 1/x	33	RCL 4	R_7	$\Sigma W_i Y_i$
09	STO 2	34	R/S		
10	R/S	35	÷		
11	RCL 1	36	R/S		
12	R/S	37	RCL 7		
13	x	38	RCL 4		
14	RCL 0	39	÷		
15	RCL 1	40	R/S		
16	x	41	RCL 6		
17	RCL 2	42	GTO 00		
18	+				
19	÷				
20	STO + 4				
21	STO 1				
22	x				
23	STO + 5				
24	x				
25	STO + 6				

Switch to RUN, press f PRGM, f REG.

Input constant (b^2) into register.

Input data: X_i, ↑, σ_x, ↑, Y_i, ↑, σ_y, R/S.

Output individual point results: $\omega(X_i)$, R/S, $\omega(Y_i)$, R/S, W_i.

Repeat above two steps until all data is entered.

Press GTO 32, R/S.

Output final results: ΣW_i, R/S, $\bar{X}$, R/S, $\bar{Y}$, R/S, $\Sigma W_i X_i^2$.

D) HP 25 "least-squares cubic", step two.

Switch to PRGM, press f PRGM, then key in program.

line #	key entry	line #	key entry
01	R↓	26	x⇄y
02	STO 2	27	x
03	R↓	28	f LAST x
04	RCL 0	29	R↓
05	-	30	x⇄y
06	x⇄y	31	STO 2
07	RCL 1	32	÷
08	-	33	STO + 4
09	x⇄y	34	x⇄y
10	R↓	35	R↓
11	x	36	x
12	f LAST x	37	RCL 2
13	x	38	÷
14	STO + 7	39	STO + 5
15	f LAST x	40	R↓
16	R↓	41	RCL 2
17	x⇄y	42	x
18	x	43	x
19	STO ÷ 2	44	STO + 6
20	f LAST x	45	GTO 00
21	R↓		
22	R↓		
23	RCL 2		
24	g 1/x		
25	STO + 3		

registers	
R_0	$\bar{Y}$
R_1	$\bar{X}$
R_2	$\omega(X_i)$, $\omega/W_i^2U_i^2$, U
R_3	$\Sigma[W_i^2U_i^2/\omega(X_i)]$
R_4	$\Sigma[W_i^2U_iV_i/\omega(X_i)]$
R_5	$\Sigma[W_i^2V_i^2/\omega(X_i)]$
R_6	$\Sigma(W_iU_iV_i)$
R_7	$\Sigma(W_iU_i^2)$

Switch to RUN, press f PRGM, f REG.

Input constants ($\bar{X}$, $\bar{Y}$) into registers.

Input data: X_i, ↑, Y_i, ↑, $\omega(X_i)$, ↑, W_i, R/S.

Repeat until all data is entered.

Retrieve results from registers: RCL 3, $\Sigma[W_i^2U_i^2/\omega(X_i)]$, RCL 4, $\Sigma[W_i^2U_iV_i/\omega(X_i)]$, RCL 5, $\Sigma[W_i^2V_i^2/\omega(X_i)]$, RCL 6, $\Sigma(W_iU_iV_i)$, RCL 7, $\Sigma(W_iU_i^2)$.

D) HP 25 "least-squares cubic", step three.

Switch to PRGM, press f PRGM, then key in program.

line #	key entry	line #	key entry	registers	
01	RCL 4	26	3	R_0	α
02	2	27	CHS	R_1	$\beta, \sqrt{\alpha^2-\beta}$
03	x	28	x	R_2	
04	RCL 3	29	+	R_3	$\Sigma[W_i^2U_i^2/\omega(X_i)]$
05	3	30	2	R_4	$\Sigma[W_i^2U_iV_i/\omega(X_i)]$
06	x	31	÷	R_5	$\Sigma[W_i^2V_i^2/\omega(X_i)]$
07	÷	32	RCL 0	R_6	$\Sigma(W_iU_iV_i)$
08	STO 0	33	g x^2	R_7	$\Sigma(W_iU_i^2)$
09	R/S	34	RCL 0		
10	f LAST x	35	x		
11	RCL 5	36	+		
12	RCL 7	37	RCL 0		
13	-	38	g x^2		
14	x⇄y	39	RCL 1		
15	÷	40	-		
16	STO 1	41	f $\sqrt{x}$		
17	R/S	42	STO 1		
18	RCL 6	43	3		
19	RCL 3	44	f y^x		
20	÷	45	÷		
21	CHS	46	g $\cos^{-1}$		
22	R/S	47	R/S		
23	x⇄y	48	3		
24	RCL 0	49	÷		
25	x				

Switch to RUN, press f PRGM.

Input constants (sums from previous step) into registers.

Output results: R/S, α, R/S, β, R/S, γ, R/S, ϕ, R/S.

Complete calculations: STO 2, f cos, RCL 1, 2, x, STO 1, x, +, b_1, RCL 2, 120, +, f cos, RCL 1, x, RCL 0, +, b_2, RCL 2, 240, +, f cos, RCL 1, x, RCL 0, +, b_3.

b_3 is usually the root of the cubic equation that satisfies the data as the best fit.

D) HP 25 "least-squares cubic", step four.

Switch to PRGM, press f PRGM, key in program.

line #	key entry	line #	key entry	registers
01	STO 5	21	2	R_0 $\bar{Y}$
02	R↓	22	-	R_1 $\bar{X}$
03	RCL 0	23	÷	R_2 b
04	-	24	f $\sqrt{x}$	R_3 ΣW_i
05	x⇄y	25	R/S	R_4 $\Sigma W_i X_i^2$
06	RCL 1	26	RCL 0	R_5 W_i
07	-	27	RCL 1	R_6 $\Sigma W_i(bU_i - V_i)^2$
08	RCL 2	28	RCl 2	R_7 $\Sigma W_i U_i^2$
09	x	29	x	
10	x⇄y	30	-	
11	-	31	R/S	
12	g x^2	32	R↓	
13	RCL 5	33	g x^2	
14	x	34	RCL 4	
15	STO + 6	35	RCL 3	
16	GTO 00	36	÷	
17	RCL 6	37	x	
18	RCL 7	38	f $\sqrt{x}$	
19	÷	39	GTO 00	
20	x⇄y			

Switch to RUN, press f PRGM.

Input constants ($\bar{Y}$, $\bar{X}$, b, ΣW_i, $\Sigma W_i X_i^2$, $\Sigma W_i U_i^2$) into registers and 0, STO 6.

Input data: X_i, ↑, Y_i, ↑, W_i, R/S.

Repeat until all data is entered.

Press # of data points, GTO 17, R/S.

Output final results: σ_b, R/S, intercept (a), R/S, σ_a.

APPENDIX 4: Ion Probe Parameters, Early Attempts.

A number of sets of analytical conditions were explored for the Cameca IMS 3f while searching for optimum results. They were discarded for various reasons and this list is an attempt to summarize them.

Primary Beam							
current (nA)	diameter (μm)	Rastered area side length (μm)	Raster/no raster option*	Imaged field (μm)	Field aperture	2ndary voltage offset (V)	Reason for abandoning
6	∿10	50	n	25	1	-80	slow penetration rate
6	∿10	50	n	25	2	-75	slow penetration rate
6	∿10	100	y	25	2	-75	deep pit at center of hole
6	∿10	100	y†	25	2	-75	rough bottom, irreproducible positioning
10	∿15	50	n	25	2	-75	slow penetration rate
20	∿20	50	n	25	2	-75	large tail on surface test
20	∿20	100	n	25	2	-75	intermediate penetration rate

*Raster turned off for one cycle in every fifteen cycles.

†Sample position shifted for each no raster cycle, then shifted back to original position.